Design of a general plasma simulation model : fundamental aspects and applications

Document status and date:
Published: 01/01/2000

Document Version:
Publisher's PDF, also known as Version of Record (includes final page, issue and volume numbers)

Please check the document version of this publication:

• A submitted manuscript is the version of the article upon submission and before peer-review. There can be important differences between the submitted version and the official published version of record. People interested in the research are advised to contact the author for the final version of the publication, or visit the DOI to the publisher's website.
• The final author version and the galley proof are versions of the publication after peer review.
• The final published version features the final layout of the paper including the volume, issue and page numbers.

Link to publication

Download date: 16. Nov. 2023

Design of a General Plasma Simulation Model, Fundamental Aspects and Applications

PROEFONTWERP

ter verkrijging van de graad van doctor
aan de Technische Universiteit Eindhoven,
op gezag van de Rector Magnificus, prof.dr. M. Rem,
voor een commissie aangewezen door het College
voor Promoties in het openbaar te verdedigen op
woensdag 4 oktober 2000 om 16.00 uur

door

Gerard Maria Janssen

geboren te Roermond

Dit proefontwerp is goedgekeurd door de promotoren:

prof.dr.ir. D.C. Schram

en

prof.dr.ir. H.W.M. Hoeijmakers

Copromotor:

dr. J.A.M. van der Mullen

Contents

iv

Chapter 1

General Introduction

1.1 Introduction

Through their wide variety of operational conditions, plasma sources offer a tremendous freedom in the generation of radiation and the creation of chemical compositions. As a result the field of technological and industrial plasma applications is expanding strongly. Several plasma applications are found in the literature:

- High-efficiency light sources. Examples are the well-known TL-lamp and the less known QL-lamp and S-lamp. Both the QL- and S-lamp are electrode-less lamps. For the QL-lamp the energy is inductively coupled into an argon-mercury gas mixture [1], whereas for the S-lamp microwave energy is coupled into sulphur gas [2]. Another example of the use of plasmas as a light source is the plasma display panel (PDP) [3].

- Material processing, such as deposition, etching, cutting, welding, cleaning and surface modification (see for example Fauchais [4] and Boulos *et al.* [5]). Typical applications are the deposition plasmas used in the solar cell industry for depositing high-quality material, e.g. thin films of hydrogenated amorphous silicon. We may distinguish here between the use of

  1. RF-plasmas, used in plasma enhanced chemical vapour deposition (PECVD) reactors [6];
  2. expanding thermal plasmas (ETP), for instance created by a cascaded arc [7, 8], and
  3. inductively coupled plasmas or microwave (MW) induced plasmas [9].

  A rather unexpected application is the treatment of archeological artifacts [10] (this could be characterised by etching, cleaning or surface modification). Another remarkable application is the creation of dust particles in plasmas [11].

- Spectrochemical analysis (analytical chemistry). Examples are inductively coupled plasmas (ICP) [12] and microwave-induced plasmas (MIP) like the Beenakker cavity [13], the surfatron [14] and the Torche à Injection Axiale (TIA) [15] that can be used for element detection with very low detection limits.

- Particle sources. Apart from the microwave plasmas for the production of negative ions, used in neutral beam injectors [16] for the heating of Tokamak plasmas, also the cascaded arc plasmas can be used for this purpose [10]. An example of a positive ion source can be found in this thesis (chapters 4 and 5) where a hydrogen cascaded arc plasma is optimised to achieve high ion power fluxes, to simulate the plasma near the divertor plates in a Tokamak.
- Waste treatment (e.g. detoxification). For this purpose thermal plasma torches [17] and cascaded arc plasmas [18] or microwave plasmas [16] are used.

The plasmas referred to above all have their particular characteristics, with differences in energy coupling mechanisms, gas mixtures, pressure, flow, and so on. In the next section, their characteristics will be classified.

1.2   Characteristics of the plasmas considered

The features and parameters of the plasmas studied in this thesis can be classified in three main groups. First we have the *configuration* which, apart from the specific operational conditions, also deals with the different ways of energy coupling into the plasma. Second, we have the *transport* properties with as main division the open ('convective' driven) versus confined systems. Third, we have the chemical *composition*, which on its most basic level leads to the degree of ionisation and dissociation.

1.2.1   Configuration

Apart from the global operation conditions of the plasmas, such as pressure and power, it is useful to distinguish the several ways to couple energy into a plasma. The cascaded arc (CA) is driven by a direct current (DC), the ICP and QL-lamp are inductively coupled plasmas whereas the S-lamp, the plasma used for optical fibre production (in the following abbreviated as POF) and the Torche à Injection Axiale (TIA) are microwave (MW) induced plasmas. Especially for the latter group the skin depth is an important feature.

1.2.2   Transport

Transport can make a distinction between confined and open plasma configurations. The confined configurations (the TL-lamp, the low pressure QL- and high pressure S-lamp) generate diffusion-dominated plasmas. On the other hand the open ICP, the CA, the vacuum chamber and the MW POF are dominated by the flow, i.e. they are strongly convective plasmas.

1.2.3   Composition

The most striking property of a plasma, namely the presence of charged particles immediately leads to the main division of the plasma into two groups: the electrons and the heavy particle species. In many cases, both groups have their own temperatures. Only so-called low-

temperature plasmas, with electron temperatures around 1 eV, are considered in this thesis. The pressure in the plasmas varies from low pressure (around $10 - 20$ Pa in a vacuum chamber) to atmospheric pressures and higher (around 5×10^4 Pa at the inlet of a cascaded arc and around 5×10^5 Pa in the S-lamp). As a consequence, the species in the plasmas are usually not in equilibrium, so that the heavy particle temperature differs from the electron temperature.

We will make a distinction between *thermal equilibrium*, a situation in which all the species present in the plasma (i.e. electrons and heavy particle species) have equal temperatures, and *chemical equilibrium*, a situation in which no net production or destruction of species occurs, i.e. the number densities of all species present in the plasma obey the Saha equation for ionisation/recombination equilibrium and the Guldberg-Waage equation for dissociation/association equilibrium. Thermal equilibrium does not automatically imply chemical equilibrium and vice-versa. Local Thermal Equilibrium (LTE) is the situation where both thermal and chemical equilibrium are achieved[a], though the equilibrium characteristics (such as the temperature) can depend on the location. In order to reach LTE the pressure must be so high that the elastic energy transfer from electrons to heavy particle species is effective enough. Another condition for the presence of LTE is that the electron number density is so high that three-particle recombination can compete with the efflux of charged particles.

Another characteristic of a plasma is its dissociation degree. This implies a division in atomic (like argon) and molecular plasmas (like hydrogen and oxygen). There is a large difference between these two types of plasmas. In atomic plasmas, the description of kinetics is already complex, although the number of transport-sensitive (TS) species is limited. The latter refers to species for which the timescale in which chemical reactions take place is of the same order of magnitude as the timescale in which the species is transported to other regions in the plasma. For the TS species the full mass balances have to be solved. On the other hand we have local chemistry (LC) species, which are determined by the TS species and the elementary processes. For the LC species, transport is relatively unimportant and their number densities are related to those of the TS species by so-called Collisional-Radiative (CR) models. For a clarification we take here the argon plasma as an example. The TS species are the argon atom in the ground state and the argon ion. All excited states are considered as LC species and their number densities depend on that of the TS species, the electron temperature and number density. In dealing with an argon-mercury mixture, such as in the TL- and QL-lamp, it is useful to treat the first excited state also as a TS species. By doing so, it is possible to treat the influence of diffusion and radiation transport on the first excited state.

Molecular plasmas are even more complicated. Apart from the number of species being higher than in an atomic plasma, one has to take into account dissociation/association processes, rovibrational excitation processes and possibly the multi-temperature behaviour of the heavy particle species. Apart from a heavy particle temperature one can distinguish between excitation, rotation and vibration temperatures which can all be different. However, for the molecular plasmas considered in this thesis we will assume only two temperatures, one for the electrons and one for the heavy particle species.

Another factor is the influence of recombination processes. In molecular plasmas dissociative

---

[a] These plasmas are referred to as *thermal plasmas* in literature.

recombination processes can be very important, since the associated reaction rates can easily overrule that of the three-particle recombination. We will see an example of this in chapter 5 of this thesis, which discusses the influence of the molecular ion H_2^+ in the chemistry in a hydrogen cascaded arc plasma.

1.3   The need for a plasma simulation tool

From the considerations in the previous section, it is clear that due to the wide range of operating conditions, the plasma state offers a tremendous chemical freedom. This implies that plasmas are suitable for a lot of applications, of which a few were discussed in the general introduction. However, improving and optimising the plasmas used in industry is not carried out very efficiently at this moment:

- The choice of the chemical composition of plasmas is in many cases a matter of trial and error.
- Optimising plasma sources, which in nowadays practice generally means designing, constructing and testing different sources, is not only very time-consuming but is also a substantial investment in resources.

To avoid excessive empirism another approach is needed. It is generally recognised that in the design of efficient industrial processes, simulation by means of computational methods, can be a powerful approach. Main advantages of numerical simulation over experiments can be found in:

- A reduction of time and costs.
- The ability to study the fundamental phenomena in detail and consequently gain improved insight into the processes occurring in the plasma sources.
- The possibility to optimise the plasma source and therewith the industrial process by considering a multitude of possible configurations and conditions.
- The generation of detailed local information, information that might be difficult to obtain in experiments.

Numerical simulation has proven its value in the aircraft industry, where computational methods are used not only in research groups, but also in the design and development of for example an aircraft and its components such as wings and propulsion installations. In the field of chemical vapour deposition (CVD) several computational methods are available nowadays to optimise reactor geometries [19, 20]. One of the more recent developments is the use of computational methods to numerically simulate plasmas. The existing commercially availably numerical tools (PHOENICS, FLUENT, FLOW3D, STAR-CD and CFX) were originally designed for the numerical simulation of flows and/or CVD processes (e.g. PHOENICS CVD). As a consequence, the typical characteristics of plasmas, like the multi-temperature character and the presence of charged species, can not always be handled properly by these tools. Sometimes, an option is to link a method that computes the flow field and heat transfer to a method for the plasma, which implies a weak interaction. Therefore the need exists for a plasma simulation tool which is capable of handling plasma sources used in research and industrial applications, i.e.: for equilibrium

and non-equilibrium situations in atomic and molecular gas mixtures and in flowing and non-flowing configurations. Before we discuss the design of such a model in section 1.4, we will take a look at the tools that already exist in the field of plasma physics.

1.3.1   State of the art

In the field of plasma physics, only one computational method is commercially available: the so-called SIGLO code[b], developed by Boeuf, Pitchford, the Centre de Physique des Plasmas et Applications de Toulouse (CPAT) and Kinema Research & Software (France). It is software for non-thermal plasmas, with low ionisation degree (approximately below 10^{-4}). Its main applications are the numerical simulation of PDP's and low-pressure RF discharges, which both are not in the present field of interest.

Several other groups have developed numerical simulation tools for plasmas, for their own specific goals. For example, the group of Goedheer at FOM-Institute 'Rijnhuizen' (Nieuwegein, The Netherlands) developed a method for the numerical simulation of two-dimensional low-pressure RF-discharges [6, 21]. The Plasma Technology Research Center (CRTP) in Sherbrooke (Canada) developed software for numerically simulating axi-symmetric ICP torches. It is based on a model which includes non-LTE effects, see for example [22, 23], and also includes a turbulence model for LTE plasmas [24]. Of the other groups in the field of ICP's, we mention the von Karman Institute for Fluid Dynamics (Rhode-Saint-Genèse, Belgium), that developed a powerful tool for the numerical simulation of an axi-symmetric ICP with laminar flow, for LTE/non-LTE and with a two-dimensional electromagnetic field formulation [25]. In the field of flowing thermal plasma jets, we have to mention the LAVA-code, developed by Ramshaw and Chang [26]. LAVA can numerically simulate flowing thermal plasma jets in the absence of electromagnetic fields. Furthermore, computational methods for DC torches are popular. Examples are the work of Bauchire *et al.* [27], Suzuki *et al.* [28] and Paik *et al.* [29]. The DC torches are different from the cascaded arc configurations used in Eindhoven: plasma expansion takes place at atmospheric conditions, and the methods for these torches are all based on LTE models.

The methods mentioned all have their own specific application field (except for the SIGLO code), for which they are perfectly suitable. However, there are two main reasons to develop a new numerical simulation tool. First, due to the diversity of plasma sources that we want to consider, separate methods for each plasma source could be very inefficient to maintain and update in practice. Second, although there are large differences between the various plasma sources, in the computational models for these sources one can find also large resemblances. This will be made clear in section 1.6.2. By utilising these resemblances, a modular plasma simulation tool can be developed, which meets all requirements (see section 1.4.1).

1.4   The design of the plasma simulation tool PLASIMO

The need for a numerical simulation tool for plasmas described in section 1.3 is especially felt in the Eindhoven region, where the university is surrounded by various high-tech companies

---

[b]Internet address: http://www.sni.net/siglo/

that use plasmas (for example Philips and Plasma Optical Fibre). That is why in the group Equilibrium and Transport in Plasmas of the Eindhoven University of Technology the so-called PLASIMO-project (PLASIMO stands for "PLAsma SImulation MOdel") was initiated about a decade ago. First pioneers were Fey, De Jong [30] and Benoy [31] who numerically simulated the open argon ICP's. The work on confined ICP's was performed by Van Dijk [32]. Following this, the application range of PLASIMO expanded, from the QL-lamp [33] to the cascaded arc [34] (employing the knowledge gained from a predecessor of PLASIMO, i.e. the numerical simulation tool of Beulens *et al.* [35]), TL- and S-lamp, and microwave cavities. For a complete list of the current PLASIMO applications, see section 1.4.2.

PLASIMO, is a general computational method based on the finite-volume method that solves the conservation equations for mass, momentum and energy (i.e. it is a fluid model) in a specified computational domain. It is set-up in such a way that multi-component plasmas, in a wide pressure range (10^1 to 10^6 Pa), from non-LTE to LTE, and with different energy coupling principles can be numerically simulated. We will discuss the capabilities and limitations of PLASIMO in section 1.4.1. The applications that are currently handled with PLASIMO are described in section 1.4.2. Here we refer also to the internet-page of PLASIMO:

http://www.etp.phys.tue.nl/gum/gum.htm.

1.4.1   Design specifications: capabilities and limitations of PLASIMO

The mathematical model underlying the current version of PLASIMO has the following features:

- The plasma under study behaves as a (isotropic) fluid, i.e. as a continuum for which the mass, momentum and energy balances are solved. This immediately implies a limitation: if the plasma can not be considered as a continuum, PLASIMO is not adequate and the use of kinetic models such as the particle-in-cell Monte Carlo model (PIC-MC) of Birdsall and coworkers [36] or hybrid models (i.e. the combination of a continuum model with a PIC-MC model) [37, 38] are necessary.

- The flow must be axi-symmetric, steady and laminar. If the flow is expected to become turbulent, a turbulence model has to be included. An example is the so-called $k - \varepsilon$ model which involves solving two additional transport equations, one for the turbulent kinetic energy, k, and one for the rate of dissipation of turbulent kinetic energy, ε [39]. The implementation of a $k - \varepsilon$ model into PLASIMO would be straightforward, due to PLASIMO's modular structure, but is not pursued within the present study. An example of circumventing the axi-symmetry constraint is given in chapter 6 of this thesis, in which in the application of PLASIMO to the numerical simulation of a plasma in a vacuum chamber, the pump has been replaced by an axi-symmetrical pumping ring. However, comparing results of the simulations with experimental results reveals that this is not a large restriction.

- The plasma is quasi-neutral (separation of charges is not included in PLASIMO) and characterised by at most two temperatures: one for the electrons and one for the heavy particles. This implies that in molecular plasmas the rotational and vibrational temperatures

are equal to the heavy particle or electron temperature. The validity of this assumption has to be checked when applying PLASIMO to molecular plasmas, see also chapter 5 of this thesis.

- It is assumed that the equation of state $p = \rho R T$ can be employed, with p the pressure, ρ the mass density, R the gas constant and T the temperature. Note that the given equation of state restricts the allowed pressure and temperature range, see Hirschfelder *et al.* [40].

- The plasma is assumed to behave as a Newtonian fluid. If it is not a Newtonian fluid, then the formulation of the viscous stress tensor will be more complex, since only in a Newtonian fluid the viscous stress is proportional to the rates of deformation.

- It is assumed that Fourier's law of heat conduction, which relates the heat flux to the local temperature gradient is applicable.

- The plasmas are not or weakly-magnetised, so that the magnetic field does not change the formulation of the transport properties. However, the Lorentz force term is included in the mathematical model underlying PLASIMO.

- The kinetic energy distributions of all (material) species in the plasmas are assumed to be Maxwellian. This restriction affects the calculation of rate coefficients and the calculation of the electric conductivity and electron thermal conductivity using Frost's formulation [41]. The assumption of a Maxwellian energy distribution excludes for example the case of the low-pressure capacitively coupled RF-discharge used for the deposition of hydrogenated amorphous silicon [6]. In the near future, it will be possible to use PLASIMO for the numerical simulation of plasmas for which the electron energy distribution function can be approached using two or three temperatures.

- Sheath-associated heating mechanisms are not taken into account. For example, the emission of secondary electrons or collisionless heating which play a role in RF glow discharges can not be taken into account.

1.4.2 Application field of PLASIMO

The previous section might suggest that, due to the limitations, the application field of PLASIMO is drastically reduced. However, there is a wide variety in the plasmas that currently can be handled by PLASIMO:

- **Open configurations**
  1. CA plasmas at sub-atmospheric pressure ($p \approx 10^3$ to 5×10^4 Pa), with a DC power coupling. See chapters 2 (argon), 4 and 5 (hydrogen) of this thesis and Burm *et al.* [42] (argon).
  2. ICP at atmospheric pressure, with inductive power coupling. See Benoy [43] (argon).
  3. MW plasma for optical fibre production at low pressure ($p \approx 10^3$ Pa), with microwave power coupling. See chapters 7 (argon) and 8 (oxygen) of this thesis.
  4. Expanding plasmas in a vacuum chamber at very low pressure ($p \approx 10 - 20$ Pa). See chapter 6 of this thesis (argon and argon-silane gas mixture).
- **Confined configurations**

1. QL-lamp, at low operating pressure ($p \approx 10^3$ Pa) with inductive power coupling. See Jonkers *et al.* [44] and Benoy *et al.* [45] (argon-mercury gas mixture).

2. S-lamp, at high operating pressure ($p \approx 6 \times 10^5$ Pa) with microwave power coupling. See Johnston [2] (sulphur).

3. TL-lamp, at low operating pressure ($p \approx 10^3$ Pa) with DC power coupling (argon-mercury gas mixture).

Due to the transparent modular structure (see section 1.6.2) of PLASIMO it is relatively easy to extend the existing model or to broaden the application field in the future. Current projects to improve PLASIMO's capabilities are:

- The introduction of a radiative transport module, which is needed to improve the results for the QL-, S- and TL-lamp.

- The introduction of time dependence.

- The introduction of a non-Maxwellian electron energy distribution which can be described by two or three temperatures. This is a necessity to improve the numerical simulation of the TL- and QL-lamp.

1.5   Aim of this work

We identify the following goals:

- Design of a general plasma simulation tool, PLASIMO, in such a way that multi-component plasmas can be simulated for a wide pressure range (approximately from 10^1 to 10^6 Pa), with LTE or non-LTE and with different energy coupling mechanisms. This demands a transparent modular set-up of the PLASIMO-software (in this way, new modules with additional capabilities can easily be implemented). This is explained in section 1.6.2.

- Design of a correct self-consistent formulation of diffusion in a plasma in thermal and chemical non-equilibrium. This is a necessity to adequately simulate molecular plasmas.

- Application of PLASIMO to a few open plasma configurations[c]:
  1. CA plasmas, operating on argon and hydrogen. This resulted in the design of an efficient hydrogen plasma source based on the cascaded arc, for the FOM-Institute for Plasma Physics 'Rijnhuizen' (Nieuwegein, The Netherlands).
  2. Expanding plasmas in a vacuum chamber at low pressure. The PLASIMO results are compared with the results of the commercial PHOENICS CVD code.
  3. Microwave plasmas used for optical fibre production. This is the work performed for Plasma Optical Fibre B.V. (Eindhoven, The Netherlands).

- Gain more fundamental insight into the physical phenomena and the operation of the above plasma sources.

---

[c]Also use was made of confined configurations, because of the easier testing of molecular chemistry of hydrogen and oxygen.

1.6 PLASIMO management

1.6.1 Organisation of the PLASIMO management

In general, PLASIMO management contains two different aspects: how to deal with a team of developers and how to deal with the complexity of the software? The first question will be handled in this section, the second question will be dealt with in section 1.6.2. Also the role of the PLASIMO-user will be discussed briefly, in section 1.6.3.

From the list of applications and projects to improve PLASIMO, it is clear that this is not the work of one person, but of a team. Currently, the PLASIMO-team consists of 7 people, each being a specialist in a certain field. Consequently, development of the PLASIMO-software is handled by more than one person at the same time. The most important dangers in the development of a large code are:

- Modifying software usually generates (new) bugs.
- The changes, that other team-members implemented, can be overwritten by another team-member.

Fortunately, these dangers can be minimised by using a control system. We use a publicly available software control system on Unix platforms, named "Concurrent Versions System" (CVS), which provides network-transparent source control for groups of developers[d]. The most important advantages of CVS are:

- It records the history of all changes made to the software (each directory tree). This makes the tracing of possible bugs very easy, by retrieving an older version of the code.
- Parallel development of a code, with more than one developer working on the same source at the same time, is permitted; the work of each developer is merged by CVS. Overwriting changes made in the software by others is not possible anymore.
- It provides reliable access to its directory trees from remote hosts. This is important when different hosts are used, as is the case in the PLASIMO-team.

In applying CVS one should only be careful not to "over-use" it: CVS is not a substitute for communication between developers. It proved that working with CVS makes the development of the PLASIMO-code much easier. Also from a programming point of view, a strict organisation is necessary to distinguish between the different (independent) parts of the PLASIMO-code. We will focus on this in section 1.6.2.

1.6.2 Organisation in the PLASIMO-code

The elements of PLASIMO are slightly different from the ones of commercial codes, where mainly a vertical division is made into a pre-processor, a solver and a post-processor. These parts are of course also present in the PLASIMO-code, but because of the diversity of the plasmas that have to be described, we have to introduce more parts. The standard pre-processing part contains definition of the computational domain, the selection of the governing physical and chemical

---

[d]Available via internet: http://www.cvshome.org

phenomena and the definition of the boundary conditions. The solver contains the method for solving the conservation equations. The post-processor generates the desired data, often by using sophisticated graphical visualisation tools.

Apart from a vertical division into an input part, a central part and an output part, also a horizontal division is made. This is shown in figure 1.1. The heart is formed by the transport part, which is comparable with the usual solver part. Different are the configuration and composition parts which are horizontally linked to the transport part. The configuration part describes the plasma source and is subdivided into modules for the electromagnetic energy coupling, the boundary conditions and the geometry of the plasma source. The composition part contains all information about the gas mixtures.

The horizontal division is a one-way division: configuration and composition are only input for the transport part, no information is directed from the transport part to the configuration and composition parts. There is also no direct information channel from the input part to the transport part; all the information is passed via the configuration or composition parts and is unidirectional. Although the configuration and the composition parts could be seen as merely a part of the pre-processor, this is not completely true: the PLASIMO-user has only limited possibility to change the configuration and composition parts. In these parts, just as in the transport part, general physical methods are used. For example the calculation of transport properties (in the composition part) or the electromagnetic energy coupling mechanisms (in the configuration part) are based on standard concepts.
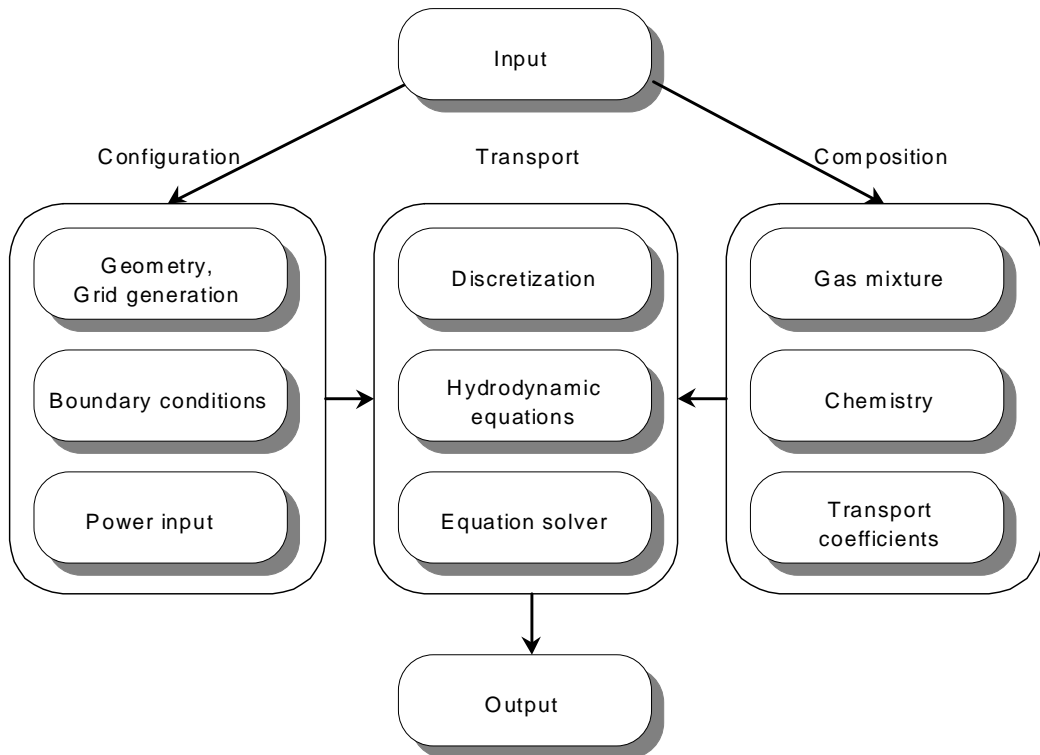
Figure 1.1: A schematic view of the organisation in the PLASIMO-code.

The subdivision of the three main parts into modules is shown in figures 1.2, 1.3 and 1.4. The configuration part contains sub-modules, shown in figure 1.2, that describe the energy coupling mechanisms for each individual plasma source. So the energy coupling is not divided in **type** but in **application**. For example, the DC energy coupling is described in the module *Cascaded arc*, whereas the MW energy coupling used for POF is described in the module *MW-POF*.

The transport part, shown in figure 1.3, forms the heart of PLASIMO. The conservation equations (mass, momentum, energy), all written as a ϕ-equation following Patankar [46], are described here. The set of Stefan-Maxwell equations, that are needed for the correct description of diffusion (see chapter 3 of this thesis), are part of the *Mass* module.

The composition part contains three sub-modules, shown in figure 1.4, in which the chemical composition of the available gas mixtures are described. The subdivision is as follows: *state*, *gas* and *mixture*. A gas is the set of states (we will use the nomenclature *species* in this thesis) of the same kind. For example, a hydrogen gas can consist of states H_2, H, H^+ and H_2^+. A mixture can consist of more than one gas, for example the argon gas plus the mercury gas plus the electron gas. The PLASIMO-software has more or less the structure as depicted in figures 1.1 to 1.4.
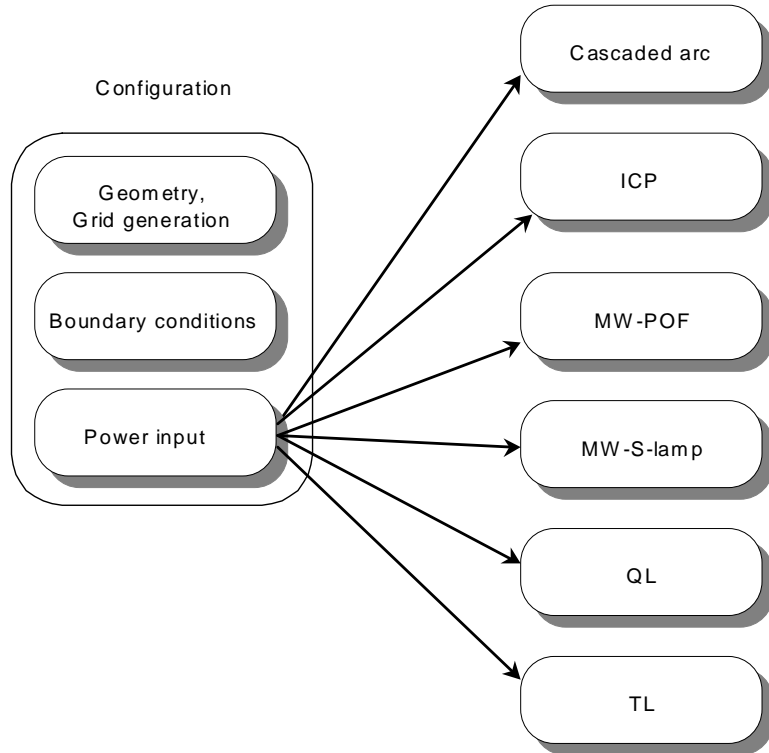
Figure 1.2: The modular subdivision in the configuration part.

The PLASIMO-software is written in the programming language C / C^{++}. Computations can be performed on Unix or Linux supporting platforms and windows pc's.
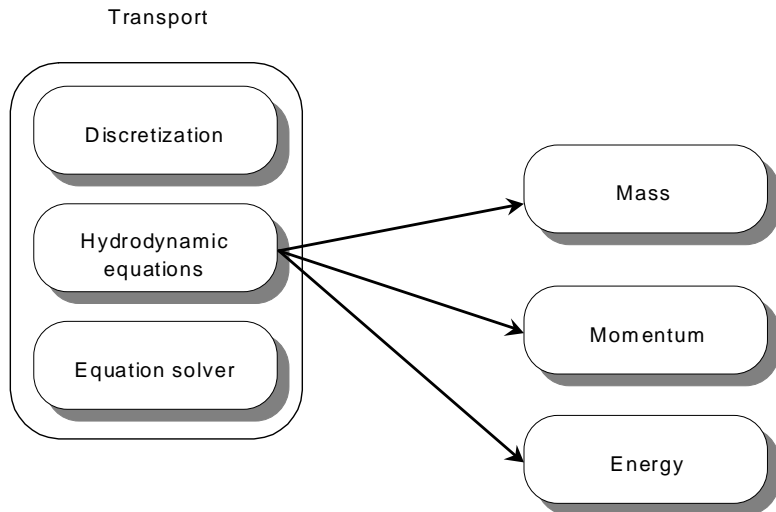
Transport

Figure 1.3: The modular subdivision in the transport part.
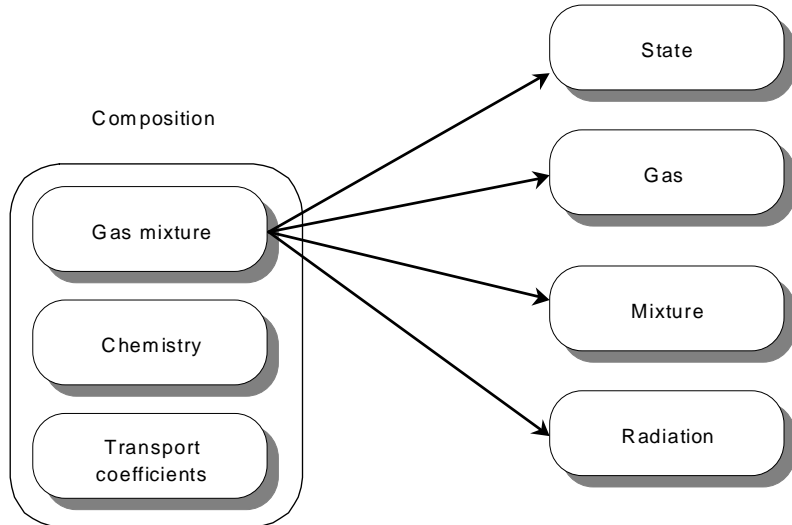
Composition

Figure 1.4: The modular subdivision in the composition part.

1.6.3   User control

PLASIMO employs a strongly implicit procedure for solving the non-linear system of equations (see chapter 2 of this thesis), which needs some control. This control is offered via the input-file. Apart from the normal user-input (operating conditions, dimensions, grid and initial guess for the solution), the user controls:

- The conservation equations that are solved. Terms within equations or complete equations can be switched off. An example is a numerical simulation of a plasma in LTE. In this case only one energy equation has to be solved (the energy balance of the mixture) whereas the

specific mass balances do not need to be solved. There are analytical relations between the number densities of all species. Also thermal and chemical equilibrium can be switched on/off independently, just as the influence of the various diffusion types (see chapter 3 of this thesis).

- The relaxation factors (factors that can enhance the convergence rate of the solution process, in principle every plasma parameter that is solved has its own relaxation factor). Usually, these factors are adjusted dynamically by PLASIMO during the iteration process. However, the user can choose his own set of (fixed) relaxation factors.

- The boundary conditions. For each plasma source a default set of (realistically chosen) boundary conditions exists. However, the user can specify a different set of boundary conditions.

A user manual is available, which is divided into three parts: a theoretical part, containing the necessary plasma physics, a PLASIMO user's guide, which describes how the user can run numerical simulations with PLASIMO, and a numerics and implementation part, for the PLASIMO-developer and the user who wants to contribute to the developing of PLASIMO.

1.7   Thesis outline

A detailed description of PLASIMO is presented in chapter 2. It is divided into the description of the physical model and that of the numerical method. Also the application range of PLASIMO is made clear. As a first example PLASIMO is used to simulate a non-LTE (atomic) argon cascaded arc plasma. Comparison of the results of the numerical simulations with experimental data are presented.

Switching from an atomic plasma to molecular plasmas (hydrogen and oxygen) showed that the treatment of the particle balances, as presented in chapter 2, was incorrect in most cases. Therefore a study was performed to treat the particle balances more correctly. The result was the set-up and solution of the so-called Stefan-Maxwell equations which solve equations for conserved quantities, i.e. the mass fractions, instead of number densities. The theory of the application of the Stefan-Maxwell equations to plasmas, in which thermal non-equilibrium can be present and electric fields drive the charged particle species, is presented in chapter 3.

An efficient hydrogen plasma source based on the cascaded arc was designed during the AIO-2 period[e]. This work was performed for the FOM-Institute for Plasma Physics 'Rijnhuizen' (Nieuwegein, The Netherlands) and was based on the idea to use a hydrogen CA plasma as a source of high atomic hydrogen ion fluxes for simulating the operation of divertor plasmas in Tokamaks. The LTE hydrogen model is presented in chapter 4 together with a comparison with all available experimental data for a hydrogen cascaded arc plasma.

A follow-up project of numerical simulation of the hydrogen LTE plasma (chapter 4), is the extension to a non-LTE hydrogen model. This proved to be necessary, since the LTE assumption is questionable at sub-atmospheric conditions. The non-LTE hydrogen model and the results of the numerical simulations for a hydrogen CA plasma are discussed in chapter 5.

---

[e] AIO-2: the two-year programme leading to the degree of Master of Technological Design.

Besides experimental validation, a different validation possibility is the code-to-code validation: comparing the PLASIMO results with results of a generally accepted commercially available code. For this purpose a vacuum chamber used in deposition processes is simulated by PLASIMO and by PHOENICS CVD. In the comparison special attention is paid to thermal diffusion. The results of the code-to-code validation and a code-to-experiment validation of an expanding argon plasma are presented in chapter 6.

The last one-and-a-half year a part of the modelling work was focused on the numerical simulation of the microwave plasma used by Plasma Optical Fibre B.V. (Eindhoven) for optical fibre production. The self-consistent diffusion description in chapter 3 is part of this work. Chapters 7 and 8 discuss the first steps towards fully modelling the microwave plasma. Chapter 7 discusses the special microwave energy coupling module that had to be designed for PLASIMO and presents results of numerical simulations for argon. The extension to an oxygen plasma is presented in chapter 8. The conclusions from the present investigations are summarised in chapter 9.

Chapter 2

PLASIMO, a General Computational Method: I Applied to an Argon Cascaded Arc Plasma

G.M. Janssen, J. van Dijk, D.A. Benoy, M.A. Tas, K.T.A.L. Burm, W.J. Goedheer[2], J.A.M. van der Mullen and D.C. Schram

Department of Applied Physics, Eindhoven University of Technology, P.O. Box 513, 5600 MB Eindhoven, The Netherlands

[2] FOM-Institute for Plasma Physics 'Rijnhuizen', P.O. Box 1207, 3430 BE Nieuwegein, The Netherlands

Abstract

A non-LTE argon cascaded arc plasma is numerically simulated, employing the general plasma simulation program PLASIMO. The structure of PLASIMO is flexible and transparent, so that apart from the study given in the present paper several other multi-component steady plasmas in a wide pressure range (10^{-4} to 1 bar), from local thermal equilibrium (LTE) to non-LTE, and with different energy coupling mechanisms can be simulated as well. The strong modularity makes PLASIMO easy to handle and easy to adjust or expand. Results of PLASIMO applied to the cascaded arc are compared with experimental data and show reasonable agreement. The influence of the boundary conditions on the simulation results is discussed.

2.1   Introduction

In the group Equilibrium and Transport in Plasmas (ETP) at the Eindhoven University of Technology (EUT) a PLAsma SImulation MOdel (PLASIMO) is under development. PLASIMO is a computational tool for numerically simulating plasmas, which is constructed in such a way that

multi-component plasmas, in a wide pressure range (10^{-4} to 1 bar), from non-LTE to LTE, and with different energy coupling principles can be simulated. Consequently, apart from handling the cascaded arc [42], it must be capable of handling for example the ICP and QL-lamp. This is already described briefly in [43] (ICP) and [33, 44] (QL-lamp). It must be possible to study other plasma sources as well.

The structure of PLASIMO is transparent and can be divided in three major parts: the transport, the configuration and the composition part. Each part is divided into modules. The organisation of the PLASIMO-code is already discussed extensively in chapter 1.

The main part of this chapter is devoted to a detailed description of the physical model and the computational method. In sections 2.2 and 2.3 PLASIMO is described from a physical and numerical point of view, i.e. the transport part shown in figure 1.1. Sections 2.4 and 2.5 discuss specific configuration aspects and section 2.6 the composition features. Finally, as a first example the application of PLASIMO to the numerical simulation of an argon cascaded arc (CA) plasma is discussed in sections 2.7 and 2.8. In this respect it is good to refer to other research carried out for similar plasma set-ups. Ramshaw and Chang [26] developed a method (LAVA) for flowing thermal plasma jets in the absence of electromagnetic fields. Bauchire *et al.* [27] considered an application in which a DC torch and the resulting plasma jet are combined. The torch used by Bauchire and others, for example Suzuki *et al.* [28] and Paik *et al.* [29], is different from the CA used in this study. In all examples LTE is assumed and expansion takes place in air and not in a chamber at low pressure. Only the computational method of Beulens *et al.* [35], which is a predecessor of PLASIMO, describes the same arc plasma. In Beulens' method, which was meant for monatomic gases only, no wall reactions were taken into account, the formulation of the transport coefficients and source terms was incomplete, and finally the boundary conditions differed, see section 2.7.

This paper is the first in a series in which the numerical simulation is discussed of various plasmas with different gases and/or gas mixtures. Short descriptions of the application of PLASIMO to the ICP and QL-lamp are already given in [33, 43, 44].

2.2   Physical model

2.2.1   Main assumptions

The construction of the physical model is based on the distinction between slow and fast plasma activities. On the one hand we have fast microscopic activities (collisional and radiative processes), on the other hand relatively slow macroscopic activities (such as convection, conduction and diffusion). Since the timescales of these microscopic and macroscopic activities are totally different (a typical timescale for microscopic activity is 10^{-8} s, for macroscopic activity 10^{-3} s), the plasma can be considered as a fluid in which at every location plasma parameters can be defined.

The macroscopic or fluid description of plasmas is based on the hydrodynamical transport equations. These transport equations, derived by taking velocity moments of the Boltzmann equation [41], describe the flow field and for each plasma component the spatial distribution of

its temperature and concentration. In this description the following assumptions are made. The flow is

1. laminar: it is characterised by relatively low values of the Reynolds number;
2. steady state: $\frac{\partial}{\partial t} = 0$, if an AC field is applied, its frequency should be much larger than the inverse macroscopic relaxation time;
3. axi-symmetric: the geometry of the plasma source and the resulting flow are axi-symmetric;
4. quasi-neutral: $\sum_\alpha Z_\alpha n_\alpha = 0$, where Z_α and n_α denote the charge number and number density of species α, respectively;
5. characterised by two temperatures: the electrons have a temperature T_e and all the heavy particle species have one temperature T_h, in general $T_e \neq T_h$;
6. that the ideal gas law can be applied;
7. Newtonian.

These assumptions lead to the following limitations:

1. The kinetic energy distribution of the material species is necessary for calculating energy-averaged cross-sections and rate coefficients. Currently all kinetic energy distributions are assumed to be Maxwellian. Although deviations can be incorporated, e.g. in the high energy tail, PLASIMO is not capable of simulating plasmas in which large deviations from Maxwellian distributions can be expected.
2. The plasmas considered consist of the following species: electrons {e} and heavy particles {h}, that is the collection of molecules, atoms, and ions in the ground state or in various excited states. At this moment photons are not incorporated as interacting species in the model, they are only produced and lost locally by the plasma in radiative decay processes (free-free, free-bound, and bound-bound transitions). Consequently, radiative energy transport from one plasma part to another (absorption and re-emission) is not considered.
3. Due to the assumption of the existence of only one heavy particle temperature, it is not possible to describe plasmas at extremely low pressure in which neutrals and ions differ in temperature.
4. It is not possible to describe sheath-associated heating mechanisms. At low pressures the sheath potential in RF or DC glow discharges can be more than 100 V and secondary electrons or collisionless heating may play a role. These effects are not included in PLASIMO.
5. The net charge density is taken to be zero (i.e. Poisson's equation is not solved).

Due to the transparent modular structure it should be possible to broaden the application field of PLASIMO, e.g. by introducing different temperatures for ions and neutrals, or by introducing radiation transport. For modelling the QL-lamp radiation transport is very important. Therefore a start has been made to introduce it in PLASIMO, as was presented by Van Dijk *et al.* at LS-8 [47].

2.2.2 Basic equations

For the given assumptions the plasmas of interest are macroscopically fully described by the following set of equations.

- Particle balance equations for heavy particle species h:[a]

$$\vec{\nabla} \cdot (n_h \vec{u}) - \vec{\nabla} \cdot \left(D_h \vec{\nabla} n_h \right) = S_h \tag{2.1}$$

  where D_h and $\vec{u}$ denote the diffusion coefficient of species h and the plasma bulk velocity, respectively. The latter is defined as: $\vec{u} = \sum_\alpha n_\alpha m_\alpha \vec{u}_\alpha / \rho$ with $\rho = \sum_\alpha m_\alpha n_\alpha$ where m_α is the mass, $\vec{u}_\alpha$ the mean velocity of species α and ρ is the mass density of the mixture. The net production of species h due to collisional-radiative processes and chemistry is represented by S_h. The number density of electrons is calculated from the quasi-neutrality assumption. In LTE the particle balance equations (2.1) are not solved, because then analytical relations exist between the number densities of all species, based on the equation of state (equation (2.7)), Saha and Guldberg-Waage equations.

- Continuity equation for the plasma as a whole, i.e. as a mixture of all components:

$$\vec{\nabla} \cdot (\rho \vec{u}) = 0 \tag{2.2}$$

- Momentum balance for the mixture (u_i - component, where i denotes the axial (z) or radial (r) component):

$$\left(\vec{\nabla} \cdot (\rho \vec{u} \vec{u}) \right)_i = - \left(\vec{\nabla} p \right)_i + \left(\vec{\nabla} \cdot \tau \right)_i + \left(\vec{j}_q \times \vec{B} \right)_i \tag{2.3}$$

  with p the plasma pressure related to the number densities and temperatures through the equation of state (2.7). The components τ_{ij} of the viscous stress tensor τ are functions of $\vec{u}$ and the dynamic viscosity μ. Under the assumption that the plasma can be considered as a Newtonian fluid the components τ_{ij} are written as $\tau_{ij} = 2\mu(\Gamma_{ij} - \frac{1}{3}(\vec{\nabla} \cdot \vec{u})\delta_{ij})$ with $\Gamma_{ij} = \frac{1}{2}(\partial u_i / \partial x_j + \partial u_j / \partial x_i)$ and δ_{ij} the Kronecker delta. The dynamic viscosity μ is calculated using mixture rules and is treated in section 2.6.3. The term $\vec{j}_q \times \vec{B}$, with $\vec{j}_q$ the current density, denotes the time-averaged influence on momentum of an externally applied or generated magnetic field $\vec{B}$.

- Energy balance for the heavy particles $\{h\}$:

$$\vec{\nabla} \cdot (\sum_X \rho_X \epsilon_X \vec{u}) + \sum_X p_X \vec{\nabla} \cdot \vec{u} + \vec{\nabla} \cdot \vec{q}_h = \tau_h : \vec{\nabla} \vec{u} + Q_h \tag{2.4}$$

  where ϵ_X is the internal energy per unit mass of heavy particle species X. The heat flux is $\vec{q}_h = -\lambda_h \vec{\nabla} T_h$ and Q_h denotes the energy gain or loss through elastic/inelastic reactions with electrons and/or chemical reactions between the heavy particles, including the so-called inter-diffusion term. The viscous dissipation (again Newtonian) $\tau_h : \vec{\nabla} \vec{u}$ is given by $\tau_h : \vec{\nabla} \vec{u} = 2\mu(\sum_{ij} \Gamma_{ij} \Gamma_{ij} - \frac{1}{3}(\vec{\nabla} \cdot \vec{u})^2)$.

---

[a]Currently the mass fraction balances are solved instead of particle balances, using the full set of Stefan-Maxwell equations that describe diffusion self-consistently. See chapter 3 in this thesis.

- Energy balance for the electrons $\{e\}$:

$$\vec{\nabla} \cdot (\rho_e \epsilon_e \mathbf{u}) + p_e \vec{\nabla} \cdot \mathbf{u} + \vec{\nabla} \cdot \vec{\mathbf{q}}_e = Q_{\mathrm{Ohm}} + Q_e \tag{2.5}$$

with $\vec{\mathbf{q}}_e = -\lambda_e \vec{\nabla} T_e$. The electron viscous dissipation term $\tau_e : \vec{\nabla}\mathbf{u}$ is neglected. Q_{Ohm} is the energy gain through Ohmic heating, Q_e is the energy loss/gain through elastic/inelastic reactions with heavy particles and through radiative processes.
The power input Q_{Ohm} is given by:

$$Q_{\mathrm{Ohm}} = \vec{\mathbf{j}}_q \cdot \vec{\mathbf{E}} \tag{2.6}$$

with $\vec{\mathbf{E}}$ the electric field. For AC plasmas the time average of $\vec{\mathbf{j}}_q$ and $\vec{\mathbf{E}}$ is taken. In LTE only one temperature exists for all particle species; in this case the energy balance of the mixture (i.e. the sum of equations (2.4) and (2.5)) is solved.

- Equation of state, given by Dalton's law of partial pressures and the perfect gas law:

$$p = \sum_{\alpha} p_{\alpha} \qquad \text{with} \quad p_{\alpha} = n_{\alpha} k_b T_{\alpha} \tag{2.7}$$

with k_b the Boltzmann constant.

The physical model with its basic set of equations ((2.1) to (2.7)) forms the heart of PLASIMO. To solve this set of second-order partial differential equations a numerical method is constructed, which is described in section 2.3. Note that the specific properties belonging to the plasma configuration and the chemical composition, chosen by the PLASIMO-user, enter the physical model via the boundary conditions, the energy coupling term Q_{Ohm} (equation (2.6)), the source terms S_h (equation (2.1)), Q_h (equation (2.4)), Q_e (equation (2.5)) and the transport coefficients D_h, σ, λ_h, λ_e and μ. These configuration and composition features are described in sections 2.4 to 2.6.

2.3   Numerical method

2.3.1   The ϕ-equation

In the construction of the numerical method it is appropriate to write each of the relevant differential equations (equations (2.1) to (2.5)) as a particular case of the so-called ϕ-equation. This means that only one procedure is needed to solve a generalised conservation equation. This procedure can then be applied to the various plasma quantities which renders the program structure transparent. The ϕ-equation used in PLASIMO is a modified version of the general form given by Patankar [46]. To write the transport equations in terms of the plasma parameters an extra factor f is introduced:

$$\vec{\nabla} \cdot (f_\phi \rho \mathbf{u} \phi) - \vec{\nabla} \cdot (\lambda_\phi \vec{\nabla} \phi) = S_\phi \tag{2.8}$$

The first term at the left-hand side (LHS) denotes the convection term and the second term the diffusion term. The factors f_ϕ and λ_ϕ can be considered as a convection and diffusion coefficient,

respectively. The term S_ϕ at the right-hand side (RHS) denotes the source term. The coefficients f_ϕ, λ_ϕ, and S_ϕ are different for each ϕ-variable and are defined in such a way that the conservation equations (2.1) to (2.5) can be rewritten in the general form of equation (2.8). The results are given in table 2.1. However, the mixture continuity equation (2.2) is treated separately as a pressure-correction equation. This is explained in section 2.3.2.

Table 2.1: Expressions for ϕ and ϕ-factors f_ϕ, λ_ϕ and S_ϕ for the equations (2.1) to (2.5), where α refers to the kind of species and i to the spatial component (axial (z) or radial (r)).

ϕ	f_ϕ	λ_ϕ	S_ϕ	Eq.
n_α	$1/\rho$	D_α	S_α	(2.1)
1	1	0	0	(2.2)
u_i	1	μ	$-(\vec{\nabla}p)_i + (\vec{\nabla} \cdot \tau)_i + (\vec{j}_q \times \vec{B})_i - \vec{\nabla} \cdot (\mu\vec{\nabla}u_i) - K_i$	(2.3)
T_h	$\sum_X (c_{v,X} + 1)k_b n_X/\rho$	λ_h	$\vec{u} \cdot \vec{\nabla}(\sum_X p_X) + \tau_h : \vec{\nabla}\vec{u} + Q_h$	(2.4)
T_e	$2.5 k_b n_e/\rho$	λ_e	$\vec{u} \cdot \vec{\nabla}p_e + Q_{\mathrm{Ohm}} + Q_e$	(2.5)

The momentum balance (2.3) contains a tensor quantity (the divergence of a dyad) whereas the generalised form of equation (2.8) contains divergences of vector quantities. For curvilinear coordinates the differences have to be compensated by changing the source terms in the RHS. Therefore a modification term K_i is introduced. For component i: $K_i = (\vec{\nabla}\cdot(\rho\vec{u}\vec{u}))_i - \vec{\nabla}\cdot(\rho\vec{u}u_i)$.

Note that in order to write the energy equations (2.4) and (2.5) in the general form of equation (2.8) the rate of work due to expansion, $p_\alpha\vec{\nabla} \cdot \vec{u}$, is rewritten as $\vec{\nabla} \cdot (p_\alpha\vec{u}) - \vec{u} \cdot \vec{\nabla}p_\alpha$. The first term is then combined with $\vec{\nabla} \cdot (\rho_\alpha\epsilon_\alpha\vec{u}) = \vec{\nabla}(c_{v,\alpha}n_\alpha k_b T_\alpha\vec{u})$ so that f_{T_α}, being actually the heat capacity, changes from $c_{v,\alpha}k_b n_\alpha/\rho$ to $(c_{v,\alpha} + 1)k_b n_\alpha/\rho$. The second term, $\vec{u} \cdot \vec{\nabla}p_\alpha$, is regarded as a source term. To write the momentum balance in the form of equation (2.8) a term $\vec{\nabla} \cdot (\mu\vec{\nabla}u_i)$ is subtracted from the LHS and RHS of equation (2.3).

2.3.2   The modified SIMPLE algorithm

In order to calculate the pressure and flow fields, a combined solution of the mixture continuity equation (2.2) and the momentum balances (2.3) is needed. For this purpose a modified version of the Semi-Implicit Method for Pressure-Linked Equations (SIMPLE) developed by Patankar [46] is used in PLASIMO. This SIMPLE algorithm is based on the velocity field having to obey both the mixture continuity equation and the momentum balances. The modified SIMPLE algorithm as applied in PLASIMO consists of the following steps:

1. From an initial guess of the pressure the velocity field is calculated using equation (2.3).

2. Since the calculated velocity field will in general not satisfy the mixture continuity equation (2.2), the mixture continuity equation can be used to find a correction for the velocity and pressure fields. For this purpose this equation is rewritten into a pressure-correction equation which is treated as a ϕ-equation.

3. The other ϕ-equations that influence the flow field are solved.

4. The whole sequence of steps 1 to 3 is repeated until convergence is reached (see section 2.3.6).

In the transformation of the mixture continuity equation into a pressure-correction equation we follow Patankar [46], however with the following modifications:

- Rather than a staggered-grid approach as given in [46] (i.e. the velocity components are located on the faces of the control volumes), the velocity components are defined at the main grid points just as all other physical quantities. This co-located grid method was developed by Rhie and Chow [48] and is used in PLASIMO together with the momentum-interpolation scheme at the control volume faces (see section 2.3.4) of Majumdar [49]. The use of co-located grids instead of staggered grids is more appropriate when the physical grid is curved so that no need exists to evaluate the curvature terms on the faces of the control volumes.

- To describe incompressible as well as compressible flows the formulation of the pressure-correction equation according to Karki and Patankar [50] is used. In this formulation an extra term is included which accounts for pressure-induced density changes. At low Mach numbers ($M < 1$), the system of partial differential equations is elliptic. Crossing $M = 1$, it changes from elliptic to hyperbolic. The choice of using the pressure as a primary variable in the modified SIMPLE algorithm is motivated by the finite pressure changes (in contrast to the mass density changes) irrespective of the flow Mach number. More details can be found in Karki and Patankar [50].

For confined plasma configurations (e.g. low pressure lamps) the modified SIMPLE-algorithm is not used, since then the velocity field is taken zero. In this case from the conservation of mass the number densities are scaled and the pressure is calculated using the equation of state (2.7).

2.3.3   Grid generation

To solve the ϕ-equations for different plasma geometries they are written in a generalised boundary-fitted orthogonal curvilinear coordinate system. In this coordinate system an arbitrary geometry is mapped onto an equidistant computational grid. The main advantage is that no restriction on geometry exists: not only straight cylindrical geometries (like the straight CA or ICP) but also curved geometries (like the QL-lamp [43] or the geometrically pinched CA [42]) can be handled. The main task in the grid generation is the determination of the mapping between the grid points (x, y) in the physical plane to the grid points in the computational plane (ξ_1, ξ_2). A one-to-one mapping between the physical plane and computational plane is established using a two-dimensional differential equation method based on the Poisson equation, which is described by Benoy [51]. After constructing in this way a two-dimensional grid, it may be refined locally in plasma regions where steep gradients are expected following the method described by Mobley and Stewart [52]. More details about the orthogonal curvilinear coordinate system can be found in Benoy [51].

2.3.4   Discretisation

The control volume (CV) method is used to discretise the elliptic system of ϕ-equations. In this method the computational domain is divided into non-overlapping CV's where each (nodal) grid point is centred in one CV. The field variables ϕ are defined at the nodal grid points whereas the fluxes are defined on the CV-faces. The orthogonality of the coordinate system makes the calculation of fluxes across a CV-face straightforward, since the flux is directed perpendicular to that CV-face. The most important feature of the CV-method is the *exact* integral conservation of mass, momentum and energy over *any* group of CV's. The discretised equations are obtained by integrating the ϕ-equations over a control volume. The applied discretisation scheme is hybrid. The mesh Peclet number (Pe), which is the mesh-size dependent ratio between the magnitude of the convection and diffusion terms, determines which discretisation scheme is used: first-order upwind (convection dominance: $|\mathrm{Pe}| > 2$) or second-order central difference (diffusion dominance: $|\mathrm{Pe}| \leq 2$). The CV-discretisation method is described by Patankar [46].

2.3.5   Equation solver

The Modified five-point Strongly Implicit Procedure (MSIP) [53, 54] is used to solve the discretised equations [31]. Since this procedure is very robust, it is appropriate for systems that are very sensitive to instabilities. The plasma sources that are to be numerically simulated with PLASIMO are good examples of such unstable systems. The instability occurs because of the strong coupling between the equations and the exponential character of the source terms. This renders the system of equations very sensitive for small changes in the source terms: the system is stiff.

2.3.6   Iteration scheme

Using the numerical methods described above, PLASIMO solves the set of equations (2.1) to (2.5) iteratively, following the flow chart shown in figure 2.1. To close the set of equations the PLASIMO-user has to define the configuration features. That is: the geometry of the plasma source must be given and an appropriate set of boundary conditions must be chosen. The choice of the chemical composition of the gas determines the chemical source terms and transport coefficients, and the chosen plasma configuration determines the energy coupling principle.

Note that the particle balance equations (2.1) are not used for all heavy particle species. One neutral particle species is calculated from the equation of state (2.7). The electron number density is calculated from the quasi-neutrality assumption, as was mentioned before.

In LTE the energy balance of the mixture (the sum of equations (2.4) and (2.5)) is solved. The particle balance equations are not solved; the number densities of the species are calculated using the analytical relations that exist between the number densities of all species, the pressure and the temperature.

Convergence has been achieved when two stop criteria are fulfilled simultaneously: the maximum value of the relative residue and the change of the relative residue of all ϕ-equations are below a preset value, typically 10^{-7} and 10^{-4}, respectively. The second criterion is necessary to ex-
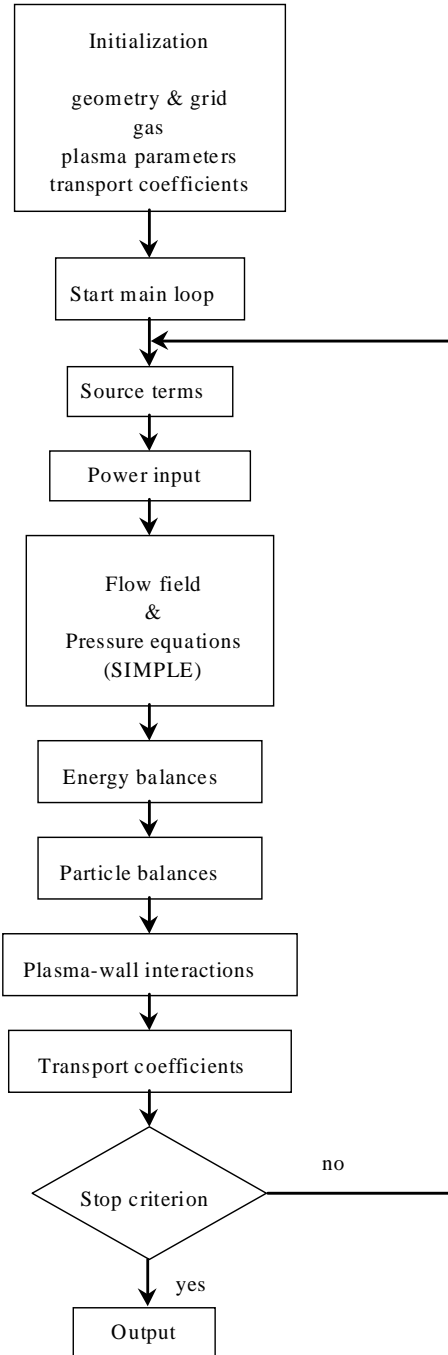
Figure 2.1: Flow chart of PLASIMO.

clude (semi-)converged solutions of which the residues, and consequently the physical quantities, may still change considerably over a large number of iterations. To enhance the stability of the iteration process a linear under-relaxation of the ϕ-variables is used: $\phi^{n'} = a_\phi \phi^n + (1 - a_\phi)\phi^{n-1}$ with a_ϕ the under-relaxation factor of variable ϕ ($0.1 < a_\phi \leq 1$) and $\phi^{n'}$ the final value of

ϕ at iteration n (i.e. after relaxation). To increase the convergence speed, in PLASIMO dynamic relaxation is used, which means that a_ϕ changes during the iteration process (depending on the relative change in the residue). Note that the dynamic relaxation is fully determined by PLASIMO and not by the user.

The output of PLASIMO includes two-dimensional fields of flow properties (pressure and velocity), concentrations (number densities), and temperatures. Also variables deduced from these primary plasma variables are output, such as the separate terms in the conservation equations.

The numerical method is implemented in the programming language C. The calculations can be performed on Unix or Linux supporting computer systems and windows pc's.

2.4   Power input

The power input in the plasma depends on the type of plasma source that is modelled. PLASIMO is capable of handling inductive (e.g. the ICP and QL-lamp), as well as DC-plasma sources (e.g. the CA), and in the near future microwave plasma sources (e.g. the TIA). These sources have a totally different electromagnetic energy coupling principle. As a consequence the calculation of the power input, given by equation (2.6), forms a separate module in PLASIMO, with different sub-modules describing the electromagnetic field for:

- Inductively coupled sources; using Maxwell's equations the electromagnetic field is formulated in terms of a vector potential [43, 55]. The vector potential equation is an elliptic equation that is solved with MSIP [53, 54] extended to solve equations with complex variables [51].

- DC-sources; based on a one-dimensional electric field formulation that is discussed in section 2.7.1.

Note that when a magnetic field is present it results in the term $\vec{j}_q \times \vec{B}$ in the momentum balance (equation (2.3)). This term is not taken into account in this chapter, for application in the CA it is presented in chapter 5.

2.5   Boundary conditions

The solution of the general ϕ-equation (2.8) is determined by the applied boundary conditions. Therefore, the PLASIMO-user has to specify conditions for all ϕ-variables at each of the four boundaries of the configuration (north, south, west and east). These boundaries may be physical boundaries or symmetry boundaries. Of course the boundary conditions depend on the chosen plasma source. Two kinds of boundary conditions have to be considered:

- Dirichlet, characterised by a known value of ϕ, that is: $\phi_K = \Phi$, where Φ is a fixed value or a function of other plasma parameters, and K the boundary: W(est), E(ast), S(outh) or N(orth).

- Neuman, characterised by a given flux at the boundary: $\partial\phi/\partial n|_K = F(\phi_K)$. If F is zero this is a homogeneous Neuman condition.

A special class of Neuman conditions is needed for species reacting at the boundaries. One type of species (α) is produced at a boundary by the reaction of other types of species ($\beta \neq \alpha$). So the properties of the reacting species, and especially the number densities, have to be known in determining the boundary value of the number densities of the created species. Consequently, the Neuman conditions for the number densities of species α and β are coupled.

The flux $\Gamma_{\alpha,w}^{in}$ of species α that reacts at a boundary K (i.e. destruction of species α) is described by [56]:

$$\Gamma_{\alpha,K}^{\text{in}} = n_{\alpha,K} \bar{u}_{\alpha,K} \frac{\gamma_{\alpha,K}}{1 - \gamma_{\alpha,K}/2} \tag{2.9}$$

with $\gamma_{\alpha,K}$ the reaction probability for species α at the wall K (no sticking is assumed). The mean thermal velocity of species α perpendicular to K is $\bar{u}_{\alpha,K} = \frac{1}{4}(8k_b T_{\alpha,K}/\pi m_\alpha)^{1/2}$.

The total creation of species α at the wall through reactions of species $\beta \neq \alpha$ is described by the flux $\Gamma_{\alpha,K}^{\text{out}}$:

$$\Gamma_{\alpha,K}^{\text{out}} = \sum_{\beta \neq \alpha} \aleph_{\beta\alpha} \Gamma_{\beta,K}^{\text{in}} \tag{2.10}$$

with $\aleph_{\beta\alpha}$ the stoichiometric coefficient for transforming species β into species α. For example, in a hydrogen plasma, the reaction $H + \text{wall} \rightarrow \frac{1}{2}H_2$ causes a flux $\Gamma_{H_2,K}^{\text{out}} = \frac{1}{2}\Gamma_{H,K}^{\text{in}}$.

The net flux of species α at the boundary K equals its diffusive flux:

$$-D_\alpha(\partial n_\alpha/\partial n)_K = \Gamma_{\alpha,K}^{\text{out}} - \Gamma_{\alpha,K}^{\text{in}} \tag{2.11}$$

where the derivative in the LHS is taken in the direction n (z or r) perpendicular to K. Note that in equation (2.11) it is assumed that at walls no net flow exists: $\vec{u} = \vec{0}$.

Using equation (2.11) the calculation of the boundary values of the number densities involved (i.e. the boundary values of the reacting and created species) is performed in the module "plasma-wall interactions" (see figure 2.1) nearly at the end of the iteration cycle, since at that point the properties of all species are known.

2.6 Transport coefficients

2.6.1 Introducing transport coefficients in PLASIMO

The PLASIMO-user has three options available for incorporating transport coefficients:

1. Look-up tables. The disadvantage is the multi-dimensionality of such tables since they are at least two-dimensional (temperature and pressure dependence). In the case of gas mixtures an additional dimension is introduced, namely the dependence on the gas-mixture ratio.

2. Approximate formulas. These formulas can be based on the mean-free-path concept, see Mitchner and Kruger [41], or the user can define his own formula. For example for the diffusion coefficient of species α he can use $D_\alpha = \frac{1}{3}l_\alpha \bar{u}_\alpha$, with l_α the mean free path and $\bar{u}_\alpha$ the mean thermal velocity of species α. The advantage is the relative simplicity and consequently higher calculation speed; a disadvantage is the approximate character of the formula.

3. Full modelling based on Frost mixture rules [57] and Chapman-Enskog-Burnett theory (CEB) [40]. This option is the standard option in PLASIMO and is discussed in sections 2.6.2 and 2.6.3 for the electron and heavy particle transport coefficients.

2.6.2   Electrons

For partially ionised gases with an ionisation degree between 10^{-6} and 1, the Frost mixture rules [57] are suitable to calculate the electron transport properties in the absence of a magnetic field. With the Frost mixture rules the electric conductivity (σ) and electron thermal conductivity (λ_e) can be calculated taking into account the electron-electron, electron-ion and electron-atom interactions. Since we are interested in the whole range of ionisation degrees the mixture rules are used in PLASIMO. If a magnetic field is present an extension of the Frost mixture rules, proposed by Kruger *et al.* [58] and Schweitzer and Mitchner [59] has to be used.

2.6.3   Heavy particle species

The heavy particle transport coefficients are calculated according to CEB [40]. For mixtures the formulas according to Hirschfelder *et al.* [40] and Devoto [60] are used in which the transport coefficients are expressed in terms of Sonine-polynomial expansion coefficients. In PLASIMO the viscosity is used in the first-order approximation; the electron contribution is neglected. The heavy particle thermal conductivity is used in the third-order approximation; the electron-heavy particle collision terms are neglected.

2.7   Application to an argon cascaded arc plasma

As a first application of PLASIMO, the cascaded arc is simulated. Following the structure of PLASIMO given in figure 1.1, the user has to define the configuration aspects (features of the source, left column in figure 1.1) and the chemical composition (right column). In this example the cascaded arc is taken as the plasma source; argon is used as the gas. The features belonging to an argon cascaded arc plasma are given in sections 2.7.1 (configuration) and 2.7.2 (composition).

2.7.1   Configuration features

Plasma source and geometry

The plasma is created in the CA [61, 62] shown in figure 2.2.

The gas is fed via a mass flow controller into the cathode side of the arc where it is ionised. The plasma flows through the channel, is accelerated and expands at the anode side into a vacuum chamber at low pressure (typically 40 Pa). The dotted line shown in the figure represents the part of the arc that is numerically simulated. The length of the channel is 60 mm; the radius is 2 mm. The west boundary is located at the first cascade plate which means that the voltage drop between the (three) cathodes and first cascade plate is not accounted for. For describing the voltage drop

1: end-on viewing window
2: Tungsten-Thorium cathode (3x)
3: cascade plate
4: anode plate
5: nozzle plug
6: gas inlet
7: plasma channel
8: cathode housing

Computational domain
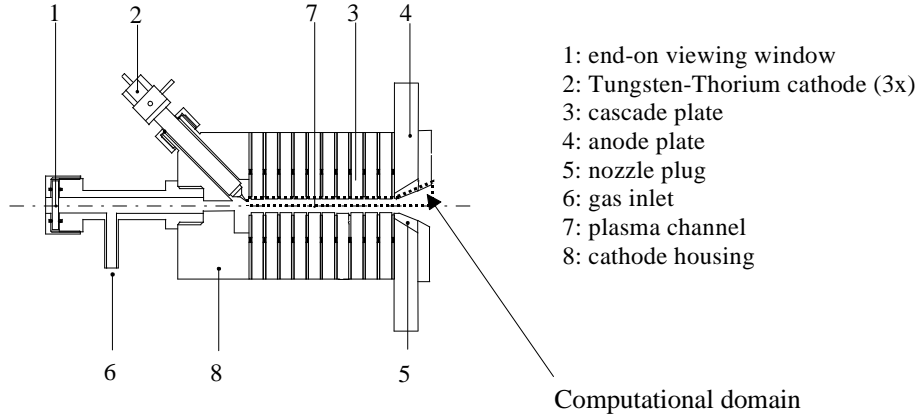
Figure 2.2: The cascaded arc configuration. The dotted line represents the part of the arc that is numerically simulated.

we refer to Benilov and Marotta [45]. The east boundary is located at the outlet of the arc. The north boundary is formed by the channel wall. The individual character of the cascade plates is not taken into account, i.e. in the simulation the north boundary is treated as one continuous surface. Although this implies that the plasma-wall boundary layer is not described properly this does not affect the description of the major part of the plasma. The south boundary is the symmetry axis. A grid of 30×30 points is used.

Power input

For the CA a one-dimensional electric field formulation is used. Since sheath effects are neglected in PLASIMO the radial electric field E_r in the CA will be small; it is assumed that $E_r = 0$. The axial component E_z is independent of radial position and is calculated from the current I through the arc (given by the user) and a cross-sectional averaged electric conductivity $\bar{\sigma} = \frac{1}{\pi R^2} 2\pi \int_0^R \sigma r dr$:

$$E_r = 0, \qquad E_z = \frac{I}{\pi R^2 \bar{\sigma}} \tag{2.12}$$

with R the radius of the plasma channel and r the radial position in the channel. An axisymmetrical formulation based on the gradient of the potential distribution is more complicated because of the boundary condition at the outlet of the arc. According to Gielen [63] a part of the current will reach the anode plate via the vacuum chamber which highly complicates the definition of a correct boundary condition. The simplified Ohm's law gives an expression for the local current density $\vec{\mathbf{j}}_q$:

$$j_{q,r} = 0, \qquad j_{q,z} = \sigma E_z. \tag{2.13}$$

Equations (2.12) and (2.13) are substituted in equation (2.6) to obtain the power input Q_{Ohm}. In this example no magnetic field is applied.

Boundary conditions

The boundary conditions for a flowing argon plasma in the CA are specified below. We assume that the plasma consists of only three different species: argon atoms in the ground state (Ar), argon ions (Ar$^+$) and electrons. This implies that only one particle balance equation (2.1) has to be considered and supplied with boundary conditions: the Ar$^+$ equation. The argon neutral number density is calculated from the equation of state (2.7).

- West: The inlet flow velocity profile is assumed to have the following parabolic form:

$$u_{z,\text{in}}(r) = u_{\text{in}}^{\max} \left[1 - \left(\frac{r}{R} \right)^2 \right], \qquad u_{r,\text{in}}(r) = 0 \tag{2.14}$$

  with $u_{\text{in}}^{\max}$ the axial velocity component at the channel axis calculated from a given mass flow rate. This rate is calculated from the inlet flow in scc s^{-1} (i.e. the flow at standard conditions of 1 atm and 273.15 K) given by the user, the inlet temperature and the pressure which follows (iteratively) from the simulation. The value of 2 for the exponent in equation (2.14) may not be fully correct for plasmas, however using different exponential values up to 5 shows negligible influence. At the inlet, a zero axial component of the pressure gradient is assumed[b]. The uniform inlet temperature for electrons and heavy particles is 300 K and an ionisation degree of 10^{-6} determines the ion number density. The effect of different inlet values on the simulations is discussed in section 2.8.

- East: With respect to the axial velocity component on the plasma axis we use the so-called $M = 1$ condition. $M = 1$ means that the axial velocity equals the velocity of sound u_{sound}. The latter is defined as $u_{\text{sound}}^2 = (\partial p / \partial \rho)_{s,\alpha}$, with subscript s, α denoting a constant entropy and constant ionisation degree. Then, under the assumption that the expansion in the low-pressure vacuum chamber is adiabatic and that the ionisation degree is constant, $u_{\text{out}}^{\max}$ is determined from a combination of the energy balance of the mixture (equations (2.4) plus (2.5)) and the continuity equation of the mixture (2.2):

$$u_{\text{out}}^{\max} = \left(\frac{5}{3} \frac{p}{\rho} \right)^{1/2} \tag{2.15}$$

  where we assumed $c_p / c_v = 5/3$, with c_p and c_v the heat capacity at constant pressure and volume, respectively. This assumption implies that argon is considered as a calorically perfect gas. We do not take into account the study of Burm *et al.* [64] who showed that for plasmas the ratio c_p / c_v is lower than for gases (for argon at 1 atm, $c_p / c_v \approx 1.16$ instead of 1.67). For the outlet velocity profile a power law is used of the form of equation (2.14) in which the exponent 2 is replaced by 5. Chang and Ramshaw [65] used the same condition, and found that the best value of the exponent was 5 for their simulations. The effect of different exponents is negligible as is discussed in section 2.8. A constant axial component of the pressure gradient is assumed: $\frac{\partial p}{\partial z} = C$. This condition implies a Neuman pressure

---

[b]It is better to assume a constant axial component of the pressure gradient. This condition is used in the rest of this thesis.

boundary condition which value (C) is determined during the iteration process. The axial components of the gradients of the other plasma variables are set to zero.

- North: A no-slip condition is used: the axial and radial velocity components are zero. The radial component of the pressure gradient is zero. The ion number density is determined from equation (2.11), because at the channel wall the argon ions will recombine to form argon atoms. It is assumed that these atoms will be in the ground state. For argon ions the recombination factor $\gamma_{\mathrm{Ar^+,N}}$ is taken as 0.8, i.e. 8 out of the 10 argon ions colliding with the channel wall will recombine. In the model this sink for the ions is of course also included as a particle source for the argon atoms (cf section 2.5). For the temperatures the following values are assumed: $T_{h,\mathrm{north}} = 500$ K (the cascade plates are water cooled) and $T_{e,\mathrm{north}} = 6000$ K as was also used by Laufer *et al.* [66]. In contrast, Beulens *et al.* [35] used $T_{e,\mathrm{north}} = 1000$ K. Simulations show that changing this last boundary condition to a zero radial derivative has not much influence on the results, see section 2.8.

- South: The radial velocity component is zero and the radial component of the gradients of all other variables are taken as zero.

The main differences in the configuration features between PLASIMO and its predecessor model of Beulens *et al.* [35] are found in the boundary conditions. Beulens used an overdetermined set of boundary conditions, since besides the mass flux inlet condition and Mach number outlet condition, the inlet pressure was specified (which was in fact an experimental value). Also the wall electron temperature value was fixed at a far too low value (1000 K compared to the more correct 6000 K).

2.7.2   Composition features

Transport coefficients

The electric conductivity, the heat conductivity of the electrons and heavy particles and the plasma viscosity for argon are calculated using the standard formulations discussed in sections 2.6.2 and 2.6.3. The diffusion coefficient of the ions (D_i), used in equation (2.1), is equal to the ambipolar diffusion coefficient (D_{amb})^c for a two temperature plasma given by Jonkers *et al.* [15]:

$$D_{\mathrm{amb}} = \frac{3k_b\left(T_h + T_e\right)}{8\rho\Omega^{11}_{\mathrm{Ar^+Ar}}} \tag{2.16}$$

with $\Omega^{11}_{\mathrm{Ar^+Ar}} = \left(3.03 + 6.82 \times 10^{-4}T_h - 3.7 \times 10^{-8}T_h^2 + 9.15 \times 10^{-13}T_h^3\right) \times 10^{-16}$ (in m^3 s^{-1}) a first approximation to the Ar-Ar$^+$ collision integral valid for the temperature range 3000 to $15000K$. This temperature range is sufficient for the simulations of the cascaded arc.

Source terms

From the particle balance equations (2.1) only the Ar$^+$ balance has to be solved since n_e is determined from the quasi-neutrality assumption and n_{Ar} from the equation of state (equation

---

^{c}In the rest of this thesis, the mass fraction balances are solved instead of the particle balances. Since we will use effective diffusion coefficients for all species, there is no longer the need to define an ambipolar diffusion coefficient.

Table 2.2: Fit coefficients a_i for recombination term α_{CR} for different n_e-values.

n_e (m^{-3})	a_0	a_1	a_2	a_3	a_4
10^{19}	-16.004	-4.115	-2.043	3.023	- 0.851
10^{20}	-11.443	-23.219	23.278	-11.401	2.170
10^{21}	-10.996	-23.431	24.004	-11.891	2.280
10^{22}	-10.096	-23.369	23.992	-11.896	2.282

(2.7)). Note that the occupation of the argon excited states is not described in the model. There is no need to simulate this occupation since the influence of excited states on step-wise ionisation can be treated in a separate Collisional-Radiative (CR) model in such a way that the production of argon ions can be expressed in n_e, $n(1)$ (the number density of argon atoms in the ground state) and T_e. These quantities are computed in this PLASIMO application. Note also that the CR model does not form a part of PLASIMO; only the results of this CR model are used in PLASIMO. So the net production term of Ar$^+$ (S_{Ar+}) is deduced from the CR model of Benoy *et al.* [67] in which a hybrid cut-off technique, described by Van der Mullen [68], is used. In this model the number of excited levels in the argon atom is reduced to 21. The resulting Ar$^+$-source term is given by:

$$S_{Ar+} = n_e n_{Ar} S_{CR} - n_e n_{Ar+} \alpha_{CR} \qquad (\text{m}^{-3}\ \text{s}^{-1}) \qquad (2.17)$$

with S_{CR} and α_{CR} the CR ionisation and recombination coefficient, respectively. The CR model calculates S_{CR} and α_{CR} for the electron density range 10^{19} - 10^{23} m^{-3} which includes the n_e-values found in a CA plasma. The CR ionisation coefficient S_{CR} is implemented in the model using fit-functions of an Arrhenius form: $S_{CR} = 7.34 \times 10^{-15} T_e^{1/2} \exp\left(-1.04 E_i / k_b T_e\right)$ in m^{-3} s^{-1}, with $E_i = 1.85 \times 10^{-18}$ J the first step excitation energy. For argon this formula is valid for n_e-values in the given range. The recombination coefficient α_{CR} is implemented using a fourth-order polynomial expression: $\alpha_{CR} = 10^{F(\hat{T}_e)}$, with $F\left(\hat{T}_e\right) = \sum_{l=0}^{4} a_l \hat{T}_e^l$ and $\hat{T}_e$ the electron temperature in eV. The fit coefficients are listed in table 2.2. For evaluating α_{CR} for different n_e-values linear interpolation is applied.

In the momentum balance (equation (2.3)), the $\vec{j}_q \times \vec{B}$-term is neglected since for an argon cascaded arc plasma this Lorentz force is much smaller than the $\vec{\nabla} p$-term in the absence of an externally applied magnetic field.

The source term Q_e in the electron energy balance (2.5) is divided into the elastic energy transfer between electrons and heavy particle species (Q_{eh}^{elas}), the radiation losses (Q_{rad}) and the ionisation losses (Q_{ion}). Q_{eh}^{elas} is given by Mitchner and Kruger [41]:

$$Q_{eh}^{elas} = n_e \sum_{h} \left(\frac{2m_e}{m_h}\right) \frac{3}{2} k_b \left(T_e - T_h\right) \langle \nu_{eh} \rangle \qquad (2.18)$$

where $\langle \nu_{eh} \rangle$ is the collision frequency for $e - h$ collisions with $h = $ Ar or Ar$^+$, averaged over a

Table 2.3: Fit coefficients a_i for radiation terms ε_1 and ε_+ for different n_e-values.

n_e (m^{-3})	ε_1					ε_+			
	a_0	a_1	a_2	a_3	a_4	a_0	a_1	a_2	a_3
10^{19}	-24.74	72.61	-80.27	41.81	-8.302	4.288	-3.356	-0.601	0.099
10^{20}	-20.32	56.09	-58.25	29.13	-5.627	7.416	-10.39	6.712	-1.597
10^{21}	-20.39	56.09	-58.09	28.98	-5.587	8.255	-10.40	6.819	-1.638
10^{22}	-20.41	56.13	-58.12	29.00	-5.589	9.225	-10.38	6.812	-1.638

Maxwellian electron energy distribution. For argon atoms it is written as:

$$\langle \nu_{e-\mathrm{Ar}} \rangle = n_{\mathrm{Ar}} \frac{\langle K_{e-\mathrm{Ar}} E \rangle}{\frac{3}{2} k_b T_e} \tag{2.19}$$

The term $\langle K_{e-\mathrm{Ar}} E \rangle$, with $K_{e-\mathrm{Ar}}$ the reaction coefficient for momentum transfer between e and Ar (in m^3 s^{-1}) and E the electron energy (in J), is evaluated by using the cross-section data given by NIST [69] for momentum transfer between electrons and argon atoms. A fit is used in the model: $\langle K_{e-\mathrm{Ar}} E \rangle = 1.28 \times 10^{-32} \hat{T}_e^3 \exp(-0.35 \hat{T}_e)$ (in J m^3 s^{-1}), with $\hat{T}_e$ in eV. This fit is valid for temperatures below 5 eV. For argon ions the collision frequency for e-Ar$^+$ collisions, averaged over a Maxwellian electron energy distribution, $\langle \nu_{e-\mathrm{Ar}^+} \rangle$, is evaluated using the Coulomb cross-section for collisions between charged particles: $\langle \nu_{e-\mathrm{Ar}^+} \rangle = 3.638 \times 10^{-6} n_e \ln \Lambda / T_e^{1.5}$ (in s^{-1}), with $\ln \Lambda$ the Coulomb logarithm. In the application of $\ln \Lambda$ the Debye shielding length l_D is used with ion screening included [70]:

$$\frac{1}{l_D^2} = \frac{e^2}{\varepsilon_0 k_b} \left(\frac{n_e}{T_e} + \frac{n_{\mathrm{Ar}^+}}{T_h} \right) \tag{2.20}$$

The radiation loss term Q_{rad} describes the energy loss due to the escape of optically thin line radiation (Q_{line}), free-bound (Q_{fb}) and free-free radiation (Q_{ff}). The loss of optically thick resonance radiation is neglected. In argon cascaded arc plasmas line radiation is dominant [71]. The results of the CR model of Benoy are incorporated in the numerical method as:

$$Q_{\mathrm{line}} = n_{\mathrm{Ar}} \varepsilon_1 + n_{\mathrm{Ar}^+} \varepsilon_+ \qquad (\mathrm{W \ m}^{-3}) \tag{2.21}$$

with ε the coefficient of radiation (in W) generated due to the population of radiative states from the ground state (ε_1) or ion state (ε_+). In the model they are treated in the same way as the CR recombination coefficient α_{CR}, i.e. they are written as a polynomial of the order 4 and 3, respectively. The fit coefficients are included in table 2.3.

The contribution of free-free and free-bound radiation are conform the work of Benoy *et al.* [72]:

$$Q_{\mathrm{ff}}^{e-\mathrm{Ar}^+} + Q_{\mathrm{fb}} = 4\pi n_e^2 \sum_{i=0}^{3} f_i T_e^i \tag{2.22}$$

$$Q_{\mathrm{ff}}^{e-\mathrm{Ar}} = 4\pi n_e^2 \left(\frac{6 C_1 k_b}{hc} \right) \frac{T_e^{2.5}}{\alpha} Q_{\mathrm{mom}}^{e-\mathrm{Ar}} (T_e) \tag{2.23}$$

Table 2.4: Fit coefficients used in equation (2.23).

C_1	1.026×10^{-34}	(W m^2 K$^{-3/2}$ sr^{-1})
f_0	$- 3.811 \times 10^1$	(W m^3)
f_1	$- 1.530 \times 10^{-4}$	(W m^3 K^{-1})
f_2	1.330×10^{-8}	(W m^3 K^{-2})
f_3	$- 3.570 \times 10^{-13}$	(W m^3 K^{-3})

with h Planck's constant, c the velocity of light, α the ionisation degree, and $Q_{\mathrm{mom}}^{e-\mathrm{Ar}}$ the cross-section for momentum transfer between electrons and argon atoms according to NIST [69]. The fit coefficients f_i and C_1 are given in table 2.4.

The energy loss of the electrons due to ionisation of argon atoms, Q_{ion}, is given by $Q_{\mathrm{ion}} = S_{\mathrm{Ar+}} e(\hat{E}_{1+} - \delta\hat{E})$, with $\hat{E}_{1+}$ the ionisation energy of the argon atoms in the ground state (15.759 eV) and $\delta\hat{E}$ the lowering of the ionisation energy. For singly ionised species it is written as [73] $\delta\hat{E} = 2.086 \times 10^{-11}(2n_e/T_e)^{1/2}$ ($\delta\hat{E}$ in eV).

The predecessor model of Beulens *et al.* [35] used different formulations of most of the transport coefficients and source terms. The source term $S_{\mathrm{Ar+}}$ in Beulens' model was a polynomial fit of results of a CR model, which, compared to experimental values, was too low at higher temperatures (above 13900 K). Also the radiation loss term and heavy particle transport coefficients in Beulens were calculated using fit functions, whereas in PLASIMO these are calculated using the more accurate results of the CR model of Benoy *et al.* [72] and the CEB-theory, respectively.

The simulation results for the argon CA plasma, with the configuration and composition characteristics described in this section, are discussed in section 2.8.

2.8   Results and discussion

To validate the results of the simulations performed with PLASIMO for a flowing argon CA plasma, the computed results are compared with experimental data. For this purpose experimental data of Kroesen [74] and Beulens *et al.* [75] are used. To show the influence of the boundary conditions on the simulations, different boundary conditions are applied. The simulations are performed for a CA at a constant current $I = 50$ A, and with three different argon flow rates of 50, 100 and 200 scc s^{-1}.

The pressure distribution along the channel wall was measured by Kroesen [74] and Beulens *et al.* [75] and is compared in figure 2.3 with the results of the present simulations. Since the pressure is uniform over the arc cross-section, this comparison is allowed. As can be seen in figure 2.3, PLASIMO slightly underestimates the pressures at the outlet of the CA. Assuming that the experimental results are correct, there are three possible reasons: first, the implementation of the pressure boundary condition could be inaccurate. The influence of the pressure outlet condition has to be investigated in future studies. Second, the $M = 1$ condition at the outlet of the arc can cause problems. The effect on the pressure distribution of Mach values smaller than

unity is shown in figure 2.4, where the Mach value varies between 0.6 and 1.0. It is seen that a better match exists between experiments and model for $M = 0.7$ or $M = 0.8$ instead of $M = 1$. This is not possible for an isentropic gas, but for a plasma the effects of viscosity and heat input can result in $M = 1$ located in the vacuum chamber and not at the arc outlet [76]. Third, there is some discussion if the measured pressure is the *static* pressure or the *stagnation* pressure, defined as $p_{\text{stag}} = p_{\text{static}} + \frac{1}{2}\rho u^2$. Assuming that the measured pressure is the stagnation pressure and using $c_p/c_v \approx 1.2$ cf Burm *et al.* [64], the stagnation pressures calculated from the numerical simulations at the outlet of the CA agree well with the experimental pressures.
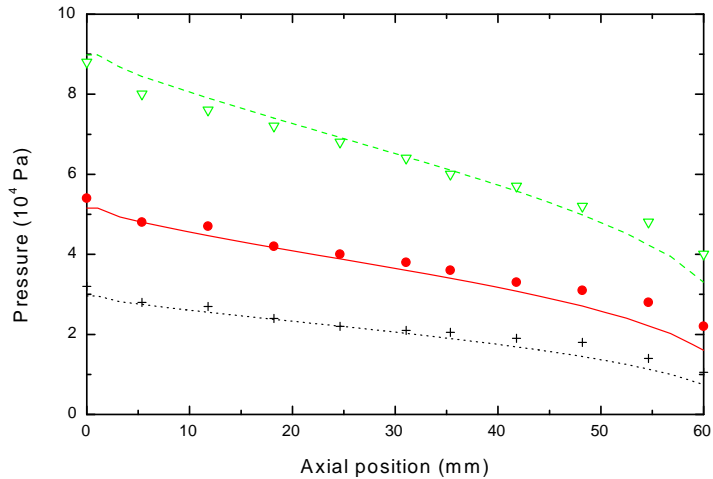
Figure 2.3: The pressure distribution along the arc for different argon flow rates. Experiments (Kroesen [74], Beulens et al. [75]): + 50 scc s^{-1}, ● 100 scc s^{-1}, ▽ 200 scc s^{-1}. Present simulations (PLASIMO): dotted line 50 scc s^{-1}; solid line: 100 scc s^{-1}; dashed line: 200 scc s^{-1}.

Because Beulens *et al.* [35] in the predecessor model used the experimentally known inlet pressure as input, the axial pressure distribution in their simulations shows a slightly better agreement with the experimental data.

The axial velocity component on the axis of the arc channel is shown in figure 2.5. Unfortunately there are no experimental data available for a comparison. The outlet velocity values for the three different flow rates do not differ much from each other since the plasma temperature (used in the calculation of the velocity of sound, see equation (2.15)) at the outlet does not change much for different flow rates (cf figures 2.7 and 2.9). Simulations with different outlet velocity profiles, i.e. with different exponent values in equation (2.14), ranging from 2 to 6, show negligible influence on the results: the ionisation degree at the arc exit increases from 7.85 to 7.97% for an argon flow rate of 100 scc s^{-1}. Changing the inlet velocity profile has a negligible effect on the outlet results.

The electron temperature is compared with experimental data of [74] and [75] for an argon flow rate of 100 scc s^{-1} in figure 2.6. In this figure the cross-sectional averaged T_e distribution is
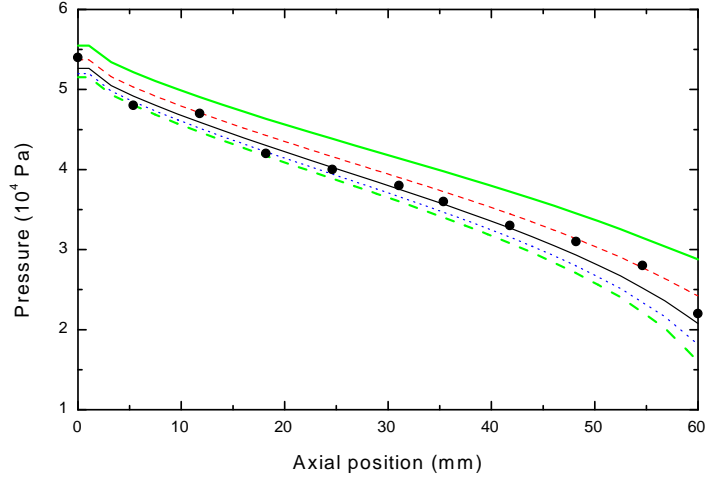
Figure 2.4: The pressure distribution along the arc (at 100 scc s^{-1}) for different velocity outlet conditions. Experiments (Kroesen [74], Beulens et al. [75]): •. Present simulations (PLASIMO) with different Mach numbers: solid grey line (thick), $M = 0.6$; dashed line, $M = 0.7$; solid line, $M = 0.8$; dotted line, $M = 0.9$; dashed grey line (thick), $M = 1.0$.

plotted for three different inlet temperature conditions. Besides the condition $T_e = T_h = 300$ K, two other inlet conditions are shown: (1) $T_e = 8000$ K and $T_h = 300$ K and (2) $T_e = T_h = 3000$ K. It is concluded that the use of different inlet values for the temperatures has an effect on T_e only in the first 25% of the arc channel and no effect at all on the outlet values. The simulated values for T_e are somewhat higher than the experimental values, but the behaviour along the arc is approximately the same. For the predecessor model of Beulens *et al.* [35] the same conclusion applies. This is not unexpected, since the inaccurate formulation of the radiation loss term in that model, does not have a big effect on the results because in strongly flowing arcs the radiation loss term is relatively small. The different inlet temperatures have a substantial influence on the cross-sectional averaged T_h at the inlet region of the plasma, as is shown in figure 2.7. In order to study the effect of different radial T_e boundary conditions we plotted T_e in figure 2.8 with $T_{e,\text{wall}} = 6000$ K (Dirichlet) and $\left(\frac{\partial T_e}{\partial r}\right)_{\text{wall}} = 0$ (homogeneous Neuman) for three different axial positions: $z = 16$ mm, $z = 46$ mm and $z = 60$ mm. The effect of this different T_e boundary condition on T_h is shown in figure 2.9. It is concluded from figures 2.8 and 2.9 that the condition $\left(\frac{\partial T_e}{\partial r}\right)_{\text{wall}} = 0$ influences T_e close to the channel wall up to 30%, at half radius the influence is diminished to a maximum of 2%. The effect on T_h is below 10% everywhere. That the argon CA plasma is not in thermal equilibrium is seen from comparison of figures 2.6 and 2.8 (T_e) with figures 2.7 and 2.9 (T_h). Especially at the inlet of the CA strong deviations from LTE exist. The same applies for the plasma close to the channel wall.

The simulated electron density distribution along the arc is compared with the experimental results [74, 75] in figure 2.10. The global behaviour corresponds with the one found in the
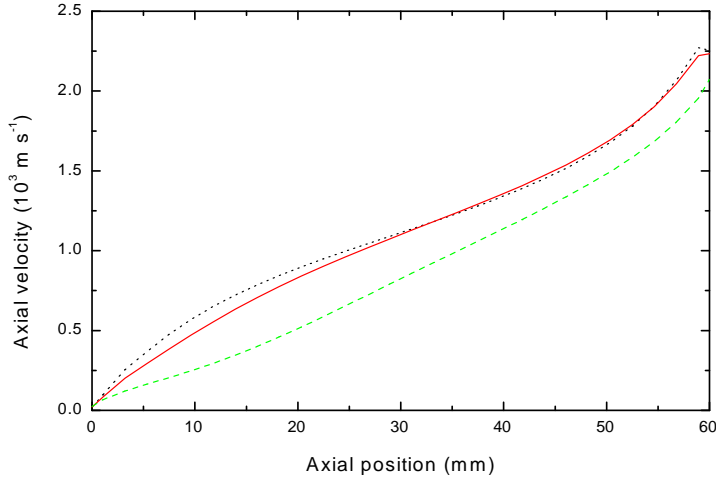
Figure 2.5: The axial velocity component along the arc axis for different argon flow rates (PLASIMO). Lines cf figure 2.3.

experiments, although differences exist in the local values. In the predecessor model of Beulens *et al.* [35], the global behaviour was slightly worse, whereas the local values were closer to the experimental ones. The wrong values of S_{Ar^+} at higher temperatures (above 13900 K, not reached with a current of 50 A) affect the results of the simulations considerably when using higher power input with arc currents above 100 A.

To check the power input in the CA the computed electric field is compared to experimental values [74, 75] in figure 2.11. It is concluded that the numerically simulated electric field agrees well with the experimental values and that the behaviour is correct, so that we can conclude that the assumption of a one-dimensional electric field is allowed. The predecessor model of Beulens *et al.* [35], although using the same formulation of the electric field, shows a somewhat too high electric field in the arc. The reason is found in Beulens' boundary condition for T_e at the wall: $T_{e,w} = 1000$ K, which reduced the effective radius of the plasma channel. Together with approximately the same σ this gives a higher electric field.

2.9 Conclusions

The plasma modelling tool PLASIMO is developed for simulating multi-component plasmas, in a wide pressure range (10^{-4} to 1 bar), in LTE as well as non-LTE, and with different energy coupling principles. As a first example, PLASIMO is applied to a flowing argon plasma in a cascaded arc (CA) with a straight plasma channel. The results of the numerical simulations agree well with the experiments. The influence of different boundary conditions at the inlet and the channel wall show that the inlet conditions are not very important for the result at the outlet, and
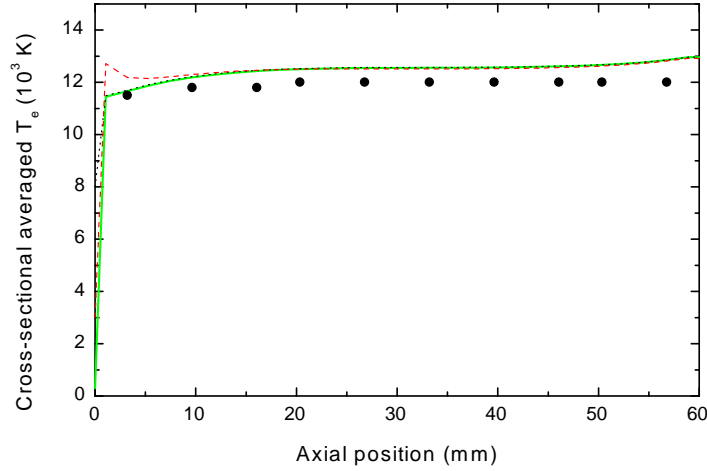
Figure 2.6: The electron temperature distribution averaged over the cross-section of the arc channel (argon flow rate: 100 scc s^{-1}). Experiments (Kroesen [74], Beulens et al. [75]): $\bullet$. Present simulations (PLASIMO) with different inlet values of T_e and T_h: solid grey line (thick), $T_e = T_h = 300$ K; dotted line, $T_e = 8000$ K, $T_h = 300$ K; dashed line $T_e = T_h = 3000$ K.
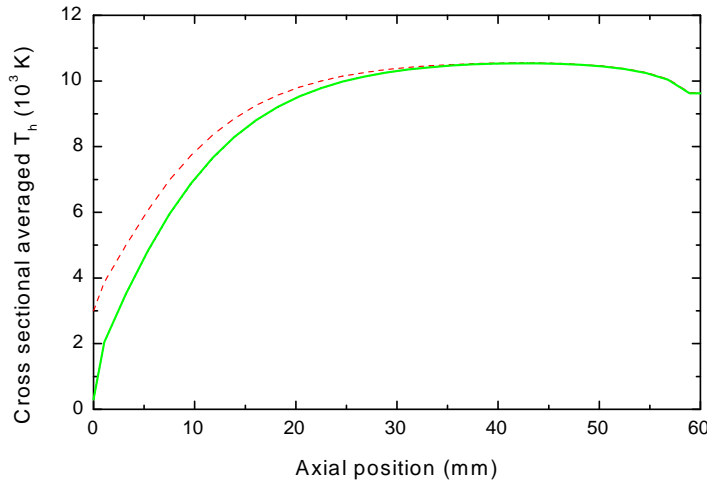
Figure 2.7: The heavy particle temperature averaged over the cross-section of the arc channel (argon flow rate: 100 scc s^{-1}) for different inlet values of the temperatures (PLASIMO). Lines cf figure 2.6.
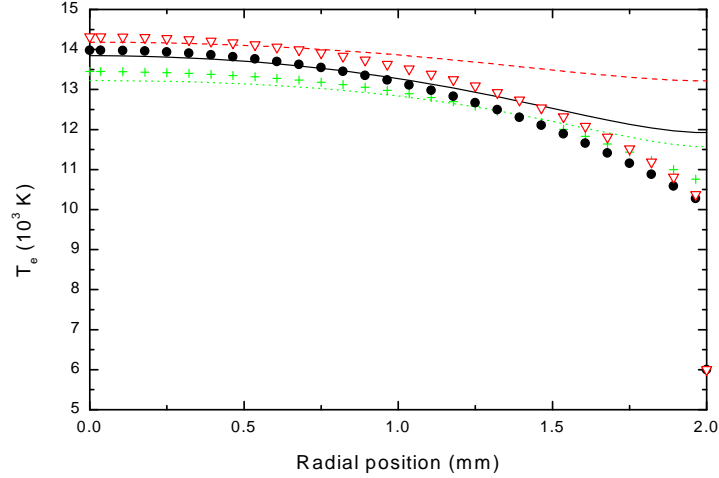
Figure 2.8: The effect on the electron temperature of a different boundary condition at the channel wall (PLASIMO): lines denote the $\partial T_e / \partial r = 0$ boundary condition; dotted line, $z = 16$ mm; solid line, $z = 46$ mm; dashed line, $z = 60$ mm. Markers denote the boundary condition $T_{e,\text{wall}} = 6000$ K; + $z = 16$ mm; $\triangledown$ $z = 46$ mm; $\bullet$ $z = 60$ mm (argon flow rate: 100 scc s^{-1}).
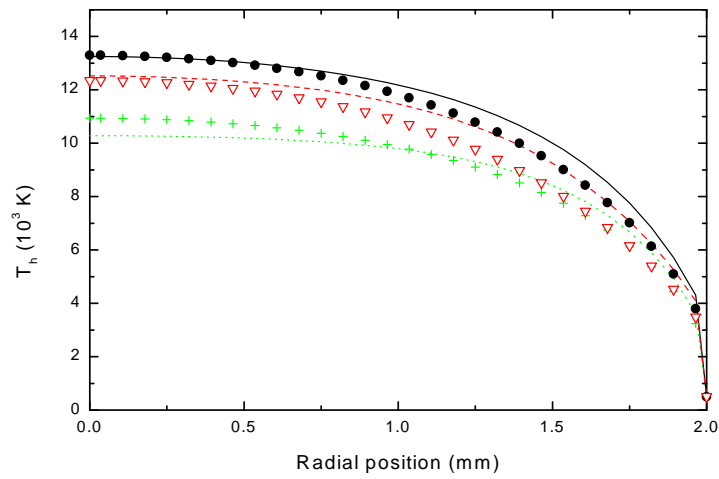
Figure 2.9: The effect on the heavy particle temperature of a different electron temperature boundary condition at the channel wall (PLASIMO): lines and markers cf figure 2.8.

that the boundary conditions at the channel wall only influence the plasma behaviour near that wall. Different outlet boundary conditions for the axial velocity component (i.e. different Mach
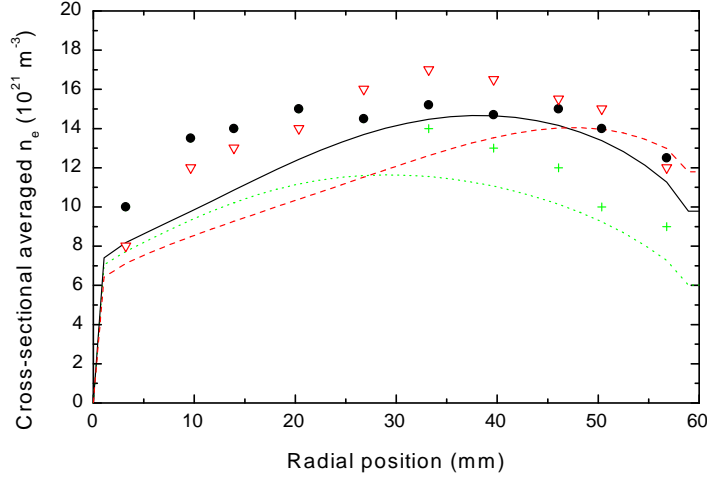
Figure 2.10: The electron density averaged over the cross-section of the arc channel for different argon flow rates. Lines and markers cf figure 2.3.
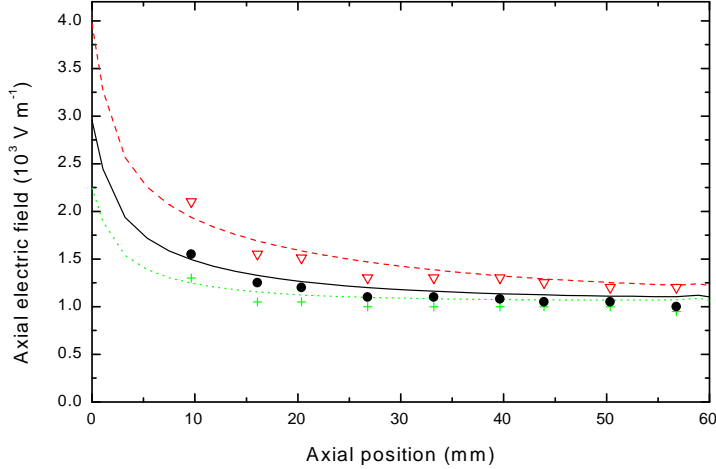
Figure 2.11: The electric field distribution along the arc axis for different argon flow rates. Lines and markers cf figure 2.3.

values) show that the plasma is influenced in the whole CA, as is seen from the pressure distribution. Finally, the energy coupling in the plasma is simulated very well with a one-dimensional model for the electric field.

Acknowledgements

Chapter 3

Multi-Component Diffusion in Non-Equilibrium Plasmas

G.M. Janssen, J. van Dijk, W.J. Goedheer[1] and J.A.M. van der Mullen

Department of Applied Physics, Eindhoven University of Technology, P.O. Box 513, 5600 MB
Eindhoven, The Netherlands
[1] FOM-Institute for Plasma Physics 'Rijnhuizen', P.O. Box 1207, 3430 BE Nieuwegein, The Netherlands

Abstract

A complete description of self-consistent multi-component diffusion in non-equilibrium plasmas is presented. It is based on the exact solution of the Stefan-Maxwell equations as discussed by Sutton [77] and the description for plasmas by Ramshaw [78, 79]. In the application of the Stefan-Maxwell equations on the plasma sources modelled by the plasma computational method PLASIMO, we concentrate mainly on the flowing systems. It is shown that the inelastic collision term in the specific mass and momentum balances, not treated by others, does indeed have no influence in the Stefan-Maxwell equations. The relative importance of the various types of diffusion, i.e. pressure, thermal and forced diffusion, compared to ordinary diffusion is studied. This study proves that in most plasmas forced diffusion can not be neglected, whereas the effect of pressure diffusion and thermal diffusion on the simulations is limited in most cases. As an example the effect of forced diffusion in a hydrogen cascaded arc plasma is studied. It is found that forced diffusion mainly has an effect on the plasma composition in the arc. The effect on temperature and flow fields is negligible.

3.1   Introduction

The diffusion of species in multi-component ionised gas-mixtures has a large impact on the physical processes in non-flowing (e.g. the QL, TL and HID-lamps) and flowing (e.g. the hydrogen cascaded arc plasma) plasma-configurations. For example demixing, that is the partial separation of gases or species, occurs in the presence of temperature or pressure gradients or in the presence of externally applied or self-induced electric fields. Thus the following driving forces are important ingredients in the description of the segregation between the various types of particles in a plasma mixture: the gradient in concentrations (leading to ordinary diffusion), the gradient in pressure (pressure diffusion), the gradient in temperature (thermal diffusion) and (external) forces (forced diffusion). For instance the applied direct current (DC) may cause segregation in constituents in high- or low-pressure lamps, with as a result that the emission of the lamp is non-uniform along its axis, whereas in high-pressure lamps the presence of the gravitational field may lead to a visible vertical segregation. Furthermore we have the examples of the segregation in plasmas in a deposition chamber where the heavy species tend to move to colder regions, forcing the lighter particles to the hotter parts of the plasma [80]. Many more examples can be given and the diversity of this subject makes it understandable that the various sub-disciplines of plasma physics each have there own approaches. On one hand there is the classical gas-discharge physics where the concept of ambipolar diffusion is developed and where Fick's law (ordinary diffusion) is used combined with the Einstein relation between diffusion and mobility [81, 82]. On the other hand we have the field of aerothermodynamics where for instance attention is paid to the phenomena associated with the re-entry of space vehicles in earth's atmosphere. The studies in these fields are based on a solution of the so-called Stefan-Maxwell equations, which describe a relation between the diffusive fluxes and the responsible diffusional driving mechanisms for all species in the mixture.

In this contribution we attempt to bridge the gap between the various application fields. Therefore we will be guided by the description as used in the field of aerothermodynamics of Sutton, Ramshaw (and Murphy), whereas in the appendix "translations" to the field of classical gas-discharge physics will be made.

Our approach is based on the studies of (among others) Sutton [77], Murphy [83, 84] and Ramshaw [26, 78, 79, 85, 86, 87, 88][a]. Sutton described in [77] a way to solve the Stefan-Maxwell equations exactly and consistently for ordinary diffusion. Thereby he limited the discussion to an equi-temperature mixture of neutral gases (this also excludes diffusion driven by an electric field).

In the approach of Murphy [83, 84] multi-component diffusion in plasmas in thermal equilibrium was described in terms of a combined diffusion coefficient formulation, that is diffusion formulated in terms of gases relative to one another, rather than of species[b]. However, the main

---

[a]Kolesnikov and Tirskii [89] presented already in 1979 in Russia an accurate and complete self-consistent set of Stefan-Maxwell equations for multi-component diffusion in a two-temperature plasma. The English version was presented only recently, in 1999 [90, 91] and could not be taken into account in this thesis. Considering the Sonine-polynomial expansion only up to first order, the model of Kolesnikov and Tirskii reduces to the model of Ramshaw and Chang [78].

[b]The term *gas* is defined here as consisting of all species derived from one element; hence a hydrogen gas

difference with Sutton is that apart from the ordinary diffusion also the effects of thermal, pressure and forced diffusion[c] where taken into account, see for example [92, 93].

On the contrary, Ramshaw [78, 79, 85, 87] developed a self-consistent effective binary diffusion approximation for multi-temperature gas mixtures. The extension to plasmas was made by Ramshaw in different articles in which he described forced diffusion [78] and thermal diffusion [79] in ionised gas mixtures. His approach is an approximate one, since the linear system of equations for the diffusive mass fluxes relative to the mass-averaged velocity of the mixture is not solved exactly. Instead, an effective binary diffusion approximation is used.

In the group Equilibrium and Transport in Plasmas at the Eindhoven University of Technology a computational method for the numerical simulation of plasmas, PLASIMO, is used for the investigation of various plasma sources [34], ranging from the flowing cascaded arc (CA), inductively coupled plasmas (ICP) and microwave induced plasmas to confined plasma-systems as the QL-lamp [47] and the Sulphur lamp [2]. Due to the diversity in plasma sources with their specific characteristics that are modelled with one and the same method a complete multi-component diffusion description has to be used for multi-temperature ionised gas mixtures. We have chosen to combine the exact solution of the Stefan-Maxwell equations described by Sutton with the extension to plasmas as described by Ramshaw. This study describes the result and the effect of the different diffusion types in plasmas, with the hydrogen cascaded arc plasma as an example. The full set of Stefan-Maxwell equations for a multi-component multi-temperature ionised gas mixture with the solution method are described in section 3.2. In section 3.3 the calculation of the diffusion coefficients is discussed. The implementation in PLASIMO is presented in section 3.4. The boundary conditions necessary for the set of Stefan-Maxwell equations are given in section 3.5. A simple estimation of the relative importance of the various diffusion types is given in section 3.6. The effect of forced diffusion in a hydrogen CA plasma is shown in section 3.7. Conclusions are presented in section 3.8.

3.2 Self-consistent multi-component diffusion

Basically a weakly-magnetised[d] steady plasma is driven by two external control parameters: the mass flow and the electric current (power). In order to determine how the current evolves in the plasma we need a combination of Ohm's law and the current conservation, whereas the development of the mass flow is basically described by a combination of the mass balance and the momentum balances for the mixture as a whole. The power supply is linked to the energy balances which will not be considered in this study. It is supposed that these balances (one for the electrons and one for the heavy particle species) will give rise to, in principle, two different temperature fields, which on their turn may determine the values of the various transport coefficients in the mass and momentum balances. As we will see, a current conservation equation together with Ohm's law can be used to describe the electron fluxes, whereas the set of mass and

---

contains hydrogen molecules, atoms and ions (atomic/molecular).

[c]This is the so-called cataphoresis: demixing (i.e. partial separation of different species) driven by electric fields.

[d]Magnetisation effects will be neglected, for example in the formulation of the transport coefficients.

momentum balances will be used to derive the behaviour of the heavy particles. We will first concentrate on the latter topic.

3.2.1   The motion of the plasma bulk

The development of the mass flow in the plasma is described by a combination of the conservation of mass and momentum. In a steady and inviscid plasma these read:

$$\vec{\nabla} \cdot (\rho \vec{u}) = 0 \tag{3.1}$$

$$\vec{\nabla} \cdot (\rho \vec{u} \vec{u}) = -\vec{\nabla} p + \sum_i \rho_i \vec{F}_i \tag{3.2}$$

with $\rho = \sum_i \rho_i$ the mass density of the mixture, $\rho_i = m_i n_i$ the partial mass density where m_i and n_i are the mass and number density of species i, respectively; p is the pressure and $\vec{F}_i$ is the body force per unit mass acting on species i. The mass-averaged fluid (or bulk) velocity of the mixture, $\vec{u}$, is given by:

$$\vec{u} = \sum_i \frac{\rho_i}{\rho} \vec{u}_i \tag{3.3}$$

with $\vec{u}_i$ the mean (or systematic) velocity of species i. In equation (3.2) we neglected the influence of viscosity. For the solution of the set of equations formed by (3.1) and (3.2) a modified version of Patankar's SIMPLE algorithm is used in PLASIMO [34, 46]. In this procedure the influence of the viscosity can be taken into account.

3.2.2   The motion of the various plasma constituents

In order to describe the particular behaviour of the various species we have to use the specific mass and momentum balance for species i:

$$\vec{\nabla} \cdot (\rho_i \vec{u}_i) = S_i \tag{3.4}$$

$$\vec{\nabla} \cdot (\rho_i \vec{u}_i \vec{u}_i) = -\vec{\nabla} p_i + \vec{u}_i S_i + \rho_i \vec{F}_i + \sum_j \vec{F}_{ij} \tag{3.5}$$

with p_i the partial pressure, whereas the source term S_i represents the net volumetric rate of production of species i (in kg m^{-3} s^{-1}) due to collisional-radiative processes. This source term is not found in the works of Sutton, Murphy and Ramshaw. Sutton only considered non-reacting gaseous diffusion and Murphy used an LTE assumption, implying that $S_i = 0$. However, also Ramshaw neglected the influence of S_i in reacting plasmas. We will see later on, that indeed terms involving S_i drop out of the Stefan-Maxwell equations.

At this point we have to make a remark about the specific momentum balance as given in equation (3.5). Summing over all specific momentum balances, the result has to be the momentum balance of the mixture, equation (3.2). It can easily be shown that this appears not to be the case here. However, one has to take into consideration that in the momentum balance of species "i", the pressure is referred to the mean velocity of that species, $\vec{u}_i$, whereas in the momentum balance of the mixture, the pressure must be referred to the mass-averaged fluid velocity of the

mixture, $\vec{\mathbf{u}}$. Therefore, the specific momentum balances, as given in equation (3.5) including the pressure term, have to be rewritten in terms of $\vec{\mathbf{u}}$, before summation is performed.

Since we consider here only the case where $\vec{\mathbf{u}}_i \approx \vec{\mathbf{u}}$, we are not interested in the exact formulation of the summation of the specific momentum balances. For this procedure we refer to Holt and Haskell [94] (pp. 151-174). Of course, for a derivation of the Stefan-Maxwell equations, which is valid when $\vec{\mathbf{u}}_i$ differs considerably from $\vec{\mathbf{u}}$, in principle the exact route presented by Holt and Haskell has to be followed.

The relation between p_i and ρ_i is given by the equation of state: $p_i = \rho_i R_g T_i / M_i = n_i k_b T_i$, with M_i the molar mass of species i, k_b the Boltzmann constant, T_i the temperature of species i and R_g the universal gas constant (in J mol^{-1} K^{-1}). The mean force per unit volume exerted by species j on species i is $\vec{\mathbf{F}}_{ij} = -\vec{\mathbf{F}}_{ji}$. We assume that $\vec{\mathbf{F}}_{ij}$ is a linear combination of frictional and thermophoretic forces $\vec{\mathbf{F}}_{ij}^{\text{frict}}$ and $\vec{\mathbf{F}}_{ij}^{\text{therm}}$ [87][e]:

$$\vec{\mathbf{F}}_{ij} = \vec{\mathbf{F}}_{ij}^{\text{frict}} + \vec{\mathbf{F}}_{ij}^{\text{therm}} \tag{3.6}$$

$$\vec{\mathbf{F}}_{ij}^{\text{frict}} = \frac{p z_i z_j}{D_{ij}} \left(\vec{\mathbf{u}}_j - \vec{\mathbf{u}}_i \right) \tag{3.7}$$

$$\vec{\mathbf{F}}_{ij}^{\text{therm}} = \beta_{ij} \frac{1}{T_j} \vec{\nabla} T_j - \beta_{ji} \frac{1}{T_i} \vec{\nabla} T_i \tag{3.8}$$

The pressure fraction is $z_i = p_i / p$. Note that $\sum_i z_i = 1$ and that for the partial pressure p_i the relation $p = \sum_i p_i$ holds. The thermal diffusion factor β_{ij}[f] and the (ordinary) binary diffusion coefficient D_{ij} will be described in section 3.3.

Since the flow of the mass of the mixture is already described by the combination of equations (3.1) and (3.2) it is useful to relate the flow of the various constituents to the plasma bulk flow. This is done by introducing a diffusive mass flux $\vec{\mathbf{J}}_i$ (in kg m^{-2} s^{-1}) of species i:

$$\vec{\mathbf{J}}_i = \rho_i \left(\vec{\mathbf{u}}_i - \vec{\mathbf{u}} \right) \tag{3.9}$$

$$\sum_i \vec{\mathbf{J}}_i = 0 \tag{3.10}$$

with $\vec{\mathbf{u}}_i - \vec{\mathbf{u}} \equiv \vec{\mathbf{u}}_i^d$ the diffusion velocity of species i. According to this convention all the differences between the mean velocity of a plasma constituent and the bulk are denoted as diffusion. Thus even the drift of electrons as created by an electric field is denoted as diffusion. Note that for an n component gas mixture only $n - 1$ diffusive mass fluxes are independent, since due to the definition of the plasma bulk velocity (equation (3.3)), the n diffusive mass fluxes sum up to zero, conform equation (3.10). Together with the fact that $\sum_i S_i = 0$ (there is no creation nor destruction of mass in chemical processes) this implies that the n mass balances sum up to the continuity equation of the mixture (3.1), This means that there are $n - 1$ independent mass

---

[e]In the formulation of equation (3.7) the pressure p follows from the assumption that we deal with ideal gases.

[f]In contrast to Ramshaw [87] we will not call β_{ij} (in kg m^{-1} s^{-2}) a thermal diffusion coefficient because its dimension is different from the conventional multi-component thermal diffusion coefficient (in kg m^{-2} s^{-1}) given by Hirschfelder *et al.* [40]. Instead we will call β a thermal diffusion factor.

balances. Introducing the diffusive mass flux into the specific mass balance (3.4) we get:

$$\underbrace{\vec{\nabla} \cdot (\rho_i \vec{u})}_{\text{convection}} + \underbrace{\vec{\nabla} \cdot \vec{J}_i}_{\text{diffusion}} = \underbrace{S_i}_{\text{source}} \tag{3.11}$$

The specific momentum balance of the various species is needed to get insight in their velocities. However, these equations of the form (3.5) do not provide direct information on the behaviour of $\vec{J}_i$. Instead, information is given on the velocity differences between the various plasma constituents, i.e. $\vec{u}_i - \vec{u}_j$. This is a result of the friction term $\vec{F}_{ij}^{\text{frict}}$ in equation (3.7), which because of its central role will be rewritten in a more fundamental form. We will use the formula of the binary diffusion coefficient D_{ij}, which will be given in equation (3.29), which reveals that this friction force can be written as:

$$\vec{F}_{ij}^{\text{frict}} = C n_i m_{ij} \left(\vec{u}_j - \vec{u}_i \right) \nu_{ij} \tag{3.12}$$

with ν_{ij} the collision frequency, n_i the number density of species i, C a constant of order unity and $m_{ij} = m_i m_j / (m_i + m_j)$ the reduced mass of the (i, j) system. Equation (3.12) states that the momentum transfer per unit volume from species j to species i is proportional to the product of the number density of species i, the amount of momentum received by i (from j) per collision, $m_{ij}(\vec{u}_j - \vec{u}_i)$, and the collision frequency $\nu_{ij} = u_{ij}^{\text{therm}} \sigma_{ij} n_j$. In this expression σ_{ij} is the cross-section for momentum transfer between species i and j whereas $u_{ij}^{\text{therm}} = |u_i - u_j| = (8 k_b T_{ij} / \pi m_{ij})^{1/2}$ is the thermal velocity in the (i, j) system which is determined by the effective temperature of the binary mixture: $T_{ij} = (m_i T_j + m_j T_i) / (m_i + m_j)$.

So instead of relating the velocities of the various species to the plasma bulk velocity, they will be related by means of the friction terms in equations of the type of (3.5). In treating the balance between this friction term and the other driving forces we will follow Ramshaw *et al.* [87], who used the so-called large-friction limit, that is $|\vec{u}_i - \vec{u}| \ll |\vec{u}|$. We will first present a short description of this approach and discuss its applicability afterwards.

In the following we make use of the fact that $\vec{\nabla} \cdot (\rho_i \vec{u}_i \vec{u}_i) = (\rho_i \vec{u}_i \cdot \vec{\nabla}) \vec{u}_i + \vec{u}_i \vec{\nabla} \cdot (\rho_i \vec{u}_i)$ and $\vec{\nabla} \cdot (\rho \vec{u} \vec{u}) = (\rho \vec{u} \cdot \vec{\nabla}) \vec{u}$. Since $\vec{u}_i \approx \vec{u}$ for all species i, the term $(\rho_i \vec{u}_i \cdot \vec{\nabla}) \vec{u}_i$ in the left-hand side (LHS) of the specific momentum balance (3.5) can be regarded as $\rho_i / \rho = y_i$ (with y_i the mass fraction) times the term $(\rho \vec{u} \cdot \vec{\nabla}) \vec{u}$ in the LHS of the momentum balance of the mixture (3.2). This makes it possible to replace $(\rho_i \vec{u}_i \cdot \vec{\nabla}) \vec{u}_i$ in equation (3.5) by y_i times the right-hand side (RHS) of equation (3.2). After some algebra we obtain the generalised Stefan-Maxwell equations:

$$\sum_{j \neq i} \frac{p z_i z_j}{D_{ij}} \left(\vec{u}_i - \vec{u}_j \right) = \vec{G}_i^* \tag{3.13}$$

$$\vec{G}_i^* = \vec{H}_i^* + \left(\rho_i \vec{F}_i - y_i \sum_j \rho_j \vec{F}_j \right) \tag{3.14}$$

$$\vec{H}_i^* = -\vec{\nabla} p_i + y_i \vec{\nabla} p + \sum_{j \neq i} \left(\beta_{ij} \frac{1}{T_j} \vec{\nabla} T_j - \beta_{ji} \frac{1}{T_i} \vec{\nabla} T_i \right) \tag{3.15}$$

where $\vec{G}_i^*$ is the volumetric friction force and $\vec{H}_i^*$ represents the volumetric driving forces for ordinary (concentration), pressure and thermal diffusion.

The Stefan-Maxwell equations (3.13) are written in a slightly different form than used by Ramshaw. The relation between $\vec{\mathbf{G}}_i^*$ used in this study, and $\vec{\mathbf{G}}_i$ used by Ramshaw is: $\vec{\mathbf{G}}_i^* = -p\vec{\mathbf{G}}_i$[g]. For $\vec{\mathbf{H}}_i^*$ we have: $\vec{\mathbf{H}}_i^* = -p\vec{\mathbf{H}}_i$. The notation we use here is closer to that of the classical gas-discharge physics. However for the definition of the various types of diffusion we stick to Ramshaw's approach:

$$\frac{1}{p}\vec{\mathbf{G}}_i^* = \frac{1}{p}\vec{\mathbf{H}}_i^* + \underbrace{\frac{1}{p}\left(\rho_i\vec{\mathbf{F}}_i - y_i\sum_j \rho_j\vec{\mathbf{F}}_j\right)}_{\text{forced diff.}} \tag{3.16}$$

$$\frac{1}{p}\vec{\mathbf{H}}_i^* = - \underbrace{\vec{\nabla}z_i}_{\text{ordinary diff.}} \underbrace{- (z_i - y_i)\frac{1}{p}\vec{\nabla}p}_{\text{pressure diff.}} + \underbrace{\frac{1}{p}\sum_{j\neq i}\left(\beta_{ij}\frac{1}{T_j}\vec{\nabla}T_j - \beta_{ji}\frac{1}{T_i}\vec{\nabla}T_i\right)}_{\text{thermal diff.}} \tag{3.17}$$

In the expression for the diffusive mass flux the following diffusion mechanisms are taken into account in the term $\vec{\mathbf{G}}_i^*$:

- Ordinary diffusion[h], due to gradients in the partial pressure.
- Pressure diffusion, due to a pressure gradient which separates species with different molecular weights and temperature.
- Thermal diffusion (Soret effect), i.e. due to temperature gradients a separation of the gas mixture can occur.
- Forced diffusion, due to forces acting on the species. These forces include gravitation, externally applied electric fields $\vec{\mathbf{E}}^e$ and the (ambipolar) electric field $\vec{\mathbf{E}}^a$ that arises because of the tendency of the electrons to diffuse more rapidly than ions.

Of course not all four diffusion mechanisms are equally important. In various (plasma) configurations different mechanisms can play a leading role, as will be shown in section 3.7.

The set of equations (3.13) to (3.15) are generally used in literature for various applications. Note however that viscous effects are neglected and furthermore, that the inelastic collision term dropped out, and finally, that the equations (3.13) to (3.15) are derived for the approximation $\vec{\mathbf{u}}_i \approx \vec{\mathbf{u}}$.

Introducing the diffusion mass fluxes (equation (3.9)) in the Stefan-Maxwell equation (3.13) we get the following expression:

$$\sum_{j\neq i}\frac{pz_iz_j}{D_{ij}}\left(\frac{\vec{\mathbf{J}}_i}{\rho_i} - \frac{\vec{\mathbf{J}}_j}{\rho_j}\right) = \vec{\mathbf{G}}_i^* \tag{3.18}$$

Using an effective diffusion coefficient $D_i^{\text{eff}} = \left(\sum_{j\neq i} z_j/D_{ij}\right)^{-1}$, equation (3.18) can be rewritten

---

[g]The minus sign, because the left-hand side of equation (3.13) is written as $(\vec{\mathbf{u}}_i - \vec{\mathbf{u}}_j)$ instead of $(\vec{\mathbf{u}}_j - \vec{\mathbf{u}}_i)$.

[h]This diffusion type is often called *concentration* diffusion. We use the adjective *ordinary* since this diffusion type is always included in the mass fraction balances.

to give an expression for the diffusive mass fluxes $\vec{\mathbf{J}}_i$:

$$\vec{\mathbf{J}}_i = \frac{m_i}{k_b T_i} D_i^{\text{eff}} \vec{\mathbf{G}}_i^* + y_i D_i^{\text{eff}} \sum_{j \neq i} \frac{z_j \vec{\mathbf{J}}_j}{y_j D_{ij}} \tag{3.19}$$

This expression shows that the diffusive mass flux of species i is the result of the driving diffusion forces acting on species i (first term in the RHS) and the friction of i with other plasma constituents (second term in the RHS). The factor $m_i D_i^{\text{eff}}/(k_b T_i)$ can be seen as a generalisation of the mobility μ_i, which relation with the diffusion coefficient follows from the Einstein relation [95]:

$$\frac{D_i}{\mu_i} = \frac{k_b T_i}{e} \tag{3.20}$$

with e the elementary charge.

Equation (3.19) represents a set of n equations, with n the total number of species present in the mixture. Due to equation (3.10) only $n-1$ of these equations are independent. Solving this system consistently is pursued following Sutton [77], see section 3.4.

3.2.3 Forced diffusion

If the only body forces are gravity and electric forces (acting on the charged species), then $\vec{\mathbf{F}}_i = \vec{\mathbf{g}} + q_i \left(\vec{\mathbf{E}}^e + \vec{\mathbf{E}}^a \right)$, with $\vec{\mathbf{g}}$ the acceleration of gravity and $q_i = Z_i e/m_i$ the charge per unit mass of species i with $Z_i e$ and m_i its charge and mass, respectively. Note that for the electrons $Z_e = -1$. The electric field is $\vec{\mathbf{E}}$ and consists of an external and ambipolar component. Note that in this study the Lorentz force term $\vec{\mathbf{j}}_q \times \vec{\mathbf{B}}$ is neglected, with $\vec{\mathbf{j}}_q$ the current density and $\vec{\mathbf{B}}$ the externally applied or generated magnetic field. This is a valid assumption in cascaded arc plasmas. In an ICP or lamps the Lorentz force has to be taken into account.

We can now rewrite $\vec{\mathbf{G}}_i^*$ by using the quasi-neutrality assumption $\sum_i q_i \rho_i = 0$ (i.e. no net charge density) as:

$$\vec{\mathbf{G}}_i^* = \vec{\mathbf{H}}_i^* + q_i \rho_i \left(\vec{\mathbf{E}}^e + \vec{\mathbf{E}}^a \right) \tag{3.21}$$

In section 3.2.2 it was noted that if $\vec{\mathbf{u}}_i$ differs much from $\vec{\mathbf{u}}$, the specific momentum balances have to be rewritten in terms of $\vec{\mathbf{u}}$. In the case of a confined configuration, for which $\vec{\mathbf{u}} = 0$, it can be shown from the specific momentum balance, with the assumption that for each heavy particle species the diffusion velocity is much smaller than the thermal velocity, that the following (approximate) equations hold:

$$\vec{\mathbf{G}}_i^{*,\text{confined}} = \vec{\mathbf{H}}_i^{*,\text{confined}} + \rho_i \vec{\mathbf{g}} + q_i \rho_i \left(\vec{\mathbf{E}}^e + \vec{\mathbf{E}}^a \right) \tag{3.22}$$

$$\vec{\mathbf{H}}_i^{*,\text{confined}} = -\vec{\nabla} p_i + \sum_{j \neq i} \left(\beta_{ij} \frac{1}{T_j} \vec{\nabla} T_j - \beta_{ji} \frac{1}{T_i} \vec{\nabla} T_i \right) \tag{3.23}$$

For electrons the Stefan-Maxwell equations are not used. Instead, the current conservation equation will be used for the calculation of the diffusive mass flux of the electrons. This will be explained next.

The current density $\vec{\mathbf{j}}_q$ in the plasma is related to the diffusive mass fluxes via the current density:

$$\vec{\mathbf{j}}_q = \sum_i q_i \vec{\mathbf{J}}_i = \sum_i q_i \rho_i \vec{\mathbf{u}}_i \tag{3.24}$$

This equation can be used to determine the electron diffusive mass flux:

$$\vec{\mathbf{J}}_e = \frac{1}{q_e} \left[\vec{\mathbf{j}}_q - \sum_{j \neq e} q_j \vec{\mathbf{J}}_j \right] \tag{3.25}$$

In steady state, $\vec{\mathbf{E}}^a$ slows down the diffusion of the electrons and speeds up the diffusion of ions in such a way that charge neutrality is maintained. The current density on its turn is prescribed by the simplified Ohm's law [i]:

$$\vec{\mathbf{j}}_q = \sigma \vec{\mathbf{E}}^e \tag{3.26}$$

with σ the electric conductivity. If $\vec{\mathbf{E}}^e = 0$ we get the ambipolar condition $\vec{\mathbf{j}}_q = 0$. See also [83].

An expression for σ can be obtained by substituting equations (3.19), (3.21) and (3.24) into equation (3.26) and equating the terms containing $\vec{\mathbf{E}}^e$ in the LHS and RHS. This gives:

$$\sigma = \sum_i \frac{q_i^2 \rho_i m_i}{k_b T_i} D_i^{\mathrm{eff}} \tag{3.27}$$

Note that using the Frost mixture rules for the electric conductivity [41] (which is often done) is not possible here, since it could lead to an inconsistency. The other terms in the LHS and RHS give an expression for the ambipolar field $\vec{\mathbf{E}}^a$:

$$\vec{\mathbf{E}}^a = -\frac{1}{\sigma} \left[\sum_i \frac{q_i m_i}{k_b T_i} D_i^{\mathrm{eff}} \vec{\mathbf{H}}_i^* + \sum_i q_i y_i D_i^{\mathrm{eff}} \sum_{j \neq i} \frac{z_j \vec{\mathbf{J}}_j}{y_j D_{ij}} \right] \tag{3.28}$$

We will show in the appendix that for a three-species mixture, consisting of atoms, positive ions and electrons, the formulation of $\vec{\mathbf{E}}^a$ reduces to the well-known expressions given in the literature [81]. For these types of mixtures also the well-known ambipolar diffusion coefficient can be derived from the expressions given above.

3.3   Diffusion Coefficients

The binary diffusion coefficient D_{ij} for a multi-temperature mixture is defined to the first approximation by Ramshaw [79]:

$$D_{ij} = \frac{3}{16} \frac{f_{ij} k_b^2 T_i T_j}{p m_{ij} \Omega_{ij}^{(1,1)}(T_{ij})} \tag{3.29}$$

---

[i] The generalised Ohm's law is given by [96]:

$$\vec{\mathbf{j}}_q = \sigma \left(\vec{\mathbf{E}}^e + \frac{\vec{\nabla} p_e}{e n_e} + 1.71 \frac{k_b \vec{\nabla} T_e}{e} \right)$$

The last two terms in the right-hand side are negligible in most cases.

Note that when species i and j have the same temperature T, T_{ij} reduces to T; $\Omega_{ij}^{(1,1)}$ is the collision integral in first approximation, given in Hirschfelder *et al.* [40]. We will write $\Omega_{ij}^{(1,1)}$ as [40]:

$$\Omega_{ij}^{(1,1)}(T_{ij}) = \left(\frac{8k_bT_{ij}}{\pi m_{ij}}\right)^{1/2}\frac{1}{4}\pi d_{ij}^2\Omega_{ij}^{(1,1)*} \tag{3.30}$$

$$\Omega_{ij}^{(1,1)*} = \frac{[\Omega_{ij}^{(1,1)}]}{[\Omega_{ij}^{(1,1)}]_{\text{rigsph}}}$$

with d_{ij} the rigid-sphere binary collision diameter, whereas $\Omega_{ij}^{(1,1)*}$ denotes the deviation of any particular collision model from the idealised rigid-sphere model, e.g. for no deviation this term is 1. Note that for all types of collisions (neutral-neutral, neutral-charged and charged-charged, so also for Coulomb collisions) the collision cross-sections are translated into a rigid-sphere cross-section of the form $\frac{1}{4}\pi d_{ij}^2$.

The correction factor f_{ij} in equation (3.29) (and later on in equation (3.33)) is necessary for describing charged species pairs involving electrons. If the electron is not involved then $f_{ij} = 1$. If one of the charged species i, j is an electron then $f_{ie} = f_{ei} = f(Z_i)$ with Z_i the charge number of species i: $f(1) = 1.97$, $f(2) = 2.33$ and $f(3) = 2.53$. For ion-ion pairs equation (3.29) is used with f_{ij} set to 1, i.e. the standard expression for D_{ij} is then used.

Equation (3.29) with equation (3.30) substituted gives:

$$D_{ij} = 7.67486 \times 10^{-36}\frac{f_{ij}T_iT_j/\left(T_{ij}m_{ij}\right)^{1/2}}{pd_{ij}^2\Omega_{ij}^{(1,1)*}} \quad (\text{m}^2\text{ s}^{-1}) \tag{3.31}$$

For the thermal diffusion factor β_{ij} we have to make a distinction between neutral-neutral, charged-neutral, and charged-charged pairs (i.e. either ions or electrons). For neutral-neutral pairs β_{ij} is given by [88]. For charged-neutral pairs β_{ij} is much smaller than that for charged-charged pairs [79], so we neglect it. For charged-charged pairs β_{ij} is given by [79]. The equations read:

$$\text{neutral-neutral pairs: } \beta_{ij} = -\frac{1}{2}\frac{pz_iz_j\tau_j}{D_{ij}}\frac{m_{ij}}{m_j^2}\frac{k_bT_j^2}{T_{ij}} \tag{3.32}$$

$$\text{charged-charged pairs: } \beta_{ij} = \frac{3}{2}\frac{f_{ij}pz_iz_j\tau_j}{D_{ij}}\frac{m_{ij}}{m_j^2}\frac{k_bT_j^2}{T_{ij}} \tag{3.33}$$

with τ_j the mean time between collisions of a particle species j with all other particles, i.e. particles of any species including species j, given by Ramshaw [78]. Especially in plasmas with a distinct difference between electron and heavy particle temperature the multi-temperature description can be of importance. Also when there are temperature differences between the various heavy particle species (not included in PLASIMO at this moment), thermal diffusion becomes important.

3.4   Implementation into PLASIMO

To include the diffusive mass fluxes correctly in the particle balance equations (3.11), the diffusive fluxes $\vec{\mathbf{J}}_i$ of **all** species i have to be calculated. Due to the mutual dependencies the $\vec{\mathbf{J}}_i$'s are calculated iteratively. For all heavy particle species equation (3.19) is used and for the electrons equation (3.25). As a first guess of $\vec{\mathbf{J}}_i$ of the heavy particle species, the first term on the RHS of equation (3.19) is used. After iteration N in the Stefan-Maxwell iteration cycle, we will in general find that despite of equation (3.10) $\sum_i \vec{\mathbf{J}}_i^N \neq 0$. This residual value will be distributed over the constituents according to their relative mass density y_i, so that $\vec{\mathbf{J}}_i$ for iteration $N+1$ will be:

$$\vec{\mathbf{J}}_i^{N+1} = \vec{\mathbf{J}}_i^N - y_i \sum_j \vec{\mathbf{J}}_j^N \tag{3.34}$$

Note that in equation (3.34) the summation is performed over all particle species j including the electrons. The process is repeated for a user-specified number of iterations (usually 10 is enough). So during each main iteration cycle (i.e. solution of mass, momentum and energy balances) of PLASIMO, a sub-iteration cycle is performed for solving the Stefan-Maxwell equations.

If there are n heavy particle species in the mixture, in principle $n-1$ heavy particle mass fraction balances (3.11) need to be solved, because of the constraint $\sum_i y_i = 1$. The last heavy particle species should then be a neutral species, since the mass fraction of the electrons, y_e, is calculated from the quasi-neutrality assumption, rewritten as: $\rho \sum_i q_i y_i = 0$. However, faster convergence is achieved by using a similar procedure for the mass balances as for the Stefan-Maxwell equations: solve all heavy particle mass balances, calculate y_e from the quasi-neutrality assumption, and correct then all mass fractions y_i according to: $y_i^{\text{new}} = y_i / \sum_j y_j$.

The main assumptions and limitations of PLASIMO, together with a description of the physical model and numerical method, are given in [34]. With respect to the implementation of self-consistent multi-component diffusion in PLASIMO it is important to note that in the construction of the numerical method each of the hydrodynamic transport equations is written as a particular case of the so-called ϕ-equation [46], that reads:

$$\vec{\nabla} \cdot \left(f_\phi \rho \vec{\mathbf{u}} \phi \right) - \vec{\nabla} \cdot \left(\lambda_\phi \vec{\nabla} \phi \right) = S_\phi \tag{3.35}$$

with the factors f_ϕ and λ_ϕ a convection and diffusion coefficient, respectively and S_ϕ the source term.

To write the particle balance (3.11) in the form of equation (3.35) it is written in terms of mass fractions y_i. In the LHS a convection and a diffusion term have to be present, therefore the expression of the diffusive fluxes, i.e. equation (3.19) combined with equation (3.34) is rewritten so that a diffusive term conform the second term in the LHS of equation (3.35) appears, the rest of the diffusive flux is added to the RHS. It can be shown that the ϕ-equation factors for the mass fraction balance become: $\phi = y_i$, $f_\phi = 1$, $\lambda_\phi = \rho D_i^{\text{eff}}$, and $S_\phi = -\vec{\nabla} \cdot \vec{\mathbf{J}}_i' + S_i$ with $\vec{\mathbf{J}}_i'$ the part of the diffusive mass flux $\vec{\mathbf{J_i}}$ that can not be written in terms of $\vec{\nabla} y_i$.

3.5   Boundary conditions

- At walls, the net total mass flux of the species "i" normal to the wall must equal the net mass flux R_i due to production or consumption of the species at the wall:

$$\vec{\mathbf{n}} \cdot \left(\rho y_i \vec{\mathbf{u}} + \vec{\mathbf{J}}_i \right) = R_i \tag{3.36}$$

with $\vec{\mathbf{n}}$ the unit vector perpendicular to the wall. In the configurations discussed in this thesis, the velocity components normal to (any) surface are taken to be zero (no-slip and no net gaseous production at surfaces), so that equation (3.36) reduces to: $\vec{\mathbf{n}} \cdot \vec{\mathbf{J}}_i = R_i$, with R_i given by:

$$R_i = m_i \left(\Gamma_{i,w}^{\text{out}} - \Gamma_{i,w}^{\text{in}} \right) \tag{3.37}$$

with $\Gamma_{i,w}$ the flux (in $\text{m}^{-2}\text{s}^{-1}$) describing the gain or loss of species i at the wall w, discussed in chapter 2. In the absence of consumption or production of chemical species, i.e. no mass production/destruction at the wall, the diffusive fluxes of the species perpendicular to the wall must be zero: $\vec{\mathbf{n}} \cdot \vec{\mathbf{J}}_i = 0$.

- At inlets, the total mass flow of species i must correspond to the inlet flow φ_i. If the inlet flows φ_i are given in scc s^{-1}, the mass flow per species (in kg s^{-1}) is given by:

$$
\begin{aligned}
\Phi_{\text{mass},i} &= 10^{-6} \frac{p_{st} M_i}{R_g T_{st}} \varphi_i \quad (\text{kg s}^{-1}) \\
&= \vec{\mathbf{n}} \cdot \left[2\pi \int_0^{R_{\text{in}}} \left(\rho \vec{\mathbf{u}} y_i + \vec{\mathbf{J}}_i \right) r \, dr \right]
\end{aligned}
\tag{3.38}
$$

R_{in} is the radius of the inlet opening, p_{st} and T_{st} are the pressure and temperature at standard conditions: 1 atm and 273.15 K.

Equation (3.38) is satisfied by taking each of the mass fractions over the inlet opening fixed:

$$y_i = \frac{M_i \varphi_i}{\sum_j M_j \varphi_j} \tag{3.39}$$

and by prohibiting diffusion of species i through the inlet opening:

$$\vec{\mathbf{n}} \cdot \vec{\mathbf{J}}_i = 0 \tag{3.40}$$

- At outlets, the gradient of y_i perpendicular to the outlet plane is assumed to be zero:

$$\vec{\mathbf{n}} \cdot \vec{\nabla} y_i = 0 \tag{3.41}$$

3.6   Relative importance of the four diffusion types

We can estimate the importance of the four types of diffusion (ordinary (OD), pressure (PD), forced (FD) and thermal diffusion (TD)), by looking at the ratios of them. Since ordinary diffusion usually is the dominant diffusion type, we will look at the ratios PD / OD, FD / OD and

TD / OD. For this purpose the expressions of the four diffusions as given in equations (3.16) and (3.17) are simplified by introducing gradient lengths Λ^{OD}, Λ^{PD}, Λ^{FD} and Λ^{TD}. The ratios PD / OD, FD / OD and TD / OD are then written for species i as:

$$\frac{\mathrm{PD}}{\mathrm{OD}} = \left(1 - \frac{y_i}{z_i}\right) \frac{\Lambda^{\mathrm{OD}}}{\Lambda^{\mathrm{PD}}} \tag{3.42}$$

$$\frac{\mathrm{FD}}{\mathrm{OD}} = \frac{1}{\hat{T}_i} Z_i \left(\left|\vec{\mathbf{E}}^e\right| + \left|\vec{\mathbf{E}}^a\right|\right) \Lambda^{\mathrm{OD}} \tag{3.43}$$

$$\frac{\mathrm{TD}}{\mathrm{OD}} = \frac{1}{p_i} \sum_{j \neq i} (\beta_{ij} - \beta_{ji}) \frac{\Lambda^{\mathrm{OD}}}{\Lambda^{\mathrm{TD}}} \tag{3.44}$$

with $\hat{T}_i$ the temperature of species i in eV. Equations (3.42), (3.43) and (3.44) provide a tool to estimate the importance of the diffusion types in a plasma source.

3.7   Results

We will investigate the influence of forced diffusion on a hydrogen cascaded arc (CA) plasma[j]. Since in a CA the radial pressure distribution is rather uniform, PD will not play a role in that direction. In axial direction PD can have a small effect (for an argon arc the pressure difference between in- and outlet can reach 4×10^4 Pa). Thermal diffusion will only play an important role if the mass difference between the species is large. An example of its influence in an argon-silane gas mixture in a vacuum chamber at low pressure is presented in chapter 6 of this thesis.

We will focus on the effect of forced diffusion on the behaviour of the hydrogen CA plasma for the standard configuration applied in chapters 4 and 5 of this thesis. Summarised, the operation conditions are: a straight CA channel with radius $R = 2$ mm, length $L = 25$ mm, current $I = 50$ A and inlet flow $\varphi = 100$ scc s^{-1}.

The radial profiles of the mass fractions at an axial position of 11.8 mm with and without forced diffusion included are shown in figure 3.1. In the central region of the plasma, the effects on H and H$^+$ are the highest: including FD increases y_{H} with 3% whereas $y_{\mathrm{H^+}}$ is decreased by 11%. In the outer plasma region, near the channel wall the effects on H$_2$ and H$_2^+$ are the highest: $y_{\mathrm{H_2}}$ decreases with 5%, whereas $y_{\mathrm{H_2^+}}$ decreases with 12%. The radial profiles of T_e and T_h are shown in figure 3.2. The effect of forced diffusion on the temperature fields is negligible: it is less than 0.1% at any position in the arc. This is a result also found by Murphy [93]. Also the influence on the flow field (not shown) is very small.

One can conclude that forced diffusion has its influence on the composition in the arc, but does not alter the other arc properties significantly. We gave a recipe to estimate the possible influence of forced diffusion in section 3.6, which proved that under certain conditions it could be of the same importance as ordinary diffusion. Murphy [93] showed that forced diffusion could be of influence especially in gas mixtures where the gases have different ionisation energies.

---

[j]Note that if forced diffusion is switched off, in PLASIMO the effect of the externally applied electric field is still taken into account, only the ambipolar influence is neglected in that case.

The generated ambipolar electric field and the difference in electric conductivity using Frost formulation and the self-consistent formulation presented in this study are shown in figures 3.3 and 3.4, respectively. The radial component of the ambipolar electric field, E_r^a, shown in figure 3.3 is near the channel wall in the same order of magnitude as the externally applied electric field: $E_z \approx 5 \times 10^3$ V m^{-1} and can certainly not be neglected in that region. From the comparison of the self-consistent formulation of the electric conductivity, equation (3.27) and the formulation according to Frost, we can conclude that that it is really necessary to use the self-consistent formulation, since otherwise a serious error is introduced in the arc behaviour: a wrong electric conductivity implies a wrong electric field and has consequently a serious influence on the composition in the arc.

3.8   Conclusions

We presented a complete description of self-consistent multi-component diffusion in plasmas. Included are the two-temperature character of a plasma and the influence of the various types of diffusion. It is based on the exact solution of the Stefan-Maxwell equations as discussed by Sutton [77] and the description for plasmas by Ramshaw [78, 79]. Combining the work of Sutton, Ramshaw and Murphy [83, 84] the influence of ordinary, pressure, forced and thermal diffusion are taken into account. The inelastic collision term in the specific mass and momentum balances, not treated by others, does indeed have no influence in the Stefan-Maxwell equations. A recipe is given for estimating the influence of the various types of diffusion in applications. In this way, only the most important diffusion types can be taken into account in the simulations, which is time-saving.

The influence of forced diffusion on a hydrogen cascaded arc plasma is investigated. Forced diffusion does not alter significantly the temperature distribution in the arc. A bigger influence is seen in the radial distribution of the mass fractions (maximum 11%). It is to be expected that for gas mixtures (for example argon-mercury in a TL-lamp) with significantly different ionisation energies (argon: 15.76 eV, mercury: 10.44 eV) the effect of forced diffusion is larger. The influence of thermal diffusion can be large when the mass differences between species are large (for example in an argon-hydrogen plasma or in an argon-silane gas mixture, see chapter 6 of this thesis).

Acknowledgements
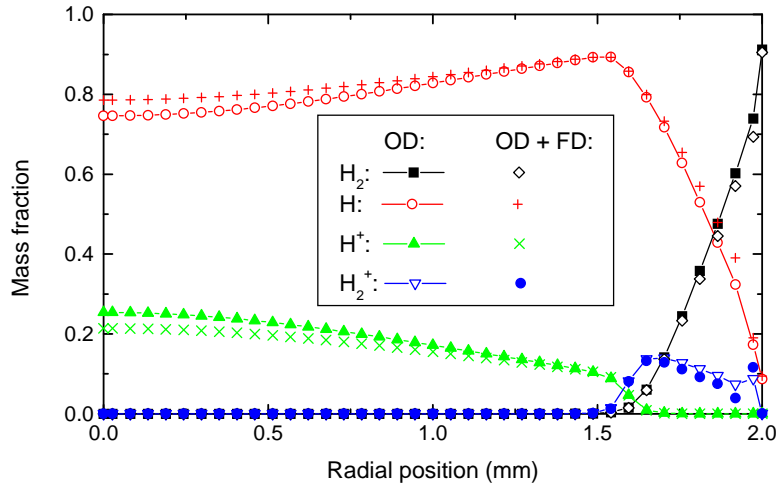
Figure 3.1: The radial profiles of the mass fractions of H_2, H, H^+ and H_2^+ in a hydrogen cascaded arc plasma, at $z = 11.8$ mm, for two cases: with (OD + FD) and without (OD) forced diffusion.

Figure 3.2: The radial profiles of the electron and heavy particle temperatures in a hydrogen cascaded arc plasma, at $z = 11.8$ mm, for two cases: with (OD + FD) and without (OD) forced diffusion.
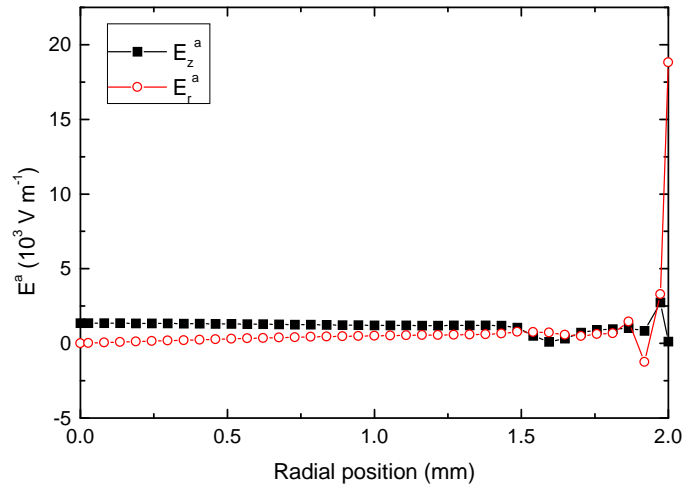
Figure 3.3: The radial profiles of the axial and radial component of the ambipolar electric field in a hydrogen cascaded arc plasma, at $z = 11.8$ mm, with forced diffusion (OD + FD).
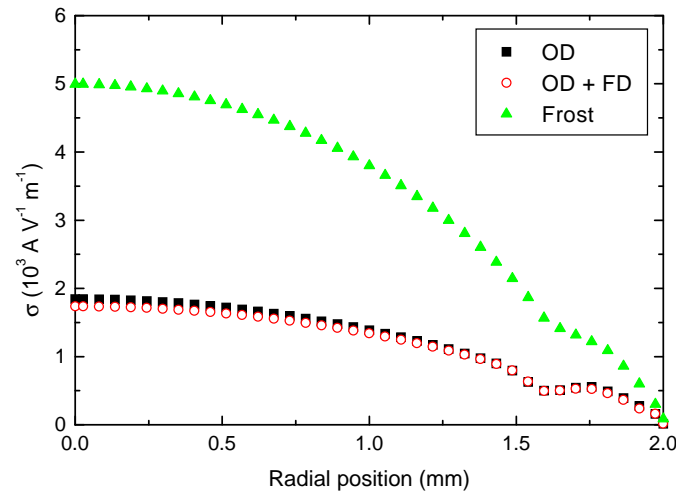
Figure 3.4: The radial profile of the electric conductivity at $z = 11.8$ mm, according to the Frost formulation (up triangles) and the self-consistent formulation, equation (3.27) for two cases: with (OD + FD) and without (OD) forced diffusion.

Appendix of chapter 3

In section 3.2 we made a remark about ambipolar diffusion. The motion of $\{e\}$ and $\{h\}$ are closely coupled, in view of the quasi-neutrality condition. Diffusion at conditions for which the fluxes of the charged species are equal and $\vec{\mathbf{j}}_q = 0$ (i.e. no externally applied electric field: $\vec{\mathbf{E}}^e = 0$) is commonly referred to as ambipolar diffusion, see for example Mitchner and Kruger [41] and especially Golant *et al.* [81]. In this case an *ambipolar* diffusion coefficient D_{amb} is formulated, which relates the diffusion of the charged species to each other. In many textbooks the example of a three-species mixture, containing only neutral atoms ("A"), positive ions ("I") and electrons ("e") can be found. Unfortunately, in a multi-component mixture the formulation of an ambipolar diffusion coefficient is much more complicated than the relatively straightforward three-species example. For instance, if negative ions come into play (for example in an oxygen plasma), the motion of positive ions is drastically changed.

In the treatment of diffusion, presented in this study, no longer a need exists to calculate an ambipolar diffusion coefficient; use is made of *effective* diffusion coefficients, whereas the ambipolar constraint is already captured in the formulation of the diffusive mass fluxes and the current conservation.

We will demonstrate here that the application of the theory from section 3.2 to the standard textbook example of a three-species mixture gives the same result[k].

We start with equation (3.18) applied to the positive ion I, with equation (3.21) substituted. Assuming $\vec{\mathbf{E}}^e = 0$, that the electron diffusive mass flux (due to $\vec{\mathbf{J}}_e = \frac{m_e}{m_I}\vec{\mathbf{J}}_I$) and the inelastic collision term can be neglected, we get:

$$\frac{z_I z_A}{D_{IA}} \left(\frac{\vec{\mathbf{J}}_A}{\rho_A} - \frac{\vec{\mathbf{J}}_I}{\rho_I} \right) = \vec{\mathbf{H}}_I - \frac{q_I \rho_I}{p}\vec{\mathbf{E}}^a \tag{A.1}$$

Using equation (3.10), stating that $\vec{\mathbf{J}}_A = -\vec{\mathbf{J}}_I$, we get:

$$\vec{\mathbf{J}}_I = -\frac{\rho_I \rho_A D_{IA}}{\rho z_I z_A} \left(\vec{\mathbf{H}}_I - \frac{q_I \rho_I}{p}\vec{\mathbf{E}}^a \right) \tag{A.2}$$

where we also neglected the electron contribution to the total mass density ρ so that $\rho_A^{-1} + \rho_I^{-1} = \rho/(\rho_A \rho_I)$.

---

[k]Ramshaw [86, 78] did the same exercise for his self-consistent effective binary diffusion approximation, which, in the derivation of ambipolar diffusion in a three-species mixture, is not different from the discussion here.

An expression for the ambipolar electric field $\vec{\mathbf{E}}^a$ can be found from equation (3.28). For this purpose we also need an expression for the electric conductivity σ. Due to their large mobility the diffusion of electrons will be dominant, and it can be shown that for the three-species mixture considered that:

$$\sigma \approx \frac{e^2 n_e}{kT} D_e^{\text{eff}} \tag{A.3}$$

Substituting the expression for D_e^{eff} this reduces, after some algebra, to the well-known expression $\sigma = e^2 n_e / (m_e \nu_{eh} n_h Q \bar{u})$ given in the textbooks, with $\nu_{eh} = n_h Q \bar{u}$ where Q is the cross-section and $\bar{u} = (8kT/\pi m_{ij})^{1/2}$ the mean relative velocity of the particles. Here, $m_{eh} \approx m_e$.

An expression for the ambipolar electric field $\vec{\mathbf{E}}^a$ can now be found by rewriting equation (3.28) for the three-species mixture. However, this implies a lot of tedious work, which we will not present here. A more simple approach is the following. First we sum equation (3.18) over the heavy particles I and A. Knowing that $\sum_{i \neq e} \vec{\mathbf{H}}_i = -\vec{\mathbf{H}}_e$ and $\sum_{i \neq e} q_i \rho_i = -q_e \rho_e$ it follows that:

$$\vec{\mathbf{E}}^a = \frac{p}{q_e \rho_e} \vec{\mathbf{H}}_e \tag{A.4}$$

This expression reduces to the standard formulation given in literature [41, 81] if one assumes zero gradients in T_h and T_e. Using $y_e \ll z_e$ in equation (3.17) gives:

$$\vec{\mathbf{E}}^a = -\frac{kT_e \vec{\nabla} n_e}{e n_e} \tag{A.5}$$

which is exactly the textbook result.

Substitution of equation (A.4) in equation (A.2) gives:

$$\vec{\mathbf{J}}_I = -\frac{\rho_I \rho_A D_{IA}}{\rho z_I z_A} \left(\vec{\mathbf{H}}_I + \vec{\mathbf{H}}_e \right) \tag{A.6}$$

If we limit ourselves to the case where the gradients in p, T_h and T_e are zero we arrive at:

$$\vec{\mathbf{J}}_I = -\frac{\rho_I \rho_A}{\rho z_I z_A} \left(1 + \frac{T_e}{T_h} \right) D_{IA} \vec{\mathbf{H}}_I \tag{A.7}$$

This equation states that due to the ambipolar electric field the ion diffusion is enhanced by a factor of $1 + T_e/T_h$, which is exactly the result given in literature [41, 81].

Chapter 4

PLASIMO, a General Computational Method: II Design of an Efficient Hydrogen Plasma Source Based on the Cascaded Arc

G.M. Janssen, C.W. Johnston, W.J. Goedheer[1], J.A.M. van der Mullen and D.C. Schram

Department of Applied Physics, Eindhoven University of Technology, P.O. Box 513, 5600 MB Eindhoven, The Netherlands

[1] FOM-Institute for Plasma Physics 'Rijnhuizen', P.O. Box 1207, 3430 BE Nieuwegein, The Netherlands

Abstract

The plasma simulation method PLASIMO is used to investigate the hydrogen cascaded arc plasma and to determine the optimal conditions for the production of atomic hydrogen ion fluxes. For this purpose, a high ionisation degree, dissociation degree and energy efficiency are required. These characteristic parameters are monitored for the case of a flowing hydrogen cascaded arc (CA) plasma in local thermal equilibrium and compared with available experimental results. Optimised are operating conditions (inlet flow and applied current) as well as the geometrical configuration (arc length, radius and shape of the arc channel wall). It is concluded that the prospects are very good to use a hydrogen CA plasma for the study of divertor-like plasmas.

4.1 Introduction

A general plasma simulation model, PLASIMO [34], is constructed in the group Equilibrium and Transport in Plasmas at the Eindhoven University of Technology. It is a fluid model for

multi-component plasmas, in a wide pressure range (10^1 to 10^6 Pa), from LTE (Local Thermal Equilibrium) to non-LTE, and with different energy coupling modes. Consequently, apart from the numerical simulation of plasmas in the cascaded arc (CA) [34] which is driven by a direct current, it can be used also for numerical simulation of inductively coupled plasmas (ICP, see [43]), the QL-lamp [33, 44] and microwave induced plasmas. The main assumptions within the PLASIMO method are that the flow is axi-symmetric, steady and laminar. Furthermore, the plasma is assumed to be quasi-neutral. An extensive description of the physical model, numerical implementation and the iteration procedure is given in [34]. It also provides a description of PLASIMO's capabilities, limitations and an application to an argon cascaded arc plasma. For the CA application a one-dimensional electric field formulation is used.

In this study the same configuration is considered (CA) for a different feed gas: hydrogen. We will limit ourselves to an LTE description. The reasons for this are the following. For argon in [34] deviations from LTE were observed only close to the wall. Furthermore, assuming LTE reduces the complexity of the mixture considerably. Finally, the energy exchange between electrons and hydrogen species is more effective than between electrons and argon species, due to the smaller mass of hydrogen compared to argon. This implies that thermal equilibrium is a better approximation in a hydrogen CA than in an argon CA. However, the small hydrogen mass has the disadvantage that the ambipolar diffusion coefficient is larger than for argon. Consequently it is to be expected that deviations from the ionisation-recombination equilibrium as prescribed by Saha will be larger than in the argon case. A fundamental discussion about non-equilibrium aspects, focused on ICP and MIP plasmas can be found in [97]. Since, in contrast to the argon CA, the radial temperature profile in a hydrogen CA plasma is mainly determined by the association/dissociation equilibrium, possible deviations from Saha are not expected to be a problem. Therefore, this study is confined to the radial temperature profile and how this determines the dissociation degree.

Compared to argon the radial temperature profile in the hydrogen arc will not be approximately parabolic but will be thermally constricted, i.e. it consists of one central peak and one plateau at the periphery. We will use the term "sombrero-like profile" for this type of distribution. This profile is primarily due to the change in thermal conductivity, for which in the temperature range of interest, two peaks exist: one dissociation peak ($H_2 \rightarrow 2H$) and one ionisation peak ($H \rightarrow H^+$). This has consequences for the plasma composition in the arc. For argon the effective radius for the active plasma zone (i.e. where the energy coupling takes place) is almost equal to the channel radius [98], whereas for hydrogen the active plasma zone will be constricted to a small region around the symmetry axis. The remaining non-active zone can be divided into two regions: a region where mainly atomic hydrogen exists and a region where mainly molecular hydrogen exists. The last region is located near the channel wall, the atomic hydrogen region is located between the active zone and the molecular hydrogen region. Experimentally the thermal constriction was observed by Kessels *et al.* [99] who looked at the effect of admixing hydrogen in an argon CA plasma. Other authors who mention the "sombrero" profile are for example Verboom [100] who investigated the energy balance of a high temperature arc discharge in hydrogen, Qing *et al.* [101] and Dresvin [102]. The "sombrero" profile is not seen in for example the theoretical work of Scott and Incropera [103] who did not include molecules and as a consequence saw a parabolic-like temperature profile (like in argon, see [34]).

The investigation in this study is motivated by the CA being an interesting source for an expanding hydrogen plasma. In such a configuration, a CA plasma expands supersonically in a chamber at low pressure. Such a plasma produces high densities and high flow velocities, resulting in high particle fluxes. Therefore, expanding hydrogen CA plasmas can be used in a variety of applications. They can produce atomic hydrogen which is important for the chemical treatment of surfaces and archeological artifacts [10]. Furthermore, they can produce high atomic hydrogen ion fluxes which can be used for approximating the operation of divertor plasmas, one of the fields of interest of the FOM-Institute for Plasma Physics 'Rijnhuizen'. This institute participates in the European research programme on the gain of energy out of nuclear fusion. To this end a Tokamak-plasma is used [104]. The Tokamak consists of a toroidal vacuum chamber in which hydrogen gas is injected which is ionised to form the plasma. The plasma is confined by an externally applied magnetic field. One of the main concerns for the future use of a Tokamak reactor is the exhaust of helium and impurities from the reactor [105]. For this purpose, the outermost zone of the plasma is diverted into the so-called divertor chamber. Here, high ion power fluxes (~ 10 MW m^{-2}) onto material in contact with the plasma will lead to strong evaporation of surface material, which considerably reduces the divertor lifetime. This is an intolerable situation, which may be relieved however, by the generation of a strongly radiating plasma of high density and low temperature. Since a divertor is not easy to access, in-situ experiments on it in a Tokamak reactor are not possible. It may be an option to use a hydrogen CA plasma (which also approximates a deuterium-tritium mixture) that expands supersonically in a vacuum chamber at low pressure (≤ 10 Pa) to investigate the influence of high power fluxes onto the divertor surface. For this purpose the plasma created by the CA should have an ion power flux comparable with the Tokamak situation: 10 MW m^{-2}. Up till now, it was not known whether or not this is possible. To investigate this possibility PLASIMO is used to predict an optimal ion power flux in a hydrogen CA plasma by optimising energy efficiency, dissociation degree and ionisation degree. Optimisation of these parameters is achieved via different sets of operating conditions and geometrical parameters of the CA. These can easily be handled with the modular PLASIMO-code, see [34]. This study is limited to the differences from [34]. The features of the CA configuration are given in section 4.2 (configuration) and section 4.3 (composition). In that section the principle of transition temperatures and how they determine the thermal conductivity profile and consequently the radial temperature profile in the CA is discussed. The results of the numerical simulations are validated with available experimental data in section 4.4 in which also a limited sensitivity analysis is presented.

4.2   Configuration features

4.2.1   Plasma source and geometry

The wall-stabilised CA [61, 62] is used as a plasma source. A CA with a conically-shaped channel is depicted in figure 4.1. It consists of three cathodes positioned in a cathode housing, a stack of electrically isolated cascaded plates, and an anode plate. The cathodes are sharpened pins of thoriated tungsten and are positioned concentrically in the cathode housing. The copper

cascade plates, with a thickness of 5 mm, have a central bore which forms the plasma channel. The plates are electrically isolated by boron nitride spacing rings with a thickness of 1 mm. The modular set-up of the CA (basically just a stack of cascade plates) makes it very easy to design an arc of different length or with a varying channel diameter. The length of the CA can be varied by varying the number of cascade plates between the cathode housing and the anode plate. By using CA plates with different bore radii the changing channel diameter is achieved. In figure 4.1 a four plate CA is depicted with a plasma channel length of 25 mm and with varying channel diameter. In the anode plate the nozzle plug is screwed, which bore can have different shapes (to change the shape of the jet as it expands). An additional point of concern is the thermal stress endured by the cascade plates, since different bore radii imply different sizes of the cascade plates and consequently different cooling capacity. For a detailed discussion of this subject, see Pijpers [18] who made a model to predict the heat load of the CA plates for high power arcs.

1: cathode housing: copper
2: cathode holder: copper
3: cathode tip (3x): thoriated tungsten
4: isolation: see 9 - 12
5: cascade plate: copper
6: anode plate: copper
7: nozzle plug: copper
8: gas entrance channel: copper

9: spacing ring: PolyVinylChloride (PVC)
10: vacuum seal: Viton O-ring
11: shielding ring: boron nitrid
12: plasma channel
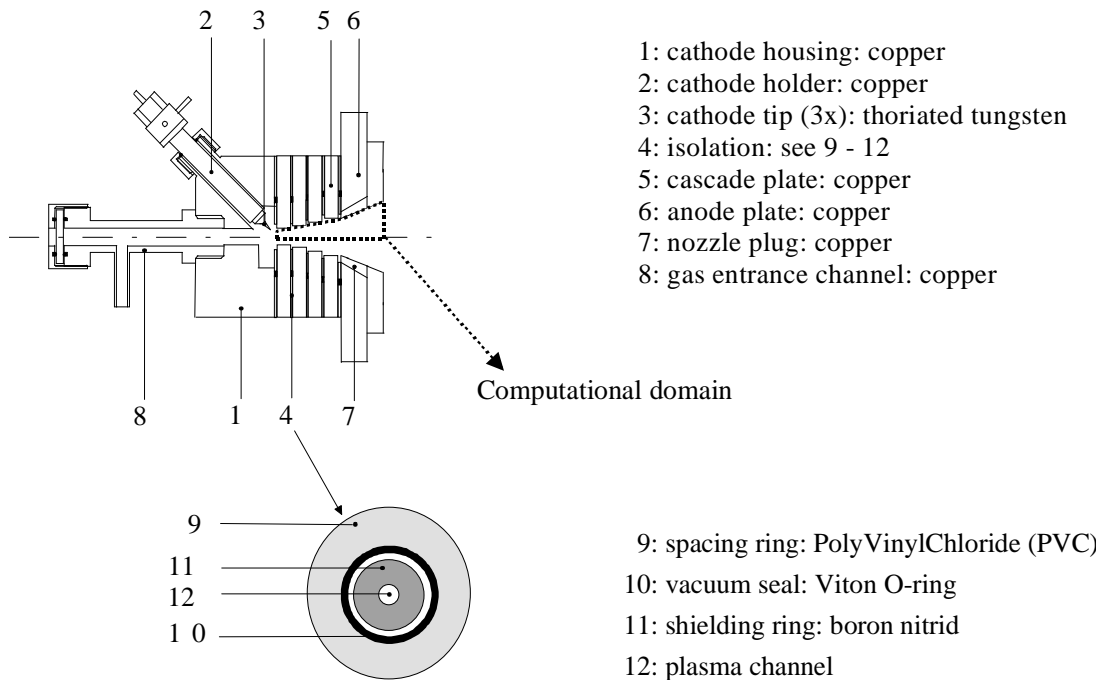
Figure 4.1: A four-plate cascaded arc configuration with different bore radii. The dotted line represents the part of the arc that is considered in the numerical simulations.

During operation hydrogen gas is fed through a mass flow controller into the cathode side of the arc. A current is drawn from the cathodes to the anode plate. Due to this current a plasma is created inside the CA. The plasma flowing through the channel is accelerated and expands supersonically at the anode side into a chamber at low pressure.

The configuration considered in the numerical simulations was already discussed in [34]. A uniform grid of 29 (axial) × 113 (radial) grid points is used. The configuration that is used as the "standard configuration" in this study is given by radius $R = 2$ mm (straight arc channel), length $L = 25$ mm, current $I = 50$ A (current is input parameter, not power), and inlet flow $\varphi = 100$ scc s^{-1}. In this study the CA configuration is optimised by tuning the length and radius of the

plasma channel, the shape of the channel wall, the inlet gas flow, and the applied current through the CA. Although in practice discontinuous edges exist between CA plates with different bore radii, in the numerical simulations the channel wall will be kept continuous. For this purpose use was made of a polynomial function to describe the shape of the channel wall.

4.2.2   Boundary conditions

The applied boundary conditions for the hydrogen cascaded arc plasma are listed in table 4.1. As can be seen in table 4.1 we assume that the velocity profiles at inlet and outlet have a simple power law shape $[1 - (r/R)^n]$. At the inlet we assume that $n = 2$. The maximum inlet velocity at the axis (r = 0) u_{in}^{max} is dictated by the mass flow Φ_{in} and mass density ρ_{in} at the inlet:

$$\Phi_{in} = 2\pi u_{in}^{max} \int_0^{R_{in}} \rho_{in} \left[1 - \left(\frac{r}{R_{in}} \right)^2 \right] r dr \qquad (4.1)$$

where r is the local radial position and R_{in} the radius of the plasma channel at the inlet of the CA. The mass flow Φ_{in} in equation (4.1) is calculated from the flow, temperature and pressure at the inlet. The inlet temperature $T_{in} = 2000$ K. The maximum velocity at the axis of the outlet is u_{out}^{max}. Since the hydrogen plasma expands supersonically into a vacuum chamber at low pressure, at the outlet at r = 0 a Mach number (M) of one is assumed. The exact value of M at the outlet does not have a large influence on the numerical results, as was shown in [34]. From the M = 1 condition u_{out}^{max} is calculated: $M = u_z/u_{sound}$, with the velocity of sound u_{sound} defined as:

$$u_{sound}^2 = \left(\frac{\partial p}{\partial \rho} \right)_{s,\alpha} \qquad (4.2)$$

with ρ the mass density of the plasma and p the pressure. The subscripts on the right hand side of equation (4.2) denote constant entropy (s) and constant ionisation degree (α). The effect of different exponential factors n in the velocity power law structure is negligible, as was also shown in [34]. Chang and Ramshaw [65] also found that $n = 5$ was best for their simulations. For the pressure at inlet and outlet a constant axial component of the pressure gradient is assumed. The constant C is updated during the iteration process.

As can be seen in table 4.1 the heavy particle temperature at the channel wall T_{wall} is determined from the equality of the heat flux from the plasma to the wall and the heat flux from the wall to the cooling water (with temperature T_{aq}); R is the local radius of the plasma channel, i.e. a constant in the case of a straight plasma channel and a function of axial position in the case of a varying channel radius. We do not take into account the whole cascade plate but only the part between the plasma channel and the cooling water channel inside the cascade plate, represented by distance $\delta_w = 12$ mm (whereas 1.0 mm $\leq R \leq 3.0$ mm). The temperature of the cooling water is estimated at $T_{aq} \approx 320$ K, which is the experimentally determined upper limit as measured by Qing [106]. Above this limit melting of the plastic tubes, connecting the cascade plates and the water supply, was observed. The thermal conductivity of the copper channel wall is almost constant in the temperature range of interest [107]: $\lambda_w \approx 360$ W m^{-1} K^{-1}. The thermal conductivity of the plasma λ_{pl} is determined at the wall reciprokely following Patankar [46]. The

different approach of Bourdin *et al.* [108] using $\bar{\lambda} = \frac{1}{T_\infty - T_{\text{wall}}} \int_{T_{\text{wall}}}^{T_\infty} \lambda(T) dT$ leads to temperatures above the melting point of copper (1356 K [107]).

Table 4.1: Boundary conditions applied to the LTE hydrogen cascaded arc plasma. The pressure is p, u_z and u_r are the axial and radial velocity components, respectively, T is the plasma temperature.

Par.	Inlet	Outlet	Axis	Channel wall
p	$\frac{\partial p}{\partial z} = C$	$\frac{\partial p}{\partial z} = C$	$\frac{\partial p}{\partial r} = 0$	$\frac{\partial p}{\partial n} = 0$
u_z	$u_z = u_{\text{in}}^{\max}\left[1 - \left(\frac{r}{R_{\text{in}}}\right)^2\right]$	$u_z = u_{\text{out}}^{\max}\left[1 - \left(\frac{r}{R_{\text{out}}}\right)^5\right]$	$\frac{\partial u_z}{\partial r} = 0$	$\mathbf{n} \cdot \mathbf{u} = 0$
u_r	$u_r = 0$	$\frac{\partial u_r}{\partial z} = 0$	$u_r = 0$	
T	$T = T_{\text{in}}$	$\frac{\partial T}{\partial z} = 0$	$\frac{\partial T}{\partial r} = 0$	$\lambda_{\text{pl}}\frac{\partial T}{\partial n} = \frac{\lambda_w(T_{\text{aq}} - T_{\text{wall}})}{R \ln\left(\frac{R + \delta_w}{R}\right)}$

4.3 Composition features

4.3.1 Equilibrium composition

Molecular hydrogen gas (H_2) is injected at the cathode side of the cascaded arc. Downstream of this point a multitude of reactions can take place, resulting in various possible reaction products. In this study we initially take into account the species H, H_2, H^+, H^-, and H_2^+. In LTE the number densities of the electrons and different hydrogen species are coupled through the analytically prescribed degrees of ionisation and dissociation via the Saha equation and Guldberg-Waage equation, respectively. Both are reactions of the same type. This is illustrated considering the following generalised reaction balance:

$$AB + (E) \leftrightarrow A + B \tag{4.3}$$

where AB is the 'dissociating' molecule, A and B are the 'dissociation' products and E is the reaction energy. If equation (4.3) is used to describe the ionisation/recombination balance, A can be the H^+ ion and B the electron. The reaction energy E can play the role of dissociation energy ($H_2 + (E_{H_2 \leftrightarrow 2H}) \leftrightarrow 2H$), ionisation energy ($H + (E_{H \leftrightarrow H^+}) \leftrightarrow H^+ + e$, $H_2 + (E_{H_2 \leftrightarrow H_2^+}) \leftrightarrow H_2^+ + e$) or detachment energy ($H + e + (E_{H \leftrightarrow H^-}) \leftrightarrow H^-$).

In equilibrium the elementary mass action law [68, 109] leads to the relation:

$$\eta_{AB} = \eta_A \eta_B \left(\frac{h}{\sqrt{2\pi m_{AB} k_b T}}\right)^3 \exp\left(\frac{E}{k_b T}\right) \tag{4.4}$$

with $\eta_i = n_i/Q_i$, n_i the number density and Q_i the partition function of species i (i.e. AB, A or B), k_b is Boltzmann's constant and h is Planck's constant. The term $V = (h/\sqrt{2\pi m_{AB} k_b T})^3$ represents the thermal de Broglie volume. It is the cube of de Broglie wavelength $h/\sqrt{2\pi m_{AB} k_b T}$ in which $\sqrt{2\pi m_{AB} k_b T}$ can be seen as an averaged momentum of the reduced mass m_{AB} ($m_{AB} = m_A m_B/(m_A + m_B)$).

Together with the equation of state ($p = \sum_i n_i k_b T_i$) and the assumption of quasi-neutrality ($\sum_i Z_i n_i = 0$, with Z_i the charge number of species i), equation (4.4) analytically relates the number densities of all the species present in the hydrogen mixture.

For the partition functions Q of the species the same formulation was used as given by Chen and Eddy [110]. The rotational and vibrational constants used in these expressions are taken from Radzig and Smirnov [111]. We assume that the rotational, vibrational, electronic excitational and translational temperatures of the electrons and heavy particle species are equal. In the simulations the pressure ranges from approximately 10^3 to 10^4 Pa. The equilibrium composition for these two values of the pressure as a function of temperature is shown in figure 4.2.

As can be seen in figure 4.2, the dominant species at low temperatures ($T < 7000$ K) are H_2 and H and at higher temperatures (7000 K $< T <$ 20000 K) H and H^+. The H^+ ion is by far the most dominant ion, with the H^+ and e densities in figure 4.2 almost equal. The number densities of H_2^+ and H^- are approximately four orders of magnitude lower than the electron density. Due to the low dissociation energies for heavier molecular ions H_3^+ and H_5^+ (not shown in figure 4.2) and the relatively high plasma temperatures, the exponent in equation (4.4) is small, implying that these ions (as well as H_2^+) are destructed very rapidly and very easily. Therefore, in the following it is justified to consider only the species H_2, H, H^+ and e.

4.3.2 Transition temperatures

We will now take a closer look at equation (4.4). Since $m_{AB,\text{ionization}} \ll m_{AB,\text{dissociation}}$ for ionisation of H ($H + e \leftrightarrow H^+ + 2e$, the same is true for the ionisation of H_2^+) and dissociation of H_2 ($H_2 + X \leftrightarrow 2H + X$, with $X = e$, H or H_2) and applying equation (4.4), immediately reveals that at the same temperature $V_{\text{ionization}} \gg V_{\text{dissociation}}$. As a direct consequence $\eta_{H_2}/\eta_H \eta_H \ll \eta_H/\eta_{H^+} \eta_e$, neglecting at this point the difference between ionisation and dissociation energy. We can conclude that at the same temperature (and same reaction energy), the dissociation degree is much larger than the ionisation degree.

Furthermore, a statement can be made on the temperature values at the transition points $T_{\text{transition}}$ (also shown in figure 4.2), i.e. the points that are defined by $n_{AB} = n_A$ with AB $\sim H_2$ and A, B $\sim$ H for the dissociation of H_2 and AB $\sim$ H and A $\sim H^+$, B $\sim e$ for ionisation of H. Substituting $n_{AB} = n_A$ in equation (4.4) gives:

$$1 = \frac{Q_{AB}}{Q_A Q_B} n_B V \exp\left(\frac{E}{k_b T_{\text{transition}}}\right) \tag{4.5}$$

There are two dominant factors in the right hand side: first, obviously the exponent. Since the ionisation energy of H (13.6 eV) is much higher than the dissociation energy of H_2 (4.478 eV) the ionisation transition point is located at much higher temperature than the dissociation transition point. Second, of importance is the reduced mass appearing in V, which, as discussed
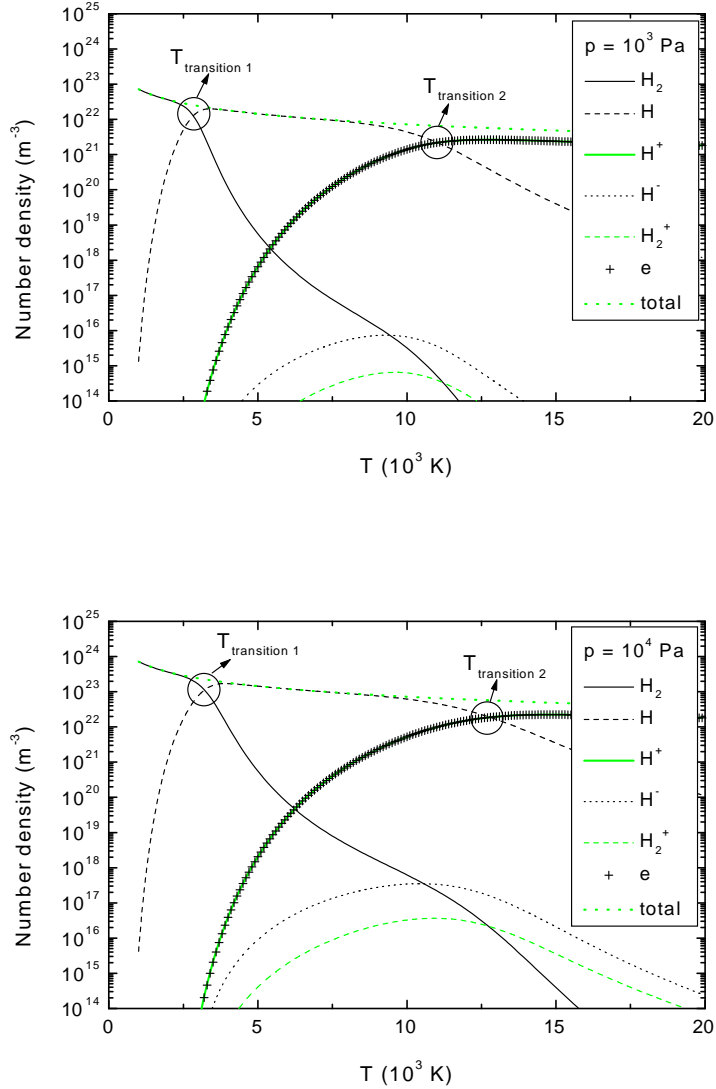
Figure 4.2: *Equilibrium composition in a hydrogen plasma at $p = 10^3$ Pa (top) and $p = 10^4$ Pa (bottom). The transition temperature for the dissociation/association equilibrium of H_2 is $T_{\mathrm{transition1}}$, for the ionisation/recombination equilibrium of H it is $T_{\mathrm{transition2}}$.*

before, differs orders of magnitude for dissociation and ionisation. Finally, as can be seen in figure 4.2, the number density n_B is approximately constant in the temperature range of interest: $n_{H^+} \approx 10^{21}$ m^{-3} and $n_H \approx 10^{23}$ m^{-3}, both at $p = 10^4$ Pa, so that equation (4.5) is only very weakly dependent on n_B.

By rewriting equation (4.5) an expression for the transition temperature is derived, using that

for the dissociation of H_2 and the ionisation of H $n_{AB} = n_A = n_B$, so that $n_B \approx p/3k_bT$:

$$T_{\text{transition}} = \frac{E}{k_b \ln \left[\frac{Q_A Q_B}{Q_{AB}} \frac{3k_b T}{pV} \right]} \tag{4.6}$$

A rough estimation for the average volume V and the ratios of the partition functions can be made, which together with the reaction energy, gives us an estimation of the transition temperatures. As a result, it is easily shown that the H_2 dissociation peak is located at a much lower temperature than the H ionisation peak.

Due to the weak dependence of the transition temperature $T_{\text{transition}}$ on the pressure (see equation (4.6)) the values of $T_{\text{transition}}$ are almost the same for the two pressures shown. The transition temperatures are very important, since they determine the location of the peaks in the thermal conductivity profile. This will be clear upon comparing figure 4.2 with figure 4.3 in section 4.3.3. The thermal conductivity profile determines the radial temperature profile in the CA, which will be made clear in section 4.4.1.

4.3.3   Transport coefficients

The electrical conductivity σ is determined using Frost's mixture rules [57]. The thermal conductivity of the mixture λ_{total} is written as the sum of a frozen contribution λ_f (if the chemical reactions are 'frozen'), an electron contribution λ_e and a reactive contribution λ_r (due to chemical reactions leading to a shift of the equilibrium). The frozen contribution (and the viscosity) is calculated with the mixture rules given by Mitchner and Kruger [41] using hard-sphere cross-sections. Also the electron contribution is calculated using the mixture rule given by Mitchner and Kruger, its contribution in an LTE plasma at the temperatures we expect and at the low pressure used, is rather small. The reactive part is calculated using the approach of Butler and Brokaw [112]. In this approach the binary diffusion coefficients are crucial. In principle, they are based on collision integrals. However, we use hard-sphere cross-sections because of great differences in reported λ_r when different collision integrals are used [5]. Due to this "confusion" we use hard spheres and save computational effort [2]. A limited sensitivity analysis is performed on our final results to gauge the possible influence of using different collision integrals (i.e. potential parameters). The pressure dependence of λ_{total} is shown in figure 4.3 for pressures of 10^3 Pa to 10^5 Pa.

Comparing figure 4.2 with figure 4.3 reveals that the locations of the transition temperatures determine the locations of the dissociation/ionisation peaks of the thermal conductivity. In turn, the thermal conductivity will determine the radial temperature profile in the CA. This will be discussed in section 4.4.

4.3.4   Source terms

The total energy balance of an LTE plasma requires two source terms, the Ohmic power input P_{input} and the radiation loss P_{rad}. P_{input} is calculated in the same way as in [34]. The radiation loss term is divided in three atomic contributions, free-free radiation (i.e. Bremsstrahlung) P_{ff},
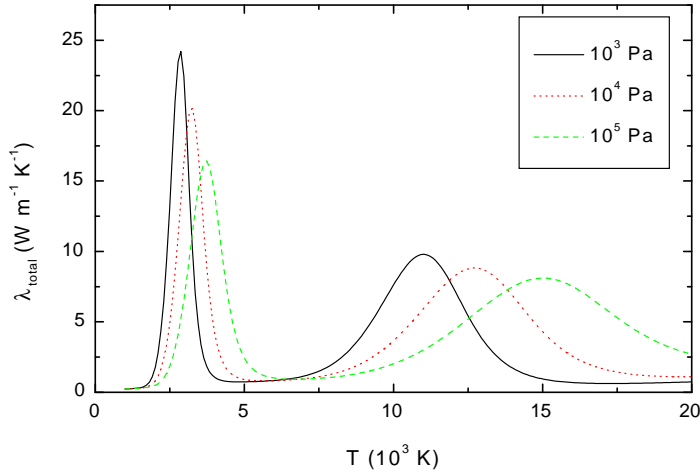
Figure 4.3: The temperature dependence of the thermal conductivity λ_{total} of an LTE hydrogen mixture for three values of the pressure.

free-bound radiation P_{fb} and line radiation P_{line}. P_{ff} and P_{fb} are taken from Mitchner and Kruger [41]. P_{bb} is taken from Van der Mullen [68], with the populations of all excited states of atomic hydrogen governed by the Boltzmann relation, whereas the density of the ground state of H is determined in the numerical method (see section 4.3.1). It is assumed that the plasma is optically thin, except for strong absorption in the Lyman series, which is usually close to actual experimental conditions according to Drawin [113]. The chosen escape factors Λ for the Lyman series are taken constant and read [114]: $\Lambda_{21} = 10^{-4}$, $\Lambda_{31} = 10^{-3}$, $\Lambda_{41} = 10^{-2}$, $\Lambda_{51} = 10^{-1}$, $\Lambda_{61} = 0.3$. For all other transitions (including free-bound) $\Lambda = 1$. Since the H$^+$ density is much higher than the H$_2^+$ density it is reasonable to neglect the radiation losses in the H$_2$ - H$_2^+$ system.

4.4 Results and discussion

4.4.1 Number density and temperature distribution

In figure 4.4 the radial profiles of the number densities of H$_2$, H and H$^+$ are shown at the outlet of the CA, for the standard configuration described in section 4.2.1. In the centre of the hydrogen CA plasma (in all simulations) a high concentration of hydrogen ions exists, from the central region to the channel wall a high concentration of atomic hydrogen is found, whereas towards the channel wall the concentration of molecular hydrogen becomes dominant. The radial temperature profile at the outlet of the CA is presented in figure 4.5. The "sombrero" profile, consisting of a strong central peak and a plateau at the periphery, is clearly visible. This thermal constriction is caused by the strong dissociative peak of the thermal conductivity at around 3000 K. The

temperature profile is almost fully determined by the heat conductivity of the hydrogen mixture, since radiation losses are small and therefore the heat term in the energy balance is the dominant source term. Comparing figures 4.4 and 4.5 shows clearly that the exponential decrease of the H_2 number density around $r = 1$ mm coincides with the transition from the low-temperature region near the periphery to the high-temperature region around the symmetry axis, where dissociation is almost complete.

4.4.2   Optimal fluxes

The task is now to find those conditions for which the effective power coupled into the plasma is large and for which the molecular hydrogen region is unimportant so that the H and H^+ yield is large. For this purpose the following parameters were monitored at the outlet of the CA:

- Energy efficiency η, defined as $\eta = P_{\mathrm{plasma}}/P_{\mathrm{input}}$, with P_{input} the Ohmic input power and P_{plasma} the power effectively coupled into the plasma: $P_{\mathrm{plasma}} = P_{\mathrm{input}} - P_{\mathrm{loss}}$. Here the total power loss is $P_{\mathrm{loss}} = P_{\mathrm{rad}} + P_{\mathrm{water}}$, that is the sum of the power loss due to radiation P_{rad} and the loss due to heat transfer to the channel wall P_{water}.
- Dissociation degree β, defined as $\beta = \varphi_{\mathrm{H,out}}/\varphi_{\mathrm{total,out}}$, with φ_{total} the proton flux, that is the total number of protons in H, H^+ plus the protons that are bound in H_2 leaving the CA per unit of time. So in fact we are looking at the fraction of incoming hydrogen atoms that are not bound in molecules but exist as free radicals ($\varphi_{\mathrm{total,out}} = 2\varphi_{\mathrm{H_2,in}}$).
- Ionisation degree α, defined as $\alpha = \varphi_{\mathrm{H+,out}}/\varphi_{\mathrm{total,out}}$.

To optimise the CA for high ion power flux, η, α and β have to be as high as possible. An approximate relationship between α, β and P_{plasma} was previously derived by De Graaf *et al.* [115] assuming that the power effectively coupled into the plasma is balanced by the power needed for heating of the flowing plasma P_{heat}, for dissociation P_{diss} and ionisation P_{ion}:

$$P_{\mathrm{plasma}} = P_{\mathrm{heat}} + P_{\mathrm{diss}} + P_{\mathrm{ion}} \tag{4.7}$$

An upper limit for P_{heat} is made considering the thermal energies of the species:

$$P_{\mathrm{heat}} = \varphi_{\mathrm{H_2,out}}\frac{5}{2}k_b\Delta T_{\mathrm{H_2}} + \varphi_{\mathrm{H,out}}\frac{3}{2}k_b\Delta T_H + \varphi_{\mathrm{H+,out}}\frac{3}{2}k_b\Delta T_{\mathrm{H+}} + \varphi_{e,\mathrm{out}}\frac{3}{2}k_b\Delta T_e \tag{4.8}$$

The powers used for dissociation P_{diss} and ionisation P_{ion} are given by:

$$P_{\mathrm{diss}} = \beta\varphi_{\mathrm{H_2,in}}E_{\mathrm{diss}} \tag{4.9}$$

$$P_{\mathrm{ion}} = 2\alpha\varphi_{\mathrm{H_2,in}}E_{\mathrm{ion}} \tag{4.10}$$

The molecules are assumed to be at a temperature of 0.4 eV since dissociation is almost complete above this temperature. The atoms, ions and electrons are assumed to be at 1 eV. Combining equations (4.7) to (4.10) gives:

$$\frac{P_{\mathrm{plasma}}}{e\varphi_{\mathrm{H_2,in}}} = 1 + 6.5\beta + 32.2\alpha \quad \text{(eV)} \tag{4.11}$$
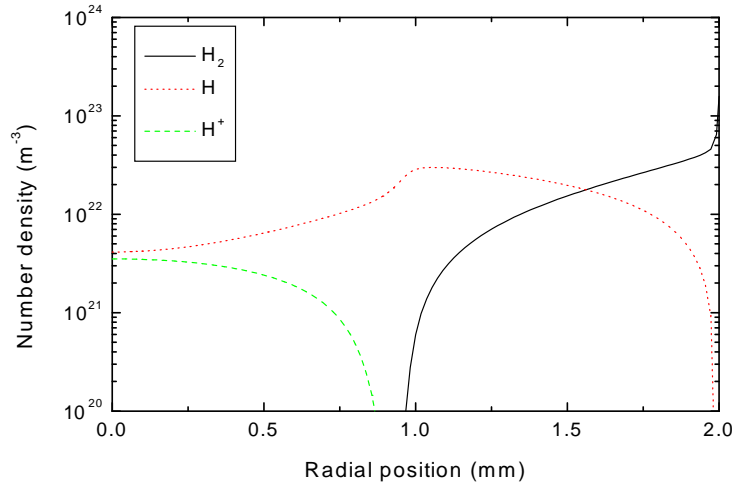
Figure 4.4: Radial profile of the number densities at the outlet of the CA for the standard config-uration: $I = 50$ A, $L = 25$ mm, $R = 2$ mm and $\varphi = 100$ scc s^{-1}.
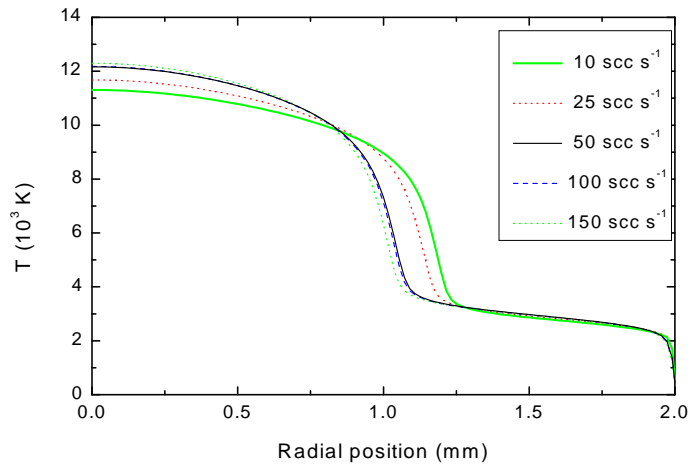
Figure 4.5: Radial temperature profile at the outlet of the CA as a function of inlet flow ($I = 50$ A, $L = 25$ mm, $R = 2$ mm, straight CA). Since the transition temperature is only weakly dependent on number density, the temperature in the region $r > 1.2$ mm is approximately equal for all flows.

with e the elementary charge. This relationship was used by De Graaf *et al.* [115] and Qing [116] to determine β. For this purpose P_{plasma} was calculated from the measured P_{input} and P_{water}

whereas α was used as a parameter to determine an upper ($\alpha = 0\%$) and lower limit ($\alpha = 2.5\%$) of β. The available results of these calculations are plotted together with the simulations in the next figures.

The LTE model as described in this study, can be used for an optimisation study. Therefore, simulations are performed for a straight arc with different

- radius and length of the plasma channel;
- applied current;
- inlet gas flow.

The results are presented in figures 4.6 to 4.11.
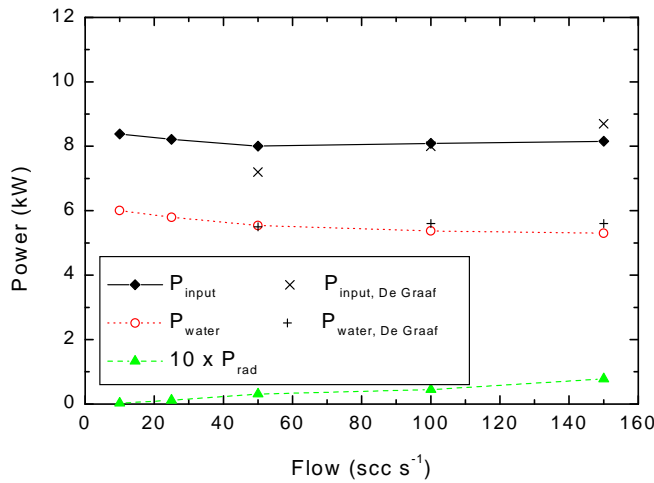
Figure 4.6: Power balance as a function of the inlet flow ($I = 50$ A, $L = 25$ mm, $R = 2$ mm). Experiments: cross: P_{input}; plus: P_{water} both according to De Graaf et al. [115].

Comparing the simulation results with the experimental results of De Graaf and Qing in figures 4.6 to 4.8 shows that:

- The values of P_{input} and P_{water} resulting from the simulations included in figure 4.6 compare very well with the experimental values.
- The predicted energy efficiency η, shown in figure 4.7, is in the same range as the experimental values.
- The predicted values of the dissociation degree β (see figure 4.8) are too low compared with the values measured by Qing and De Graaf. Of course the calculation of β from the experiments, i.e. by using equation (4.11), is not without danger because of the bold assumption used in its derivation, that atoms, ions and electrons have a temperature of 1 eV. This may be true in the centre of the CA plasma for the atoms and ions (in the standard condition for r < 1 mm), but certainly not outside that region (see for example figure 4.5).
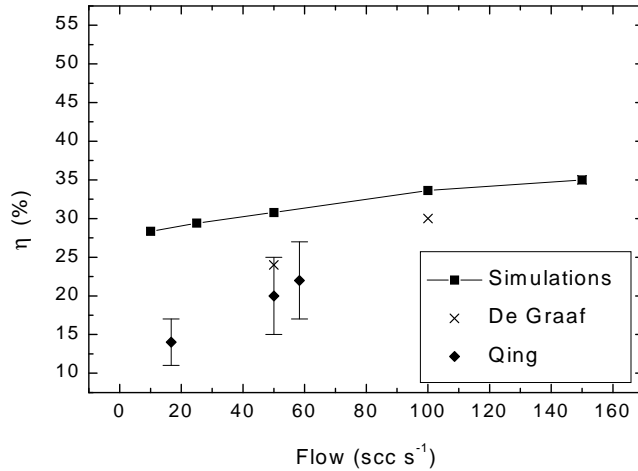
Figure 4.7: Energy efficiency η as a function of the inlet flow ($I = 50$ A, $L = 25$ mm, $R = 2$ mm). Experiments: cross: De Graaf et al. [115]; diamond: Qing [116].

What speaks against the predicted β is that, as a consequence of assuming LTE in the CA, the predicted β will probably be too high. This is because the wall association process $H + H \rightarrow H_2$ (where the wall serves as the third particle) is expected to increase the H_2 number density near the wall considerably and therefore will reduce β.

Concluding, as far as experimental results are available, the trends for the predicted powers and energy efficiency are satisfactory, except for the dissociation degree.

For an optimal α, β and η the following conclusions can be drawn:

- It is difficult to determine optimal flow conditions since flow has contrasting effects on η (see figure 4.7) and α, β (figure 4.8). At low flow rate the power input per scc s^{-1} hydrogen gas is maximum and therefore highest values for α and β are achieved (flow < 20 scc s^{-1}). At higher flow rates the Ohmic input power P_{input} remains constant, whereas the heat loss to the wall P_{water} decreases slightly. Therefore high η requires high flow rates. However, the decrease in α is larger than the increase in η, which means that the ion power flux, defined as $\alpha \eta P_{\text{input}}/A$ with A the area of the outlet opening, would drop for high flow rates. Therefore, using lower flow rates (≤ 50 scc s^{-1}) is more effective to produce ions than higher flow rates.

- By applying more current we see in figure 4.9 that the magnitude of P_{input}, P_{water} and P_{rad} increase. However the ratio between them decreases slightly. Therefore higher current means a higher power input without a better efficiency. Nevertheless, at high current α and β increase, so it is still preferable to have a high current (preferably ≈ 70 A).

- From figure 4.10 we see that the channel radius should be small (< 2 mm) but not too small, since the smallest possible radius depends on the heat load of the plasma channel
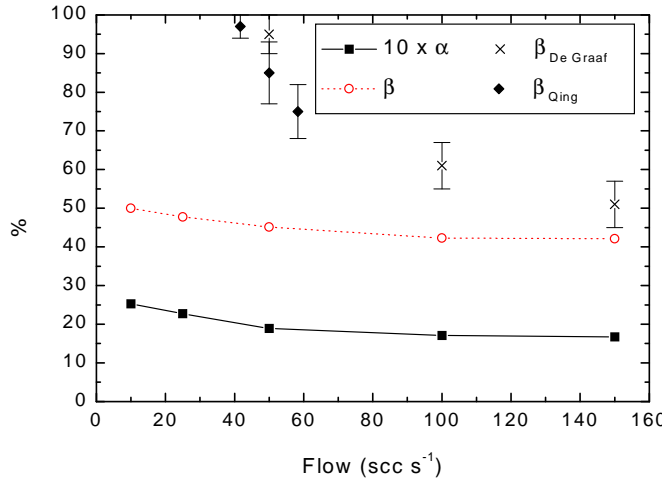
Figure 4.8: Degree of ionisation α and dissociation β as functions of the inlet flow ($I = 50$ A, $L = 25$ mm, $R = 2$ mm). Experiments: cross: De Graaf et al. [115]; diamond: Qing [116]. The error bars denote the upper ($\alpha = 0\%$) and lower limit ($\alpha = 2.5\%$) for β.

wall. This load increases significantly (and consequently η decreases) with decreasing channel radius. It is also to be expected that possible non-LTE effects play a more important role for small radii.

- The power needed to generate and sustain the plasma is determined by the arc length: the longer the arc the more input power is needed, as is seen in figure 4.11. Combined with the small increase of η for small arc length, the arc length should be chosen small (preferably < 25 mm).

Simulations have also been performed for two different conically-shaped channel walls and are compared with the results of the simulations for the straight arc with $R = 1.5$ mm, which we call configuration A. The polynomial boundary functions used are for configuration B: $R = 1.5 + 3\xi^2 - 2.1\xi^3$ and for configuration C: $R = 1.5 + 4.5\xi^2 - 3\xi^3$ with R in mm and $\xi = z/L$ the normalised axial coordinate (z is the local axial position). They are shown in figure 4.12. The radial temperature profiles at the outlet of the CA as a function of normalised radial position r/R_{out} for the three configurations are compared with each other in figure 4.13. It is seen that the active plasma zone decreases relatively with increasing rate of change of the channel radius.

The power balances for the three configurations are shown in figure 4.14. The characteristic parameters α, β and η are shown in figure 4.15. These results show the following: simulations performed using different channel geometries show that the heat load of the wall decreases with increasing rate of change of the channel radius whereas the input power is almost constant, so that η increases. However, β and α decrease significantly, β from 42.2% for configuration A to 36.3% for configuration C, and α from 1.7% to 0.7%. This implies that using a conically-shaped
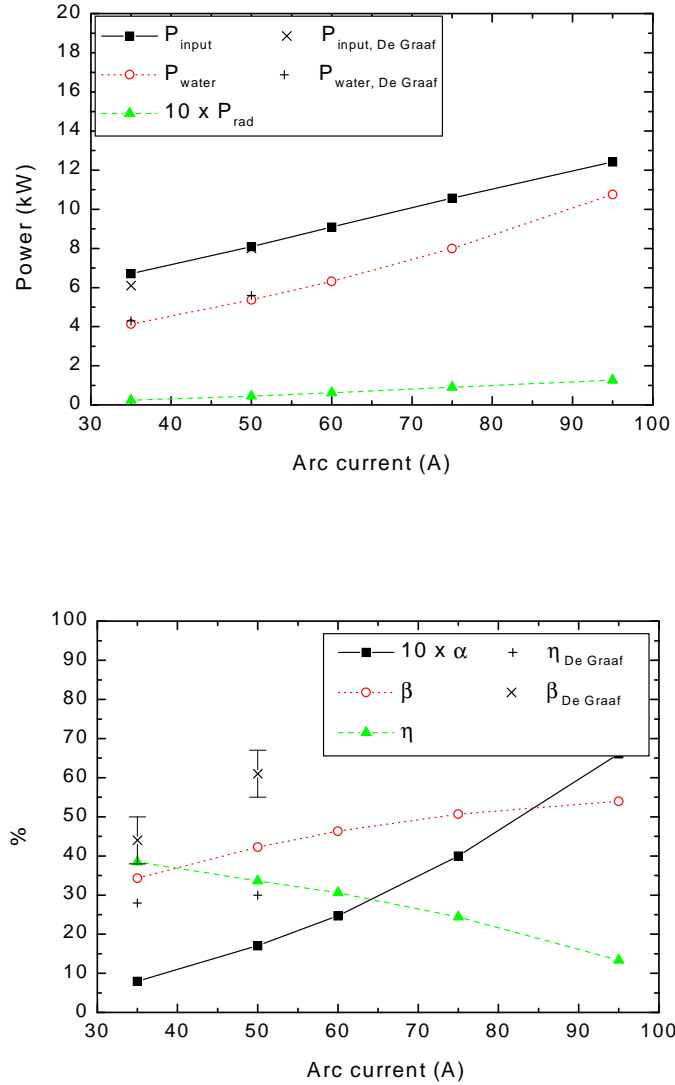
Figure 4.9: Top: power balance; bottom: η, α and β; as a function of applied arc current ($\varphi = 100$ scc s^{-1}, $L = 25$ mm, $R = 2$ mm). Experiments: De Graaf et al. [115].

arc channel is not an option unless the increase in the output power per ion is larger than the decrease in the ionisation degree. Comparing configuration A with configuration C, α decreases a factor of 2.4 whereas η increase a factor of 1.4, so a conically-shaped arc channel is not an option.

For a CA that provides optimal conditions mentioned above (we have chosen: $R = 1.5$ mm, $L = 25$ mm, $I = 70$ A and $\varphi = 30$ scc s^{-1}), the ion power flux at the outlet of the CA is
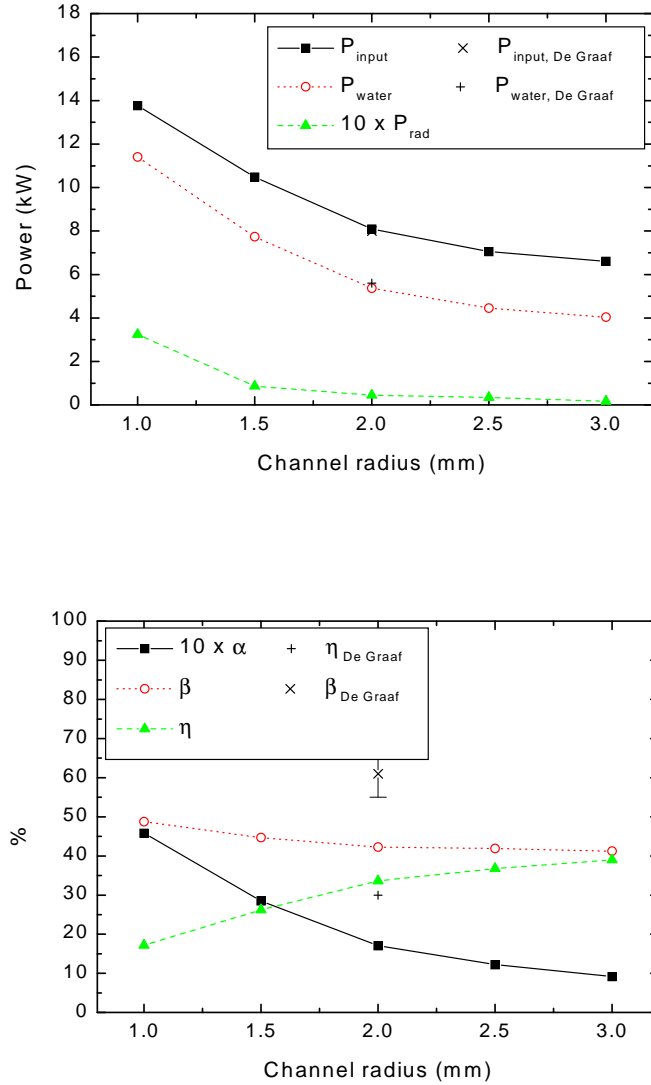
Figure 4.10: Top: Power balance; bottom: η, α and β as a function of channel radius ($\varphi = 100$ scc s^{-1}, $I = 50$ A, $L = 25$ mm). Experiments: De Graaf et al. [115].

approximately 50 MW m^{-2}.[a] Another idea for changing the channel geometry is geometrically pinching the arc by using a convergent-divergent nozzle: the plasma channel converges to the pinch location and diverges afterwards. The consequences of this approach for an argon plasma are shown by Burm *et al.* [42]. The apparent result for an argon plasma is a significant increase of the ionisation degree.

---

[a]The effect of the expansion of the CA plasma into a vacuum chamber on the ion power flux is not part of the present study. It is to be expected that the ion power flux of the plasma will be lower at the divertor plate.
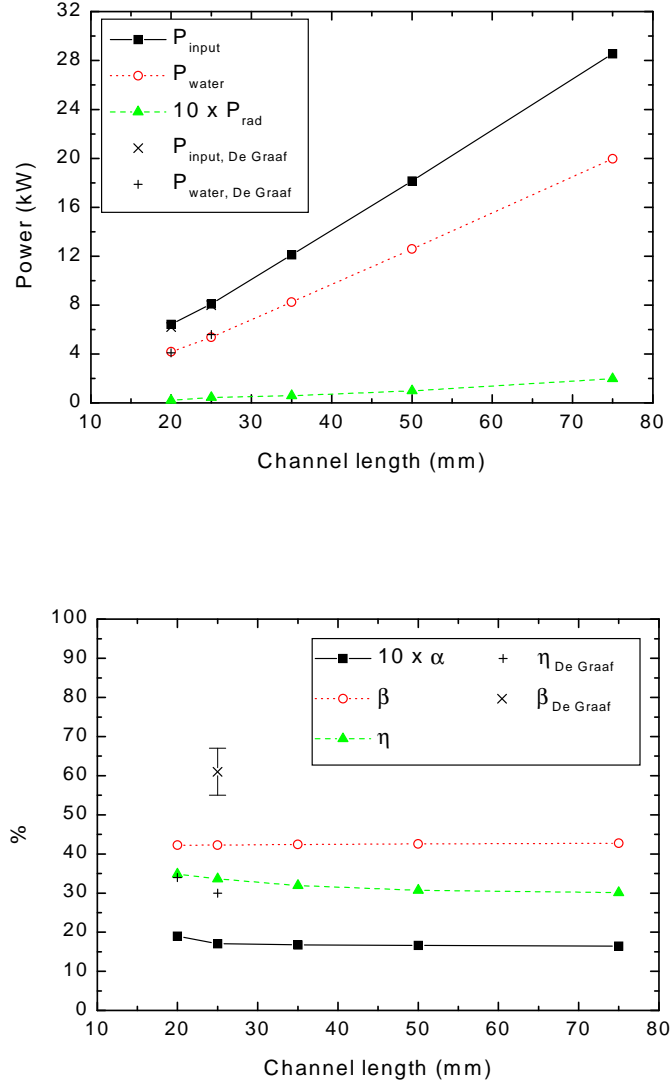
Figure 4.11: Top: Power balance; bottom: η, α and β as a function of channel length ($\varphi = 100$ scc s^{-1}, $I = 50$ A, $R = 2$ mm). Experiments: De Graaf et al. [115].

4.4.3 Sensitivity analysis

Since the thermal conductivity λ_{total} is the most important parameter in the simulations, and because there is some concern about the validity of the actual value used, we will now focus on the sensitivity of the characteristic parameters α, β, η, P_{input} and P_{water} to variations in λ_{total}. The major contribution to λ_{total} is the reactive thermal conductivity λ_r, that is the contribution to the thermal conductivity due to chemical reactions (ionisation, dissociation). Therefore we
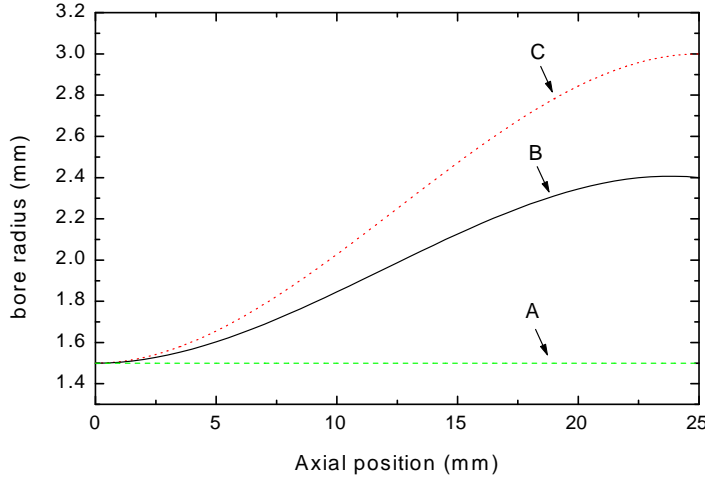
Figure 4.12: *Wall functions used for different channel wall shapes. A: $R = 1.5$ mm; B: $R = 1.5 + 3\xi^2 - 2.1\xi^3$ (in mm); C: $R = 1.5 + 4.5\xi^2 - 3\xi^3$ (in mm) with $\xi = z/L$.*
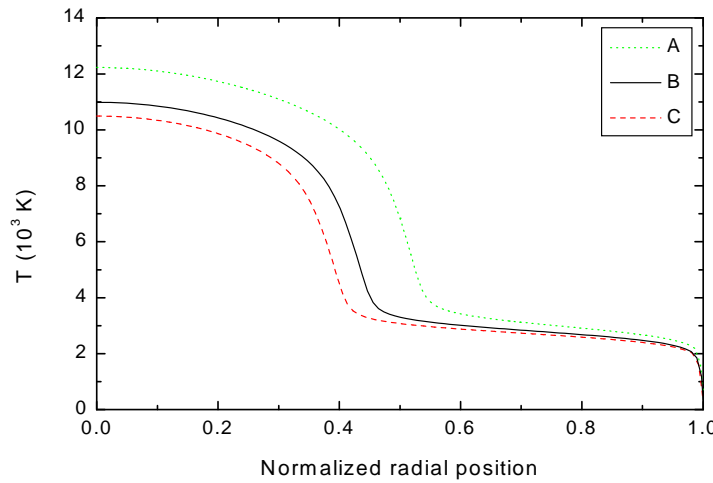
Figure 4.13: *The radial temperature profile at the CA outlet for configurations A, B and C (cf figure 4.12) as a function of normalised radial position (i.e. r/R_{out}).*

investigate the sensitivity of the simulation results on varying the heights of the dissociation and ionisation peak of λ_r. The dissociation peak was independently increased (decreased) by decreasing (increasing) the neutral-neutral collision diameter d_n by 50%. The same was done for the ionisation peak by changing the collision diameter d_i for collisions involving one or
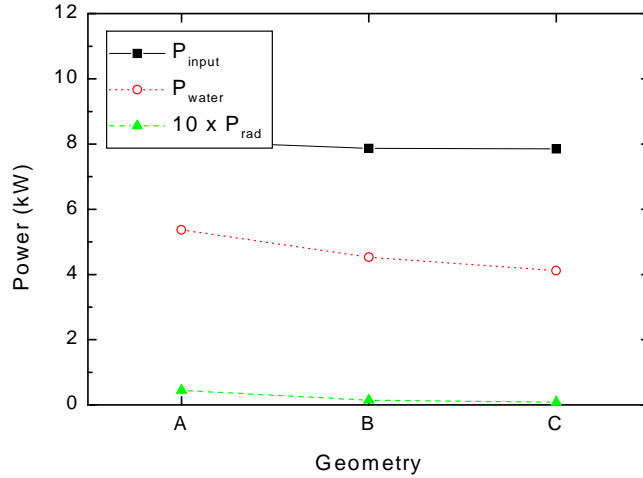
Figure 4.14: The power balance in the three arc configurations A, B and C (cf figure 4.12).
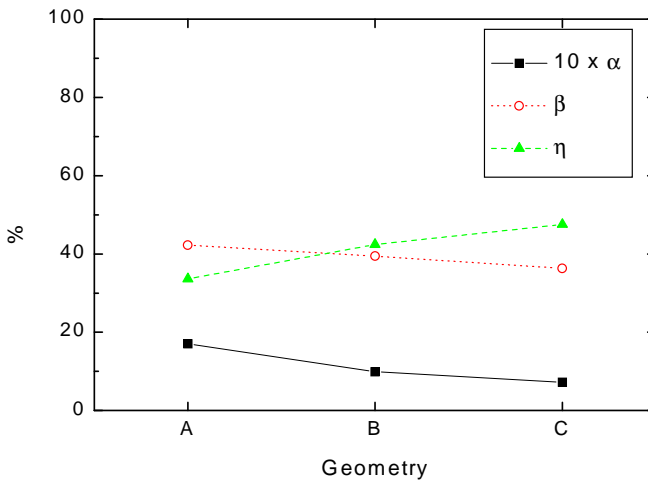
Figure 4.15: η, α and β in the three arc configurations A, B and C (cf figure 4.12).

two charged species again by 50%. The only other parameter that could have some influence is the thermal conductivity of the copper wall λ_w. Therefore also the influence of varying λ_w by 50% on the characteristic parameters is investigated. Increasing (decreasing) λ_w by 50% decreases (increases) P_{water} and consequently increases (decreases) η (maximum increase is 11% for η). Varying the height of the dissociation and ionisation peaks of λ_r has a larger influence: decreasing (increasing) the peaks increases (decreases) α and η (variation in α is approximately

50%, for η it is 25%). The variation in β is smaller (around 10%).

4.5   Conclusions

The plasma simulation method PLASIMO has been used to study the composition in a hydrogen CA plasma and for finding an optimised CA configuration, which produces hydrogen ion power fluxes of at least 10 MW m^{-2}. High ionisation degree α, dissociation degree β and energy efficiency η are required. It is found that for this purpose the arc should be short (≤ 25 mm) and have a small channel radius (< 2.0 mm). Not too small, because the heat load of the channel wall increases and the efficiency decreases with reducing the channel radius. The applied current should be high (≈ 70 A), but not too high since then the decrease in η is larger than the increase in α. The flow rate should be small since the increase in α for low flow rates has a larger impact on the ion power flux than the decrease in η. The estimated ion power flux is 50 MW m^{-2} for a CA that satisfies these conditions ($R = 1.5$ mm, $L = 25$ mm, $I = 70$ A and $\varphi = 30$ scc s^{-1}), which is above the demand of 10 MW m^{-2}. A possible further increase in the ion power flux has to be found in geometrically pinching the arc instead of using a conically-shaped channel geometry. In conclusion, the CA presents itself as an excellent candidate for divertor experiments.

Acknowledgements

Chapter 5

Modelling of a Hydrogen Cascaded Arc Plasma for Local Thermal Non-Equilibrium Conditions

G.M. Janssen, J.A.M. van der Mullen, W.J. Goedheer[1] and D.C. Schram

Department of Applied Physics, Eindhoven University of Technology, P.O. Box 513, 5600 MB
Eindhoven, The Netherlands

[1] FOM-Institute for Plasma Physics 'Rijnhuizen', P.O. Box 1207, 3430 BE Nieuwegein, The Netherlands

Abstract

The multi-component fluid computational method PLASIMO is used to simulate a hydrogen cascaded arc plasma for local thermal non-equilibrium (non-LTE) conditions. The results are compared with the results of the LTE simulations presented in our previous paper [117]. It is found that especially in the central plasma region thermal non-equilibrium is present, whereas in the channel wall region thermal equilibrium is reached. In contrast to [117], only the electron temperature shows a "sombrero" profile. The differences between results of LTE and non-LTE simulations are a result of the assumptions and restrictions of the non-LTE model or the non-validity of the LTE assumption of [117]. Furthermore, it is found that H_2^+ plays a major role in the hydrogen plasma as an "intermediate" species, although its number density usually is very small compared to the number densities of the other species. Especially its influence on the number densities of H and H_2 is huge. The wall reaction coefficient γ_H, for the wall association process $H + H + wall \rightarrow H_2$ has a large influence on the dissociation degree in the cascaded arc. Decreasing γ_H increases the dissociation degree significantly. Consequently, due to the higher H density also the H^+ density increases, although the effect is much smaller than for the dissociation degree.

5.1   Introduction

The general plasma simulation method PLASIMO [34], which has been developed in the group Equilibrium and Transport at the Eindhoven University of Technology, was used in a previous paper to model a flowing LTE (i.e. local thermal equilibrium) hydrogen cascaded arc (CA) plasma [117][a]. An important reason for the LTE assumption is the result of a study of the degree of departure from equilibrium in a CA in argon as reported in our paper [34][b]. In that paper it was shown that only at the wall a significant temperature inequality of $(T_e/T_h - 1) \approx 0.5$ can be found. Since the low mass of the hydrogen atoms and molecules makes the energy transfer from the electrons to the heavy particles much more effective than in the argon case, it is to be expected that thermal equilibrium is better approximated in a hydrogen CA than for example in an argon CA.

However it was also pointed out in [34] that deviations from the ionisation-recombination equilibrium (Saha balance) may be present. Due to the same reason, that is the low mass of H and thus its high mobility, the H^+ ions will diffuse more easily towards the wall than the Ar^+ ions in a argon plasma. At the wall, recombination will take place and this drain of charged particles might influence the Saha balance in the inner part of the plasma as well. In general, if the characteristic diffusion times or transport times for the various hydrogen species are smaller than the characteristic reaction times, local deviations from chemical equilibrium can be expected. This also applies to wall association, $H + H + wall \rightarrow H_2$, which might disturb the association/dissociation equilibrium. Therefore we will study the influence of non-equilibrium behaviour on the temperature profile, the ionisation degree and the dissociation degree in a hydrogen CA plasma and compare it with the results of the LTE simulations in [117].

Recently, Silakov *et al.* [118] presented an extensive study on the kinetic modelling of a flowing hydrogen cascaded arc plasma. In that study the emphasis was on the kinetic modelling; for the plasma dynamics a one-dimensional set of hydrodynamic equations was used. The plasma parameters were assumed to be uniform over the cross-section of the CA. As was already shown in [117] this assumption is certainly not correct, both for the temperatures and for the number densities (mass fractions). The presence of the wall has a huge effect on the plasma. Apart from acting as a cooling low-temperature bath it will also present an extensive recombination/association location, having a large reducing impact on the ionisation and dissociation degree in the adjacent plasma region. The resulting departure from equilibrium can propagate towards more central regions in the plasma.

From a kinetic point of view the model in the present study is not as extensive as that of Silakov and the collisional-radiative model of Pigarov and Krasheninnikov [119][c]; however, the plasma dynamics is solved for an axi-symmetric configuration assuming axi-symmetric flow. In this way the radial dependencies of the plasma parameters and consequently the influence of wall reactions are taken into account more correctly.

The main assumptions of PLASIMO are that the flow is axi-symmetric, steady and lami-

---

[a]Chapter 4 of this thesis.

[b]Chapter 2 of this thesis.

[c]Pigarov and Krasheninnikov [119] developed a generalised collisional-radiative atomic-molecular hydrogen model, which they applied to a recombining divertor plasma.

nar. Furthermore, the plasma is assumed to be quasi-neutral. For an extensive description of PLASIMO's capabilities as well as its limitations together with a description of the physical model, numerical implementation and the iteration procedure we refer to Janssen *et al.* [34].

For a correct description of a non-equilibrium hydrogen plasma, it is important to include the rovibrational excitation (de-excitation) of the hydrogen molecule in the electronic ground state $H_2(X^1\sum_g^+)$ due to both electron and heavy particle impact. As we will see, the presence of (excited) molecular states will not only change the chemical processes and composition drastically, it will also offer an efficient transfer channel for the kinetic energy from the electrons $\{e\}$ to the heavy particles $\{h\}$. In order to understand the role of some particular states, their presence will be artificially "switched off". So for instance we will study a purely atomic hydrogen plasma, a plasma without molecules. Comparing this merely academic H plasma with the actual H_2, H_2^+, H, H^+ mixture, will give insight in the relevance of the various molecular and atomic processes.

This study is organised as follows: the hydrogen composition characteristics, which involves the hydrogen species H, $H_2{}^d$, H^+ and H_2^+, will be discussed in section 5.2. The configuration characteristics will be discussed briefly in section 5.3. The simulation results for an atomic hydrogen and a molecular hydrogen cascaded arc plasma are presented and compared with results of the LTE simulations from [117] in section 5.4 together with the influence of wall reactions on the dissociation and ionisation degree.

5.2 Composition features

The hydrogen plasma considered contains the same species as used in the LTE treatment in [117]: H, H_2, H^+, and H_2^+. We do not consider H_3^+ and H^- but will discuss their possible influence in section 5.4.3. The four considered species are transport-sensitive (TS) species, which means that transport phenomena are important in the corresponding mass balances. The densities of the other species, the local chemistry (LC) species, directly depend on those of the TS species via elementary collisional and radiative processes. Together with the four TS species, the LC species can be grouped in three quasi-separate kinetic systems:

- The *atomic* system, involving atomic excitation/de-excitation and ionisation/recombination processes, discussed in section 5.2.1.
- The rovibrational *molecular* system, involving electron and heavy particle assisted rovibrational excitation of molecular hydrogen in the electronic ground state, see section 5.2.2;
- The *electronic* molecular system, involving H_2^+ processes, see section 5.2.3;

The coupling between the three systems is shown in figure 5.1. The complete list of included reactions is given in table 5.1. The division in these quasi-separate kinetic systems will be a guideline in discussing the various elementary processes. Apart from the effect on the composition we will also consider the impact of the various interactions on the kinetic energy exchange

---

^{d}In the rest of this study the hydrogen molecule in the electronic ground state is denoted as H_2 instead of $H_2(X^1\sum_g^+)$. Electronically excited hydrogen molecules are unstable [119] and are not separately included; H_2^+ denotes the molecular hydrogen ion in the electronic ground state; H denotes the hydrogen atom in the ground state and H^+ represents the atomic hydrogen ion in the ground state.

between $\{e\}$ and $\{h\}$.
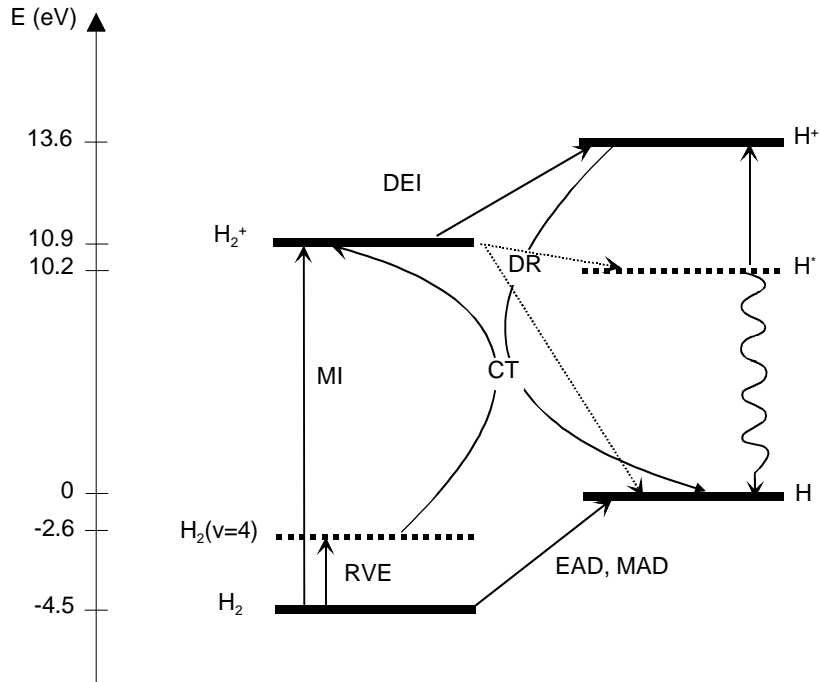
Figure 5.1: A schematic view of the coupling between the atomic, the electronic molecular and rovibrational molecular system. The symbols are explained in sections 5.2.2 and 5.2.3. The ground state of atomic hydrogen (H) is taken as energy reference level. The mass fractions of the levels represented by dotted lines are not computed in PLASIMO but are determined by local chemistry processes (i.e. they are assumed to be not transport sensitive).

5.2.1 The atomic system

The influence of the excited states of atomic hydrogen on step-wise ionisation is treated in a separate Collisional-Radiative (CR) model in such a way that the production of hydrogen ions H^+ can be expressed in the electron number density n_e, the number density of hydrogen atoms in the ground state $n(1)$ and the electron temperature T_e. These quantities are calculated in PLASIMO. We use the CR model of Hartgers *et al.* [124][e] in which a hybrid cut-off technique, described by Van der Mullen [68], is used. This reduces the number of excited levels in the hydrogen atom to 15. For the collision cross-sections the formulation of Vriens and Smeets [125] is used. The hydrogen plasma is assumed to be optically thin, except for strong absorption in the Lyman series. The chosen escape factors Λ are the same as those selected by Drawin and Emard [114] (which were also used to compute the radiative energy loss in [117]), namely: $\Lambda_{21} = 10^{-4}$, $\Lambda_{31} = 10^{-3}$, $\Lambda_{41} = 10^{-2}$, $\Lambda_{51} = 10^{-1}$, $\Lambda_{61} = 0.3$. For all other transitions

---

[e]This is a generalised version of the CR model of Benoy *et al.* [67].

Table 5.1: An overview of the set of reactions and rates which are used in this study to simulate a non-LTE hydrogen CA plasma. Symbols: $M = H$ or H_2; $X = e$, H or H^+.

	Process		Rate coeff.
	Name	Reaction	Reference
MI	Molecular Ionisation	$H_2 + e \leftrightarrow H_2^+ + e + e$	[120]
CT	Charge Transfer	$H_2(v \geq 4) + H^+ \rightarrow H_2^+ + H$	[115]
DR	Dissociative Recombination	$H_2^+ + e \rightarrow H + H^*$	[120]
DEI	Dissociation by Electron Impact	$H_2^+ + e \rightarrow H^+ + H + e$	[120]
EAD	Electron Assisted Dissociation	$H_2 + e \leftrightarrow 2H + e$	[121]
HAD	Heavy particle Assisted Dissoc.	$H_2 + M \leftrightarrow 2H + M$	[121]
RVE	RoVibrational Excit.	$H_2^{r,v=0} + X \leftrightarrow H_2^{r,v} + X$	[120, 122, 123]
	CR model:	$H(n) + e \leftrightarrow H^+ + 2e$ $H^+ + e \rightarrow H(n) + e$ $H(n) + e \leftrightarrow H(n') + e$ $H(n) \rightarrow H(n' < n) + h\nu$ $H(n) + h\nu \rightarrow H(n') + h\nu + h\nu$	[124]

(including free-bound) $\Lambda = 1$. The net H^+ production term S_{H+} in the atomic system is given by:

$$S_{H+} = m_{H+} n_e (n_H J_{1,+} - n_{H+} J_{+,1}) \tag{5.1}$$

with the coefficient of net ionisation, $J_{1,+}$ and of recombination $J_{+,1}$ (both in m^3 s^{-1}). The $J_{1,+}$ coefficient, as calculated with the CR model of Hartgers *et al.* [124], is shown in figure 5.2. For $J_{+,1}$, the formulation of Thomson [126] is used: $J_{+,1} = 2.6 \times 10^{-39} \hat{T}_e^{-4.5} n_e$, with $\hat{T}_e$ in eV. Due to the assumption that the plasma is almost optically thick for Lyman radiation, the ionisation coefficient $J_{1,+}$ is independent of n_e for $n_e > 10^{18}$ m^{-3}. It is implemented in PLASIMO using an Arrhenius like fit-function: $J_{1,+} = 1.948 \times 10^{-14} \hat{T}_e^{0.758} \exp(-9.556/\hat{T}_e)$ (m^3 s^{-1}).

The line radiation is also calculated with the CR model. The results are incorporated in the numerical model as an energy loss term in the electron energy equation:

$$Q_{line} = n_H \varepsilon_1 + n_{H+} \varepsilon_+ \tag{5.2}$$

with ε (in W) the coefficient of radiation generated due to the population of radiative states from the ground state (ε_1) or ion state (ε_+). In PLASIMO ε_1 and ε_+ are written as a polynomial of order 4: $\varepsilon = 10^{F(\hat{T}_e)}$ with $F(\hat{T}_e) = \sum_{l=0}^{4} a_l \hat{T}_e^l$ with different fit parameters a_l for different n_e. For n_e-values between two polynomial fits, linear interpolation is applied. They are depicted in figure 5.3. Free-free and free-bound radiation are included using the formulations given by Mitchner and Kruger [41].

An other important energy loss term in the electron energy balance is the one expressing the
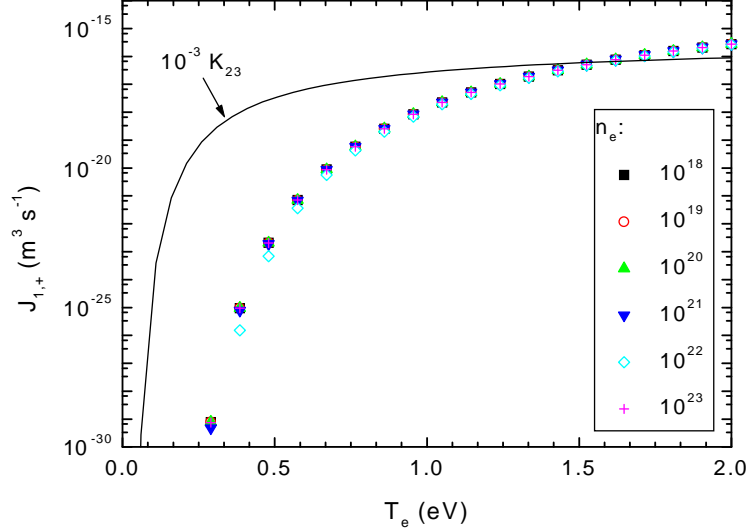
Figure 5.2: Ionisation coefficient $J_{1,+}$ from the CR model of Hartgers et al. [124] together with the excitation rate K_{23}, which is approximately equal to the ionisation rate of level $p = 2$.

elastic energy transfer from $\{e\}$ to $\{h\}$, given by:

$$Q_{eh}^{\text{elas}} = n_e \sum_X \left(\frac{2m_e}{m_X}\right) \frac{3}{2} k_b \left(T_e - T_h\right) \langle \nu_{eX} \rangle \tag{5.3}$$

with the Maxwellian-averaged collision frequency $\langle \nu_{eX} \rangle = n_X \langle K_{eX} E \rangle / (\frac{3}{2} k_b T_e)$, where K_{eX} is the rate coefficient for momentum energy transfer between electrons and heavy particle species X. Figure 5.4 gives a comparison of the ratio $< K_{eX} E > /(1.5 k_b T_e)$ (i.e. $< \nu_{eX} > /n_X$) for elastic energy transfer between electrons and argon atoms ($X = \text{Ar}$), electrons and hydrogen atoms ($X = \text{H}$) as well as electrons and hydrogen molecules ($X = \text{H}_2$). The rate for argon is taken from NIST [69], the hydrogen rates are taken from Michel *et al.* [127]. It is seen in figure 5.4 that at $T_e \leq 1$ eV, the rates for hydrogen are considerably higher than the rate for argon. Combined with the smaller mass of hydrogen, the elastic energy transfer for a hydrogen plasma will be much higher than for an argon plasma (although the electron density will be lower). Using the results in [34], where a non-equilibrium argon CA plasma is considered, this suggests that in hydrogen plasmas at comparable conditions the relation $(T_e/T_h - 1) \ll 1$ will hold.

5.2.2 The rovibrational molecular system

The hydrogen molecule-hydrogen atom coupling

The hydrogen molecule H_2 and hydrogen atom H are coupled with each other via:
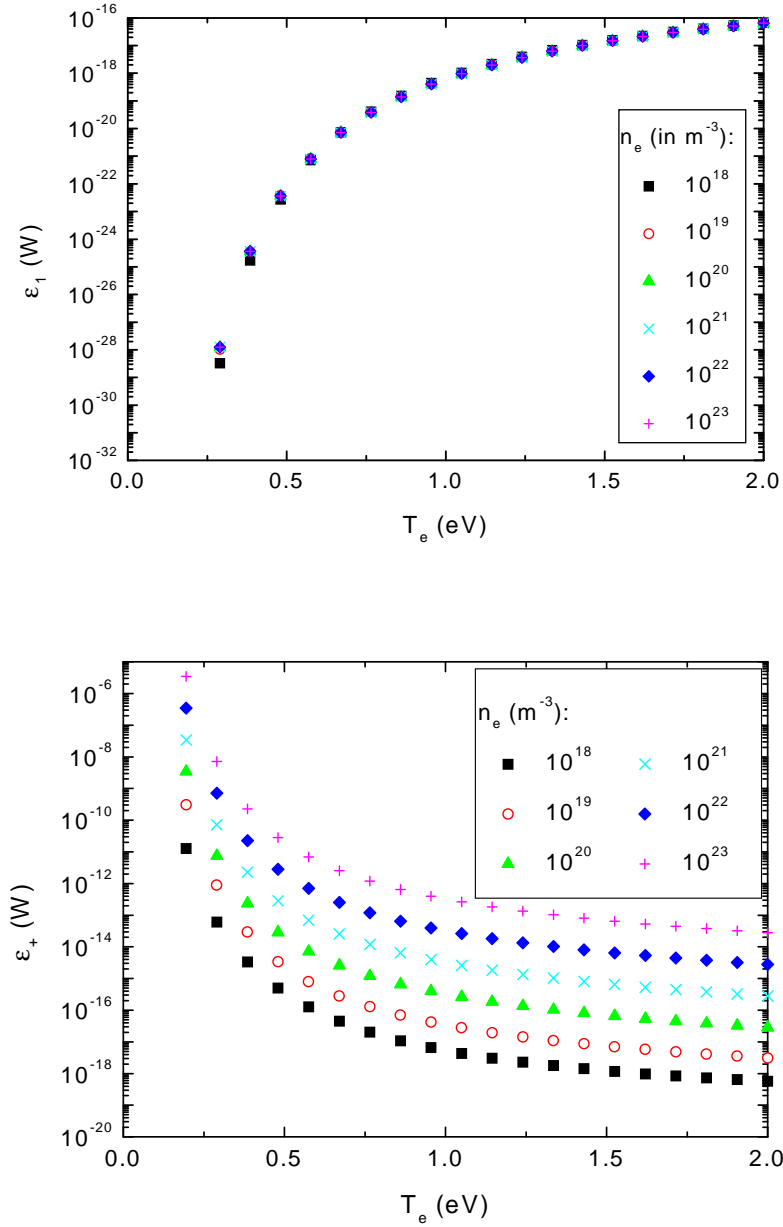
Figure 5.3: Results from the CR model of Hartgers et al. [124]. Coefficient of radiation due to the population of radiative states from: top: the ground state, ε_1; bottom: the ion state, ε_+, as function of n_e for different T_e. In the model a polynomial fit is used for each n_e.

- Electron Assisted Dissociation (EAD):

$$\mathrm{H_2 + e} \underset{EAA}{\overset{EAD}{\rightleftarrows}} \mathrm{H + H + e} \tag{5.4}$$
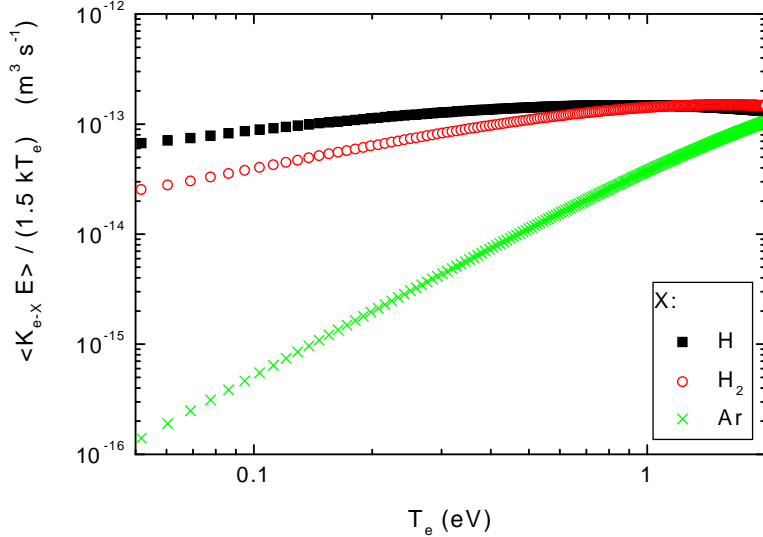
Figure 5.4: Comparison of energy-averaged rates for momentum transfer $< K_{eX}E > /(1.5k_bT_e)$ between electrons and hydrogen atoms (squares), electrons and hydrogen molecules (open circles) as well as electrons and argon atoms (crosses).

in which H is in the ground state. The reaction rates for the creation of excited hydrogen atoms are negligible for the electron temperatures found in the hydrogen CA plasma, see for example [120]. The reaction rate for the reverse process (Electron Assisted Association (EAA)) is calculated via detailed balancing.

- Heavy particle Assisted Dissociation (HAD) and its reverse process Heavy particle Assisted Association (HAA):

$$H_2 + M \underset{HAA}{\overset{HAD}{\rightleftarrows}} H + H + M \tag{5.5}$$
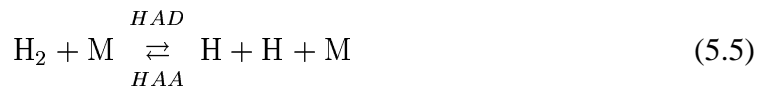
with $M = H, H_2$. In figure 5.5 the rates for EAD and HAD according to Kruger [121] are shown, the rate for HAA is calculated via detailed balancing[f].

The molecular rovibrational system

In an atomic hydrogen plasma, the most important energy transfer mechanisms between electrons and heavy particles are the energy transfer due to elastic collisions and due to stepwise ionisation/recombination. However, in a molecular hydrogen plasma, besides the extra disso-

---

[f] In the application of equation (5.5) we neglect the fact that the H_2 molecule could be rovibrationally excited [118].
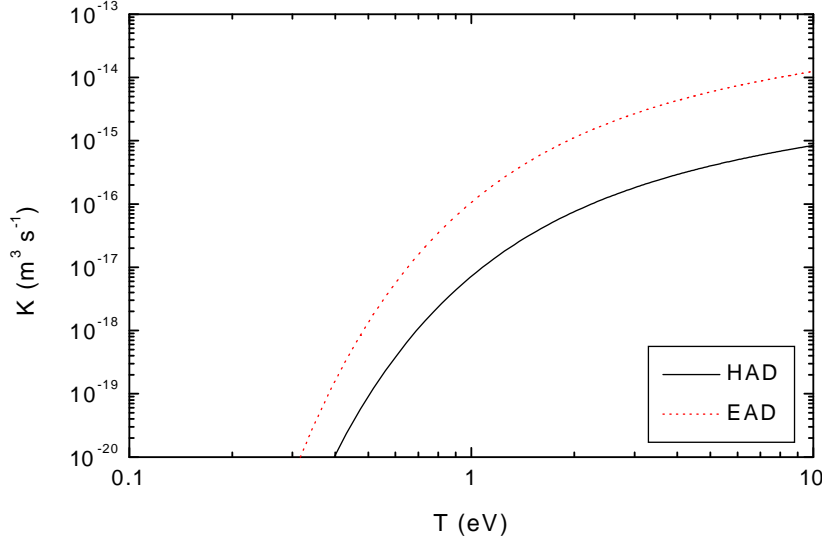
Figure 5.5: The reaction rates for Electron Assisted Dissociation (EAD) and Heavy particle Assisted Dissociation (HAD) according to Kruger [121].

ciation energy transfer term, an important mechanism of energy transfer is that via the internal states of the molecular species [128]; in this case the RoVibrational Excitation (RVE) of H_2:

$$H_2 + X \xrightarrow{\text{RVE}} H_2^{\text{r,v}} + X \tag{5.6}$$

with X an electron (e) or an heavy particle species (H, H^+). First, we concentrate on the vibrational excitation of H_2. Consider an isolated molecular two-level system, consisting of only the ground state and the first excited state of H_2, with number densities n_0 and n_1, respectively. Assuming that the for- and backward transitions are induced by $\{e\}$ and $\{h\}$ and that the radiative transitions and the ladder-like dissociation can be neglected, we find for the balance equation of n_1 that

$$\left(n_0 n_e K_{01}^e - n_1 n_e K_{10}^e\right) + \left(n_0 n_h K_{01}^h - n_1 n_h K_{10}^h\right) = 0 \tag{5.7}$$

with n_h the number density of heavy particle species H or H^+.
From equation (5.7), the ratio n_1/n_0 can be expressed as:

$$\frac{n_1}{n_0} = \frac{n_e K_{01}^e + n_h K_{01}^h}{n_e K_{10}^e + n_h K_{10}^h} \tag{5.8}$$

Since T_h is not expected to be much smaller than T_e and since $n_h \gg n_e$ whereas $K_{01}^h > K_{01}^e$ (compare figures 5.6 and 5.7) we may assume that $n_h K_{01}^h \gg n_e K_{01}^e$ and consequently also that $n_h K_{10}^h \gg n_e K_{10}^e$. This implies that the distribution of vibrational levels is almost the same as if

$\{e\}$ were absent. Consequently, the ratio n_1/n_0 given in equation (5.8) is written as

$$\frac{n_1}{n_0} \approx \frac{K_{01}^h}{K_{10}^h} = \exp\left(-\frac{\Delta E_{01}^{\text{vib}}}{k_b T_h}\right) \tag{5.9}$$

meaning that the vibrational temperature equals the heavy particle temperature[g]. The last step in equation (5.9) is based on the principle of detailed balancing (DB) applied to the heavy-particle-induced forward and backward processes. For the energy transfer from $\{e\}$ to $\{h\}$ via this molecular transition we then find that

$$Q_{eh}^{v,01} = \left(n_0 n_e K_{01}^e - n_1 n_e K_{10}^e\right) \Delta E_{01}^{\text{vib}} \tag{5.10}$$

$$= n_e n_0 K_{01}^e \Delta E_{01}^{\text{vib}} \left(1 - \exp\left[-\frac{\Delta E_{01}^{\text{vib}}}{k_b T_h} + \frac{\Delta E_{01}^{\text{vib}}}{k_b T_e}\right]\right) \tag{5.11}$$

where DB for the electron-induced processes prescribes that $K_{10}^e / K_{01}^e = \exp(+\Delta E_{01}^{\text{vib}} / k_b T_e)$. Anticipating on the assumption that $(T_e/T_h - 1) \ll 1$ we can use the following approximation: $\exp(-x) \approx 1 - x$, with $x = \Delta E_{01}^{\text{vib}}(\frac{1}{k_b T_h} - \frac{1}{k_b T_e})$. Herewith equation (5.11) reduces to:

$$Q_{eh}^{v,01} = n_e n_0 K_{01}^e \left[\Delta E_{01}^{\text{vib}}\right]^2 \left(\frac{1}{k_b T_h} - \frac{1}{k_b T_e}\right) \tag{5.12}$$

Until now we only considered the first vibrational states of H_2. However, the other stepwise vibrational transitions might also be of importance [129]; we consider here only single vibrational transitions, that is $\Delta v = 1$. An expression for the total vibrational energy transfer between electrons and heavy particles is derived assuming that the ratio of number densities for consecutive transitions are equal, that is $n_1/n_0 = n_2/n_1 = n_3/n_2 = ... = \gamma$, that the vibrational energy spacing is constant, i.e. $\Delta E_{01}^{\text{vib}} = \Delta E_{12}^{\text{vib}} = ... = \Delta E_{\text{vib}} = 0.5457$ eV and that the rate coefficients are equal. This gives:

$$Q_{eh}^{\text{vib}} \approx n_e n_0 K_{01}^e \left[\Delta E_{\text{vib}}\right]^2 \left(\frac{1}{k_b T_h} - \frac{1}{k_b T_e}\right) \frac{1}{1 - \gamma} \tag{5.13}$$

where we made use of the assumption that $1 + \gamma + \gamma^2 + \gamma^3 + ... = 1/(1 - \gamma)$, which is valid for $\gamma < 1$. This condition is fulfilled since $n_0 > n_1$.

A similar approach can be used for the rotational excitation, except that the rotational energy spacing can not be assumed to be constant. In fact, $\Delta E_{l,l+2}^{\text{rot}} = (4l + 6)E_{\text{rot}}$ with the rotational energy constant $\hat{E}_{\text{rot}} = 7.54 \times 10^{-3}$ eV [130] and l the number of the rotational level. Because of the same reasons as those given above for the vibrational excitation, we may also assume that the rotational temperature T_r equals the heavy particle temperature. The rotational energy transfer Q_{eh}^{rot} between electrons and heavy particles can now be written as:

$$Q_{eh}^{\text{rot}} \approx \sum_l n_e n_{H_2,l} K_{l,l+2}^e \left[(4l + 6) E_{\text{rot}}\right]^2 \left(\frac{1}{k_b T_h} - \frac{1}{k_b T_e}\right) \tag{5.14}$$

---

[g]Normally it is assumed that for low pressure the relations $T_v = T_e$ and $T_r = T_h$ hold, with T_r the rotational temperature (which we will use later); for higher pressure we made plausible that the relation $T_v = T_r = T_h$ is more appropriate.

Figure 5.6 shows the rates for four rotational excitations ($l = 0 \rightarrow 2$, $1 \rightarrow 3$, $2 \rightarrow 4$ and $3 \rightarrow 5$) according to England *et al.* [131] and two vibrational excitations ($v = 0 \rightarrow 1$ and $0 \rightarrow 2$) according to Morrison *et al.* [122] and Janev *et al.* [120], respectively. It can be shown from a comparison of the elastic energy transfer given in equation (5.3) with Q_{eh}^{vib} (equation (5.13)) and Q_{eh}^{rot} (equation (5.14)) that Q_{eh}^{vib} and Q_{eh}^{rot} are more efficient than Q_{eh}^{elas} in the hydrogen plasma considered.
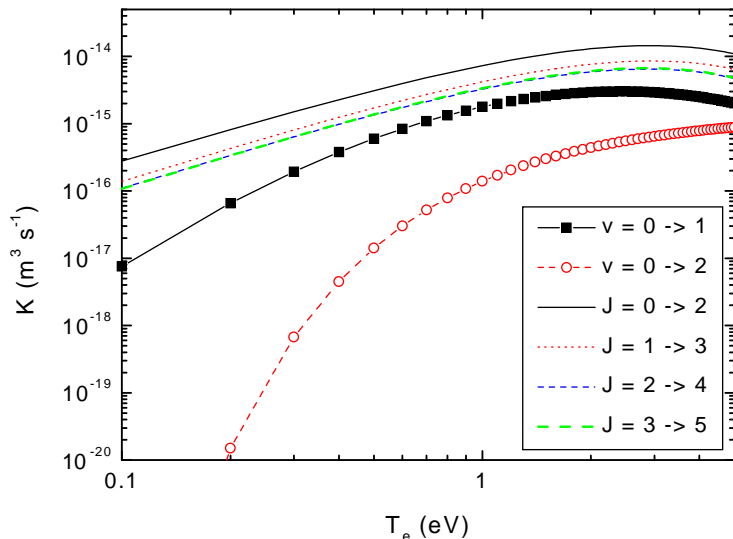
Figure 5.6: The reaction rates for rotational excitation ($l = 0 \rightarrow 2$, $1 \rightarrow 3$, $2 \rightarrow 4$ and $3 \rightarrow 5$) according to England et al. [131] and vibrational excitation ($v = 0 \rightarrow 1$ and $0 \rightarrow 2$) according to Morrison et al. [122] and Janev et al. [120], respectively, of the molecule H_2 due to electron interaction.

5.2.3 The electronic molecular system

The molecular ion H_2^+ is formed via:

- Molecular Ionisation (MI):

$$H_2 + e \xrightarrow{\mathrm{MI}} H_2^+ + e + e \qquad (5.15)$$

  The reaction rate is taken from Janev *et al.* [120]. The reverse process is also taken into account; its rate is calculated using DB.

- Charge Transfer (CT):

$$H_2(v \geq 4) + H^+ \xrightarrow{\mathrm{CT}} H_2^+ + H \qquad (5.16)$$

  where the reaction rate for CT is taken from De Graaf [115]. The ionisation energies of H^+ and H_2^+ are 13.595 eV and 15.422 eV, respectively, so that the CT reaction is most likely
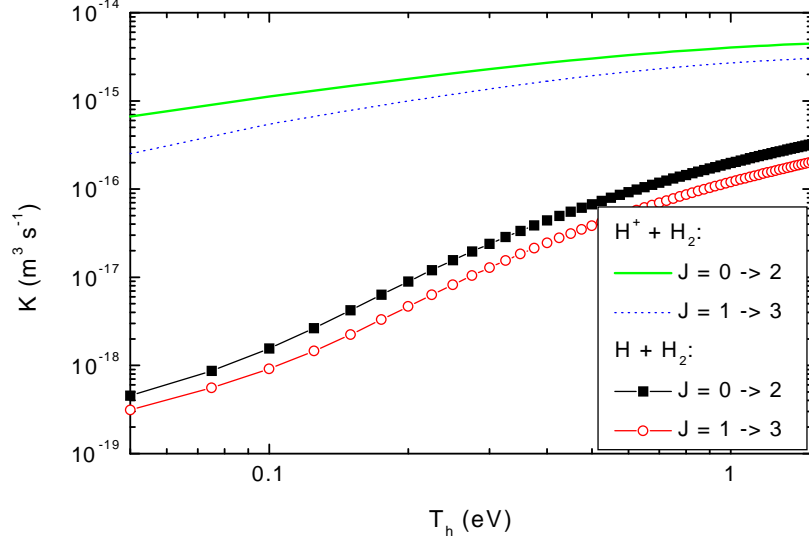
Figure 5.7: The reaction rates for rotational excitation ($l = 0 \rightarrow 2$ and $1 \rightarrow 3$) according to Phelps [123] of the molecule H_2 due to heavy particle interaction.

to take place via the H_2 molecule in the vibrational level $v = 4$ (1.89 eV)[h]. We assume a Boltzmann distribution over the vibrationally excited states of H_2, which is ruled by the vibrational temperature T_v, which almost equals the heavy particle temperature T_h as was shown in the previous section:

$$n_{H_2^v} = n_{H_2}^{\text{tot}} \frac{g_v}{Q_v^{\text{tot}}} \exp\left(-\frac{E(v)}{k_b T_h}\right) \tag{5.17}$$

with $n_{H_2}^{\text{tot}}$ the total number density of H_2 in the electronic ground state. This is a TS species in PLASIMO, which means that it is calculated by solving its mass balance. The vibrational partition function Q_v^{tot} of H_2 is given by [132]:

$$Q_v^{\text{tot}} = \sum_{v=0}^{v_{\max}} g(v) \exp\left(-\frac{E(v)}{k_b T_h}\right) \tag{5.18}$$

with $v_{\max} = E_{\text{diss}}/E_{\text{vib}} = 14$, E_{diss} is the dissociation energy of H_2 and E_{vib} is the vibrational energy spacing, which is assumed to be constant. In a more accurate description, the energy of vibrational level v is given by: $E(v) = \hbar\omega_e(v - xv^2)$ (in J) with the vibrational constants for H_2 [130] $\omega_e = 2339$ cm^{-1} and $x = 57/2339 = 0.0244$.

---

[h] In principle also H_2 molecules in vibrational levels $v = 2$ and $v = 3$ are possible, if they are rotationally excited or if they have higher kinetic energy. This implies that the CT reaction rate increases.

The MI and CT rates are depicted in figure 5.8.

The H_2^+ molecular ion is destroyed via:

- Dissociative Recombination (DR):

$$H_2^+ + e \xrightarrow{\text{DR}} H + H^* \xrightarrow{1-\chi} H + H^+ + e$$
$$\xrightarrow{\chi} H + H \qquad (5.19)$$
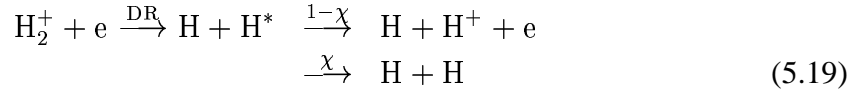
If H_2^+ is not rovibrationally excited, then the highest reachable hydrogen atom level H^* is that with principal quantum number $p = 2$ (10.2 eV)[i]. A branching ratio is used for the two follow-up reactions denoted by $1 - \chi$ (for reaction $H^* + e \to H^+ + 2e$) and χ (for reaction $H^* \to H(1) + h\nu$). The chance for the ionisation of H^* is $1 - \chi = n_e K_{2i}/(n_e K_{2i} + \Lambda_{21} A_{21})$ and the chance for (radiative) recombination to the ground level is $\chi = \Lambda_{21} A_{21}/(n_e K_{2i} + \Lambda_{21} A_{21})$. Herein K_{2i} represents the ionisation rate for the $p = 2$ level of the hydrogen atom. This is not the direct ionisation rate from $2 \to +$ but should be a combination of stepwise excitation rates, which is dominated by K_{23}. This rate is calculated using the Vriens formulae [125] and is fitted with an Arrhenius fit: $K_{23} = 1.724 \times 10^{-13} \hat{T}_e^{0.39} \exp(-1.84/\hat{T}_e)$ (m^3 s^{-1}). It is shown for comparison in figure 5.2 together with the effective ionisation rate $J_{1,+}$ from the CR model. The escape factor for radiative decay to the H ground state is taken as $\Lambda_{21} = 10^{-4}$, and $A_{21} = 4.699 \times 10^8$ s^{-1} is the transition probability. For $n_e \geq 10^{20}$ m^{-3} and $K_{23} = 10^{-13}$ m^3 s^{-1} (at $\hat{T}_e \approx$ 1 eV), the radiative branch can be neglected compared to the ionisation branch, since $\Lambda_{21} A_{21}/(n_e K_{23}) \approx 5 \times 10^{-3}$. However, in outer plasma parts where T_e is smaller and Λ_{21} is larger, the branching ratio and consequently also the energy transfer will be different. The energy gain/loss of the various species, due to reaction (5.19), is as follows:

$$Q_e^{\text{DR}} = -(1 - \chi) n_e n_{H_2^+} K_{\text{DR}} \Delta E_{1-\chi} - \chi n_e n_{H_2^+} K_{\text{DR}} \frac{3}{2} k_b T_e \qquad (5.20)$$

$$Q_h^{\text{DR}} = \chi n_e n_{H_2^+} K_{\text{DR}} \Delta E_\chi \qquad (5.21)$$

$$Q_{h\nu}^{\text{DR}} = \chi n_e n_{H_2^+} K_{\text{DR}} \Delta E_{12} \qquad (5.22)$$

with $\Delta E_{1-\chi} = (10.2 + 3.395) - (15.422 - 4.476) = 2.649$ eV, $\Delta E_\chi = (15.422 - 4.476) - 10.2 = 0.746$ eV, $\Delta E_{12} = 10.2$ eV.

The electronic molecular system has not only a large influence on the composition, but also on the radial electron temperature distribution, in spite of the small concentration of H_2^+. As we will see in section 5.4, without inclusion of the H_2^+ reactions, especially the charge transfer reaction (5.16), the "sombrero" profile such as observed in the LTE hydrogen simulations in [117], will not be present in the non-LTE simulations.

- Dissociation by Electron Impact (DEI):

$$H_2^+ + e \xrightarrow{\text{DEI}} H^+ + H + e \qquad (5.23)$$

---

[i]It was shown by Mitchell [133] that for vibrationally excited H_2^+ the H^* atoms will be predominantly in $p = 3$ or above.

Figure 5.8 shows the destruction rates for DR and DEI according to De Haan *et al.* [134] and Janev *et al.* [120], respectively. As one can see, the most dominant reaction is DR, especially at low energies. We will see later that both rates are much higher than all other reaction rates in a hydrogen plasma.
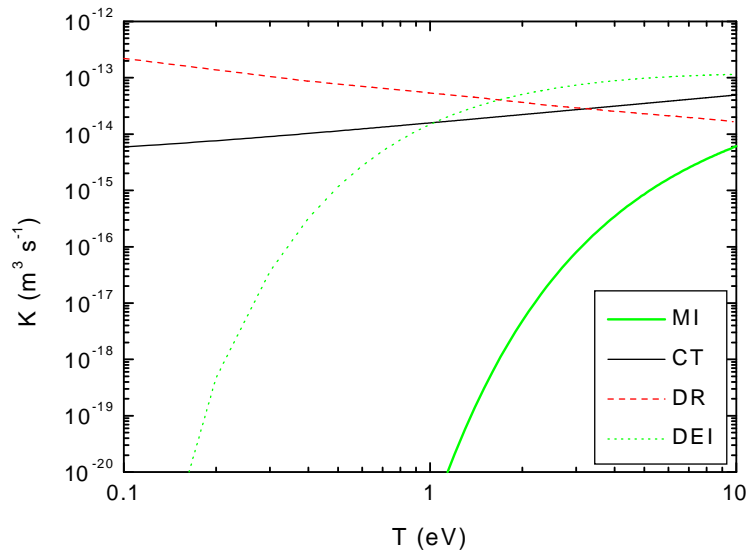
Figure 5.8: The reaction rates for destruction of H_2^+: Dissociative Recombination (DR) [134] and Dissociation by Electron Impact (DEI) [120] and production of H_2^+: Molecular Ionisation (MI) [120] and Charge Transfer (CT) [115].

5.2.4   Transport coefficients

The electron thermal conductivity λ_e is calculated using Frost's mixture rules [57]; the electric conductivity σ is calculated conform the self-consistent set of the Stefan-Maxwell equations, which is explained in chapter 3 of this thesis. The frozen part of the heavy particle thermal conductivity $\lambda_{h,f}$ and the viscosity μ are calculated with the mixture rules given by Mitchner and Kruger [41]. In contrast to [117], the reactive part of the heavy particle thermal conductivity $\lambda_{h,r}$ is not included in the thermal conductivity calculation. Instead, it enters the heavy particle energy balance as a reactive heat source term, see section 5.2.5.

5.2.5   Source terms

The mass production terms of the species in the mass fraction balances are calculated from the reactions given in sections 5.2.1 - 5.2.3 and are given by:

$$S_i = m_i \sum_k \left(\aleph^{\mathrm{f}}_{k,i} - \aleph^{b}_{k,i} \right) \left(K^f_k \prod_j n_j^{\aleph^f_{k,j}} - K^b_k \prod_j n_j^{\aleph^b_{k,j}} \right) \tag{5.24}$$

with $\aleph_{k,i}$ the stoichiometric coefficient of species i in reaction k; the superscript f and b denote the forward and backward process, respectively; K is the reaction rate.

In the momentum balance of the mixture, the influence of the generated magnetic field $\vec{\mathbf{B}}$, $\vec{\mathbf{j}}_q \times \vec{\mathbf{B}}$, is included as follows:

$$\vec{\mathbf{e}}_z \cdot \left(\vec{\mathbf{j}}_q \times \vec{\mathbf{B}} \right) = 0 \tag{5.25}$$

$$\vec{\mathbf{e}}_r \cdot \left(\vec{\mathbf{j}}_q \times \vec{\mathbf{B}} \right) = -\frac{1}{2}\mu_0 \rho \left(\frac{I}{\pi R^2} \right)^2 \tag{5.26}$$

where it is assumed that the current density $\vec{\mathbf{j}}_q = I/(\pi R^2)$ is uniform over the cross-section of the CA; R is the radius of the arc channel, I is the applied current and μ_0 is the magnetic permeability of vacuum.

In the electron energy balance the following source terms are included: the Ohmic input power, the radiation losses, the elastic energy transfer between electrons and heavy particles and the reactive heat source term. For calculating the elastic energy transfer (equation (5.3)), the cross-sections for momentum transfer between electrons and neutrals H and H_2 (used in the collision frequency) are needed; they are taken from Michel *et al.* [127]. The radiation loss term is conform [117] with the free-free and free-bound contribution according to Mitchner and Kruger [41] and the line radiation conform section 5.2.1 for an optically thin plasma, except for a strong absorption in the Lyman series. The HAD (HAA) and CT reactions are added in the reactive heat source term in the heavy particle energy balance.

5.3   Configuration features

5.3.1   Plasma source and geometry

The used plasma source is the wall-stabilised cascaded arc (CA) [61, 62], and is already discussed in [117]. We will focus on the "standard configuration", a straight CA channel with radius $R = 2$ mm, length $L = 25$ mm, current $I = 50$ A and inlet flow $\varphi = 100$ scc s^{-1}.

5.3.2   Boundary conditions

The boundary conditions that are applied on the non-LTE hydrogen CA plasma are partly the same as in [117] and are listed in table 5.2 below.

Table 5.2: Boundary conditions applied to the non-LTE hydrogen cascaded arc plasma. The pressure is p; u_z and u_r are the axial and radial velocity components, respectively; T_h and T_e are the heavy particle and electron temperature, respectively; y_i is the mass fraction of species i.

Par.	Inlet	Outlet	Axis	Channel wall
p	$\frac{\partial p}{\partial z} = C$	$\frac{\partial p}{\partial z} = C$	$\frac{\partial p}{\partial r} = 0$	$\frac{\partial p}{\partial r} = 0$
u_z	$u_z = u_{\text{in}}^{\max}\left[1 - \left(\frac{r}{R_{\text{in}}}\right)^2\right]$	$u_z = u_{\text{out}}^{\max}\left[1 - \left(\frac{r}{R_{\text{out}}}\right)^5\right]$	$\frac{\partial u_z}{\partial r} = 0$	$u_z = 0$
u_r	$u_r = 0$	$\frac{\partial u_r}{\partial z} = 0$	$u_r = 0$	$u_r = 0$
T_h	$T_h = T_{h,\text{in}}$	$\frac{\partial T_h}{\partial z} = 0$	$\frac{\partial T_h}{\partial r} = 0$	$\lambda_h \frac{\partial T_h}{\partial r} = \frac{\lambda_w\left(T_{\text{aq}} - T_{h,w}\right)}{R \ln\left(\frac{R + \delta_w}{R}\right)}$
T_e	$T_e = T_{e,\text{in}}$	$\frac{\partial T_e}{\partial z} = 0$	$\frac{\partial T_e}{\partial r} = 0$	$\frac{\partial T_e}{\partial r} = C$
y_i	$\frac{M_i\varphi_i}{\sum_j M_j\varphi_j}$ $\vec{\mathbf{n}}\cdot\vec{\mathbf{J}}_i = 0$	$\frac{\partial y_i}{\partial z} = 0$	$\frac{\partial y_i}{\partial r} = 0$	$\vec{\mathbf{n}}\cdot\left(\rho y_i\vec{\mathbf{u}} + \vec{\mathbf{J}}_i\right) = R_i$

Par.	Value	Par.	Value
φ	100 scc s^{-1}	$T_{e,\text{in}}$	2000 K
f_{H_2}	0.99	T_{aq}	320 K
f_{H}	0.009	λ_w	360 W m^{-1} K^{-1}
f_{H^+}	0.0009	R	2 mm
$f_{\text{H}_2^+}$	0.0001	δ_w	12 mm
$T_{h,\text{in}}$	2000 K		

As explained in [117] the maximum inlet velocity at the axis, $u_{\text{in}}^{\max}$, is dictated by the mass flow and mass density at the inlet. The plasma expands supersonically in a vacuum chamber at low pressure; in the outlet plane at $r = 0$ the velocity $u_{\text{out}}^{\max}$ is determined by the Mach number value of one (see [34]). A constant axial component of the pressure gradient is assumed at inlet and outlet. The value of these gradients are determined during the iteration process. The heavy particle temperature at the channel wall, $T_{h,w}$, is determined from the equality of the heat flux from the plasma to the wall and the heat flux from the wall to the cooling water (δ_w is the distance between channel wall and cooling water, the temperature of the cooling water is T_{aq}). At the inlet the composition of the hydrogen mixture is fixed, with fractions f_i of the total inlet flow φ for each individual species i (i.e. the inlet flow of species i is defined as $\varphi_i = f_i\varphi$). The fractions are given in table 5.2. At the wall, the total mass flux of species "i" perpendicular to the wall

must equal the net mass flux R_i due to production or consumption of the species at the wall: $R_i = m_i(\Gamma_{i,w}^{\text{out}} - \Gamma_{i,w}^{\text{in}})$ with $\Gamma_{i,w}$ the flux (in $\text{m}^{-2}\text{s}^{-1}$) describing the gain or loss of species i at the wall w. It is dependent on the wall reaction probability γ_i (no sticking is assumed) and is described in chapter 2 of this thesis. Wall reaction processes can play an important role in the plasma chemistry, as was shown in earlier studies like [16, 135, 136, 137, 138, 139]. The wall reaction processes included in this study are listed in table 5.3.[j]

Table 5.3: The wall reaction processes included in this study.

Reacting species	Reactants
$H + \text{wall} \rightarrow$	$\frac{1}{2}H_2$
$H^+ + \text{wall} \rightarrow$	H
$H_2^+ + \text{wall} \rightarrow$	H_2

The reaction probabilities γ_{H^+} and $\gamma_{H_2^+}$ for ionic neutralisation at the wall are assumed to be 1, the wall reaction coefficient γ_H for the wall association process of H depends on the wall temperature, the wall material and the surface conditions of the wall. For example, passivation of the surface of the wall has a large influence on γ_H: the more monolayers are deposited on the wall, the lower the γ_H. Consequently, in the literature different values of γ_H can be found, ranging from approximately 10^{-3} to 1 [135, 141, 142, 143, 144, 145]. Therefore, we will investigate the influence of γ_H on the dissociation degree in the arc, by varying γ_H in the range 10^{-3} to 0.5. Since γ_H is material dependent [135], the densities of H and H_2 can be varied by changing wall materials. Consequently, also the ionic species densities, which are influenced considerably by the resulting H and H_2 concentrations, are changed. This provides an alternative mechanism for optimizing the CA as an ion source. This could be the topic of a follow-up study.

5.4 Results

For all numerical simulations performed in this study we use the standard configuration, described in section 5.3. We first consider the results of the numerical simulation of a pure atomic hydrogen plasma, consisting of species H, H^+ and e. The radial temperature distributions of the electrons and the heavy particles are depicted in figure 5.9. As one can see in figure 5.9, the temperature distributions for an atomic hydrogen plasma have the same shapes as those for an argon CA plasma, presented in [34]. The radial distributions of the mass fractions of H and H^+ are shown in figure 5.10. The reaction coefficient for ionic neutralisation at the wall is taken $\gamma_{H^+} = 1.0$. The maximum H^+ density at the channel axis is 4.86×10^{21} m^{-3}, the ionization degree at the outlet is $\alpha = 9.5\%$. In the introduction we argued that the elastic energy transfer in a hydrogen plasma is more efficient than in an argon plasma. However, in figure 5.9 we see that

---

[j]The relaxation of vibrationally excited hydrogen molecules, H_2^v, at the wall, which may be of importance in low-pressure discharges ($p \approx 150$ Pa) [118, 140], is neglected here. This would decrease the dissociation degree in the arc.

the difference between T_e and T_h for hydrogen is higher than for argon (for those temperature profiles, see [34]). This seems to be in contradiction with the analysis of the elastic energy transfer. The answer is found in the higher thermal conductivity and higher diffusion coefficients of hydrogen.

Now the results for a molecular hydrogen plasma, consisting of species H_2, H, H^+, H_2^+ and e, will be given. The radial profiles of temperatures and mass fractions are shown in figures 5.11 - 5.12 with charge transfer included and 5.13 - 5.14 without charge transfer. As one can see in figures 5.11 and 5.12 in the central region, we mainly have an atomic system, with differences between T_e and T_h in accordance with the pure atomic hydrogen plasma. In the outer region of the plasma, we have mainly a molecular/atomic region, ruled by the association/dissociation equilibrium and the rovibrational excitation via heavy particle collisions. In this region thermal equilibrium exists.

If we compare the results of the non-LTE hydrogen simulations with the LTE simulations performed in [117] we observe the following:

- Although a "sombrero" profile is seen in the non-LTE simulations (figure 5.11), it is not as pronounced as in the results of the LTE simulations. The heavy particle temperature profile is not sombrero-like.

- It proves that thermal non-equilibrium exists in the central region, conform a pure atomic hydrogen plasma. Due to the efficient rovibrational energy exchange between electrons and hydrogen molecules, in the outer part of the plasma almost thermal equilibrium exists.

- One has to keep in mind that the description of the non-LTE hydrogen plasma, as presented here, is far from accurate. First of all, assumptions were made on the rovibrational excitation, where amongst others the influence of stepwise dissociation was neglected. Secondly, not all the reverse reactions are included in the model (for example the reverse reactions of DR and DEI). Consequently, the LTE simulations presented in [117] can not be exactly reproduced by the non-LTE simulations.

The large influence of the charge transfer (CT) reaction (5.16) on the simulations is clearly seen by comparing figures 5.11 - 5.12 with 5.13 - 5.14. Without CT a parabolic temperature profile is seen, whereas CT induced a "sombrero profile". Comparing figure 5.12 with 5.14 shows that H_2^+ is a very important intermediate species in the hydrogen plasma. Note the huge influence on the atomic hydrogen and molecular hydrogen mass fraction. The effect of H_2^+ is also seen clearly in the energy management by comparing figure 5.11 with 5.13; H_2^+ introduces a sombrero in especially T_e. This proves that although the number density of H_2^+ is small, it plays a major role as an "intermediate" species in the composition and in the energy management.

5.4.1   Influence of the wall reaction coefficient γ_H

The effect of the wall reaction coefficient γ_H (which was discussed in section 5.3) on the dissociation degree β and ionisation degree α, are shown in figure 5.15[k]. With decreasing γ_H, the mass fraction of H increases and consequently also the mass fraction of H^+ increases. The result is that both the dissociation degree and ionisation degree increase, although the increase in α is a

---

[k]The exact definitions for β and α are given in chapter 4 of this thesis.
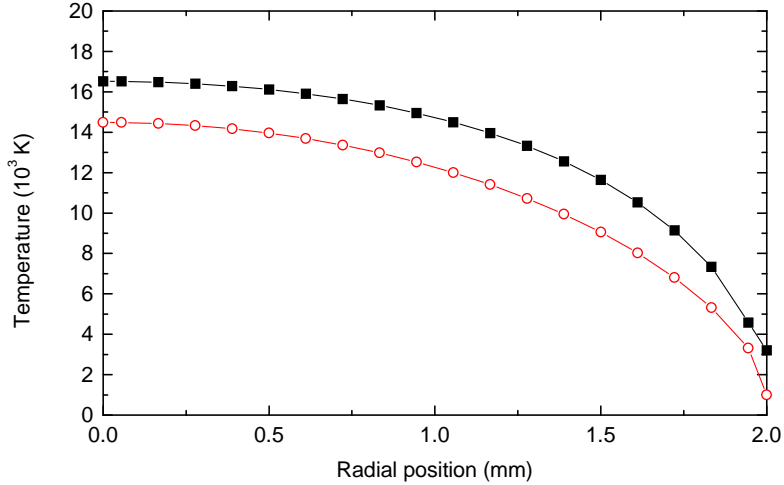
Figure 5.9: The radial temperature distribution of the electrons (squares) and the heavy particles (open circles), at $z = 11.8$ mm, for an atomic hydrogen plasma.
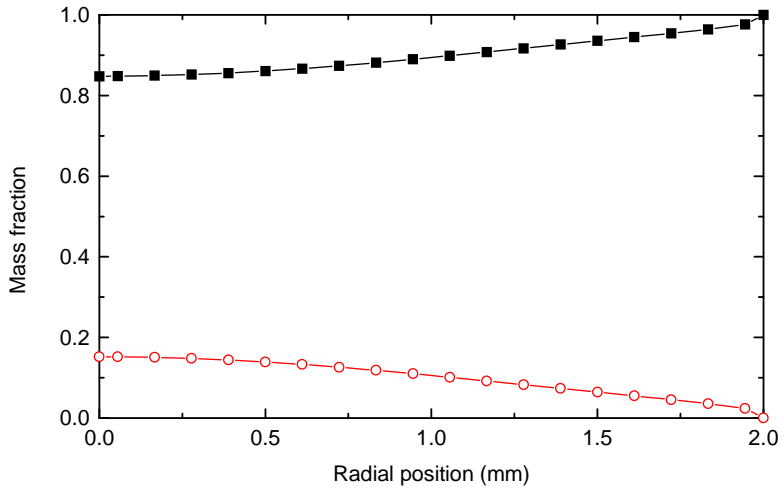
Figure 5.10: The radial mass fraction distribution of H (squares) and H^+ (open circles) at $z = 11.8$ mm, for an atomic hydrogen plasma.

marginal one: from 8.8% at $\gamma_H = 0.5$ to 10.1% at $\gamma_H = 0.001$. An accurate knowledge of the wall reaction coefficient γ_H is therefore a necessity to perform realistic simulations.
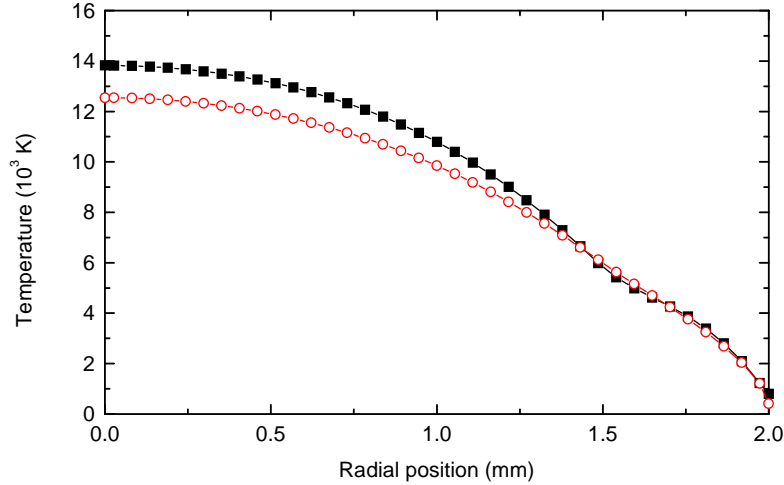
Figure 5.11: The radial temperature distribution of the electrons (squares) and the heavy particles (open circles), at $z = 11.8$ mm, for a molecular hydrogen plasma, with charge exchange included.
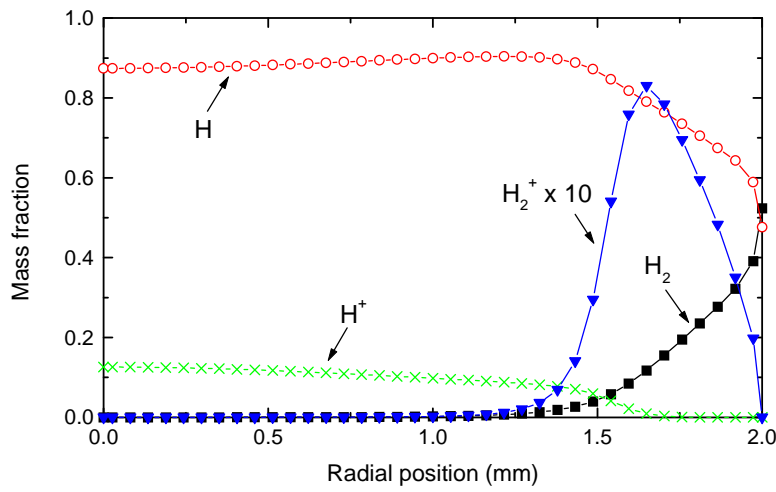
Figure 5.12: The radial mass fraction distribution of H_2 (squares), H (open circles), H^+ (crosses) and H_2^+ (down triangles) at $z = 11.8$ mm, for a molecular hydrogen plasma, with charge exchange included.
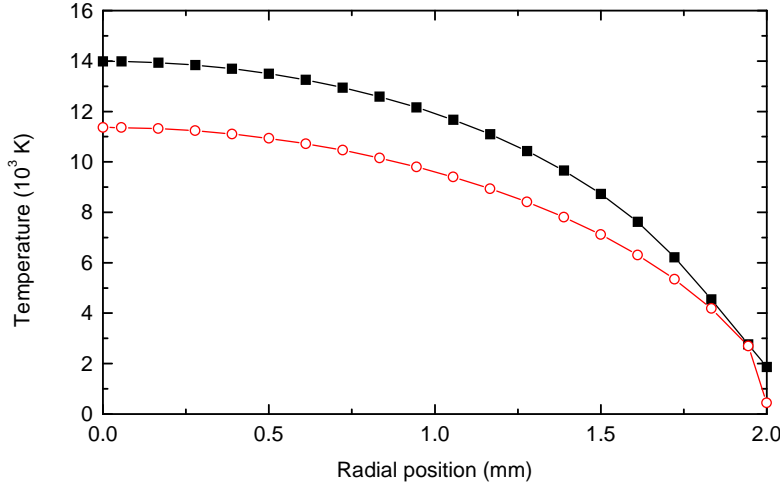
Figure 5.13: The radial temperature distribution of the electrons (squares) and the heavy particles (open circles), at $z = 11.8$ mm, for a molecular hydrogen plasma without charge transfer.
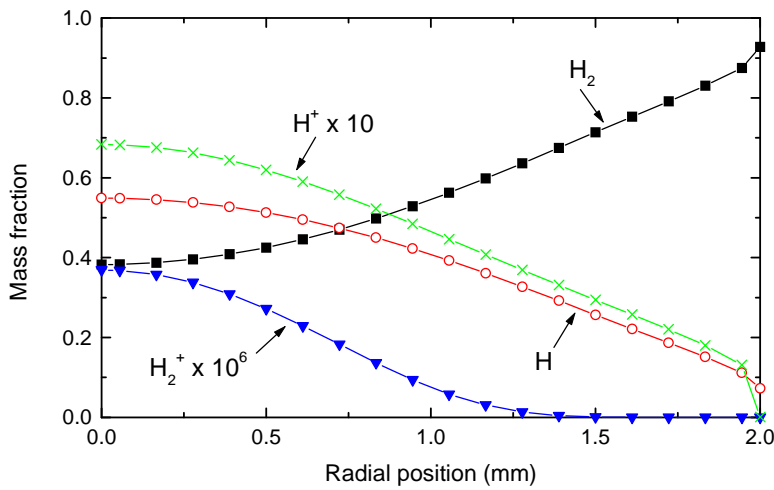
Figure 5.14: The radial mass fraction distribution of at $z = 11.8$ mm, for a molecular hydrogen plasma, without charge transfer. Markers conform figure 5.12.

5.4.2 Anomalous recombination in a hydrogen plasma jet

Rovibrationally excited hydrogen molecules can cause an anomalous fast recombination of H^+ in an expanding hydrogen plasma jet[l]. as was shown by De Graaf [10]. The chain of reactions

---

[l]A hydrogen plasma created in a cascaded arc is expanding in a vacuum chamber at low pressure. The experimental set-up used by De Graaf [10] is comparable to the deposition set-up in figure 6.1 in chapter 6.
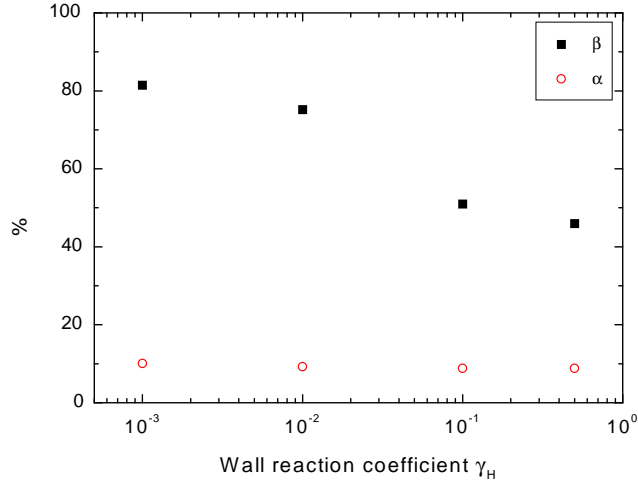
Figure 5.15: The dissociation degree β and ionisation degree α as function of wall reaction coefficient γ_{H} for a molecular hydrogen plasma (standard configuration).

that leads to this loss of H^+ is formed by charge transfer[m]:

$$\mathrm{H}^+ + \mathrm{H}_2^{\mathrm{rv}} \rightarrow \mathrm{H} + \mathrm{H}_2^+ \tag{5.27}$$

followed by dissociative recombination via:

$$\mathrm{H}_2^+ + \mathrm{e} \rightarrow \mathrm{H} + \mathrm{H}^* \tag{5.28}$$

According to De Graaf, for low ionisation degree another dissociative recombination channel will be dominant over reaction (5.28), namely:

$$\mathrm{H}_2^+ + \mathrm{H}_2 \rightarrow \mathrm{H}_3^+ + \mathrm{H} \tag{5.29}$$

followed by:

$$\mathrm{H}_3^+ + \mathrm{e} \rightarrow \mathrm{H} + \mathrm{H} + \mathrm{H} \tag{5.30}$$

or:

$$\mathrm{H}_3^+ + \mathrm{e} \rightarrow \mathrm{H}_2^{\mathrm{rv}} + \mathrm{H} \tag{5.31}$$

The reaction rate for dissociative recombination of H_3^+ (5.31) is probably of the same order of magnitude as the rate for dissociative recombination of H_2^+, reaction (5.28) [146]. De Graaf's argument for this alternative dissociative recombination channel, was that mass spectrometry measurements showed a significant amount of H_3^+ and a total absence of H_2^+ [115]. Both the

---

[m]Note that the hydrogen molecules have to be rovibrationally excited, since the charge transfer reaction is endothermic.

dissociative recombination channels (via H_2^+ and via H_3^+) are very effective. Note that two- (i.e. radiative) and three-particle recombination can not account for the experimentally observed loss of H^+ (in the range of three to four orders of magnitude), since these reactions are too slow.

The numerical simulations presented in this study, suggest that the amount of H_2 in the outer plasma region is sufficient to quench completely the H^+ emanating from the CA, without the necessity of formation of rovibrationally excited H_2 at the walls of the vacuum chamber via the reaction $H + H(adsorbed) \rightarrow H_2^{rv}(desorbed)$ followed by re-entry into the plasma beam via recirculation and diffusion.

5.4.3 Influence of H_3^+ and H^-

The molecular ion H_3^+ and the negative ion H^- are not included in the numerical simulations. Remains the possible influence of H_3^+ and H^- on the plasma behaviour in the arc. The outer plasma region near the channel wall is the only region where H_2^+ is significantly present. This is also the only region where H_2 is the dominant species. This suggests that apart from the dissociative recombination of H_2^+ (reaction (5.28)), also the formation of H_3^+ by reaction (5.29) is a real possibility. The H_3^+ molecular ion is then destroyed very fast via the dissociative reactions (5.30) and (5.31), see section 5.4.2. Especially in the outer plasma region H_3^+ can play an important role, since in that region $n_{H_2} \gg n_e$ so that reaction (5.29) will be dominant over reaction (5.28).

We then have an extra mechanism to remove H_2 from the plasma (even when reaction (5.31) is dominant, the formed H_2^{rv} will most likely dissociate, so that effectively one H_2 molecule is removed from the plasma). As a result, the dissociation degree would become higher than the values found in the present study.

The negative ion H^- is formed via dissociative attachment:

$$H_2^{rv} + e \longrightarrow H + H^- \tag{5.32}$$

where the hydrogen molecule should be vibrationally excited to at least $v = 8$ [147]. This reaction can take place only in the outer plasma region due to the lack of H_2 in the central plasma region. The negative ions recombine fast (just as H_2^+ and H_3^+)[n]:

$$H^- + H^+ \longrightarrow H^{**} + H \tag{5.33}$$

$$H^- + H_2^+ \longrightarrow H^{**} + H_2 \tag{5.34}$$
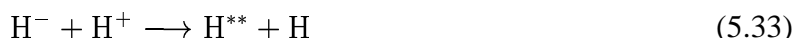
where H^{**} denotes a highly excited hydrogen atom ($p > 3$). In this way also a hydrogen molecule is removed from the plasma, so that the dissociation degree increases.

---

[n]To compare the importance of the different recombination reactions we give the reaction rates (for a temperature of 2000 K) cf [147]:

reaction	rate (in $m^3 s^{-1}$)
(5.19)	1×10^{-13}
(5.30,5.31)	6×10^{-14}
(5.33)	2×10^{-14}
(5.34)	2×10^{-13}

For both species (H_3^+ and H^-) the same arguments holds: the dissociation degree increases (removal of H_2) and the ionisation degree decreases (ions are removed). Consequently, the low-temperature shoulder of the "sombrero" moves towards the axis. The influence of H_3^+ and H^- on the results of the simulations can be a part of future study.

5.5 Conclusions

In this chapter results of PLASIMO simulations for a hydrogen cascaded arc plasma at non-LTE conditions are presented. It is shown that the non-LTE simulations do not reproduce the results of the LTE simulations presented in [117]. Especially in the central plasma region thermal non-equilibrium is present, whereas in the outer plasma regions, near the channel wall, thermal equilibrium is reached. The pronounced "sombrero" profile as found in [117] is reduced to only a slight thermal constriction for the electrons, whereas for the heavy particles no "sombrero" profile is observed. There are several reasons for the differences between the results of the LTE and non-LTE simulations. Firstly, the most logical reason is that it is not allowed to use the LTE assumption, especially at the low pressures in the hydrogen CA. Secondly, the non-LTE model is far from complete because of several assumptions and restrictions. For example, assumptions were made on the rovibrational excitations and several forward reactions are not balanced by backward reactions. Further improvement of the non-LTE model is necessary to perform more accurate non-LTE simulations and to judge if the LTE assumption from [117] is allowed. If more processes are included, it is to be expected that the results of the numerical simulations will be closer to those found in the LTE simulations.

The major role of H_2^+ as an "intermediate" species in the hydrogen plasma is made clear. Although the number density of H_2^+ in a hydrogen plasma is very small compared to the number densities of the other species, neglecting the reactions involving H_2^+ (especially the charge transfer reaction), changes the profiles of the mass fractions of the species drastically, especially those of H and H_2.

The wall reaction coefficient γ_H, for the association of 2 H at the wall to H_2 has a large influence on the dissociation degree in the CA. Decreasing γ_H from 0.5 to 0.001 increases the dissociation degree from 46% to 80%. Consequently, due to the higher H density, also the H^+ density increases, although the effect is much smaller than for the dissociation degree. To find realistic values of the dissociation degree, an accurate knowledge of γ_H is required.

Chapter 6

Numerical Simulation of Transport Phenomena in a Deposition Chamber

G.M. Janssen, A.L.C. Leroux, J.A.M. van der Mullen and W.J. Goedheer[1]

Department of Applied Physics, Eindhoven University of Technology, P.O. Box 513, 5600 MB Eindhoven, The Netherlands

[1] FOM-Institute for Plasma Physics 'Rijnhuizen', P.O. Box 1207, 3430 BE Nieuwegein, The Netherlands

Abstract

The plasma simulation method PLASIMO is validated by the commercial code PHOENICS CVD, by simulating a non-reactive argon-silane gas mixture in a deposition chamber. The agreement of the results is very good, with the behaviour of the pressure at the inlet being computed more accurately by PLASIMO than by PHOENICS CVD. The more approximate description of thermal diffusion, used by PLASIMO, gives reasonable results when compared with the results of PHOENICS CVD.

Validation of PLASIMO by experimental data is performed by simulating an argon plasma in a deposition chamber. The comparison of simulation and experiment is rather good if the principle of an expansion angle of 45° is not applied, although more experimental points are needed to validate in detail the simulated temperature and velocity profiles.

6.1   Introduction

In modern society there is a growing interest in new materials, which increases the need for surface treatment and deposition techniques. Typical applications are the production of fibres

[9] and solar cells [7]. In both applications deposition processes play an important role. High-quality, well-defined and reproducible layer properties are required, while from an economical point of view, a high throughput and low costs are required.

There are several techniques to deposit material. On the one hand we have the plasma-less chemical deposition techniques like evaporation, beam sputtering and Chemical Vapour Deposition (CVD). From these techniques CVD is generally considered to be the most promising [148]. It is capable of producing uniform films with relatively high growth rates (typically $0.5 \, \text{nm s}^{-1}$) with good control of film structure and composition. Basically, molecules containing the atoms which have to be deposited are introduced as a gas into a deposition chamber containing the substrate on which deposition takes place. Chemical reactions in the gas-phase as well as surface reactions on the substrate occur, with film deposition as a result. The energy required to drive the chemical reactions is essentially thermal.

On the other hand we have the plasma techniques, one of them is Plasma Enhanced CVD (PECVD), which mostly uses RF-plasmas [6]. Another technique is that of remote plasma deposition in which the plasma created at one position is transported towards the substrate. In the group Equilibrium and Transport in Plasmas at Eindhoven University of Technology (EUT), a remote plasma deposition technique is used: the Expanding Thermal Plasma (ETP) process [7, 8, 149] in which a DC operated cascaded arc creates a high-flow (argon or argon/hydrogen) plasma of high ionisation degree (typically $5 - 10\%$) which expands supersonically into a deposition chamber at low pressure ($< 100 \, \text{Pa}$). In the chamber the gases (e.g. silane: SiH_4) are injected into the plasma via an injection ring. Due to a chain of elementary processes, mainly consisting of hydrogen abstraction and the combination of charge transfer and dissociative recombination, the plasma breaks down the molecular bonds in the gases. The plasma flow acts as a carrier, which transports the remaining products (radicals and ions) towards the substrate. In this way, an order of magnitude higher deposition rates (typically $10 \, \text{nm s}^{-1}$) can be reached compared to CVD [7].

To understand the deposition method better so that an optimisation of the deposition process can be effectuated, the need exists to study the influence on the deposition process of flow patterns (including recirculation vortices), gas-phase chemistry and wall reactions. For this purpose the method of numerical simulation was chosen, using two codes, namely the commercial code PHOENICS CVD (abbreviated as PHO_CVD in this study) and the code PLASIMO, developed at EUT. PHO_CVD is especially designed to numerically simulate CVD processes. It contains a huge database for the material properties of various gases used in CVD processes (like silane gas), such as the properties of the species, the reaction rates in gas-phase reactions, and an extensive description of surface reactions. Its features will be described briefly in section 6.2. The PLASIMO-code developed in Eindhoven [34] is originally developed for numerically simulating various plasma sources, and not for CVD processes, which means that complicated surface chemistry is not yet included. For its characteristics and details we refer to Janssen *et al.* [34]. One of the drawbacks of using PHO_CVD in modelling the ETP process is that it lacks the ability to deal with charged species. Therefore, describing a recombining plasma flow in a vacuum chamber (not necessarily used for deposition) can be handled better by PLASIMO, but this should be validated experimentally.

This work is basically divided in two studies: first, we will present a code-to-code validation

between PLASIMO and PHO_CVD using a simplified deposition chamber set-up with a non-reacting gas mixture consisting of neutral species. Secondly, a comparison is made of the results of numerical simulations using PLASIMO with experimental results, for a plasma flowing in the vacuum chamber. The main differences between the numerical simulations using PHO_CVD and PLASIMO for the chosen chamber set-up, which result from a different treatment of thermal diffusion, will be discussed in section 6.3.

The characteristics of the chamber configurations and gas compositions for the code-to-code validation and those for the plasma simulation are given in sections 6.4 and 6.5. The results for the two studies are presented in sections 6.6.1 and 6.6.2.

6.2   The PHO_CVD and PLASIMO codes

PHOENICS CVD (abbreviated in the following as PHO_CVD) is one of the commercially available numerical flow simulation methods [150]. Its main application is the numerical simulation of CVD processes. For this purpose a detailed description of chemical processes that lead to the deposition of thin films, as well as the transport of the gaseous reactants through the CVD-reactor are implemented in PHO_CVD. To describe the CVD process, PHO_CVD solves the set of hydrodynamic equations for transport of mass, momentum and energy, supplemented by an extensive description of gas-phase and surface chemistry. The application of PHO_CVD to different CVD processes at widely varying process conditions in different reactor geometries, together with a detailed description of the method is presented by Kleijn [151].

The characteristics of PLASIMO, developed at EUT, are already extensively described in [34], so we will not discuss them here and focus on the differences between PLASIMO and PHO_CVD. In short, both PLASIMO and PHO_CVD solve numerically the same set of transport equations with the same procedure to obtain the flow field: the SIMPLE algorithm of Patankar [46]. One of the main differences between PLASIMO and PHO_CVD is that PLASIMO is aimed at the numerical simulation of *plasmas*. Plasmas are gaseous mixtures which contain charged species in temperature non-equilibrium, i.e. electrons and heavy particle species may have different temperatures. As a consequence, also two energy equations have to be solved, one for the electrons and one for the heavy particles. In contrast, one of the main characteristics of PHO_CVD is the use of only neutral species, which all have the same temperature. Another major difference between the two methods is the sophisticated description of the energy dissipation in PLASIMO, necessary for the plasma sources that are considered (e.g. inductive plasmas like the ICP and QL-lamp, or direct current plasmas like the cascaded arc plasma). This is not necessary for the CVD process where the energy is thermal.

To be able to use both codes for the same problem, the flow of a non-reacting single-temperature gas mixture[a] consisting of argon (Ar) and silane (SiH_4) is considered. The main difference remaining between PLASIMO and PHO_CVD is the model for the thermal[b] mass

---

[a] In the use of the ETP for deposition purposes, chemical reactions between the species play a major role, but for a code-to-code validation these processes can be omitted.

[b] Thermal means here: *diffusion due to temperature gradients* in contrast to thermal equilibrium where thermal refers to an equi-temperature system.

diffusion as will be shown in section 6.3.

6.3   Thermal diffusion

To describe the relation between the diffusive mass fluxes $\vec{\mathbf{J}}_i$ of species i and the corresponding driving forces for ordinary (concentration) diffusion, pressure diffusion, forced diffusion and thermal diffusion the Stefan-Maxwell equations must be used [87][c]. Neglecting pressure diffusion and forced diffusion (as is done in PHO_CVD), the diffusive mass fluxes $\vec{\mathbf{J}}_i$ of species i can be separated in two parts as:

$$\vec{\mathbf{J}}_i = \vec{\mathbf{J}}_i^{\mathrm{conc}} + \vec{\mathbf{J}}_i^{\mathrm{td}} \tag{6.1}$$

with $\vec{\mathbf{J}}_i^{\mathrm{conc}}$ the diffusive mass flux driven by concentration gradients and $\vec{\mathbf{J}}_i^{\mathrm{td}}$ the diffusive mass flux driven by temperature gradients (the thermal diffusion term).

In thermal equilibrium (i.e. the temperatures of all species are equal) $\vec{\mathbf{J}}_i^{\mathrm{conc}}$ is given by:

$$\vec{\mathbf{J}}_i^{\mathrm{conc}} = -\rho D_i^{\mathrm{eff}} \vec{\nabla} y_i - \rho y_i D_i^{\mathrm{eff}} \frac{1}{M} \vec{\nabla} M + y_i D_i^{\mathrm{eff}} \sum_{j \neq i} \frac{M \vec{\mathbf{J}}_j^{\mathrm{conc}}}{M_j D_{ij}} \tag{6.2}$$

with ρ the mass density, $y_i = \rho_i/\rho$ the mass fraction of species i, where $\rho_i = m_i n_i$ with m_i the mass and n_i the number density of species i. The reciprocal-averaged reduced molar mass of the gas mixture is $M = (\sum_j y_j/M_j)^{-1}$ with M_j the molar mass of species j (in kg mol^{-1}). In thermal equilibrium the effective diffusion coefficient D_i^{eff} of species i reads:

$$\frac{1}{D_i^{\mathrm{eff}}} = \sum_{j \neq i} \frac{z_j}{D_{ij}} = \sum_{j \neq i} \frac{x_j}{D_{ij}} \tag{6.3}$$

The last step in this equation is justified since in thermal equilibrium the pressure fraction $z_i = p_i/p$ equals the mole fraction $x_j = y_j M/M_j$.

The binary diffusion coefficient D_{ij}, which is a function of pressure, temperature and mass, is given by Hirschfelder *et al.* [40] and is presented in the appendix for an Ar - SiH$_4$ gas mixture at 20 Pa:

$$D_{ij} = \frac{3}{16} \left(\frac{2\pi k_b^3 T^3}{m_{ij}} \right)^{1/2} \frac{1}{p\pi d_{ij}^2 \Omega_D \left(T^* \right)} \tag{6.4}$$

with k_b Boltzmann's constant, T the temperature, $m_{ij} = m_i m_j/(m_i + m_j)$ the reduced mass. The symbol Ω_D refers to the dimensionless collision integral which represents the deviation from the idealised rigid-sphere model. It depends on the normalised temperature $T^* = k_b T/\varepsilon_{ij}$ with $\varepsilon_{ij} = \left(\varepsilon_i \varepsilon_j \right)^{1/2}$. The binary collision diameter of the (i, j) system is $d_{ij} = \frac{1}{2}(d_i + d_j)$. The Lennard-Jones parameters for species i are ε_i (in J) and d_i (in m) [40], ε_i is the potential energy and d_i is the collision diameter of the species.

---

[c]A complete description of the Stefan-Maxwell equations for a multi-component multi-temperature ionised gas mixture is presented in chapter 3 of this thesis.

The expressions for the diffusive mass fluxes (equation (6.2)) and binary diffusion coefficients (equation (6.4)) implemented in PHO_CVD and PLASIMO are the same. In thermal equilibrium, the expression for the thermal diffusion term $\vec{J}_i^{\,\mathrm{td}}$ is different in PHO_CVD and PLASIMO. PHO_CVD uses for $\vec{J}_i^{\,\mathrm{td}}$ the approximate expression of Clark Jones [152], whereas PLASIMO uses an approximate formulation described extensively by Ramshaw [88], i.e.

$$\vec{J}_{i,\mathrm{PHO\_CVD}}^{\,\mathrm{td}} = -D_{i,\mathrm{PHO\_CVD}}^{T}\frac{1}{T}\vec{\nabla}T \tag{6.5}$$

$$D_{i,\mathrm{PHO\_CVD}}^{T} = \sum_{j\neq i}\rho y_i y_j D_{ij} a_{ij} \tag{6.6}$$

$$\vec{J}_{i,\mathrm{PLASIMO}}^{\,\mathrm{td}} = -D_{i,\mathrm{PLASIMO}}^{T}\frac{1}{T}\vec{\nabla}T \tag{6.7}$$

$$D_{i,\mathrm{PLASIMO}}^{T} = \frac{m_i}{k_b T}D_i^{\mathrm{eff}}\sum_{j\neq i}\left(\beta_{ij}-\beta_{ji}\right) \tag{6.8}$$

where the D_i^T's (in kg m^{-1} s^{-1}) are constrained by $\sum_i D_i^T = 0$. The thermal diffusion factor a_{ij} is an extremely complicated function of temperature, the binary mixture composition and the assumed intermolecular potential. It is a dimensionless number; if species i moves to the cold region than $a_{ij} > 0$, if species j moves to the cold region $a_{ij} < 0$, see Kleijn [151]. For a binary mixture the Clark-Jones approximation is exact. In the PLASIMO formulation of thermal diffusion, β_{ij} (in kg m^{-1} s^{-2}) is the thermal diffusion factor for neutral species pairs, given by Ramshaw [88]:

$$\beta_{ij} = -\frac{1}{2}\frac{p x_i x_j \tau_j k_b T m_{ij}}{m_j^2 D_{ij}} \tag{6.9}$$

It is illustrated in the appendix for an Ar - SiH$_4$ gas mixture at a pressure of 20 Pa. The mean time between collisions of a particle species i is τ_i:

$$\tau_i = \frac{1}{2}\left(\sum_j n_j \pi d_{ij}^2\left(\frac{2k_b T}{\pi m_{ij}}\right)^{1/2}\right)^{-1} \tag{6.10}$$

It can be shown, using the expression for β_{ij} (equation (6.9)), that for a binary system (which we will consider in this study) [88]:

$$D_{i,\mathrm{PLASIMO}}^{T} = \frac{\rho y_i y_j k_b T\left(\frac{m_i}{m_j}\tau_j - \frac{m_j}{m_i}\tau_i\right)}{2\left(m_i+m_j\right)} \tag{6.11}$$

This has to be compared to the PHO_CVD expression (which is exact for a binary mixture), equation (6.6). In the derivation of β_{ij} mean free path arguments were used, instead of the more correct Chapman-Enskog theory (see Hirschfelder *et al.* [40]). Therefore, the result will be inaccurate, although the behaviour seems correct, as was observed by Ramshaw. This will be confirmed in section 6.6.

Summarising, differences between results of PHO_CVD and PLASIMO will be expected mainly due to the influence of thermal diffusion. It is known from CVD processes that in cold-wall reactors thermal diffusion phenomena can be very important, especially in the wall region. Therefore the influence of thermal diffusion on the computations is investigated in section 6.6.

6.4 Configuration features

6.4.1 Assumptions

For the mathematical model of the flow underlying the PHO_CVD and PLASIMO methods, the mixture should be such that it can be considered as a continuum. A measure for the validity of the continuum assumption for the gas mixture in the chamber is the Knudsen number:

$$\text{Kn} = \frac{\xi}{L} \tag{6.12}$$

with ξ the mean free path of the molecules in the chamber and L a typical length scale of the smallest detail in the chamber that needs to be resolved in the numerical simulation. In this study the smallest detail in the vacuum chamber is the outlet opening, which is shown in figure 6.1. In general, a continuum approach is certainly valid for Kn < 0.01 [153]. If Kn approaches unity the flow enters the regime of transitional flow. Significant errors in the prediction of the transport coefficients in the continuum approach occur at Kn > 0.1 according to Coronell [154]. From kinetic theory ξ is estimated by [40]:

$$\xi = \frac{1}{\sqrt{2}} \frac{k_b T}{p \pi d^2} \tag{6.13}$$

with d again the collision diameter. Using equation (6.13) and assuming $d \approx 3 \times 10^{-10}$ m, $T = 500$ K, $p = 20$ Pa and $L = 10^{-2}$ m, equation (6.12) gives Kn < 0.1. So even at these low pressures it is allowed to use the continuum approach, although we are close to the limit of the validity criterion.

   The gas flow in the deposition chamber is assumed to be axi-symmetric, steady and laminar. This latter assumption is related to the value of the Reynolds number, defined as:

$$Re = \frac{\rho u L}{\mu} \tag{6.14}$$

with L a characteristic length scale for the gradients in the geometry, usually the reactor scale, u the velocity and μ the dynamic viscosity. For the flow in the chamber, i.e. a free jet flow, Re has to be smaller than 1.5×10^3 in order to have laminar flow [155]. For the subsonic flow region of the chamber, where $u \leq 1000$ m s^{-1}, $L = 10^{-2}$ m, $\rho \leq 2 \times 10^{-4}$ kg m^{-3} and $\mu \leq 4 \times 10^{-5}$ kg m^{-1} s^{-1}, equation (6.14) gives $Re \approx 50$ so that the laminar flow assumption is valid.

   In principle, the vacuum chamber is not axi-symmetric, due to the location of the pump (see figure 6.1). However, the computational domain is taken to be axi-symmetric, with the pump replaced by a pumping ring, see figure 6.1. This is a perfectly valid assumption for the goals of this study.
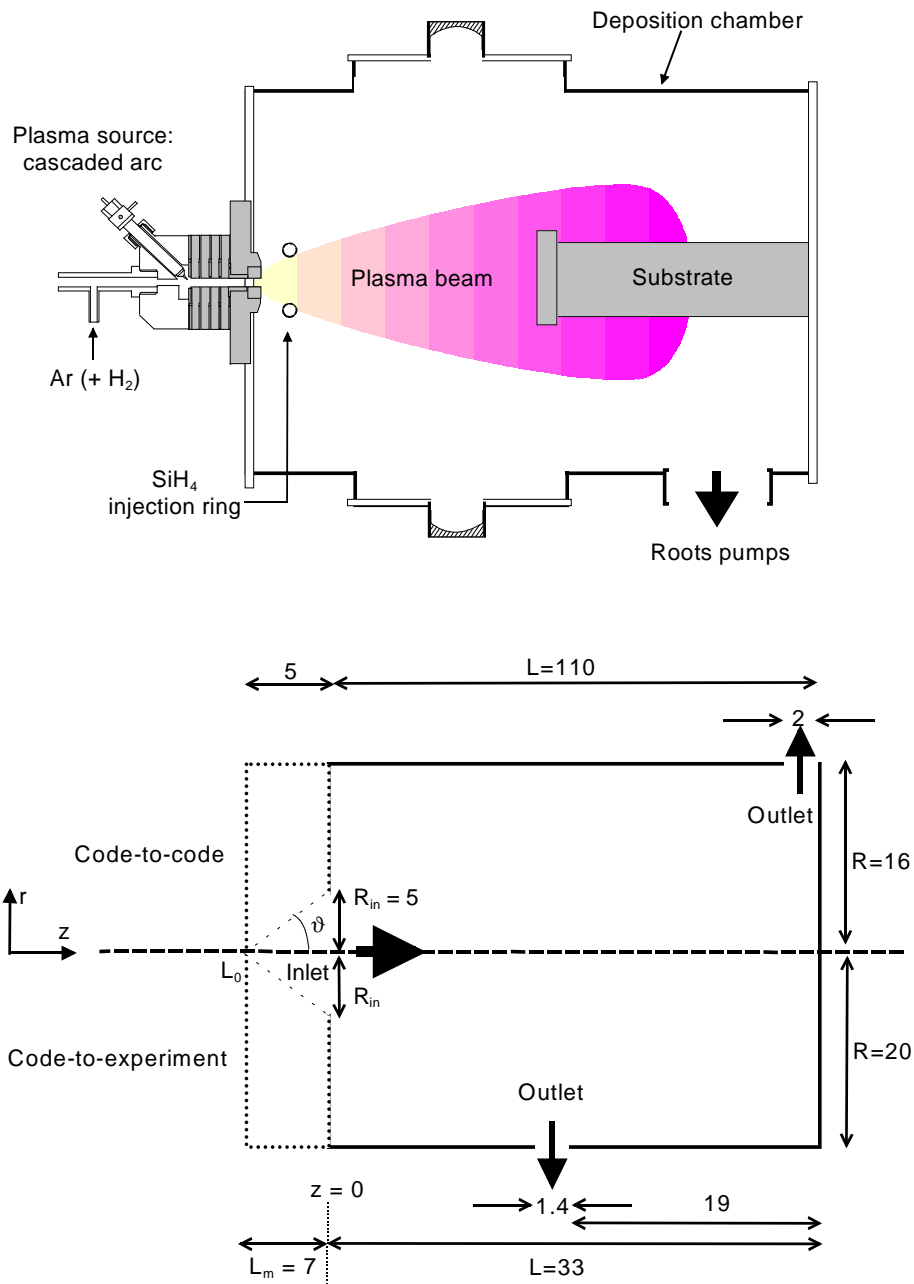
Figure 6.1: The vacuum chamber used for comparing results of PLASIMO and PHO_CVD with experimental results. Top: actual configuration; bottom: computational domain. The part above the symmetry axis represents the chamber set-up for the code-to-code validation; the part below the symmetry axis represents the chamber for the plasma simulation (code-to-experiment validation). In both cases the simulation domain is at the west side bound by the dotted / solid line. Note that the axial scale of the upper and lower chamber are not the same. Dimensions are given in cm.

6.4.2   Computational domain

We will only consider the subsonic flow region of the deposition chamber shown in figure 6.1. The gas mixture expands supersonically from the cascaded arc into the vacuum chamber with an expansion angle ϑ of approximately 45°. A normal shock is formed (which position depends on the ratio of stagnation pressure in the arc and the background pressure in the chamber, see later) and downstream of the shock the gas mixture flows with subsonic speed into the vacuum chamber. The gas mixture will diffuse towards the walls of the chamber, while moving further downstream. To remain close to the experimental conditions, the dimensions of the subsonic flow region have to be estimated. For this purpose, the position of the shock is calculated from the empirical relation obtained by Ashkenas *et al.* [156] for the position of a stationary shock front after the supersonic expansion of a free jet:

$$\frac{L_m}{D} = 0.67 \left(\frac{p_{\text{stag}}}{p_{\text{back}}} \right)^{1/2} \tag{6.15}$$

in which L_m is the distance of the Mach disk to the position L_0 of the virtual source from which the streamlines in the vacuum chamber appear to originate. We assume that L_0 is located at the outlet of the cascaded arc, see figure 6.1. The constant 0.67 in equation (6.15) is only weakly dependent on the gas mixture used, according to Young [157]. The stagnation pressure in the arc is p_{stag}, while p_{back} is the background pressure in the chamber and D is the diameter of the outlet opening of the cascaded arc. For the present chamber configurations, $D = 4$ mm, $p_{\text{back}} = 20$ Pa (code-to-code validation) or $p_{\text{back}} = 10$ Pa (plasma simulation) and $p_{\text{stag}} \approx 7 \times 10^3$ Pa, we get $L_m \approx 50$ mm and $L_m \approx 70$ mm, respectively. This means that the axial extension of the computational domain is equal to the chamber length minus $L_m = 50$ mm (code-to-code validation) or $L_m = 70$ (plasma simulation). The "inlet" of the simulation region is given by an aperture of radius R_{in}. For the code-to-code validation, $R_{\text{in}} = 50$ mm, exactly matching the 45° expansion angle. For the plasma simulation R_{in} is chosen such, that the experimental conditions are matched, see section 6.6.

In the lower part of figure 6.1 the computational domains for the code-to-code validation and the code-to-experiment validation are shown: code-to-code validation above the symmetry axis, code-to-experiment validation, i.e. a plasma simulation, below the symmetry axis. Both computational domains are axi-symmetric. The dimensions of the domains are given in the figure. The boundaries of the subsonic flow region are depicted with a continuous line. The two computational domains are different from each other, because for the plasma simulation, experimental results were available for a different chamber set-up with different dimensions and different location of the pump (see figure 6.1). In both cases, a non-uniform grid of 55 (axial) $\times 32$ (radial) grid points is used, with grid refinement in the pumping region. However, it did not seem possible to use exactly the same grids in PHO_CVD and PLASIMO, so for a comparison the PLASIMO results are interpolated to match the PHO_CVD grid locations exactly.

6.4.3 Boundary conditions

The boundary conditions applied in PLASIMO for both the argon-silane gas mixture and the argon plasma in the vacuum chamber are the same and are listed in table 6.1. The boundary conditions used in PHO_CVD are slightly different as will be explained at the end of this section. Also listed in table 6.1 are the fixed parameters at inlet, pump and wall locations.

Table 6.1: PLASIMO Boundary conditions applied to argon-silane gas mixture (for code-to-code validation) and argon plasma simulations (for code-to-experiment validation) in the deposition chamber. Note that T_e is only used for the plasma simulations, for which $T \equiv T_h$.

Par.	Inlet	Outlet	Axis	walls
p	$\frac{\partial p}{\partial z} = C$	$\frac{\partial p}{\partial r} = C$	$\frac{\partial p}{\partial r} = 0$	$\frac{\partial p}{\partial n} = 0$
u_z	$u_z = u_{\mathrm{in}}^{\mathrm{max}} \left[1 - \left(\frac{r}{R_{\mathrm{in}}} \right)^2 \right]$	$u_z = 0$	$\frac{\partial u_z}{\partial r} = 0$	$u_z = 0$
u_r	$u_r = 0$	$u_r = u_{\mathrm{pump}}$	$u_r = 0$	$u_r = 0$
T	$T = T_{\mathrm{in}}$	$T = T_{\mathrm{pump}}$	$\frac{\partial T}{\partial r} = 0$	$T = T_{\mathrm{wall}}$
T_e	$T_e = T_{\mathrm{in}}$	$\frac{\partial T_e}{\partial r} = 0$	$\frac{\partial T_e}{\partial r} = 0$	$\vec{n} \cdot \vec{\nabla} T_e = 0$
y_i	$y_i = \frac{M_i \varphi_i}{\sum_j M_j \varphi_j}$ $\vec{n} \cdot \vec{J}_i = 0$	$\frac{\partial y_i}{\partial r} = 0$	$\frac{\partial y_i}{\partial r} = 0$	$\vec{n} \cdot \left(\rho y_i \vec{u} + \vec{J}_i \right) = 0$

Par.	Code-to-code validation	Code-to-experiment validation
φ_{Ar}	50 scc s^{-1}	16.67 scc s^{-1}
$\varphi_{\mathrm{SiH_4}}$	10 scc s^{-1}	
R_{in}	5.0 cm	$1.5 - 2.5$ cm
L_{pump}	2.0 cm	1.4 cm
T_{in}	3000 K	$4500 - 5500$ K
T_{wall}	500 K	300 K
T_{pump}	400 K	300 K
u_{pump}	17.5 m s^{-1}	9.62 m s^{-1}

As can be seen in table 6.1 we assume that the velocity profile at the inlet has a simple parabolic shape. The maximum inlet velocity at the axis (r = 0) $u_{\mathrm{in}}^{\mathrm{max}}$ is dictated by the mass flow

Φ_{in} (in kg s^{-1}) and mass density ρ_{in} (in kg m^{-3}) at the inlet:

$$\Phi_{\text{in}} \;=\; 2\pi u_{\text{in}}^{\max} \int_0^{R_{\text{in}}} \rho_{\text{in}} \left[1 - \left(\frac{r}{R_{\text{in}}} \right)^2 \right] r \, dr \tag{6.16}$$

$$=\; 10^{-6} \frac{p_{\text{st}}}{R_g T_{\text{st}}} \sum_i M_i \varphi_i \qquad (\text{kg s}^{-1}) \tag{6.17}$$

with r the local radial position and R_{in} the radius of the inlet opening in the computational domain; p_{st} and T_{st} are the pressure and temperature at standard conditions: 1 atm and 273.15 K. The inlet flow φ_i is given in scc s^{-1} and R_g is the universal gas constant (in J mol^{-1} K^{-1}). The inlet mass flow of each species i, given by $\Phi_{i,\text{in}} = 2\pi \int_0^{R_{\text{in}}} \vec{\mathbf{n}} \cdot (\rho y_i \vec{\mathbf{u}} + \vec{\mathbf{J}}_i) r \, dr$, must correspond to φ_i. This is done by setting the boundary condition for y_i and the additional constraint on $\vec{\mathbf{J}}_i$ as listed in table 6.1. At the non-reacting walls a no-slip boundary condition is imposed. The dimensions of the stainless steel deposition chamber are such that (water) cooling of the walls is not necessary. Therefore an isothermal boundary condition is imposed on the temperature. Since the walls are assumed to be non-reacting, the mass flux vector normal to the walls (with $\vec{\mathbf{n}}$ the normal vector) is zero for all species. From this condition and equations (6.1) to (6.8) an expression for $\vec{\nabla} y_i$ is found.

The deposition chamber is pumped by a system of roots blowers with a maximum capacity of $\dot{V}_{\max} = 1200$ m^3 hr^{-1} (code-to-code validation) and $\dot{V}_{\max} = 1000$ m^3 hr^{-1} (code-to-experiment validation). The pumping capacity used in the simulations is adjusted to achieve the required experimental background pressure in the chamber: $p_{\text{back}} = 20$ Pa for the code-to-code validation and $p_{\text{back}} = 10$ Pa for the code-to-experiment validation. From the known outlet pressure, outlet temperature and inlet mass flow the actual pumping capacity $\dot{V}$ is calculated. The velocity at the outlet, u_{pump}, is then calculated from $\dot{V}$ and the area of the outlet. This leads to the outlet velocities listed in table 6.1. In practice the outlet (i.e. the pump) is located at one fixed azimuthal position. However, since one of the restrictions of PLASIMO is axi-symmetry of the configuration (this is not a restriction of PHO_CVD), the outlet in the computational domain is in fact a ring, but with the same area as the outlet in the experiments. The width of the ring, L_{pump}, is calculated from $A_{\text{pump}} = 2\pi R_{\text{chamb}} L_{\text{pump}}$, with A_{pump} the known area of the outlet opening in the chamber. Note that the gradient of the pressure at the inlet and the outlet is assumed to be constant, which value is determined during the iteration process. Finally, in the direction perpendicular to the outflow opening zero gradients for the mass fractions of all species are imposed.

PHO_CVD can not use exactly the same set of boundary conditions, since only standard boundary conditions are allowed (a Dirichlet value or a Neuman condition: a zero derivative). For example, a constant first derivative for the pressure and a quadratic profile for the inlet velocity are not possible. Therefore, the velocity at the inlet in PHO_CVD must be taken uniform, whereas the pressure at the inlet is given (21.4 Pa). At the outlet a zero derivative for p is specified.

6.5 Composition features

6.5.1 Code-to-code validation

A non-reacting gas mixture consisting of the neutral species Ar (argon) and SiH_4 (silane) is used. Because of the "black box" character of some parts of PHO_CVD, it was chosen to use in PLASIMO the same formulations for the transport coefficients as are used in PHO_CVD (valid for neutral species with all the same temperature). In this formulation, the viscosity μ and thermal conductivity λ are given by [158]:

$$\mu = \sum_i \frac{x_i \mu_i}{\sum_j x_j \phi_{ij}^\mu} \tag{6.18}$$

$$\phi_{ij}^\mu = \left[8 \left(1 + \frac{M_i}{M_j} \right) \right]^{-1/2} \left[1 + \left(\frac{\mu_i}{\mu_j} \right)^{1/2} \left(\frac{M_j}{M_i} \right)^{1/4} \right]^2$$

$$\mu_i = \frac{5}{16} \frac{(\pi m_i k_b T)^{1/2}}{\pi d^2 \Omega_\mu(T^*)}$$

$$\lambda = \sum_i \frac{x_i \lambda_i}{\sum_j x_j \phi_{ij}^\lambda} \tag{6.19}$$

$$\phi_{ij}^\lambda = \left[8 \left(1 + \frac{M_i}{M_j} \right) \right]^{-1/2} \left[1 + \left(\frac{\lambda_i}{\lambda_j} \right)^{1/2} \left(\frac{M_j}{M_i} \right)^{1/4} \right]^2$$

$$\lambda_i = \left[2.5 \left(\frac{1.5 k_b}{m_i} \right) + 1.32 \left(\frac{c_{v,i} - 1.5 k_b}{m_i} \right) \right] \mu_i$$

with $c_{v,i}$ the specific heat coefficient at constant volume of species i. The dimensionless collision integral Ω_μ is given by [158]:

$$\Omega_\mu (T^*) = \frac{A_\mu}{T^{*B_\mu}} + \frac{C_\mu}{\exp[D_\mu T^*]} + \frac{E_\mu}{\exp[F_\mu T^*]} \tag{6.20}$$

with $A_\mu = 1.16145$, $B_\mu = 0.14874$, $C_\mu = 0.52487$, $D_\mu = 0.77320$, $E_\mu = 2.16178$ and $F_\mu = 2.43787$. The normalised temperature is denoted by $T^* = k_b T / \varepsilon_{ij}$. The dimensionless collision integral Ω_D used in the expression for the binary diffusion coefficient (equation (6.4)) is given by [158]:

$$\Omega_D (T^*) = \frac{A_D}{T^{*B_D}} + \frac{C_D}{\exp[D_D T^*]} + \frac{E_D}{\exp[F_D T^*]} + \frac{G_D}{\exp[H_D T^*]} \tag{6.21}$$

with $A_D = 1.06036$, $B_D = 0.15610$, $C_D = 0.19300$, $D_D = 0.47635$, $E_D = 1.03587$, $F_D = 1.52996$, $G_D = 1.7644$ and $H_D = 3.89411$.

The Lennard-Jones parameters for the argon-silane mixture used in the simulations follow from Svehla [159] and are given in table 6.2.

Since the species in the gas mixture do not react, the source terms in the particle balances (see [34]) are zero. Combined with the fact that no energy is dissipated into the system and radiation losses are neglected, also the source terms in the total energy balance (also given in [34]) are zero; viscous heating and heat conduction are taken into account.

Table 6.2: Lennard-Jones parameters for the argon-silane mixture. Data from Svehla [159].

Species	σ_i (Å)	ε_i/k_b (K)
Ar	3.542	93.3
SiH$_4$	4.084	207.6

6.5.2   Code-to-experiment validation

For the recombining argon plasma the heavy particle transport coefficients are calculated using the mixture rules of Mitchner and Kruger [41]. The electron transport coefficients are calculated using Frost mixture rules [57]. In the subsonic region of an argon plasma in a vacuum chamber, ionisation processes can be neglected due to the low electron temperature and density. The two most important processes will be three-particle recombination and radiative recombination [160, 161]:

$$Ar^+ + e + e \overset{K_{rec,3}}{\rightarrow} Ar + e \tag{6.22}$$

$$Ar^+ + e \overset{K_{rec,2}}{\rightarrow} Ar + h\nu \tag{6.23}$$

where the argon atom Ar can be excited. Three-particle recombination heats the electron gas, because the remaining electron gains a part of the ionisation energy (in the de-excitation flow to the argon ground state). In the radiative recombination reaction (6.23) one electron is lost with the average electron energy of $\frac{3}{2}kT_e$. The main loss mechanism for electrons and ions is diffusion to the walls of the chamber. The mass balance source term S_{Ar+} and electron energy source term Q_e originating from reactions (6.22) and (6.23) are as follows:

$$S_{Ar+} = -m_{Ar+}\left(K_{rec,3}n_e^2 n_{Ar+} + K_{rec,2}n_e n_{Ar+}\right) \tag{6.24}$$

$$Q_e = +n_e^2 n_{Ar+}K_{rec,3}\Delta E_{rec,3} - n_e n_{Ar+}K_{rec,2}\frac{3}{2}k_b T_e \tag{6.25}$$

where it was assumed that the plasma is optically thin (escape factor equals 1) except for the resonance radiation for which it is assumed that the plasma is completely optically thick, and that in the radiative recombination reaction a thermal electron is lost. The rate constant for three-particle recombination $K_{rec,3}$ is taken from Van der Mullen [68], the energy gain of the electrons equals approximately the ionisation energy of the first excited state of argon, the metastable state Ar^*: $\Delta E_{rec,3} \approx E_{2i} = 4.2$ eV. The contribution of free-free and free-bound radiation is conform the work of Benoy *et al.* [72][d].

---

[d]According to Capitelli *et al.* [162] the combination of a large concentration of metastable argon states together with low T_e values (below 3000 K) is ideal for an important contribution of super-elastic electronic collisions to the heating of the electron gas: $Ar^* + e \rightarrow Ar(1) + e$, with Ar(1) the argon atom in the ground state. Due to the super-elastic collisions, an extra electron energy source term would exist: $Q_{sup} = n_e n_{Ar^*}K_{sup}\Delta E_{sup}$. The energy gain of the electrons in this reaction is $\Delta E_{sup} = 11.55$ eV. The influence of this reaction is not discussed here.

6.6 Results and discussion

6.6.1 Code-to-code validation for a non-reacting Ar - SiH$_4$ gas mixture

The pressure and the flow field in the deposition chamber are shown in figures 6.2 - 6.3 (axial fields) and figures 6.4 - 6.6 (radial fields). The pressure distribution in the inlet region of the simulation domain is shown enlarged in figure 6.2. We see that PLASIMO and PHO_CVD give the same behaviour for the pressure, except near the inlet region. It seems that the fixed inlet pressure, used by PHO_CVD, gives a wrong behaviour at the inlet. The differences between the pressure from PLASIMO and PHO_CVD near the inlet region is also seen in the radial profile, for $z = 0.9$ cm. For higher z values the radial profiles of the pressure agree very well. The velocity profiles (axially as well as radially) obtained from PLASIMO and PHO_CVD agree well.

The axial and radial temperature profiles computed by PHO_CVD and PLASIMO are shown in figure 6.7. It is seen in the figure that the agreement between the PLASIMO and PHO_CVD axial and radial temperature profiles is very good.

The axial and radial profiles of the mass fractions of argon and silane are shown in figures 6.8 and 6.9. One can see in figures 6.8 and 6.9 that the heavier species (Ar) has a higher concentration in the cold regions near the chamber walls, whereas the lighter species (SiH$_4$) has higher (relative) concentrations in the hot centre. This behaviour found in both the PHO_CVD and PLASIMO results, is expected. We saw in section 6.3, that in general, large and heavy molecules accumulate in cold regions of the reactor ($\vec{J}^{\mathrm{td}}_{i,\mathrm{heavy}} \propto -\vec{\nabla}T$, see equation (6.5)), whereas the small and light molecules concentrate in the hot regions of the reactor ($\vec{J}^{\mathrm{td}}_{i,\mathrm{light}} \propto +\vec{\nabla}T$). Note also that, due to a limited accuracy of the output data, the mass fractions from PHO_CVD show discrete profiles instead of a smooth profile.

From the results of the numerical simulations, it can be found that the Mach number at the inlet is below 0.89. Comparing the PHO_CVD profiles with those of PLASIMO shows that the results agree very good. This is true even for the spatial distribution of the mass fractions for which we expected some differences due to the different formulations used by PHO_CVD and PLASIMO for the thermal diffusion. Concluding, both codes give results within a bandwidth of a few percent. However, this does not mean that the numerical simulations give the results that are actually observed. Therefore results of a numerical simulation with an argon plasma, performed with PLASIMO, will be compared with experimental results next.

6.6.2 Code-to-experiment validation for a recombining argon plasma

The results of the numerical simulation of an argon plasma in the chamber set-up, discussed in section 6.4, are compared with experimental results of Brussaard [163] (also shown in the next figures)[e]. Unfortunately, both T_{in} and R_{in} were not experimentally determined. Therefore, to

---

[e]In the experiments performed by Brussaard [163], the velocity and gas temperature were determined using resonant Laser Induced Fluorescence on the 4s-4p transition of Ar. Also the electron temperature was determined experimentally (using single cylindrical probe measurements), but because of the large uncertainty in these measurements ($\approx 40\%$) it does not make sense to compare measured and computed T_e.
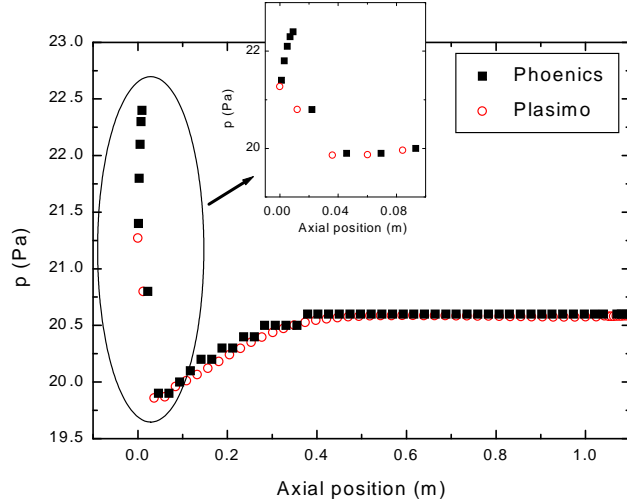
Figure 6.2: The pressure along the symmetry axis; PHO_CVD: solid squares; PLASIMO: open circles. The pressure in the inlet region is shown enlarged and reveals a spurious behaviour of the PHO_CVD results. This results from the fact that PHO_CVD does not allow $\frac{\partial p}{\partial z} = C$ as a boundary condition. Instead, $p = 21.4$ Pa was used.
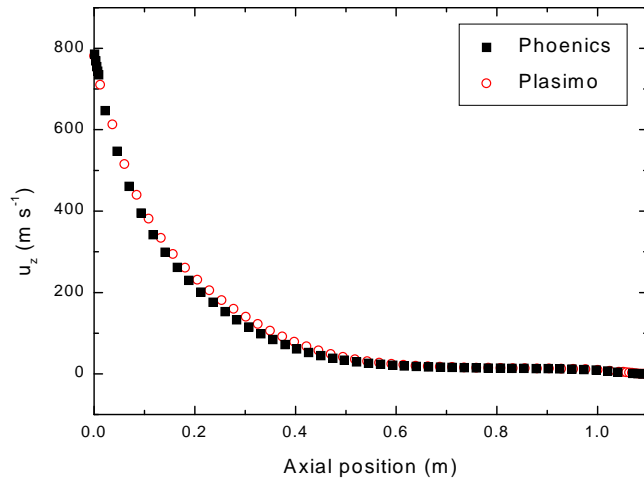

Figure 6.3: The axial velocity along the symmetry axis.

achieve a good agreement between results of simulations and experiments, the two parameters T_{in} (it is assumed that $T_{h,\text{in}} = T_{e,\text{in}}$) and R_{in} are varied in the simulations. Note that varying the inlet radius is allowed since the expansion angle can be different from 45° due to a different
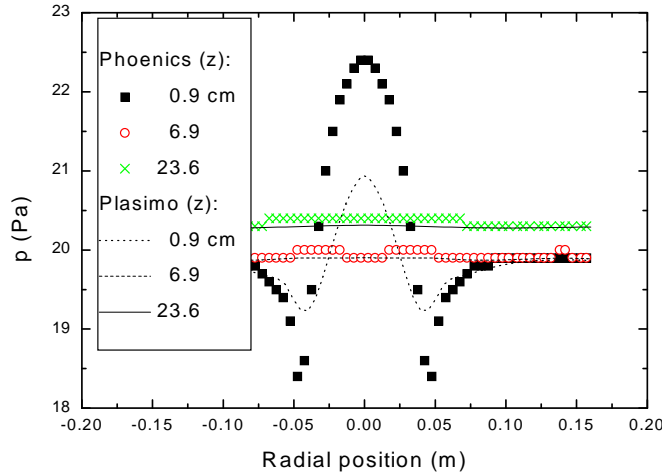
Figure 6.4: The radial profile of the pressure at three axial positions (z).
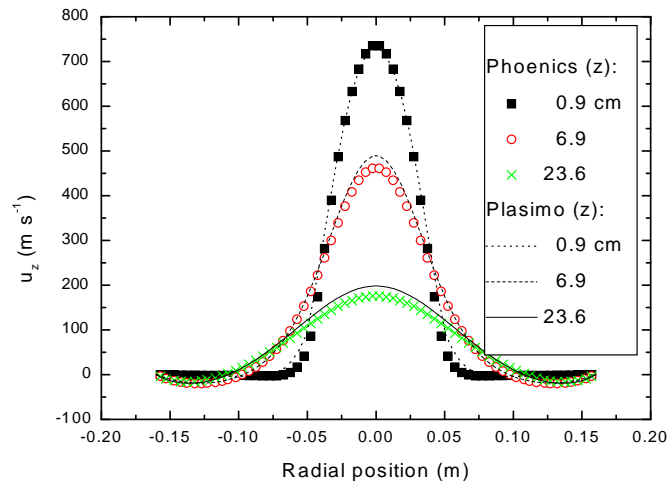

Figure 6.5: The radial profile of the axial velocity component at three axial positions (z).

shaped nozzle in the cascaded arc while also, at the end of the shock, the Mach disk contracts to a smaller diameter than predicted by the expansion angle of 45°. An inlet radius of $1.5 - 2$ cm is compatible with $M \approx 4$ before the shock, which is reasonable. The experimental and computed axial profiles of the axial velocity and the heavy particle temperature are shown in figure 6.10 and 6.11, respectively. As can be seen in figures 6.10 and 6.11 a higher inlet temperature (keeping R_{in} constant) lifts, apart from the temperature profile, also the velocity profile near the axis. The same
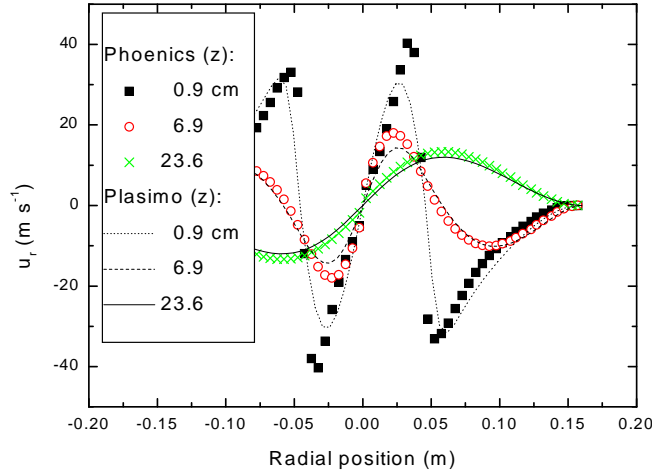
Figure 6.6: The radial profile of the radial velocity component at three axial positions (z).

effect (i.e. increasing velocity) is achieved by decreasing R_{in} (keeping T_{in} constant). However, the higher T_{in} or the lower R_{in}, the higher the Mach number M will be. For the simulation results shown in figures 6.10 - 6.11, the agreement between experiment and numerical simulation appear to be reasonably good, for $R_{in} = 1.5$ cm and $T_{in} = 5500$ K. However, this implies a value of $M_{in} = 1.5$ at the "virtual" inlet, which is too high since the computational domain starts downstream of the shock, where M must be smaller than one. Only for the numerical simulation with $R_{in} = 2.5$ cm and $T_{in} = 4500$ K, $M \approx 1$ at the inlet of the computational domain. All the other numerical simulations give $M \approx 1.5 - 2$. One of the problems encountered in the simulations that may be related to the Mach number, is the "virtual" wall at the west side of the computational domain. In reality, there is no wall at that location and therefore the recirculation vortices in the flow field would be not fully located in the computational domain. Also the boundary condition for the temperature at the "virtual" wall, $T = T_{wall}$, is not realistic.

Another point of attention is the three-particle recombination rate $K_{rec,3}$. Different authors [68, 161, 164] found that the experimental values for $K_{rec,3}$ are higher than the rate from Thomson [68]. A factor of two difference is no exception. However, since the three-particle recombination is not very effective in the subsonic region of the expansion, increasing $K_{rec,3}$ will barely increase the electron and heavy particle temperatures.

The radial profiles of u_z and T_h are shown in figure 6.12.

Although the agreement between the computation and the experiment is rather good, more experimental points closer to the inlet of the chamber are needed to validate the computed decrease in temperature and velocity in the region downstream of the shock. Also in radial direction more experimental points are necessary.
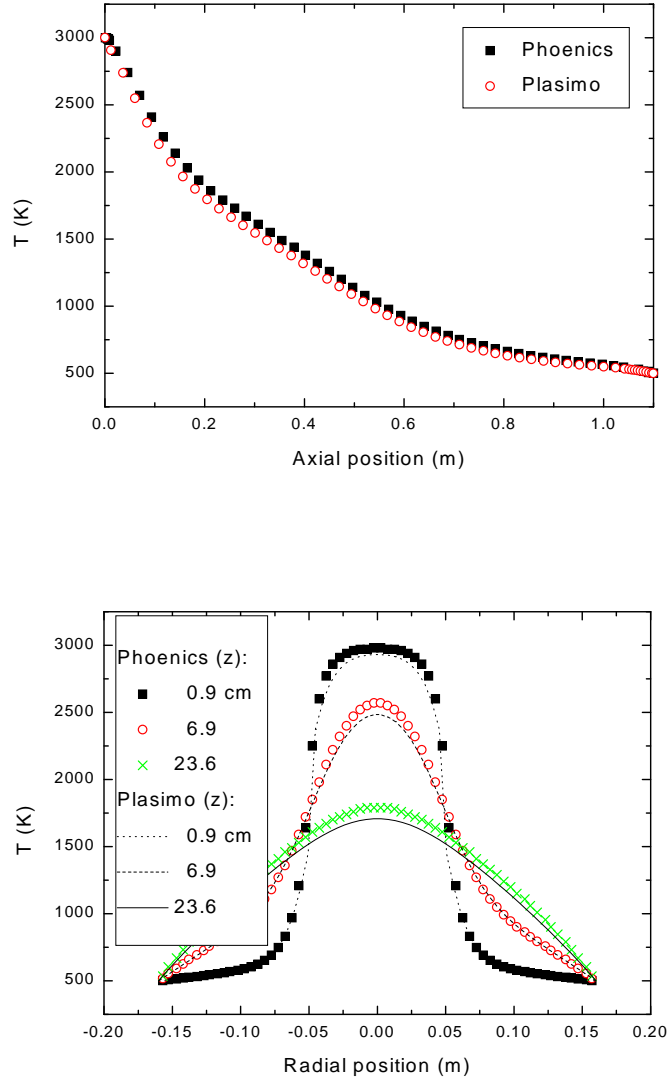
Figure 6.7: The temperature distribution computed by PHO_CVD and PLASIMO. Top: profile along the symmetry axis; bottom: radial profile at three axial positions.

6.7 Conclusions

The code-to-code validation of PLASIMO by the commercial tool PHO_CVD shows good agreement between the results for the test case chosen in this study: the flow of a non-reacting argon-silane gas mixture in the subsonic region of a deposition chamber. Also the influence of thermal diffusion on the results of the numerical simulation compares well, although the formulation of thermal diffusion in PHO_CVD and PLASIMO is quite different.
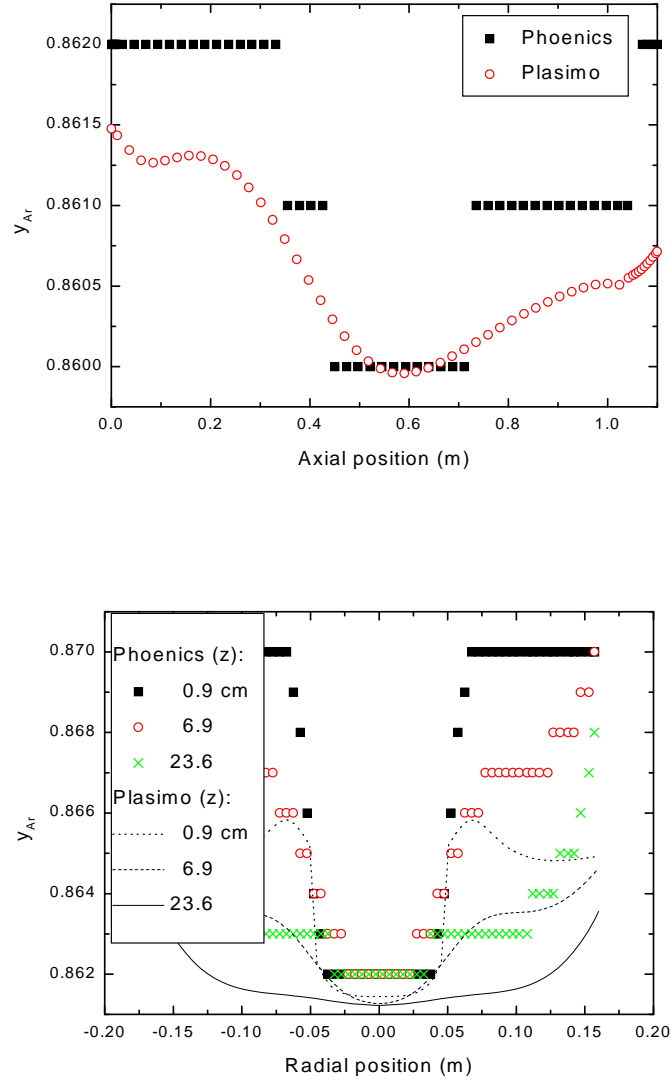
Figure 6.8: *The mass fraction y_{Ar} computed by PHO_CVD and PLASIMO. Top: profile along the symmetry axis; bottom: radial profiles at three axial positions. It can be seen that the concentration of the heaviest species Ar is higher in the cold region, i.e. close to the wall. Note that the plateaus in the PHO_CVD results originate from the limited accuracy with which the results are saved into files.*

The code-to-experiment validation shows a reasonable agreement, if the principle of an expansion angle of 45° is not applied. More experimental points, especially closer to the inlet opening of the chamber, are needed to confirm the accuracy of the computed profiles.
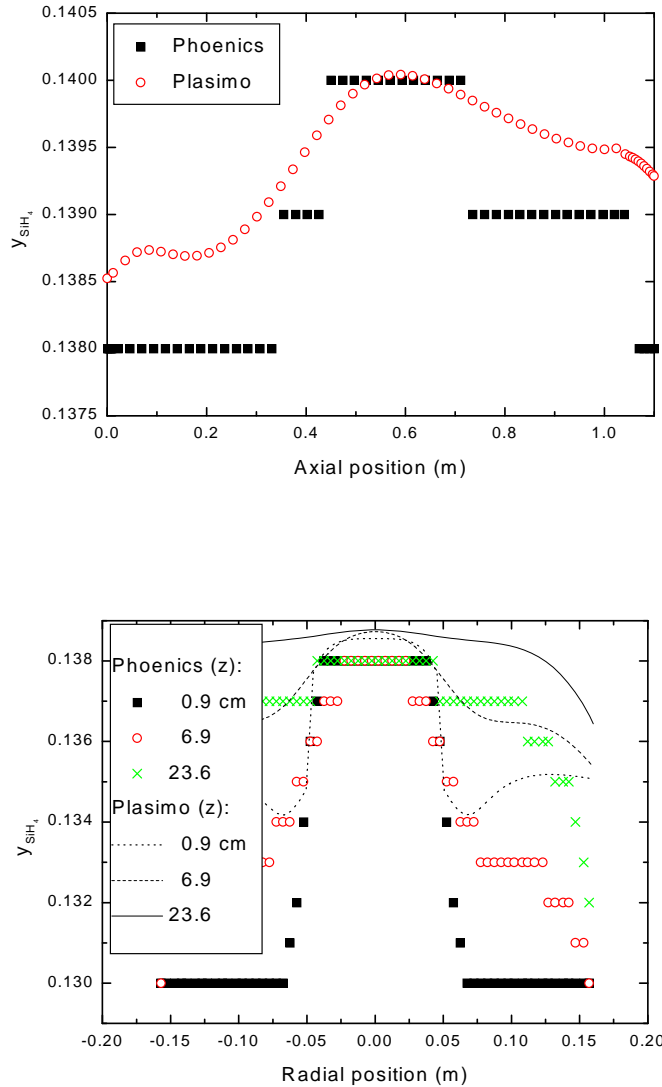
Figure 6.9: *The mass fraction* $y_{\mathrm{SiH_4}}$ *according to PHO_CVD and PLASIMO. Top: profile along the symmetry axis; bottom: radial profiles at three axial positions. Since SiH$_4$ is the lightest species in the Ar - SiH$_4$ gas mixture its relative concentration is larger in the hot central region.*

Acknowledgements
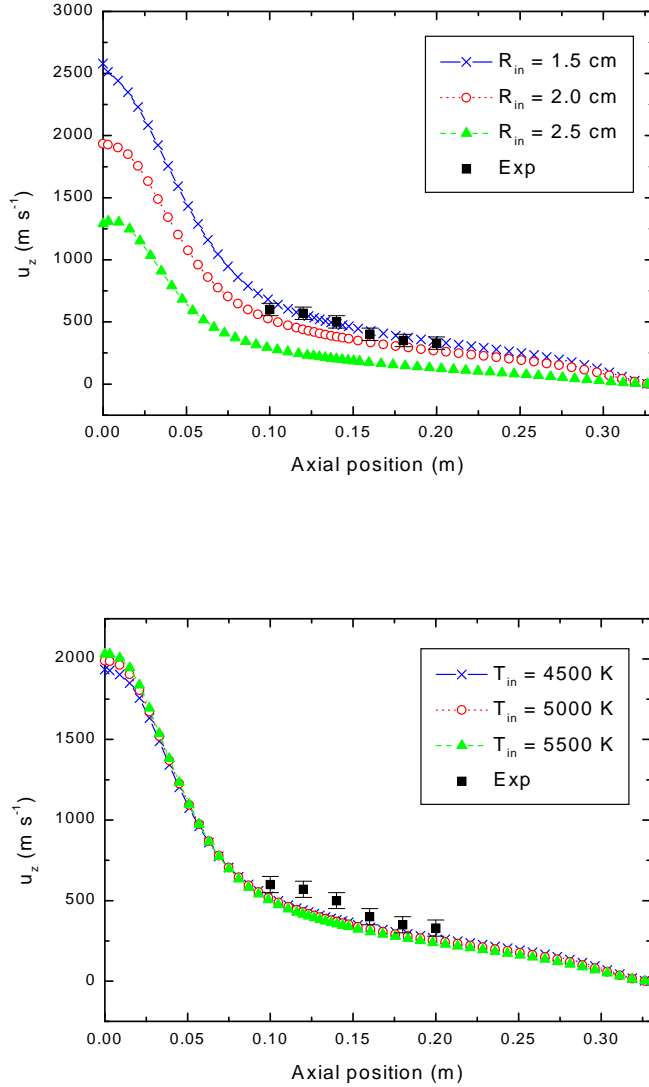
Figure 6.10: The computed axial profile of the axial velocity u_z in the code-to-experiment validation, as a function of inlet radius R_{in} (top, $T_{in} = 4500$ K) and inlet temperature T_{in} (bottom, $R_{in} = 2.0$ cm). Experimental results are from Brussaard [163].

'Nederlandse Organisatie voor Wetenschappelijk Onderzoek (NWO)'.
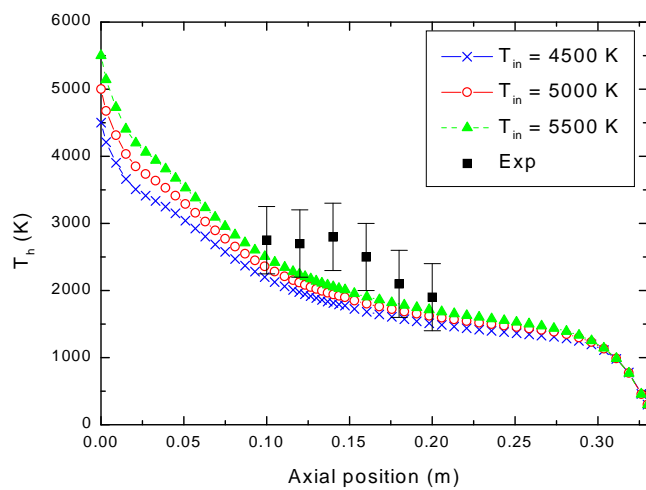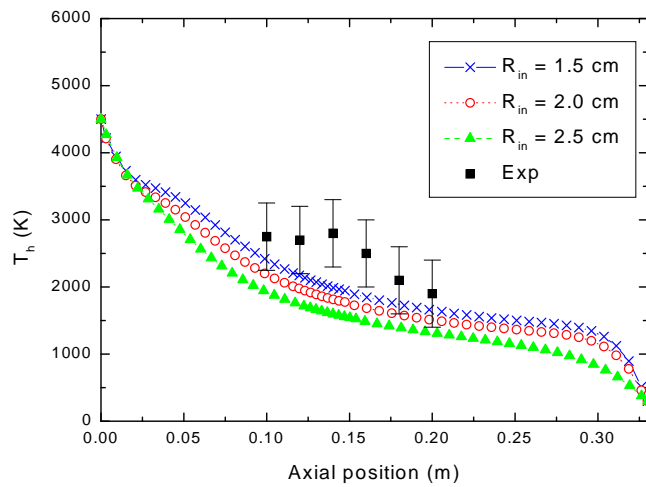
Figure 6.11: The computed axial profile of the heavy particle temperature T_h in the code-to-experiment validation, as a function of inlet radius R_{in} (top, $T_{in} = 4500$ K) and inlet temperature T_{in} (bottom, $R_{in} = 2.0$ cm). Experimental results are from Brussaard [163].
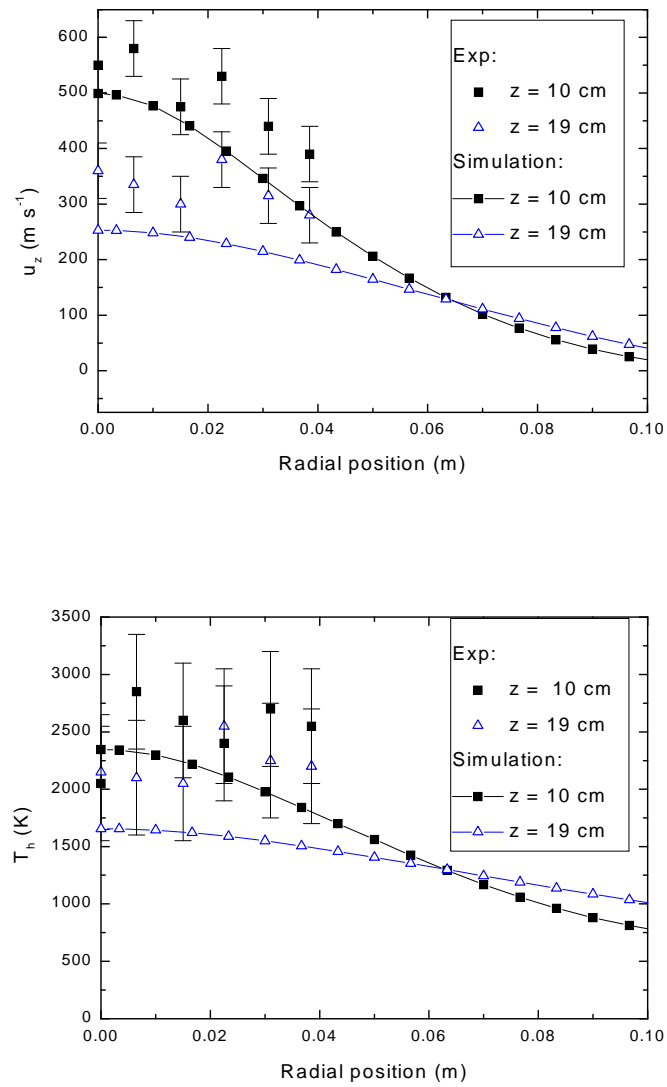
Figure 6.12: The simulated radial profiles of u_z and T_h at two axial positions. Experimental results are from Brussaard [163].

Appendix of chapter 6

The binary diffusion coefficient D_{ij} is given in equation (6.4). It has the property that $D_{ij} = D_{ji}$, and is shown in figure A.1 for an Ar - SiH$_4$ gas mixture at a pressure of 20 Pa.
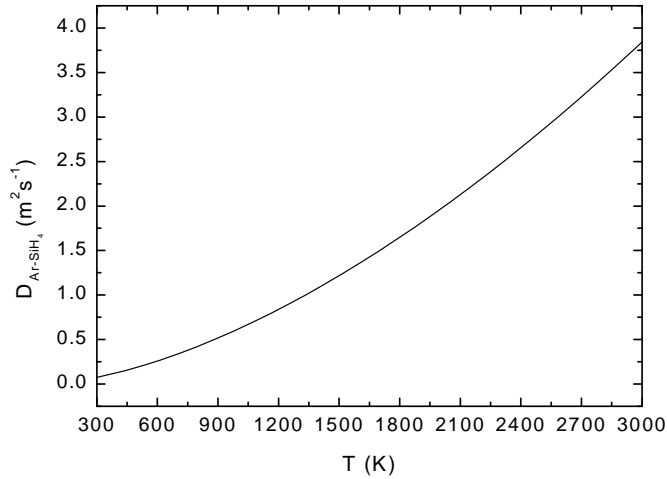
Figure A.1: Binary diffusion coefficient $D_{\mathrm{Ar-SiH_4}}$ (in m^2 s^{-1}) as a function of temperature T for an Ar - SiH$_4$ gas mixture at a pressure of 20 Pa ($D_{\mathrm{SiH_4-Ar}} = D_{\mathrm{Ar-SiH_4}}$).

The thermal diffusion factor β_{ij} as used in PLASIMO, is given in equation (6.9). Note that $\beta_{ij} \neq \beta_{ji}$, in contrast to the parameter used in PHO_CVD: $a_{ij} = a_{ji}$ (see Kleijn [151]). For the Ar - SiH$_4$ gas mixture, used for the comparison of the results of PLASIMO with the results of PHO_CVD, β_{ij} and β_{ji} are shown in figure A.2 for a pressure of 20 Pa.
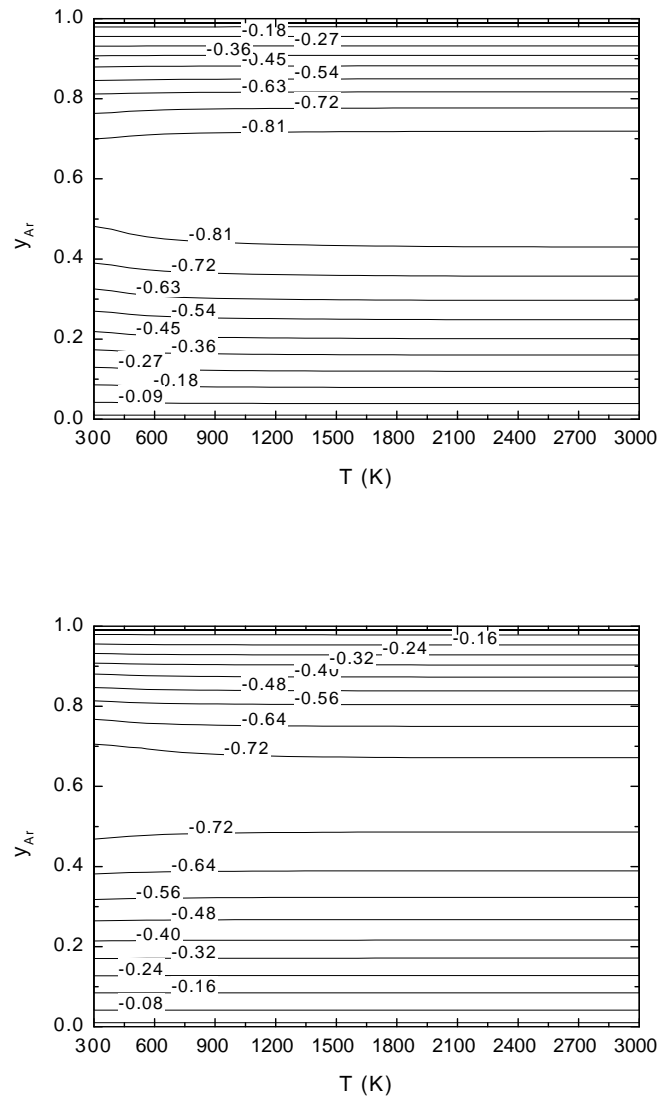
Figure A.2: Thermal diffusion factors β_{ij} (in kg m^{-1} s^{-2}) at a pressure of 20 Pa as a function of temperature T and argon mass fraction y_{Ar}: top: β_{Ar-SiH_4}; bottom: β_{SiH_4-Ar} (note that $\beta_{Ar-SiH_4} \neq \beta_{SiH_4-Ar}$).

Chapter 7

Numerical Simulation of Microwave Plasmas Used in Optical Fibre Production

G.M. Janssen[1]**, M.J.N. van Stralen**[2]**, J.A.M. van der Mullen**[1]
and A.H.E. Breuls[2]

[1] Department of Applied Physics, Eindhoven University of Technology, P.O. Box 513, 5600 MB
Eindhoven, The Netherlands
[2] Plasma Optical Fibre B.V., P.O. Box 1136, 5602 BC Eindhoven, The Netherlands

Abstract

The multi-component plasma simulation method PLASIMO will be used for numerically simulating the microwave plasma used in optical fibre production. For this purpose, a new microwave energy coupling module was developed and added to PLASIMO. As a first step towards a complete system, which must include the complex chemistry between O_2, $SiCl_4$ and $GeCl_4$, an argon microwave plasma is numerically simulated with PLASIMO. The results of the simulations are compared with experimental observations and have a good qualitative agreement. A quantitative validation will be performed in the future.

7.1   Introduction

Production of optical glass fibres for telecommunication consists mainly of two separate production steps:

- manufacturing a preform;
- drawing a glass fibre from this preform.

The interest of this study is in the manufacturing of a preform, and especially the plasma deposition process used in the manufacturing process. Since 1975, a powerful deposition method for manufacturing a preform has been developed [9, 165, 166]: the so-called Plasma-activated Chemical Vapour Deposition (PCVD) process[a], shown in figure 7.1. The substrate tube is mounted between a gas supply system and a pump. The gas mixture that is fed into the substrate tube consists of O_2, $SiCl_4$ and $GeCl_4$ and flows through the tube under relatively low pressure ($p \approx 10 - 20$ mbar). Using a moving resonator, which is mounted inside a furnace, microwave (MW) energy is coupled into the substrate tube. Consequently, a plasma of a reactive substance is created, resulting in deposition of (doped) glass[b] on the inner side of the substrate tube. The temperature of the substrate is kept constant during the deposition process at approximately 1500 K by using a furnace. After the PCVD process, by which the substrate tube is internally covered with a few thousand of deposited glass layers, the substrate tube will be subsequently collapsed into a preform rod. From this preform rod a glass fibre is drawn.

Advantages of the PCVD process over other well-known methods are found in the high deposition efficiency, precise control of the refractive index profile of the deposited layers (very thin layers of a few micron can be deposited), the lack of energy transfer through the wall of the substrate tube (i.e. the MW energy is coupled directly into the plasma region) and the high deposition rates ($\approx 4 \times 10^{-5}$ kg s^{-1}).
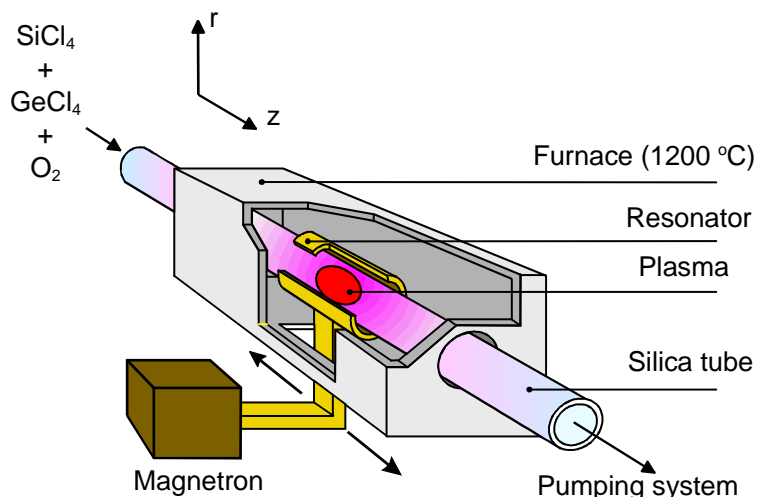
Figure 7.1: The PCVD set-up used for manufacturing preforms.

In brief, the *overall* chemical reactions that must take place in the plasma for the deposition to take place are:

$$O_2 + SiCl_4 \rightarrow SiO_2 + 2Cl_2$$

---
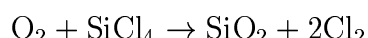
[a]The PCVD process for glass fibre deposition was introduced by Philips GmbH Forschungslaboratorium Aachen in Germany [165]. An overview of similar plasma deposition techniques for manufacturing fibre-preforms can be found in [167].

[b]The SiO_2 layer is eventually doped with GeO_2.

$$O_2 + GeCl_4 \rightarrow GeO_2 + 2Cl_2$$
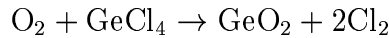
Experiments show that SiO_2 is not formed via volume reactions, but is formed via a wall reaction of SiO, formed in the volume reaction $O + SiCl_4 \rightarrow SiO + 2Cl_2$, with oxygen sticking at the wall [168].

For more details on the recent state of the art of the PCVD process for optical fibre production we refer to Van Bergen and Breuls [9].

As a part of the ongoing process of improving this deposition method, more insight is needed in the plasma physics. A powerful tool for increasing this insight is by means of computer simulations. In the 1980s the oxygen model of Rau and Trafford [169] was used for this purpose. They presented a simple model to calculate the electromagnetic fields in the resonator and electron number densities n_e and temperatures T_e in the plasma. The field strengths were calculated by solving the Maxwell equations. The gas flow profile, the mass balance for the electrons and the electron energy equation were not solved. Instead, the distributions of n_e and T_e were calculated using approximate relations assuming a constant pressure in the tube and neglecting the influence of the flow. For details of the model see [169].

For gaining more insight in the plasma physics, a more accurate and complete model is needed. Therefore it was chosen to use an already existing general plasma simulation tool, which solves all the relevant transport equations: PLASIMO [34]. It is a fluid model for multi-component plasmas, developed at Eindhoven University of Technology. The main assumptions underlying PLASIMO are that the flow is axi-symmetric, steady and laminar and that the plasma is assumed to be quasi-neutral. It is meant for simulating plasmas at LTE (i.e. Local Thermal Equilibrium)/non-LTE, from low to high pressures and for different energy coupling principles such as DC (cascaded arc) and induction (ICP, QL-lamp). For an extensive description of PLASIMO's capabilities as well as its limitations together with a description of the physical model, numerical method and iteration procedure we refer to [34], in which also as an argon cascaded arc plasma was simulated.

For simulating the PCVD plasma with PLASIMO, a novel microwave energy coupling module is developed and added. This will be described in section 7.2. The configuration characteristics are given in section 7.3. The argon composition characteristics are briefly summarised in section 7.4, since they were described in a previous paper [34]. As a first step towards a more complete simulation of the plasma deposition process, an argon plasma is considered because of the proven accuracy of the argon model in PLASIMO. This is presented in section 7.5. In chapter 8 of this thesis the results of a numerical simulation of a pure oxygen plasma are discussed.

7.2 Microwave energy coupling module

7.2.1 Computational domain

The experimental configuration is shown in figure 7.1. The part of the configuration considered is axi-symmetric, see figure 7.2. Here, we note that the electromagnetic fields will be calculated in the computational domain as a whole, whereas the hydrodynamic equations in PLASIMO are solved only in the plasma region.

The plasma region (with a radius R_{pl}) is surrounded by a glass substrate tube (outer radius R_{gl}, length L_1), an air gap (outer radius R_{air}) and a microwave resonator (length L_{res}). A slit (width b) is constructed in the microwave resonator, allowing high power microwave energy originating from a magnetron, to be coupled into the plasma region. The magnetron is operated at a frequency of about 2.46 GHz.
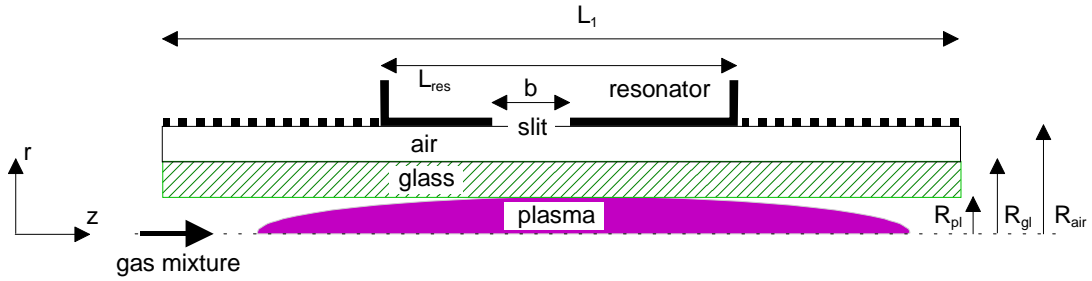
Figure 7.2: Geometry of the set-up: the plasma is surrounded by a substrate tube and resonator.

7.2.2   Formulation of the electromagnetic problem

The description of all electromagnetic problems are based upon two of Maxwell's equations. These equations in the space-time domain (x, y, z, t) read

$$\nabla \times \vec{E} + \frac{\partial \vec{B}}{\partial t} = \vec{0} \tag{7.1}$$

$$\nabla \times \vec{H} - \vec{J} - \frac{\partial \vec{D}}{\partial t} = \vec{0} \tag{7.2}$$

with $\vec{E}$ and $\vec{H}$ the electric and magnetic field strength, respectively; $\vec{D}$ and $\vec{B}$ are the electric and magnetic flux density, respectively; $\vec{J}$ is the current density.

In order to solve these equations, we need the constitutive relations. These relations describe the macroscopic properties of the media. The computational configuration considered contains glass, air and a plasma (argon) at low pressure. These media are assumed to be isotropic, linear, time-invariant, non-permeable, instantaneously reacting and locally responding. The corresponding constitutive relations are

$$\vec{J} = \sigma \vec{E} \tag{7.3}$$

$$\vec{D} = \varepsilon_0 \varepsilon_r \vec{E} \tag{7.4}$$

$$\vec{B} = \mu_0 \vec{H} \tag{7.5}$$

with $\varepsilon_0 = \mu_0^{-1} c_0^{-2}$ the permittivity in vacuum, ε_r the relative permittivity of the media, μ_0 the permeability in vacuum, σ the electric conductivity of the media and c_0 the speed of light in vacuum.

The electromagnetic formulation is based on a quasi-stationary analysis, which assumes that all field quantities depend harmonically on time with a common real angular frequency $\omega = 2\pi f$ (f is the corresponding frequency). Then every real quantity A is associated with the complex representation $\hat{A}$ through $A(x,y,z,t) = \Re[\hat{A}(x,y,z,\mathrm{j}\omega)\exp(\mathrm{j}\omega t)]$, with $\Re$ denoting the real part and $\mathrm{j} = \sqrt{-1}$. Substitution of the complex representations in the time-dependent Maxwell's equations (7.1) - (7.2), i.e. replacing the differentiation $\partial/\partial t$ by a multiplication by $\mathrm{j}\omega$, dividing by the common time factor $\exp(\mathrm{j}\omega t)$ and omitting the $\hat{}$ (except for $\hat{\varepsilon}_{\mathrm{r}}$), yields:

$$\nabla \times \vec{E} + \mathrm{j}\omega\mu_0\vec{H} = \vec{0} \tag{7.6}$$

$$\nabla \times \vec{H} - \mathrm{j}\omega\varepsilon_0\hat{\varepsilon}_{\mathrm{r}}\vec{E} = \vec{0} \tag{7.7}$$

The relative complex permittivity $\hat{\varepsilon}_{\mathrm{r}}$ is given by $\hat{\varepsilon}_{\mathrm{r}} = \varepsilon_{\mathrm{r}} + \sigma/(\mathrm{j}\omega\varepsilon_0)^c$. The relative complex permittivity of the natural quartz (glass) at 1500 K equals [169]:

$$\hat{\varepsilon}_{\mathrm{r,glass}} = 3.93 - \mathrm{j}0.22 \tag{7.8}$$

Substituting the complex electric conductivity (Lorentz expression) $\sigma = \varepsilon_0\omega_p^2/(\nu + \mathrm{j}\omega)$,[d] the relative complex permittivity of the plasma is found to be [170]:

$$\hat{\varepsilon}_{\mathrm{r,plasma}} = \varepsilon'_{\mathrm{r,plasma}} - \mathrm{j}\varepsilon''_{\mathrm{r,plasma}} \tag{7.9}$$

with

$$\varepsilon'_{\mathrm{r,plasma}} = 1 - \frac{\omega_{\mathrm{p}}^2}{\omega^2 + \nu^2} \tag{7.10}$$

$$\varepsilon''_{\mathrm{r,plasma}} = \frac{\nu}{\omega}\left(\frac{\omega_{\mathrm{p}}^2}{\omega^2 + \nu^2}\right) \tag{7.11}$$

The real part of the relative permittivity, $\varepsilon'_{\mathrm{r}}$, is the permittivity of the equivalent non-conducting or lossless plasma[e]. The imaginary part, $\varepsilon''_{\mathrm{r}}$, is a measure of the power lost to the plasma. We introduced the electron collision frequency ν and the plasma frequency ω_{p}. The latter is given by:

$$\omega_{\mathrm{p}} = \left(\frac{n_e e^2}{m_e \varepsilon_0}\right)^{1/2} \tag{7.12}$$

The electron collision frequency is given by [70]:

$$\nu = n_{\mathrm{Ar}}\langle K_{e-\mathrm{Ar}}\rangle + \frac{n_{\mathrm{Ar}^+}}{(2\pi m_e k_b^3 T_e^3)^{1/2}}\left(\frac{e^4}{6\pi\varepsilon_0^2}\right)\ln\Lambda \tag{7.13}$$

---

[c]The relation between $\hat{\varepsilon}_{\mathrm{r}}$ and the complex permittivity $\hat{\varepsilon}$ often used in the textbooks (e.g. Baden Fuller [170]) is: $\hat{\varepsilon} = \varepsilon_0\hat{\varepsilon}_{\mathrm{r}}$.

[d]Note that for low frequencies, $\omega \ll \nu$, and $\sigma \to \sigma_{\mathrm{DC}}$, with $\sigma_{\mathrm{DC}} = \varepsilon_0\omega_p^2/\nu = e^2 n_e/(m_e\nu)$, which is the same as presented in chapter 3.

[e]The term lossless refers to the case where the electrons are completely free to move, so that there is no energy transfer from the electrons to the heavy particles.

where m_e is the electron mass, e is the elementary charge, k_b is Boltzmann's constant, n_X is the number density of species X, with $X =$ Ar or Ar$^+$; $\langle K_{e-\mathrm{Ar}} \rangle$ is the rate coefficient for momentum transfer between electrons and argon atoms, averaged over a Maxwellian energy distribution and $\ln \Lambda$ is the Coulomb logarithm with ion screening included (see chapter 2).

For the axi-symmetric configuration and the axi-symmetric energy in-coupling considered, the field components E_ϕ, H_z and H_r vanish. The Maxwell equations (7.6) and (7.7) then simplify to

$$\frac{\partial E_r}{\partial z} - \frac{\partial E_z}{\partial r} + \mathrm{j}\omega\mu_0 H_\phi = 0 \tag{7.14}$$

$$\frac{\partial H_\phi}{\partial z} + \mathrm{j}\omega\varepsilon_0\hat{\varepsilon}_{\mathrm{r}} E_r = 0 \tag{7.15}$$

$$\frac{1}{r}\frac{\partial}{\partial r}\left(rH_\phi\right) - \mathrm{j}\omega\varepsilon_0\hat{\varepsilon}_{\mathrm{r}} E_z = 0 \tag{7.16}$$

Multiplying equations (7.15) and (7.16) with the characteristic impedance of vacuum, defined as $\zeta = (\mu_0/\varepsilon_0)^{1/2}$, normalising H_ϕ as $H_\phi' = \zeta H_\phi$ and introducing the wave number (propagation constant) in vacuum $k_0 = \omega/c_0$, we get:

$$\frac{\partial E_r}{\partial z} - \frac{\partial E_z}{\partial r} + \mathrm{j}k_0 H_\phi' = 0 \tag{7.17}$$

$$\frac{\partial H_\phi'}{\partial z} + \mathrm{j}k_0\hat{\varepsilon}_r E_r = 0 \tag{7.18}$$

$$-\frac{1}{r}\frac{\partial}{\partial r}\left(rH_\phi'\right) + \mathrm{j}k_0\hat{\varepsilon}_r E_z = 0 \tag{7.19}$$

From a microwave point of view, the interest is the scattering properties of the field incident on the plasma region. In particular, microwaves entering the plasma region through the slit will partly be reflected, partly be absorbed in the plasma and partly be transmitted to the environment. The MW field at the slit is described in the next section.

7.2.3   MW field at the slit

The microwaves are generated in a magnetron, transmitted through some microwave waveguide components and coupled into the configuration (the plasma plus glass plus air) via the slit. This slit is considered to be a short transmission line of cylindrical shape: a radial waveguide. The radial waveguide is only able to guide the transverse electromagnetic (TEM) mode. In principle, some of the higher order non-guiding modes have to be taken into account.

In order to focus on the plasma region itself, we decouple the plasma from the resonator by defining proper boundary conditions at the slit. This is a different approach than that of Rau and Trafford [169], who considered the plasma plus resonator. We will formulate the electromagnetic field at the slit as an infinite sum of local radial waveguide modes. Due to PLASIMO's restriction to axi-symmetrical configurations, only rotationally symmetric modes are considered, which means that only transverse electric (TE) and TM fields are present in the plasma region. We will confine ourselves to a discussion of the fundamental TEM mode.

From a spectral analysis, it can be shown (see Marcuvitz [171]) that the fundamental transverse TEM mode field is represented as:

$$E_z = -\frac{V(r)}{b} \tag{7.20}$$

$$H_\phi = \frac{I(r)}{2\pi r} \tag{7.21}$$

$$E_r = 0, \qquad E_\phi = 0 \tag{7.22}$$

$$H_r = 0, \qquad H_z = 0 \tag{7.23}$$

The mode amplitudes, voltage V and current I, obey the radial transmission line equations

$$\frac{\partial V}{\partial r} = -\mathrm{j}k_0 Z I \tag{7.24}$$

$$\frac{\partial I}{\partial r} = -\mathrm{j}k_0 Y V \tag{7.25}$$

where Z (Y) is the characteristic impedance (admittance) of the radial waveguide: $Z(r) = 1/Y(r) = \zeta b/(2\pi r)$. The solutions of the radial transmission line equation (7.24) are the Hankel functions $H_0^{(2)}(k_0 r)$ and $H_0^{(1)}(k_0 r)$. They represent waves travelling in the direction of increasing and decreasing radius, respectively, and are analogues of the exponential functions encountered in uniform transmission lines[f].

Equations (7.20) and (7.21) together with the solutions of equations (7.24) and (7.25) describe the boundary condition for the electromagnetic fields at the slit:

$$-bE_z(r) = V^{\mathrm{ref}} H_0^{(2)}(k_0 r) + V^{\mathrm{inc}} H_0^{(1)}(k_0 r), \tag{7.26}$$

$$\mathrm{j}bH_\phi'(r) = V^{\mathrm{ref}} H_1^{(2)}(k_0 r) + V^{\mathrm{inc}} H_1^{(1)}(k_0 r), \tag{7.27}$$

where V^{inc} and V^{ref} are the complex amplitudes of the incident and reflected waves, respectively. The extension to higher order modes is straightforward.

---

[f]The Hankel functions are defined as [171]:

$$H_m^{(1)}(x) = J_m(x) + \mathrm{j}N_m(x)$$
$$H_m^{(2)}(x) = J_m(x) - \mathrm{j}N_m(x)$$

with J_m and N_m two independent, standing-wave, Bessel functions of order m of the first and second kind (i.e. a Neumann function), respectively. This can be written analogously to the exponential functions encountered in uniform transmission lines as:

$$H_m^{(1)}(x) = (-\mathrm{j})^m h_m \exp\left[+\mathrm{j}\eta_m\right]$$
$$H_m^{(2)}(x) = (\mathrm{j})^m h_m \exp\left[-\mathrm{j}\eta_m\right]$$

with $h_m = (J_m^2(x) + N_m^2(x))^{1/2}$ the amplitude and $\eta_m = \frac{m\pi}{2} + \tan^{-1}\frac{N_m(x)}{J_m(x)}$ the phase of the Hankel functions.

7.2.4 Discretisation

In order to stay close to the discretisation used in PLASIMO, the Maxwell equations are discretised by the finite-difference method. The three electromagnetic field components E_z, E_r and H_ϕ are then defined on three different grids, similar to Yee's algorithm [172]. The grids are shown in figure 7.3. Compared to the E_r grid, the H_ϕ grid is shifted over a distance $\frac{1}{2}\Delta z$, with Δz the axial distance between electromagnetic (EM) grid points. Compared to the H_ϕ grid, the E_z grid is shifted over a distance $\frac{1}{2}\Delta r$, with Δr the radial distance between EM grid points. As is seen in figure 7.3, the E_r grid is composed in such a way that grid points are located at left and right boundary of the computational domain, the E_z grid is composed in such a way that its grid points are located at the plasma-glass interface, glass-air interface and the air-metallic wall interface. By doing so, the boundary conditions (BC) at the metal, interfaces and symmetry axis are naturally included. The interface BC corresponds to an equivalent medium smoothing [173], the permittivity is only averaged at the E_z grid.

The numerical boundaries at the ends of the computational window are taken to be metal walls. The electric field components parallel to a metallic wall vanish, so $E_z = 0$ at the north metallic walls and $E_r = 0$ at inlet and outlet (which were also taken as metal walls in the EM description). At the interfaces between media of different dielectric constants, E_z, $\hat{\varepsilon}_r E_r$ and H_ϕ have to be continuous; at the symmetry axis $E_r = 0$ and $H_\phi = 0$.

The number of grid points used in the microwave EM calculation is closely related to the number of grid point used by PLASIMO in the plasma region. For the computations performed in this thesis, a uniform PLASIMO-grid is used with 62 axial and 17 radial grid points, which results in 60 axial and 30 radial grid points (plasma plus glass and air region) for the EM-grid. For reasons of simplicity, an equidistant EM-grid is shown in figure 7.3; a non-equidistant grid can be used.
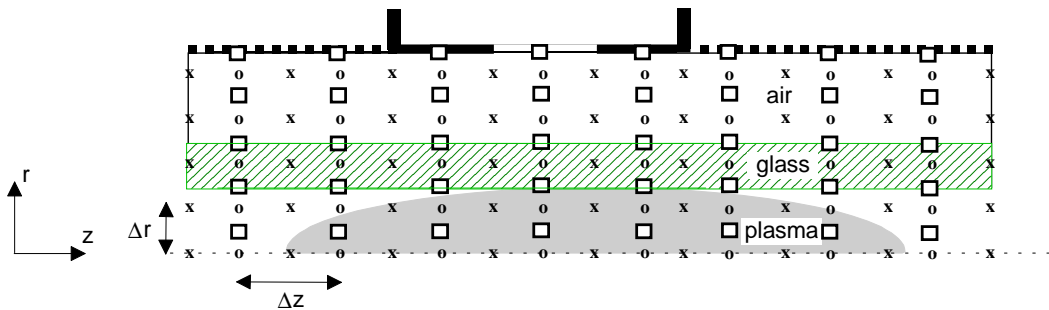
Figure 7.3: Simplified representation of the equidistant grid for the EM-module; □: E_z grid; x: E_r grid; o: H_ϕ grid. Note that the scale in radial direction is not the same as in figure 7.2, that E_z grid points are located at the north boundary, and that E_r grid points are located at the south, west and east boundaries.

Now that the relevant electromagnetic equations are described (the set of equations (7.17), (7.18), (7.19), (7.26) and (7.27)) and that a choice is made for the grid, the solution method can be discussed next.

7.2.5   Solution method

Using the Maxwell equations (7.17) - (7.19) plus the equations for E_z and H_ϕ that follow from the boundary conditions at the entrance slit, equations (7.26) and (7.27), the matrix equation to be solved is given by:

$$
\begin{pmatrix}
M_{11} & M_{12} & M_{13} & M_{14} \\
M_{21} & M_{22} & 0 & 0 \\
M_{31} & 0 & M_{33} & 0 \\
M_{41} & 0 & 0 & M_{44}
\end{pmatrix}
\begin{pmatrix}
H'_\phi \\
E_r \\
E_z \\
V^{\mathrm{ref}}/b
\end{pmatrix}
=
\begin{pmatrix}
R_1 \\
0 \\
0 \\
R_4
\end{pmatrix}
\tag{7.28}
$$

Equation (7.28) is a sparse matrix equation that is solved using the routines written by Kundert and Sangiovanni-Vincentelli [174]. The matrix components M_{ij} are given by (for the listed differential operators the finite-difference matrix representation is taken):

$$
\begin{aligned}
M_{11} &= 1 & (7.29) \\
M_{12} &= -\frac{\mathrm{j}}{k_0}\frac{\partial}{\partial z} & (7.30) \\
M_{13} &= \frac{\mathrm{j}}{k_0}\frac{\partial}{\partial r} & (7.31) \\
M_{14} &= -\frac{\mathrm{j}}{k_0 \Delta r} H_0^{(2)}(k_0 R_{\mathrm{air}}) & (7.32) \\
M_{21} &= -\frac{\mathrm{j}}{k_0}\frac{\partial}{\partial z} & (7.33) \\
M_{22} &= \hat{\varepsilon}_{\mathrm{r}} & (7.34) \\
M_{31} &= \frac{\mathrm{j}}{k_0}\frac{1}{r}\frac{\partial}{\partial r}r & (7.35) \\
M_{33} &= \hat{\varepsilon}_{\mathrm{r}} & (7.36) \\
M_{41} &= 1 & (7.37) \\
M_{44} &= \mathrm{j}H_1^{(2)}\left[k_0\left(R_{\mathrm{air}} - \Delta r/2\right)\right] & (7.38)
\end{aligned}
$$

with Δr the (equidistant) grid spacing in radial direction. Also the vector components R_i are a result of the boundary conditions at the slit and are given by:

$$
\begin{aligned}
R_1 &= \frac{\mathrm{j}}{k_0 \Delta r}\frac{V^{\mathrm{inc}}}{b}H_0^{(1)}(k_0 R_{\mathrm{air}}) & (7.39) \\
R_4 &= -\mathrm{j}\frac{V^{\mathrm{inc}}}{b}H_1^{(1)}\left[k_0\left(R_{\mathrm{air}} - \Delta r/2\right)\right] & (7.40)
\end{aligned}
$$

At the physical ends of the resonator, a special boundary condition is introduced to take account for MW reflections. At the other numerical boundaries, special boundary conditions are in development.

7.2.6 Coupling with PLASIMO

The microwave EM-module and the rest of PLASIMO are coupled via the Ohmic input power and the complex relative permittivity, equation (7.9). The MW power dissipated in the plasma, i.e. the Ohmic input power, is given by the complex Poynting vector:

$$\bar{P}_{\mathrm{plasma}} = \frac{1}{2}\Re\left(\int_V \vec{\mathbf{J}}^* \cdot \vec{\mathbf{E}}\mathrm{d}V\right) = \frac{1}{2}\Re\left(\sigma\left|\vec{\mathbf{E}}\right|^2\right) \tag{7.41}$$

where the notation $\bar{P}_{\mathrm{plasma}}$ denotes the time-averaged power in the plasma, $\Re$ denotes the real part and $*$ denotes the complex conjugate; V denotes the volume over which the integration is performed, i.e. a control volume for the local Ohmic input power and the total volume of the computational domain for the total Ohmic input power in the plasma; $|\vec{\mathbf{E}}|^2 = E_z E_z^* + E_r E_r^*$. Note that again the harmonic quasi-stationary analysis is used.

The MW power dissipated in the configuration, i.e. plasma plus glass, is given by:

$$P_{\mathrm{total}} = \frac{2}{bk_0}\left(\frac{\varepsilon_0}{\mu_0}\right)^{1/2}\left(\left|V^{\mathrm{inc}}\right|^2 - \left|V^{\mathrm{ref}}\right|^2\right) \tag{7.42}$$

Due to the discretisation of the radial transmission line equation (7.24), with Bessel functions as solutions, the calculated P_{total} can differ from $\bar{P}_{\mathrm{plasma}}$. The amplitude of the inward travelling wave, V^{inc}, is adjusted iteratively until the total dissipated MW power, given by equation (7.42), equals the desired input power P_{input} (which is chosen to be an input parameter for this plasma configuration): $V_{\mathrm{new}}^{\mathrm{inc}} = V_{\mathrm{old}}^{\mathrm{inc}}(P_{\mathrm{input}}/P_{\mathrm{total}})^{1/2}$.

There are two main differences in the discretised configuration between the microwave EM-module and PLASIMO. First, the computational domain is different: in the calculation of the electromagnetic fields, it exists of the plasma region plus the glass and air region. In PLASIMO, it contains only the plasma region shown in figure 7.2. Secondly, the PLASIMO-grid, on which the mass, momentum and energy balances in the plasma region are solved, and the microwave EM-grid, as shown in figure 7.3, are not the same. Since PLASIMO and the EM-module are coupled via the permittivity (as given in equation (7.9)) and the Ohmic input power (as given in equation (7.41)), between the two grids linear interpolation is applied for these variables.

7.3 Configuration characteristics

We will now concentrate on the configuration characteristics that are used in PLASIMO. The configuration of interest is taken similar to the one used by Rau and Trafford [169], and is shown in figure 7.2. The computational domain used in PLASIMO consists of the plasma region only. The electromagnetic module with its boundary conditions were discussed above, the boundary conditions for the computational domain of PLASIMO and the configuration characteristics are given in table 7.1. A uniform (plasma) grid is used with 62 axial and 17 radial grid points.

The maximum inlet velocity at the axis, $u_{\mathrm{in}}^{\mathrm{max}}$, is determined by the mass flow and mass density at the inlet, as was explained in [34]. The tube is pumped at the outlet side, the pressure at the outlet, p_{out}, is taken as fixed. A constant axial component of the pressure gradient is

Table 7.1: Boundary conditions for the computational domain of PLASIMO, applied to the non-LTE argon MW plasma plus the configuration characteristics (the same as those of Rau and Trafford [169]). The pressure is p; u_z and u_r are the axial and radial velocity components, respectively; T_h and T_e are the heavy particle and electron temperature, respectively; y_i is the mass fraction of species i.

Par.	Inlet	Outlet	Axis	Tube wall
p	$\frac{\partial p}{\partial z} = C$	$p = p_{\text{out}}$	$\frac{\partial p}{\partial r} = 0$	$\frac{\partial p}{\partial r} = 0$
u_z	$u_z = u_{\text{in}}^{\max}\left[1 - \left(\frac{r}{R_{\text{pl}}}\right)^2\right]$	$\frac{\partial u_z}{\partial z} = 0$	$\frac{\partial u_z}{\partial r} = 0$	$u_z = 0$
u_r	$u_r = 0$	$\frac{\partial u_r}{\partial z} = 0$	$u_r = 0$	$u_r = 0$
T_h	$T_h = T_{h,\text{in}}$	$\frac{\partial T_h}{\partial z} = 0$	$\frac{\partial T_h}{\partial r} = 0$	$\lambda_h \frac{\partial T_h}{\partial r} = \frac{\lambda_w\left(T_{\text{fur}} - T_{h,w}\right)}{R_{\text{pl}} \ln\left(\frac{R_{\text{pl}} + \delta_w}{R_{\text{pl}}}\right)}$
T_e	$T_e = T_{e,\text{in}}$	$\frac{\partial T_e}{\partial z} = 0$	$\frac{\partial T_e}{\partial r} = 0$	$\frac{\partial T_e}{\partial r} = 0$
y_i	$\frac{M_i \varphi_i}{\sum_j M_j \varphi_j}$ $\vec{n} \cdot \vec{J}_i = 0$	$\frac{\partial y_i}{\partial z} = 0$	$\frac{\partial y_i}{\partial r} = 0$	$\vec{n} \cdot \left(\rho y_i \vec{u} + \vec{J}_i\right) = R_i$

Par.	Value	Par.	Value
φ	5 scc s^{-1}	$T_{h,\text{in}}$	500 K
f_{Ar}	0.999	$T_{e,\text{in}}$	2000 K
f_{Ar^+}	0.001	T_{fur}	1500 K
L_1	300 mm	λ_w	1.047 W m^{-1} K^{-1}
L_{res}	100 mm	b	10 mm
R_{pl}	7.5 mm	slit asymmetry	-5 mm
R_{gl}	9 mm	δ_w	1.5 mm
R_{air}	15 mm	p_{out}	1000 Pa
P_{input}	400, 1000, 2000 W		

assumed at the inlet of the tube. The value of this gradient is determined during the iteration process. The heavy particle temperature at the tube wall, $T_{h,w}$ is determined from the equality of the heat flux from the plasma to the tube and the heat flux from the tube to the furnace, which temperature is kept constant at $T_{\text{fur}} = 1500$ K. At the inlet the composition of the argon mixture is fixed, with fractions f_i of the total inlet flow φ for each individual species i (i.e. the inlet flow of species i is defined as $\varphi_i = f_i \varphi$). The fractions are given in table 7.1. At the wall, the

total mass flux of species "i" perpendicular to the wall must equal the net mass flux R_i due to production or consumption of the species at the wall. This R_i is described in chapter 2 of this thesis. For argon the result is:

$$R_{\mathrm{Ar+}} = -m_{\mathrm{Ar+}}\Gamma^{\mathrm{in}}_{\mathrm{Ar+,w}} \tag{7.43}$$

$$R_{\mathrm{Ar}} = m_{\mathrm{Ar}}\Gamma^{\mathrm{out}}_{\mathrm{Ar,w}} \tag{7.44}$$

with $\Gamma^{\mathrm{in}}_{\mathrm{Ar+,w}}$ and $\Gamma^{\mathrm{out}}_{\mathrm{Ar,w}}$ the fluxes (in $\mathrm{m}^{-2}\mathrm{s}^{-1}$) describing at the wall w the loss of argon ions Ar^+ and the production of argon atoms Ar, respectively:

$$\Gamma^{\mathrm{in}}_{\mathrm{Ar+,w}} = n_{\mathrm{Ar+}}\bar{u}_{\mathrm{Ar+,w}}\frac{\gamma_{\mathrm{Ar+,w}}}{1-\gamma_{\mathrm{Ar+,w}}/2} \tag{7.45}$$

$$\Gamma^{\mathrm{out}}_{\mathrm{Ar,w}} = \Gamma^{\mathrm{in}}_{\mathrm{Ar+,w}} \tag{7.46}$$

with $\bar{u}_{\mathrm{Ar+,w}} = \frac{1}{4}(8k_bT_h/\pi m_{\mathrm{Ar+}})^{1/2}$ the mean thermal velocity of Ar^+ perpendicular to the wall. For argon only the ionic neutralisation $\mathrm{Ar}^+ + \mathrm{wall} \rightarrow \mathrm{Ar}$ is taken into account, its reaction probability is assumed to be $\gamma_{\mathrm{Ar+}} = 1$. The slit asymmetry denotes that the slit is not located exactly in the middle of the resonator, but that it is shifted (in this case to the left, towards the inlet).

7.4 Composition characteristics

For the chemical and transport properties of argon we refer to Janssen *et al.* [34], where all the argon characteristics needed in PLASIMO are discussed extensively. Here, we mention only the rate coefficient, $K_{e-\mathrm{Ar}}$, for momentum transfer between e and Ar, needed in the calculation of the electron collision frequency, since this is part of the coupling between PLASIMO and the microwave EM-module. For calculating $K_{e-\mathrm{Ar}}$ the cross-section data given by NIST [69] are used.

7.5 Results

The configuration of Rau and Trafford [169] is used to perform numerical simulations of an argon MW plasma at microwave powers of 400, 1000 and 2000 W. Here, we will present the results for the MW power absorbed in the plasma, the electron and heavy particle temperatures, the velocity, the mass fraction of the argon ions and the radiation losses.

The microwave power absorbed in the plasma is shown in figure 7.4, from which it can be seen that the microwave energy coupling to the plasma is mainly located at the plasma-tube interface. This is due to the small skin depth, which is defined as $\delta = (2/\omega\mu\sigma)^{1/2}$. It represents the depth beyond which the field strength becomes negligible. For higher frequency and larger electric conductivity, δ decreases.

The profile of the electron temperature T_e is shown in figure 7.5. The T_e profile reflects the standing microwave pattern in the plasma region that is created due to reflections at the inlet
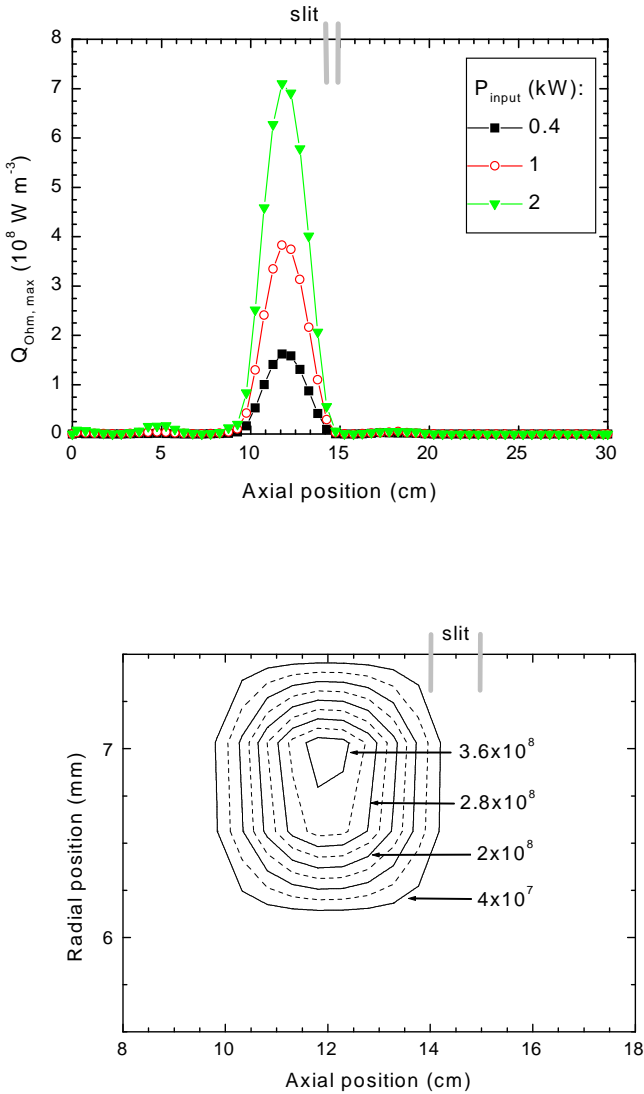
Figure 7.4: *Computed MW power in the plasma region. Top: peak value of the MW power, as function of input power at a radial position of $r = 7.25$ mm, the location of the slit is denoted by the two grey lines; bottom: contour plot for $P_{\text{input}} = 1$ kW.*

and outlet opening of the substrate tube which are considered as metal walls in the present MW module. The location of the first peak of T_e corresponds to the first (small) peak in the MW power in figure 7.4. This peak is expected to vanish, by using the new EM boundary conditions, as noted in section 7.2.5.

The heavy particle temperature T_h is shown in figure 7.6 for a MW power of 400 W. Compared to T_e, the T_h-profile is smeared out towards the symmetry axis, while near the tube wall a
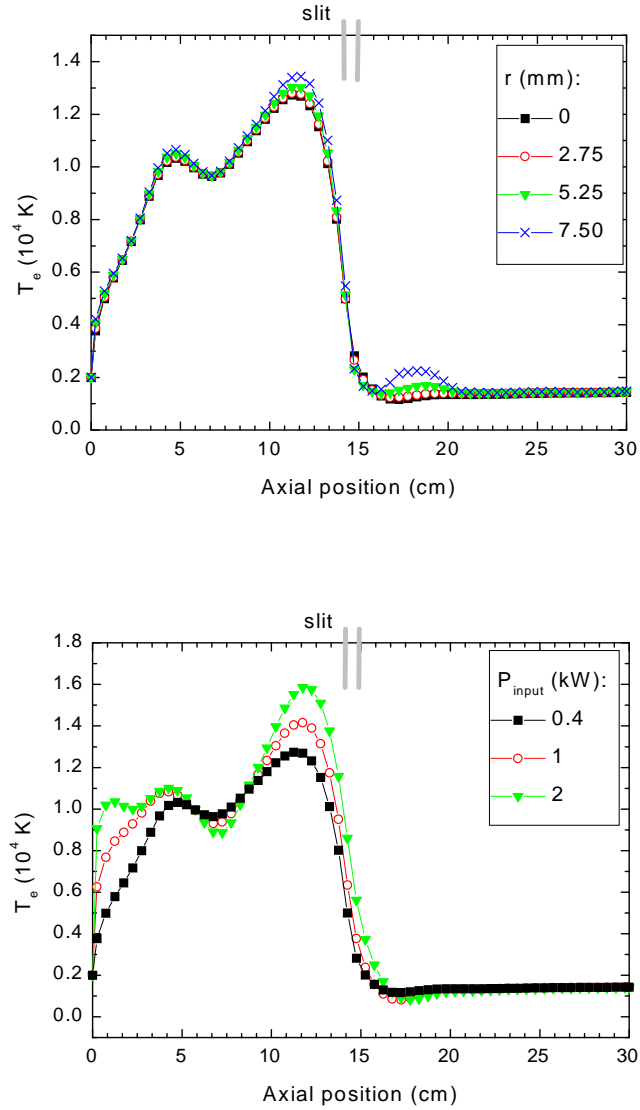
Figure 7.5: Computed electron temperature. Top: at four different radii in the plasma region, for $P_{\mathrm{input}} = 400$ W; bottom: values at the axis as function of input power.

cooling effect occurs due to heat transfer; the value of T_h at the wall is coupled via the boundary conditions with the temperature of the furnace, which is kept at 1500 K. The lower values of T_h in the inlet region of the tube are a consequence of the inlet gas temperature of 500 K. The effect of different input power is also shown in figure 7.6. Comparing T_e (figure 7.5) with T_h (figure 7.6) reveals that there is a strong non-LTE behaviour in the central plasma region, i.e. $T_h \ll T_e$.

The pressure difference between inlet and outlet is small, $\Delta p = 65$ Pa, which means that Rau's uniform pressure assumption is permitted. However, the computed axial velocity profile,
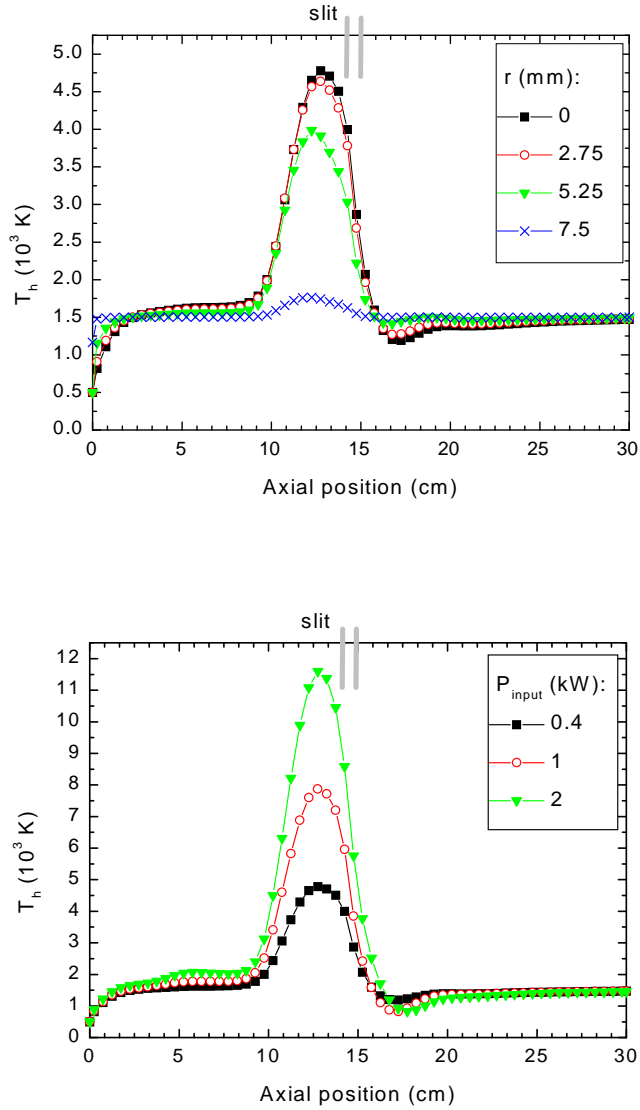
Figure 7.6: *Computed heavy particle temperature. Top: at four different radii in the plasma region, for $P_{\text{input}} = 400$ W; bottom: values at the axis as function of input power.*

shown in figure 7.7, suggests that convection is important in the region where the MW power is coupled into the plasma; convection was not taken into account by Rau and Trafford.

The computed Ar^+ mass fraction in the plasma region is shown in figure 7.8. One clearly sees two influences: the profile of y_{Ar^+} is smeared out towards the center of the tube. This is due to diffusion. Secondly, closer to the axis of the configuration, the axial profile of y_{Ar^+} is moved downstream. This is due to convection. The electron number density at $r = 5.25$ mm for $P_{\text{input}} = 400$ W is $n_e^{\max} = 6.6 \times 10^{20}$ m^{-3} ($n_{Ar} = 1.6 \times 10^{22}$ m^{-3}).
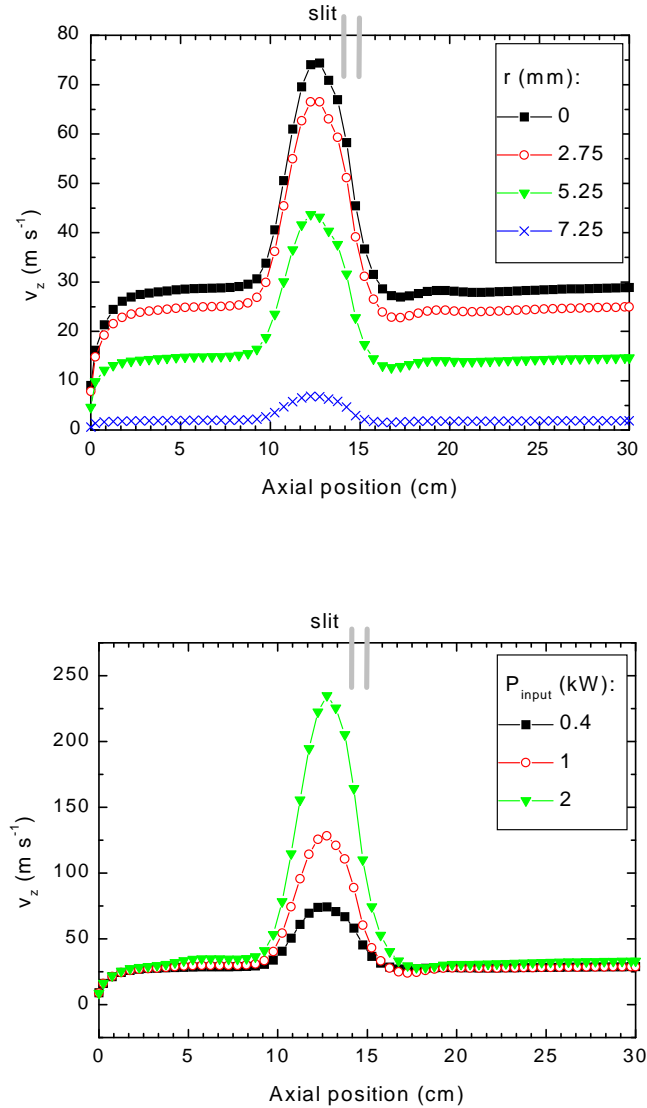
Figure 7.7: Computed axial velocity profile. Top: at four different radii in the plasma region, for $P_{\text{input}} = 400$ W; bottom: values at the axis as function of input power.

The computed radiation losses are given in figure 7.9. It appears that especially downstream of the slit an afterglow can be seen. The profile of the radiation losses is expected, since radiation losses will mainly appear in regions where T_e is low and n_e is high, i.e. downstream for this plasma configuration. A comparison of the radiation losses for low and high MW powers is shown in figure 7.9. It is seen that at high microwave powers, the afterglow is stronger. Both effects were also verified by observations.

The results of the numerical simulations agree well with observations, although detailed val-
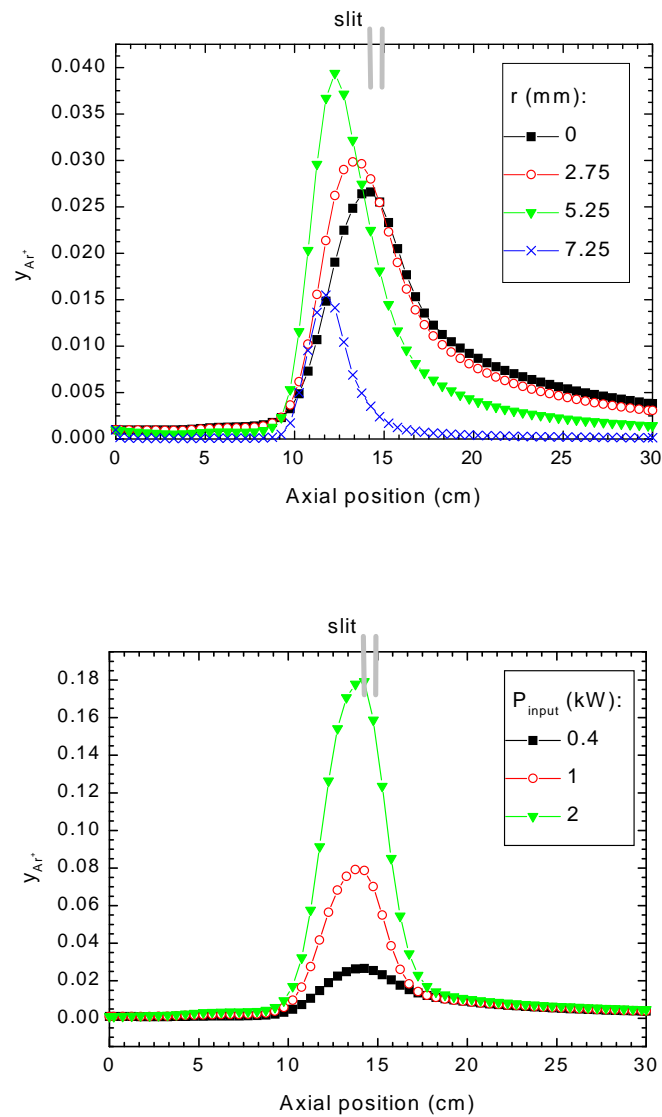
Figure 7.8: Computed mass fraction of Ar^+. Top: at four different radii in the plasma region, for $P_{\text{input}} = 400$ W; bottom: values at the axis as function of input power.

idation of the results of the simulation of the MW plasma used in optical fibre production, can only be achieved by experimental results. Due to the complicated set-up of the MW configuration used by Plasma Optical Fibre B.V., especially the moving resonator and the furnace at high temperature, it is difficult to perform experiments which can determine the relevant plasma parameters. However, some quantitative validations will be performed in the near future.
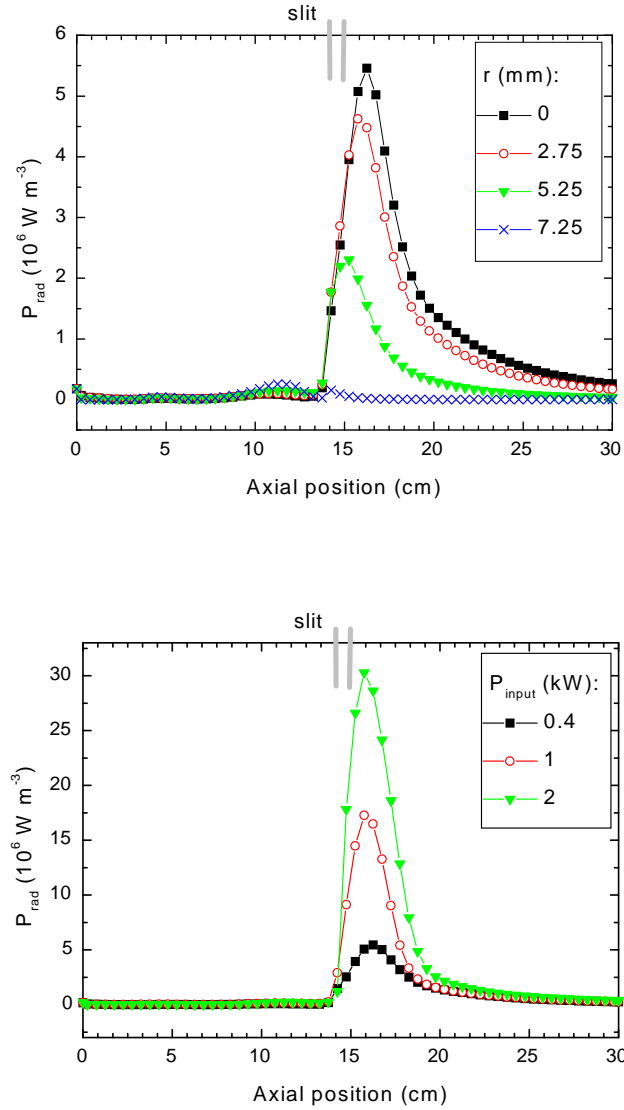
Figure 7.9: Computed radiation losses. Top: at four different radii in the plasma region, for $P_{\text{input}} = 400$ W; bottom: values at the axis as function of input power.

7.6   Conclusions

The first step in modelling the microwave plasma used in the production of optical fibres has been carried out: a new microwave energy coupling module has been designed and added to the plasma simulation tool PLASIMO. The first results of the numerical simulation of an argon microwave plasma are presented. The verification by qualitative observations shows a good agreement between simulations and observations. The results of the numerical simulations will

be quantitatively validated by experiments in the near future. The implementation of absorbing boundary conditions for the electromagnetic fields at inlet and outlet of the tube, will improve the results for the electron temperature.

Acknowledgements

Chapter 8

Numerical Simulation of Microwave Plasmas Used in Optical Fibre Production: the Non-LTE Oxygen Plasma

G.M. Janssen[1], M.J.N. van Stralen[2], J.A.M. van der Mullen[1] and A.H.E. Breuls[2]

[1] Department of Applied Physics, Eindhoven University of Technology, P.O. Box 513, 5600 MB Eindhoven, The Netherlands
[2] Plasma Optical Fibre B.V., P.O. Box 1136, 5602 BC Eindhoven, The Netherlands

Abstract

The multi-component plasma simulation method PLASIMO is used to numerically simulate an oxygen plasma allowing local thermal non-equilibrium (non-LTE) conditions in the microwave configuration, used for optical fibre production. This is the second step towards numerically simulating the complete system, which eventually will include the complex chemistry between O_2, $SiCl_4$ and $GeCl_4$. The results of the numerical simulations are compared with the results for argon presented in chapter 7 of this thesis. It proves that there are major differences between the argon and oxygen plasmas, which all are explained. Compared to the hydrogen non-LTE model presented in chapter 5, the current oxygen model is relatively simple. Possible extensions of the oxygen model are recognised, and it forms a good basis for the next steps towards the numerical simulation of the optical fibre production process.

8.1   Introduction

In the previous paper (chapter 7 of this thesis), a start was made with describing the deposition process used in optical fibre production. For this purpose, the general plasma simulation tool PLASIMO [34], which has been developed in the group Equilibrium and Transport at the Eindhoven University of Technology, is used. As a first step a new microwave energy coupling module was designed and implemented in PLASIMO. In the preceding chapter, simulations were performed for an argon MW plasma, which lead to encouraging results. Though no experimental data are available on the configuration of interest, the results were as expected, and agreed with observations.

For simulating the complete deposition process, a mixture of O_2, $SiCl_4$ and $GeCl_4$ has to be studied. The next step towards this goal is the simulation of a pure oxygen plasma. This will be carried out in the same configuration as in the previous paper [169]. Experiments will be performed in the near future, at this moment we will compare with the results of the argon plasma simulations presented in chapter 7 and analyse possible differences and the observed trends.

This chapter is organised as follows: the configuration characteristics will be discussed briefly in section 8.2. In section 8.3 the oxygen composition characteristics, which involves the oxygen species O_2, O, O^+, O_2^+ and O^-, are discussed. Compared to hydrogen (see chapter 5 of this thesis) the main difference is the larger electronegativity: in an oxygen plasma more O^- is present than H^- in a hydrogen plasma. The results of the numerical simulations for an oxygen microwave plasma are presented and compared with the results of chapter 7 in section 8.4.

8.2   Configuration features

The configuration considered is the same as the one used by Rau and Trafford [169]. It is depicted in figure 8.1.
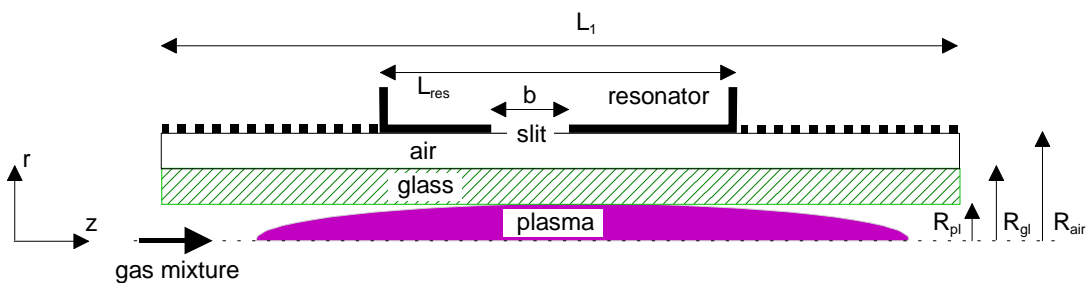
Figure 8.1: Geometry of the set-up: the plasma is surrounded by a substrate tube and resonator.

As was explained in chapter 7, we make a distinction between the computational domain for the calculation of the microwave (MW) electromagnetic (EM) field and that of PLASIMO. For the MW EM field computation, it contains the plasma region, the glass and air regions. For the PLASIMO computations it contains only the plasma region shown in figure 8.1. The boundary conditions for the PLASIMO computational domain are given in section 8.2.1.

For the description of the computational domain for the MW energy coupling calculation we refer to chapter 7.

8.2.1   Boundary conditions

The boundary conditions for the computational domain of PLASIMO applied to the non-LTE oxygen MW plasma, are similar to the ones given in chapter 7. The only differences are found in the fractions f_i of the oxygen species at the inlet of the substrate tube. At the inlet the composition of the oxygen mixture is fixed, with fractions f_i of the total inlet flow φ for each individual species i (i.e. the inlet flow of species i is defined as $\varphi_i = f_i \varphi$). The fractions of the different oxygen species are chosen as follows: $f_{O_2} = 0.99$, $f_O = 0.009$, $f_{O^+} = 0.0009$, $f_{O_2^+} = 5 \times 10^{-5}$ and $f_{O^-} = 5 \times 10^{-5}$. At the wall, the total mass flux of species "i" perpendicular to the wall must equal the net mass flux R_i due to production or consumption of the species at the wall: $R_i = m_i(\Gamma_{i,w}^{\text{out}} - \Gamma_{i,w}^{\text{in}})$ with $\Gamma_{i,w}$ the flux (in $\text{m}^{-2}\text{s}^{-1}$) describing the gain or loss of species i at the wall w, which depends on the wall reaction probability γ_i. For the formulation of the fluxes $\Gamma_{i,w}^{\text{out}}$ and $\Gamma_{i,w}^{\text{in}}$ we refer to chapter 2. As was shown before (see chapter 5 of this thesis), wall reaction processes can play an important role in the plasma chemistry. The wall reaction processes included in this study are listed in table 8.1. The reaction probabilities, γ_{O^+}, $\gamma_{O_2^+}$ and γ_{O^-}, for ionic neutralisation at the wall are assumed to be 1. Gousset *et al.* [175, 176] found that the wall association process $O + O + \text{wall} \to O_2$, has a reaction probability of $\gamma_O \approx 5 \times 10^{-3}$ for their plasma conditions; a low-pressure DC glow discharge with $p \leq 10^2$ Pa and a DC current of $I \leq 10^{-1}$ A. These conditions are very different from the conditions encountered in our set-up. The same arguments as were used before for γ_H (see chapter 5 of this thesis) are applicable to γ_O: the wall reaction coefficient depends on the wall temperature, the wall material and the surface conditions of the wall, see also Matsushita [177]. Therefore, there is a large uncertainty in the value of γ_O to be used. We have chosen $\gamma_O = 0.1$. Since it is well known that surface reactions of O play an important role [177] (compare also with the role of γ_H in the hydrogen plasma in chapter 5), experimental investigation of γ_O for plasma conditions similar to the ones encountered here, could be part of a follow-up study.

Table 8.1: The wall reaction processes included in this study.

Reacting species	Reactants
$O + \text{wall} \to$	$\frac{1}{2}O_2$
$O^+ + \text{wall} \to$	O
$O_2^+ + \text{wall} \to$	O_2
$O^- + \text{wall} \to$	O

8.3   Composition characteristics

We assume that the oxygen plasma contains the following species: O, O_2[a], O^+, O_2^+ and O^-. We do not consider the metastable states $O^*(^1D)$, $O_2^*(a^1\Delta_g)$ and $O_2^*(b^1\sum_g^+)$ but will discuss their possible influence on the chemistry and the simulation results in section 8.4.2. We do not make use of a detailed Collisional-Radiative (CR) model or an advanced kinetic model for oxygen. The main reasons for this are the following. The more transport-sensitive (TS) species we take into account the longer the numerical simulations will take. Compared to a two-species argon plasma (Ar, Ar^+), for a five-species oxygen plasma (O, O_2, O^+, O_2^+, O^-), three extra mass balances and three Stefan-Maxwell equations have to be solved, at each PLASIMO iteration. Therefore, we try to limit the kinetic scheme as much as possible.

For the five-species oxygen plasma, we distinguish three quasi-separate kinetic systems[b]:

- The *atomic* system, involving atomic ionization/recombination processes, discussed in section 8.3.1.
- The *molecular* system, involving association/dissociation processes and O_2^+ processes, see section 8.3.2;
- The O^- system, involving chemistry with O^-, see section 8.3.3.

For simplicity, we do not consider the influence of rovibrational excitation, although it is recognized that it can be of major influence in the present type of plasma (see for example chapter 5 of this thesis).

8.3.1   The atomic system

For atomic oxygen, electronic ionization is included (EI):

$$O + e \longrightarrow O^+ + 2e \tag{8.1}$$

The reaction rate is taken from Lee *et al.* [178], the rate for the reverse process is calculated via detailed balancing. Figure 8.2 shows the reaction rate for EI from the ground state and the first excited state, together with the rates for excitation of O to $O(^1D)$ and $O(^1S)$. If excitation to $O(^1D)$ is followed by step-wise ionisation (like in a hydrogen plasma, see chapter 5 of this thesis), we should use this excitation rate for the ionisation rate.

At this moment, we do not use a CR model to calculate the net production/destruction of O and O^+ and the line radiation. This will be part of a future project.

8.3.2   The molecular system

The oxygen molecule O_2 and oxygen atom O are coupled with each other via:

---

[a]The oxygen molecule in the electronic ground state is denoted as O_2 instead of $O_2(X^3\sum_g^-)$.

[b]This is to a certain extent analogous to the non-LTE hydrogen plasma in chapter 5 of this thesis, although the systems are defined differently here.
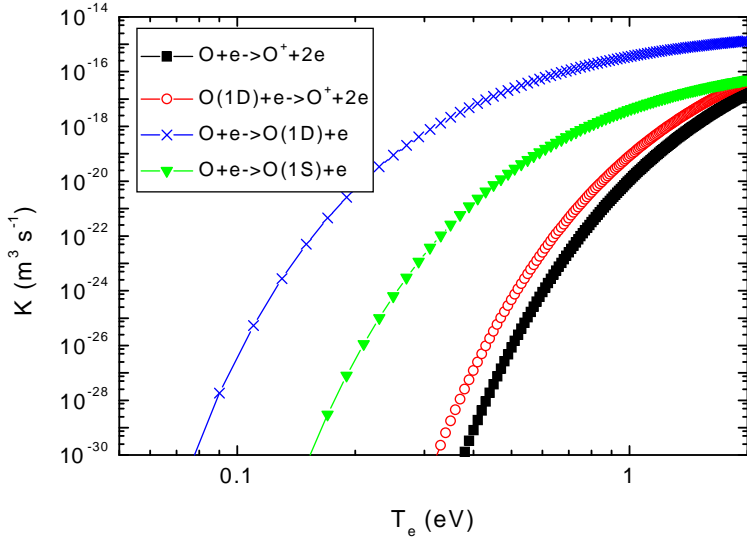
Figure 8.2: The reaction rates for Electronic Ionisation (EI) from the ground state and the first excited state according to Lee et al. [178], together with the rates for excitation of O to $O(^1D)$ and $O(^1S)$.

- Electron Assisted Dissociation (EAD) and its reverse process Electron Assisted Association (EAA):

$$O_2 + e \underset{EAA}{\overset{EAD}{\rightleftarrows}} O + O + e \tag{8.2}$$

The reaction rate for EAD is taken from Lee *et al.* [178] and is shown in figure 8.4, the rate for the reverse process (EAA) is calculated via detailed balancing.

- Heavy particle Assisted Dissociation (HAD) and its reverse process Heavy particle Assisted Association (HAA):

$$O_2 + M \underset{HAA}{\overset{HAD}{\rightleftarrows}} O + O + M \tag{8.3}$$

with $M = O$ or O_2. The reaction rate for HAA is taken from Eliasson and Kogelschatz [179] and is shown in figure 8.3. The reverse rate is calculated via detailed balancing.

- Dissociative Ionisation (DI):

$$O_2 + e \xrightarrow{DI} O + O^+ + 2e \tag{8.4}$$

The rate is taken from Eliasson and Kogelschatz [179]. See figure 8.4.
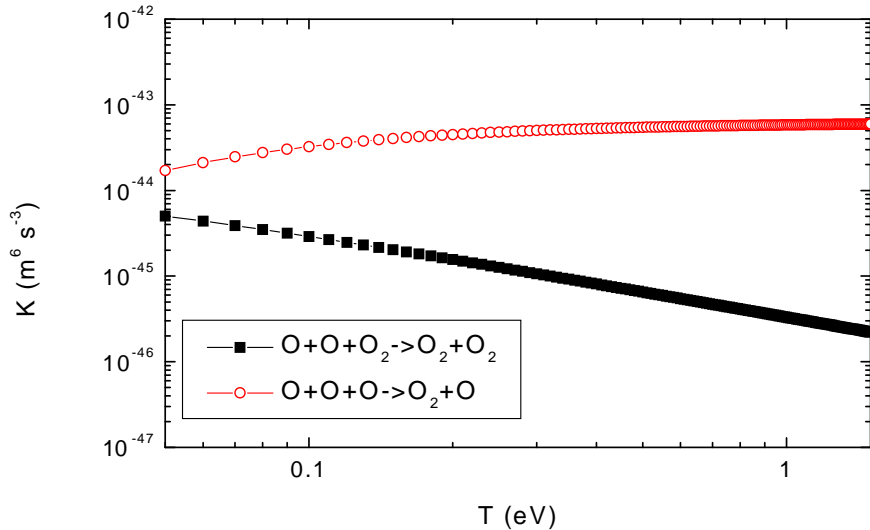
Figure 8.3: The reaction rates for HAA, for $X = \mathrm{O}, \mathrm{O}_2$, according to Eliasson and Kogelschatz [179].

The molecular ion O_2^+ is formed via:

- Molecular Ionisation (MI):

$$\mathrm{O}_2 + \mathrm{e} \xrightarrow{\mathrm{MI}} \mathrm{O}_2^+ + \mathrm{e} + \mathrm{e} \qquad (8.5)$$

  The reaction rate for MI is taken from Lee *et al.* [178]. The rate for the reverse process, Molecular Recombination (MR), is calculated using detailed balancing.

- Charge Transfer (CT):

$$\mathrm{O}_2 + \mathrm{O}^+ \xrightarrow{\mathrm{CT}} \mathrm{O}_2^+ + \mathrm{O} \qquad (8.6)$$

  The reaction rate is taken from Eliasson and Kogelschatz [179]. It appears that this rate is very small, when comparing it for example with the CT rate in a hydrogen plasma (chapter 5 of this thesis), which is around 2.5×10^{-15} m^3 s^{-1}. For oxygen, CT from the O_2 ground state is exothermic ($E_{\mathrm{O}_2}^{\mathrm{ion}} = 12.075$ eV, $E_{\mathrm{O}}^{\mathrm{ion}} = 13.61$ eV) in contrast to a hydrogen plasma in which it is endothermic ($E_{\mathrm{H}_2}^{\mathrm{ion}} = 15.42$ eV, $E_{\mathrm{H}}^{\mathrm{ion}} = 13.56$ eV). If vibrationally excited oxygen molecules play an important role in the oxygen plasma, the CT rates from these states have to be taken into account. This can be part of a future study.

O_2^+ is destroyed via:

- Dissociative Recombination (DR):

$$\mathrm{O}_2^+ + \mathrm{e} \xrightarrow{\mathrm{DR}} \mathrm{O} + \mathrm{O} \qquad (8.7)$$
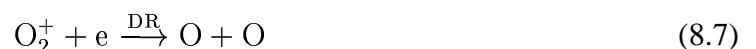
The reaction rate is taken from Hasted [180].

In figure 8.4 the rates for EAD, MI [178], CT, DI [179] and DR [180] are shown.
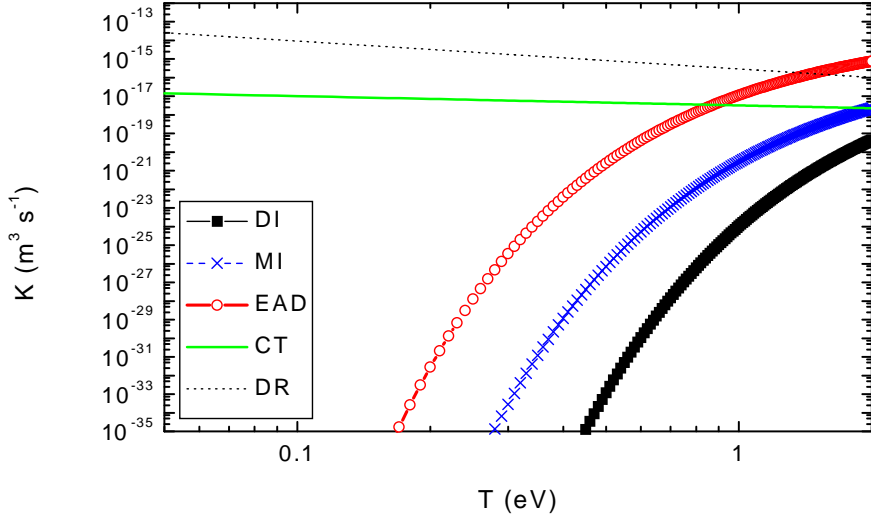
Figure 8.4: The reaction rates for EAD, MI [178], CT, DI [179] and DR [180].

8.3.3   The O$^-$ system

The negative ion O$^-$ (with $\Delta E_{\text{O}^- - \text{O}} = 1.463$ eV) is formed via the following Dissociative Electron Attachment (DEA) and Polar Dissociation (PD) reactions:

$$\text{O}_2 + \text{e} \xrightarrow{DEA} \text{O}^- + \text{O} \tag{8.8}$$

$$\text{O}_2 + \text{e} \xrightarrow{PD} \text{O}^- + \text{O}^+ + \text{e} \tag{8.9}$$

The negative O$^-$ is destroyed via Electron Impact Detachment (EID) and positive-negative ion recombinations (PIR):

$$\text{O}^- + \text{e} \xrightarrow{EID} \text{O} + 2\text{e} \tag{8.10}$$

$$\text{O}^- + \text{O}^+ \xrightarrow{PIR} 2\text{O} \tag{8.11}$$

$$\text{O}^- + \text{O}_2^+ \xrightarrow{PIR} \text{O} + \text{O}_2 \tag{8.12}$$

$$\xrightarrow{PIR} 3\text{O} \tag{8.13}$$

The reaction rates are taken from Lieberman [181], and are shown in figure 8.5.

8.3.4   Transport coefficients

The electron thermal conductivity λ_e is calculated using Frost's mixture rules [57]; the electric conductivity σ is calculated conform the self-consistent set of the Stefan-Maxwell equations,
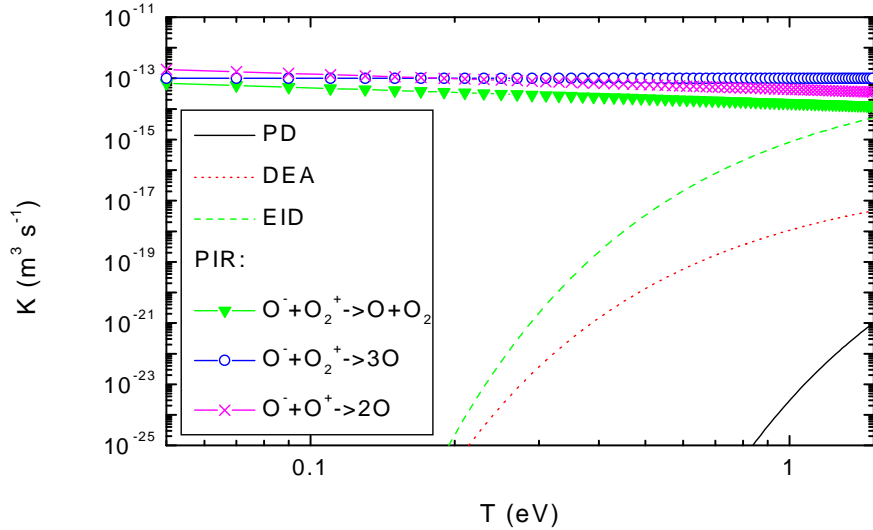
Figure 8.5: The reaction rates for production and destruction of the negative ion O^-. The reaction rates are from Lieberman [181].

which is explained in chapter 3 of this thesis. The frozen part of the heavy particle thermal conductivity $\lambda_{h,f}$ and the viscosity μ are calculated with the mixture rules given by Mitchner and Kruger [41]. The reactive part of the heavy particle thermal conductivity $\lambda_{h,r}$ is included as a reactive heat source term in the heavy particle energy balance.

8.3.5   Source terms

The net production terms in the mass balances of the species are calculated from the reactions given in sections 8.3.1 - 8.3.3. In the momentum balance of the mixture, the time-averaged influence of the generated magnetic field $\vec{\mathbf{B}}$, $\vec{\mathbf{j}}_q \times \vec{\mathbf{B}}$, with $\vec{\mathbf{j}}_q$ the current density, is neglected. The source terms in the energy balances include the elastic energy transfer between electrons and heavy particle species, the radiation losses and the reactive heat source term.

For the calculation of the elastic energy transfer term (for its formula, see chapter 5 of this thesis) and the calculation of the complex permittivity used in the MW energy coupling term (i.e. the Ohmic input power, see chapter 7 of this thesis) the electron collision frequency ν for momentum transfer from electrons to the heavy particles is needed. The expression for ν is more complicated as for the argon plasma presented in chapter 7 of this thesis. For a multi-component plasma, with more than one ion, ν is given by Shkarofsky *et al.* [70]:

$$\nu = \sum_n n_n \langle K_{en} \rangle + \frac{1}{\left(2\pi m_e k_b^3 T_e^3\right)^{1/2}} \left(\frac{e^4}{6\pi\varepsilon_0^2}\right) \sum_i n_i Z_i^2 \ln \Lambda \qquad (8.14)$$

where the subscript 'n' denotes neutral particle species and the subscript 'i' denotes ionised particle species; m_e is the electron mass, e is the elementary charge, k_b is Boltzmann's constant, n_X is the number density of species X, with X = n or i; $\langle K_{en} \rangle$ is the rate coefficient for momentum transfer between electrons and neutrals, averaged over a Maxwellian energy distribution, Z_i is the charge number of ionised species i, and $\ln \Lambda$ is the Coulomb logarithm with ion screening included. The Debye shielding length l_D, used in the Coulomb logarithm, for the multi-component oxygen plasma is given by [70]:

$$\frac{1}{l_D^2} = \frac{e^2}{\varepsilon_0 k_b} \sum_i \frac{n_i Z_i^2}{T_i} \tag{8.15}$$

which is a *total* Debye length, in which the influence of all charged species is included. The rate coefficients for momentum transfer between the electrons and the neutrals, O and O_2, are computed by using the cross-section data of Itikawa [182] (for O) and Lawton and Phelps [183] (for O_2). The radiation loss term is conform [117] with the free-free and free-bound contribution according to Mitchner and Kruger [41].

8.4   Results

8.4.1   Numerical simulations

The same configuration is used as the one presented in chapter 7 for a microwave power of 400 W. We present the computations for the power absorbed in the plasma region, the electron and heavy particle temperatures and the dominant mass fractions. A comparison is made with the argon results of chapter 7.

The comparison of the computed MW power coupling for oxygen and argon is shown in figure 8.6. The peak value in oxygen is lower than in argon. A contour plot of the MW power absorbed in the oxygen plasma is also shown in figure 8.6. One can see that in the oxygen plasma the MW power coupling is smeared out towards the axis, whereas in argon the power is very locally absorbed (figure 7.4). This can be understood by looking at the skin depth, defined as $\delta = (2/\omega\mu\sigma)^{1/2}$. In the oxygen plasma n_e is much lower (explained below) and T_e is much higher than in the argon plasma: $n_e^{\text{oxygen}} \approx 2.0 \times 10^{19}$ m^{-3} and $n_e^{\text{argon}} \approx 2.3 \times 10^{21}$ m^{-3}. Since the electric conductivity is $\sigma \approx e^2 n_e D_e^{\text{eff}}/(k_b T_e)$, it follows that $\sigma^{\text{oxygen}} < \sigma^{\text{argon}}$, which implies that the skin depth for oxygen is larger than that for argon. The location of the MW power coupling for oxygen is further downstream than in argon. This is also explained by the different σ of oxygen, which influences the MW field via the complex permittivity (see chapter 7).

The computed profile of the electron temperature T_e is shown in figure 8.7 and compared with T_e in the argon plasma computations from chapter 7. It is seen that T_e in the oxygen plasma is higher than in the argon plasma. A possible reason for this is that recombination is more effective in the oxygen plasma than in the argon plasma. Since n_e in the oxygen plasma is much lower than in the argon plasma, the coupling between $\{e\}$ and $\{h\}$ will be less stronger in the oxygen plasma (via the elastic energy transfer[c]), so that T_e has to be higher in the oxygen plasma.

[c]For the formula of the elastic energy transfer see chapter 5 of this thesis.
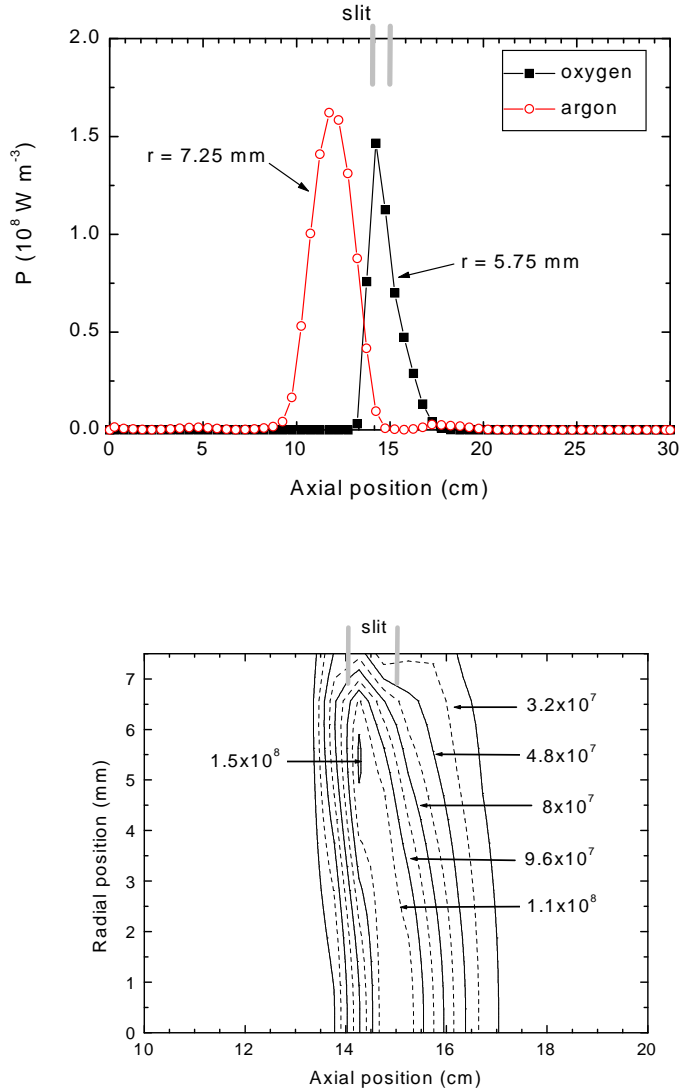
Figure 8.6: Computed MW power in the plasma region. Top: comparison of the peak values for the argon (presented in chapter 7 of this thesis) and oxygen plasmas; bottom: contour plot for the oxygen plasma.

The computed heavy particle temperature T_h is shown in figure 8.8 and is compared with the argon results of chapter 7. Like T_e, T_h is also higher in the oxygen plasma than in the argon plasma. The ratio of the peak values of the electron and heavy particle temperatures, $T_e^{\max}/T_h^{\max}$, is slightly larger in the oxygen plasma than in the argon plasma: $T_e^{\max}/T_h^{\max} \approx 3.2$ for oxygen and 2.9 for argon. This means that, with respect to the thermal coupling between $\{e\}$ and $\{h\}$, in the oxygen plasma there is a stronger non-LTE behaviour in the central plasma region than in
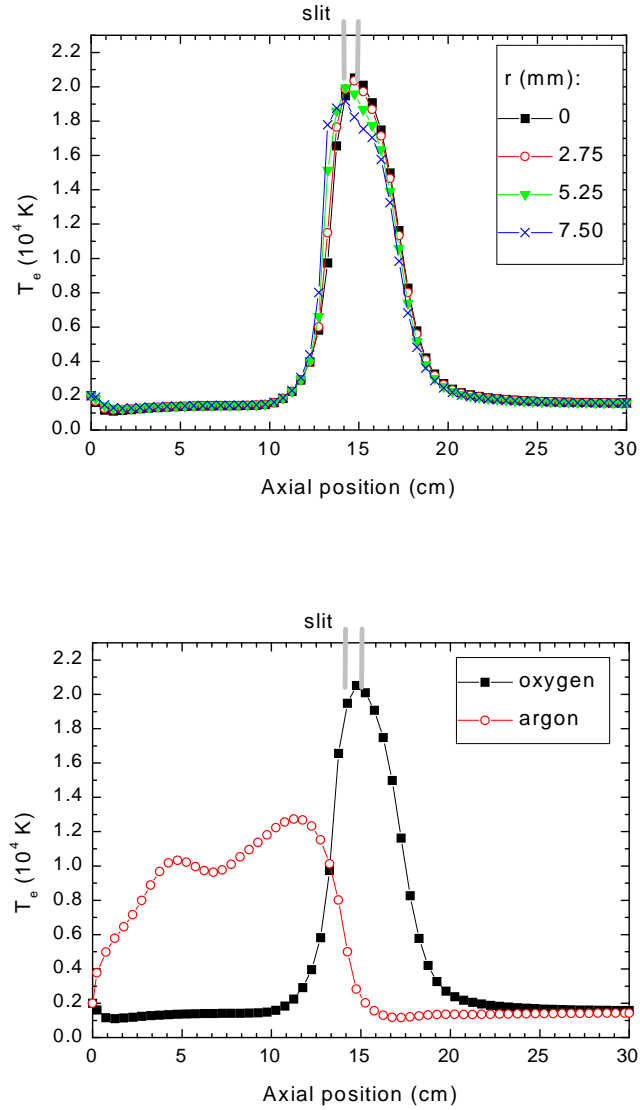
Figure 8.7: Computed electron temperature. Top: at four different radii in the plasma region; bottom: comparison of the computed maximum values, located at the symmetry axis, of the oxygen and argon results (see chapter 7).

the argon plasma.

The computed mass fraction of the dominant oxygen ion, O^+ is shown in figure 8.9. One can see that in the molecular oxygen plasma, the ionisation degree is substantially lower than in the atomic argon plasma (compare with figure 7.8). The top value of the oxygen atomic ion fraction is $y_{O^+} \approx 7.7 \times 10^{-4}$, for the argon results of chapter 7 the maximum argon ion mass fraction is $y_{Ar^+} \approx 3.9 \times 10^{-2}$. Converted to number densities, $n_e^{\text{oxygen}} \approx 2.0 \times 10^{19} \text{ m}^{-3}$ and
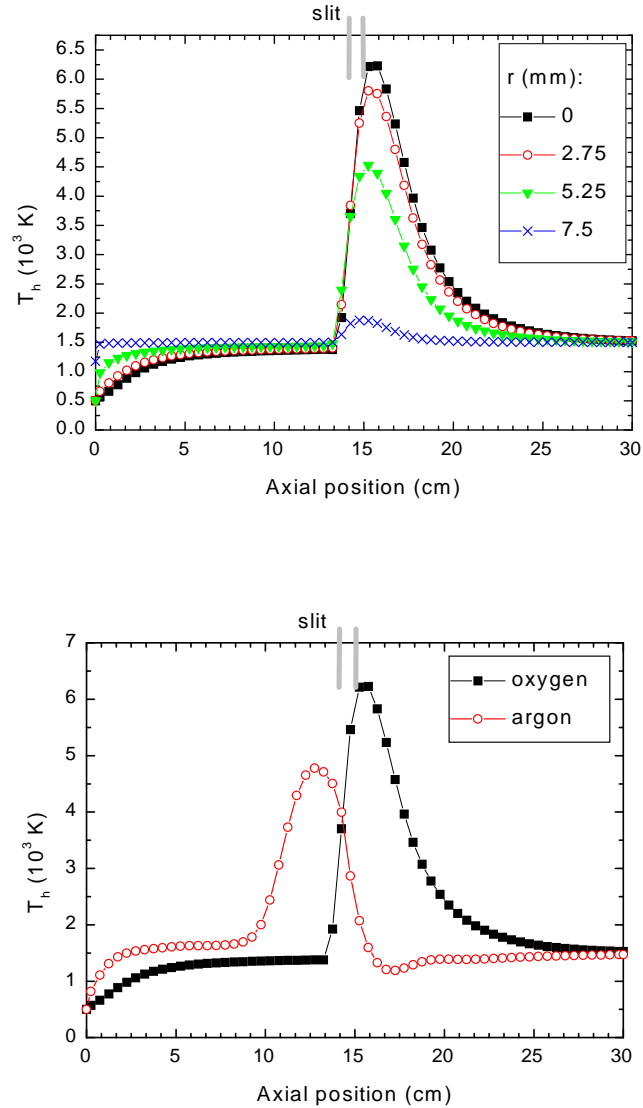
Figure 8.8: Computed heavy particle temperature. Top: at four different radii in the plasma region; bottom: comparison of the computed peak values, located at the symmetry axis, of the oxygen and argon results (see chapter 7).

$n_e^{\mathrm{argon}} \approx 2.3 \times 10^{21}$ m^{-3}. The number density n_e being lower in a molecular plasma compared to an atomic plasma can be explained by the molecular dissociation processes, given in sections 8.3.2 and 8.3.3.

The three most dominant mass fractions in the oxygen plasma, y_{O_2}, y_O and y_{O^+} are shown in figure 8.10. It is clearly seen, that at the used low input power, namely 400 W, mainly molecular and atomic oxygen are present.
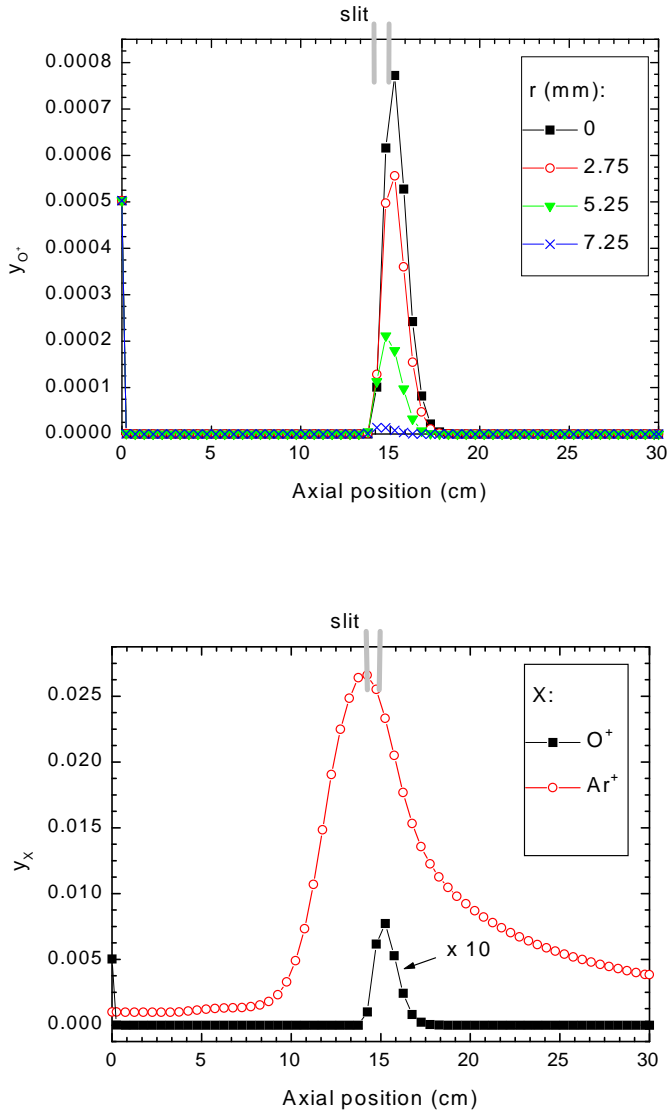
Figure 8.9: *Computed mass fraction of O^+. Top: at four different radii in the plasma region; bottom: comparison of the computed peak values, located at the symmetry axis, of the oxygen and argon results (see chapter 7).*

8.4.2   The influence of metastable states

We will now focus on the possible influence of two metastables states on the behaviour of the oxygen plasma. A future project could be to include the metastables in the oxygen model.

The most important population mechanism for the metastable molecule $O_2(a^1\Delta_g)$ (the energy
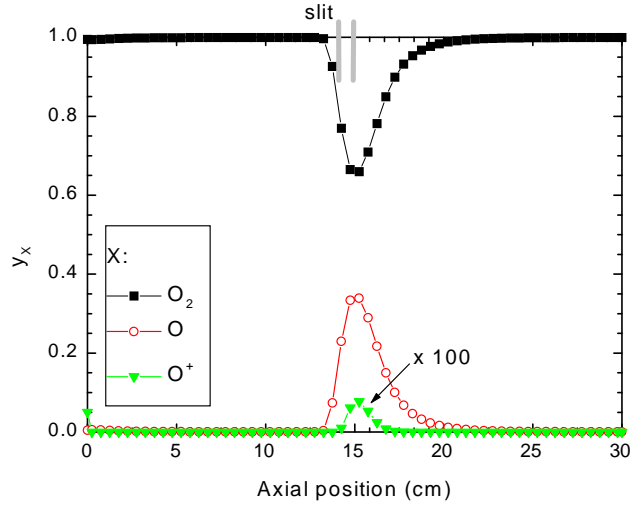
Figure 8.10: *Computed dominant mass fractions in the oxygen plasma (for $r = 0$).*

difference with the O_2 groundstate is $\Delta E_{O_2(X^3\sum)-O_2(a^1\Delta_g)} = 0.98$ eV) is:

$$O_2(X^3 \sum) + e \rightarrow O_2(a^1\Delta) + e \tag{8.16}$$
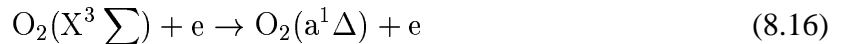
Without going into too much detail, the destruction of $O_2(a^1\Delta_g)$ can take place in various ways, the most important ones are [175]:

$$\begin{aligned}
O_2(a^1\Delta) + e &\rightarrow O_2(X^3 \sum) + e & \text{(8.17)} \\
&\rightarrow O_2(b^1 \sum) + e & \text{(8.18)} \\
&\rightarrow O^- + O(^3P) & \text{(8.19)} \\
&\rightarrow O(^1D) + O(^3P) + e & \text{(8.20)} \\
O_2(a^1\Delta) + O^- &\rightarrow O_3 + e & \text{(8.21)} \\
O_2(a^1\Delta) + O_3 &\rightarrow 2O_2(X^3 \sum) + O(^1D) & \text{(8.22)}
\end{aligned}$$
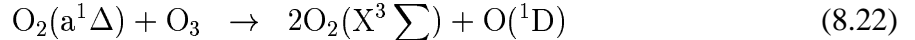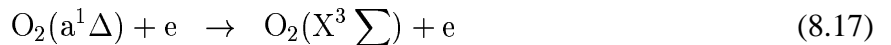
Furthermore Gousset *et al.* [175] identified a possible quenching mechanism for $O_2(a^1\Delta)$ via $O_2(c^1 \sum)$, $O_2(A^3 \sum)$ and $O_2(C^3\Delta)$. It is possible that including $O_2(a^1\Delta_g)$ in the model, would increase the dissociation degree in the oxygen plasma, via reaction (8.19) or (8.20).

The other metastable that has our attention is $O(^1D)$ (with $\Delta E_{O(^3P)-O(^1D)} = 1.968$ eV). Its possible importance for the oxygen plasma can be illustrated by the following set of reactions. Apart form the production mechanism listed above (reactions (8.20) and (8.22)) we have, following Vialle *et al.* [184]:

$$\begin{aligned}
O_2(X^3 \sum) + e &\rightarrow O(^1D) + O(^3P) + e & \text{(8.23)} \\
O(^3P) + e &\rightarrow O(^1D) + e & \text{(8.24)}
\end{aligned}$$
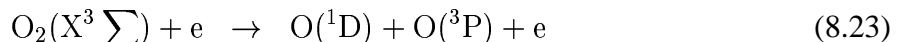
Apart from the reverse processes, it is mainly destroyed via [184]:

$$O(^1D) + O_2(X^3\textstyle\sum) \quad \rightarrow \quad O(^3P) + O_2(b^1\textstyle\sum) \tag{8.25}$$
$$\rightarrow \quad O(^3P) + O_2(a^1\Delta) \tag{8.26}$$
$$O(^1D) + O(^3P) \quad \rightarrow \quad O(^3P) + O(^3P) \tag{8.27}$$
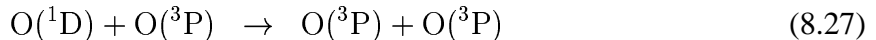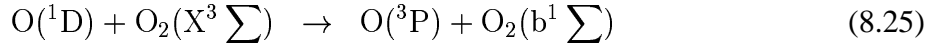
This suggests that inclusion of the metastable $O(^1D)$ could also increase the dissociation degree in the oxygen plasma, via possible dissociation of $O_2(a^1\Delta_g)$ (reactions (8.19) and (8.20)) and $O_2(b^1\textstyle\sum)$.

Not all of the above reactions are very fast [175, 184], which suggests that if $O_2(a^1\Delta_g)$ and $O(^1D)$ are taken into account in the model they have to be included as TS species.

8.5   Conclusions

The first results of the numerical simulations of the oxygen plasma at thermal non-equilibrium conditions have been presented and compared with the results of the argon simulations presented in chapter 7. Large differences exist between the results for the oxygen and argon plasmas, which can be explained. The developed oxygen model is relatively simple, compared with the non-LTE hydrogen model presented in chapter 5. Together with the possible extensions that are recognised, it will form a good basis for the next step in the numerical simulation of the optical fibre production process.

Acknowledgements

Chapter 9

General Conclusions

The present research had three main goals.

The first goal was to design a general plasma simulation tool, PLASIMO, capable of numerically simulating plasmas for a wide pressure range (approximately 10^1 to 10^6 Pa), from LTE (i.e. Local Thermal Equilibrium) to non-LTE and with different energy coupling mechanisms. By splitting the software into three main parts, namely a *configuration* part, a *transport* part and a *composition* part, a modular set-up was obtained. In this way it was possible to develop a tool for the numerical simulation of various plasma configurations. *(Chapters 1 and 2)*.

The second goal was to design a correct formulation for the self-consistent diffusion of plasmas in thermal and chemical non-equilibrium, which is needed for the numerical simulation of molecular plasmas. A complete description is presented of self-consistent multi-component diffusion in plasmas including the two-temperature character of a plasma and the influence of the various types of diffusion: ordinary, pressure, forced and thermal diffusion. It is based on the solution of the set of so-called Stefan-Maxwell equations. The influence of forced diffusion, which is expected to play an important role (apart from ordinary diffusion) in a plasma, was found to be limited in a hydrogen cascaded arc plasma. It is to be expected that for gas mixtures with (large) differences in ionisation energy and mass of the particles, the influence of forced diffusion and thermal diffusion can be large, especially in case these systems are in non-LTE *(Chapter 3)*.

The third goal was to apply PLASIMO to a few open plasma configurations. The main conclusions for the various applications are the following:

- The results of the numerical simulation of a flowing atomic argon cascaded arc (CA) plasma agree well with experimental results. It proves that the argon CA plasma is simulated adequately with a one-dimensional model for the electric field. A study has been performed on the influence of the boundary conditions on the results of the simulations. Only the outlet boundary conditions influence the plasma behaviour in the whole CA, the influence of inlet and wall boundary is limited *(Chapter 2)*.

- A thorough study is performed of the hydrogen CA plasma. An efficient hydrogen plasma source based on the CA is designed, for LTE conditions. The designed configuration produces hydrogen ion power fluxes of at least 10 MW m^{-2}, which implies that the CA is an excellent candidate for the study of divertor-like plasmas. A study of a hydrogen CA

plasma for non-LTE conditions reveals that especially in the central plasma region thermal non-equilibrium is present, whereas in the outer plasma regions, near the channel wall, thermal equilibrium is reached. The pronounced "sombrero" profile as found in the LTE hydrogen CA plasma is less pronounced in the non-LTE simulations.

The major role of H_2^+ as an "intermediate" species in the hydrogen plasma is recognised. Although its concentration is very small, the (fast) H_2^+ reactions are very important in the destruction of H_2. Accurate knowledge of the wall reaction coefficient γ_H is required, because the association of 2 H at the wall to H_2 has a large influence on the dissociation degree in the CA *(Chapters 4 and 5)*.

- The PLASIMO tool is validated in a code-to-code comparison with the commercially available tool PHOENICS CVD for the flow of a non-reacting argon-silane gas mixture in the subsonic region of a deposition chamber. The code-to-code validation shows very good agreement between the results of the two tools. The influence of thermal diffusion on the results of the numerical simulation is very similar, although the formulation of thermal diffusion in PLASIMO is more approximate than that in PHOENICS CVD. A code-to-experiment validation is performed for an argon plasma in the subsonic region of a deposition chamber. There is a reasonable agreement between experiments and the results of the numerical simulations, if the principle of an expansion angle of 45° is not used, although more experimental information is needed to confirm the accuracy of the computed profiles *(Chapter 6)*.

- The first two steps in modelling the microwave plasma used in the production of optical fibres (i.e. a plasma consisting of O_2, $SiCl_4$ and $GeCl_4$) have been taken. The first step is the realization of a microwave energy coupling module and adding it to PLASIMO. The first results of the numerical simulation of an argon microwave plasma agree with visual observations. The second step is formed by non-LTE oxygen plasma simulations. Large differences exist between the results of the numerical simulations for the oxygen and argon plasmas, which are a consequence of the different characteristics of oxygen and argon. The results of the numerical simulations have to be validated quantitatively by future experiments. The developed oxygen model, with its possible extensions, will form a good basis for the next steps in the numerical simulation of the complex optical fibre production process *(Chapters 7 and 8)*.

References

[1] J. Jonkers, M. Bakker, and J.A.M. van der Mullen, J. Phys. D: Appl. Phys. **30**, 1928 (1997).

[2] C.W. Johnston, The Sulphur Lamp - design of a numerical model ISBN 90-5282-942-X (1999).

[3] J.P. Boeuf and L.C. Pitchford, IEEE Trans. Plasma Sci. **24**, 95 (1996).

[4] P. Fauchais, High Temp. Chem. Process. **1**, 1 (1992).

[5] M.I. Boulos, P. Fauchais, and E. Pfender, editors, *Thermal Plasmas, Fundamentals and Applications, Vol.1*, (New York: Plenum Press) (1994).

[6] G.J. Nienhuis and W.J. Goedheer, J. Appl. Phys. **82**(5), 1 (1997).

[7] M.C.M. van de Sanden, W.M.M. Kessels, R.J. Severens, and D.C. Schram, Plasma Phys. Control. Fusion **41**, A365 (1999).

[8] J.W.A.M. Gielen, W.M.M. Kessels, M.C.M. van de Sanden, and D.C. Schram, J. Appl. Phys. **82**, 2643 (1996).

[9] A.H. van Bergen and T. Breuls, IWCS Proceedings **47**, 66 (1998).

[10] M.J. de Graaf, Ph.D. thesis, Eindhoven University of Technology (1994).

[11] G.H.P.M. Swinkels, Ph.D. thesis, Eindhoven University of Technology (1999).

[12] P.W.J.M. Boumans, editor, *Inductively Coupled Plasma Emission Spectroscopy*, (New York: Wiley & Sons) (1987).

[13] C.I.M. Beenakker, B. Bosman, and P.W.J.M. Bosman, Spectrochim. Acta. **33B**, 373 (1978).

[14] M. Moisan and Z. Zakrzewski, J. Phys. D: Appl. Phys. **24**, 1025 (1991).

[15] J. Jonkers, L.J.M. Selen, J.A.M. van der Mullen, E.A.H. Timmermans, and D.C. Schram, Plasma Sources Sci. Technol **6**, 533 (1997).

[16] O. Fukumasa, J. Phys. D: Appl. Phys. **22**, 1668 (1989).

[17] R. Benotti, G. Bonizzoni, and E. Sindoni, editors, *Thermal Plasmas for Hazardous Waste Treatment*, (Singapore: World Scientific) (1995).

[18] P.A.A. Pijpers, Design of a high power cascade arc ISBN 90-5282-677-3 (1996).

[19] M. Klein, Ph.D. thesis, University of California (1969).

[20] M. Meyyappan, Computational Modeling in Semiconductor Processing (Boston: Artech House) (1995).

[21] G.J. Nienhuis and W.J. Goedheer, Plasma Sources Sci. Technol. **8**, 295 (1999).

[22] J. Mostaghimi, P. Proulx, and M.I. Boulos, J. Appl. Phys. **61**(5), 1753 (1987).

[23] J. Mostaghimi and M.I. Boulos, J. Appl. Phys. **68**(6), 2643 (1990).

[24] R. Ye, P. Proulx, and M.I. Boulos, Int. J. Heat Mass Transfer **42**, 1585 (1999).

[25] D. Vanden Abeele and G. Degrez, AIAA paper 98-2825 (1998).

[26] J.D. Ramshaw and C.H. Chang, Plasma Chem. Plasma Proc. **12**(3), 299 (1992).

[27] J.M. Bauchire, J.J. Gonzales, and A. Gleizes, Plasma Chem. Plasma Proc. **17**(4), 409 (1997).

[28] M. Suzuki, Y. Sato, and H. Akatsuka, Plasma Chem. Plasma Proc. **16**(4), 399 (1995).

168

[29] S. Paik, P.C. Huang, J. Heberlein, and E. Pfender, Plasma Chem. Plasma Proc. **13**(3), 379 (1993).

[30] E.C.J.N. de Jong, Graduation report Eindhoven University of Technology VDF/NT 91-08 (1991).

[31] D.A. Benoy, Ph.D. thesis, Eindhoven University of Technology (1993).

[32] J. van Dijk, Graduation report Eindhoven University of Technology VDF/NT 96-14 (1996).

[33] D.A. Benoy, K.T.A.L. Burm, J. Jonkers, J.A.M. van der Mullen, and D.C. Schram, 7th Int. Symp. on the Sci. & Techn. of Light Sources (LS:7), Kyoto page 227 (1995).

[34] G.M. Janssen, J. van Dijk, D.A. Benoy, M.A. Tas, K.T.A.L. Burm, W.J. Goedheer, J.A.M. van der Mullen, and D.C. Schram, Plasma Sources Sci. Technol. **8**, 1 (1999).

[35] J.J. Beulens, D. Milojevic, D.C.Schram, and P.M. Vallinga, Phys. of Fluids **B 3**(9), 2548 (1991).

[36] C.K. Birdsall, IEEE Trans. Plasma Sci. **19**, 65 (1991).

[37] M.J. Kushner, J. Appl. Phys. **63**, 2532 (1988).

[38] A. Bogaerts, Ph.D. thesis, University Antwerpen (1996).

[39] H.K. Versteeg and W. Malalasekera, editors, *An introduction to computational fluid dynamics. The finite volume method*, (Harlow: Longman Group Ltd) (1995).

[40] J.O. Hirschfelder, C.F. Curtiss, and R.B. Bird, editors, *Molecular Theory of Gases and Liquids*, (New York: Wiley & Sons) (1964).

[41] M. Mitchner and C.H. Kruger, editors, *Partially Ionized Gases*, (New York: Wiley & Sons) (1973).

[42] K.T.A.L. Burm, W.J. Goedheer, J.A.M. van der Mullen, G.M. Janssen, and D.C. Schram, Plasma Sources Sci. Technol. **7**, 395 (1998).

[43] D.A. Benoy, E.C.J.N. de Jong, F.H.A.C. Fey, J.A.M. van der Mullen, and D.C. Schram, J. of High Temp. Chem. Processes **1**, 367 (1992).

[44] J. Jonkers, M. Bakker, J.A.M. van der Mullen, D.A. Benoy, K.T.A.L. Burm, and D.C. Schram, 7th Int. Symp. on the Sci. & Techn. of Light Sources (LS:7), Kyoto page 37 (1995).

[45] M.S. Benilov and A. Marotta, J. Phys. D: Appl. Phys. **28**, 1869 (1995).

[46] S.V. Patankar, editor, *Numerical Heat Transfer and Fluid Flow*, (New York: McGraw-Hill) (1980).

[47] J. van Dijk, R.M.J. Haanraads, and J.A.M. van der Mullen, 8th Int. Symp. on the Sci. & Techn. of Light Sources (LS:8), Greifswald page 408 (1998).

[48] C.M. Rhie and W.L. Chow, AIAA Journal **21**(11), 1525 (1983).

[49] S. Majumdar, Num. Heat Transfer **13**, 125 (1988).

[50] K.C.Karki and S.V. Patankar, AIAA Journal **27**, 1167 (1989).

[51] D.A. Benoy, to be published.

[52] C.D. Mobley and R.J. Stewart, Journal of Comp. Phys. **34**, 124 (1980).

[53] G.E. Schneider and M. Zedan, Num. Heat Transfer **4**, 1 (1981).

[54] H.L. Stone, SIAM J. Num. Anal. **5**, 530 (1968).

[55] E.C.J.N. de Jong, J.A.M. van der Mullen, F.H.A.G. Fey, and D.A. Benoy, 1st European Workshop on Plasma-Ion-Surface Engineering (Toulouse) page 391 (1991).

[56] P.J. Chantry, J. Appl. Phys. **62**, 1141 (1987).

[57] L.S. Frost, J. Appl. Phys. **32**, 2029 (1961).

[58] C.H. Kruger, M. Mitchner, and U. Daybelge, AIAA Journal **6**, 1712 (1968).

[59] S. Schweitzer and M. Mitchner, AIAA Journal **10**(4), 799 (1967).

[60] R.S. Devoto, Phys. of Fluids **9**(6), 1230 (1966).

[61] H. Maecker, Z. Naturforsch. **11a**, 457 (1956).

[62] G.M.W. Kroesen, D.C. Schram, and J.C.M de Haas, Plasma Chem. Plasma Proc. **10**(4), 531 (1990).

[63] H.J.G. Gielen, Ph.D. thesis, Eindhoven University of Technology (1989).

[64] K.T.A.L. Burm, W.J. Goedheer, and D.C. Schram, Phys. Plasmas **6**(6), 2622 1999.

[65] C.H. Chang and J.D. Ramshaw, Plasma Chem. Plasma Proc. **13**(2), 189 (1993).

[66] B. Laufer, A. Kaminska, and M. Dudeck, AIAA Journal (), 3204 (1997).

[67] D.A. Benoy, J.A.M. van der Mullen, and D.C. Schram, J. Quant. Spectrosc. Radiat. Transfer **46**, 195 (1991).

[68] J.A.M. van der Mullen, Phys. Rep. **191**, 109 (1990).

[69] F. Westley, J.T. Herron, and W.G. Mallard, editors, *NIST Chemical Database 17, version 4.01*, (Gaithersburg: National Institute of Standards and Technology (NIST)) (1992).

[70] I.P. Shkarofsky, T.W. Johnston, and M.P. Bachynski, editors, *The Particle Kinetics of Plasmas*, Addison Wesley (1966).

[71] A.T.M. Wilbers, J.J Beulens, and D.C. Schram, J. Quant. Spectrosc. Radiat. Transfer **46**(5), 385 (1991).

[72] D.A. Benoy, J.A.M. van der Mullen, and D.C. Schram, J. Phys. D: Appl. Phys. **26**, 1408 (1993).

[73] H.R. Griem, editor, *Plasma Spectroscopy*, (New York: McGraw-Hill) (1964).

[74] G.M.W. Kroesen, Ph.D. thesis, Eindhoven University of Technology (1988).

[75] J.J. Beulens, M.J. de Graaf, G.M.W. Kroesen, and D.C.Schram, Proc. of the Materials Research Soc., San Francisco **190**, 311 (1990).

[76] K.T.A.L. Burm, Private communication (1998).

[77] K. Sutton and P.A. Gnoffo, AIAA Journal **98-2575** (1998).

[78] J.D. Ramshaw and C.H. Chang, Plasma Chem. Plasma Proc. **13**(3), 489 (1993).

[79] J.D. Ramshaw, J. Non-Equilib. Thermodyn. **21**(3), 233 (1996).

[80] G.M. Janssen, J. van Dijk, W.J. Goedheer, and J.A.M. van der Mullen, to be submitted (2000).

[81] V.E. Golant, A.P. Zhilinsky, and I.E. Sakharov, editors, *Fundamentals of Plasma Physics*, (New York: Wiley & Sons) (1980).

[82] V.M. Lelevkin, D.K. Otorbaev, and D.C. Schram, editors, *Physics of Non-Equilibrium Plasmas*, (Amsterdam: Elsevier) (1992).

[83] A.B. Murphy, Phys. Rev. E **48**(5), 3594 (1993).

170

[84] A.B. Murphy, Phys. Rev. E **50**(6), 5145 (1994).

[85] J.D. Ramshaw, J.Non-Equilib. Thermodyn. **15**(3), 295 (1990).

[86] J.D. Ramshaw and C.H. Chang, Plasma Chem. Plasma Proc. **11**(3), 395 (1991).

[87] J.D. Ramshaw, J. Non-Equilib. Thermodyn. **18**(2), 121 (1993).

[88] J.D. Ramshaw, J. Non-Equilib. Thermodyn. **21**(1), 99 (1996).

[89] A.F. Kolesnikov and G.A. Tirskii, Proc. Models in the Mechanics of Continuum Media, (Institute of Theoretical and Applied Mechanics, Novosibirsk, Siberian Branch of Russian Academy of Sciences), 114 (1979).

[90] A.F. Koleshnikov, Self-consistent Stefan-Maxwell relations for multi-component diffusion in two-temperature plasma mixtures, VKI TN 196, von Karman Institute for Fluid Dynamics, St.-Genesius-Rode, Belgium (1999).

[91] D. Vanden Abeele and G. Degrez, AIAA paper 2000-2416 (2000).

[92] A.B. Murphy, Phys. Rev. E **55**(6), 7473 (1997).

[93] A.B. Murphy, J. Phys. D: Appl. Phys. **31**, 3383 (1998).

[94] E.H. Holt and R.E. Haskell, editors, *Foundations of Plasma Dynamics*, (New York: The Macmillan Company) (1965).

[95] A. Einstein, Ann. Physik **17**, 549 (1905).

[96] H.J.G. Gielen and D.C. Schram, IEEE Trans. Plasma Sci. **18**, 127 (1990).

[97] J.A.M. van der Mullen and J. Jonkers, Spectrochim. Acta **54B**, 1017 (1999).

[98] D.C. Schram, J.C.M. de Haas, J.A.M. van der Mullen, and M.C.M. van de Sanden, Plasma Chem. Plasma Proc. **16**(1), 19S (1996).

[99] W.M.M. Kessels, M.C.M. van de Sanden, R.J. Severens, and D.C. Schram, Progress in Plasma Proc. of Materials 1999 page 869 (1976).

[100] G.K. Verboom, Plasma Physics **11**, 903 (1969).

[101] Z. Qing, E.B. Kulumbaev, V.F. Semenov, V.M. Lelevkin, D.K. Otorbaev, M.C.M. van de Sanden, and D.C. Schram, Proc. XII ESCAMPIG (Noordwijkerhout, The Netherlands) page 428 (1994).

[102] S.V. Dresvin, editor, *Physics and Technology of Low-Temperature Plasmas*, (Ames: Iowa State University Press) (1977).

[103] R.K. Scott and F.P Incropera, AIAA Journal **11**(12), 1714 (1973).

[104] B.B. Kadomtsev, editor, *Tokamak plasma: a complex physical system*, (Bristol & Philadelphia: IOP Publishing Ltd) (1992).

[105] C.S. Pitcher and P.C. Stangeby, Plasma Phys. Control. Fusion **39**, 779 (1997).

[106] Z. Qing, Experimental characterization of a hydrogen / argon cascaded arc plasma source ISBN 90-5282-226-3 (1992).

[107] Y.S. Touloukian, R.W. Powell, C.Y. Ho, and P.G. Klemens, editors, *Thermophys. Prop. of Matter, vol. 1*, (New York: IFI / PlenumData Corp.) (1970).

[108] E. Bourdin, P. Fauchais, and M. Boulos, Int. J. Heat Mass Transfer **26**(4), 567 (1983).

[109] J.A.M. van der Mullen, D.A. Benoy, F.H.A.G. Fey, B. van der Sijde, and J. Vlček, Phys. Rev. E **50**(5), 3925 (1994).

[110] K. Chen and T.L. Eddy, J. Non-Equilib. Thermodyn. **18**, 1 (1993).

[111] A.A. Radzig and B.M. Smirnov, editors, *Reference Data on Atoms, Molecules, and Ions*, (Heidelberg: Springer-Verlag) (1985).

[112] J.N. Butler and R.S. Brokaw, J. Chem. Phys. **26**(6), 1636 (1956).

[113] H.W. Drawin, Z. Physik **225**, 483 (1969).

[114] H.W. Drawin and F. Emard, Physica **85C**, 333 (1977).

[115] M.J. de Graaf, R.P. Dahija, J.L. Jeauberteau, F.J. de Hoog, M.J.F. van de Sande, and D.C. Schram, Coll. Phys. **18 C5**, 387 (1990).

[116] Z. Qing, Ph.D. thesis, Eindhoven University of Technology (1995).

[117] G.M. Janssen, C.W. Johnston, W.J. Goedheer, J.A.M. van der Mullen, and D.C. Schram, submitted for publication to Plasma Sources Sci. Technol. (2000).

[118] V.P. Silakov, A.A. Matveyev, A.V. Chebotarev, and D.K. Otorbaev, J. Phys. D: Appl. Phys. **29**, 2111 (1996).

[119] Y. Pigarov and S.I. Krasheninnikov, Phys. Lett. A **222**, 251 (1996).

[120] R.K. Janev, W.D. Langer, K. Evans Jr., and D.E. Post Jr., editors, *Elementary Processes in Hydrogen - Helium Plasmas*, (Berlin: Springer Verlag) (1987).

[121] C.H. Kruger, Plasma Chem. Plasma Proc. **9**(4), 435 (1989).

[122] M.A. Morrison, R.W. Crompton, B.C. Saha, and Z.Lj. Petrović, Aust. J. Phys. **40**, 239 (1987).

[123] A.V. Phelps, J. Phys. Chem. Ref. Data. **19**(3), 653 (1990).

[124] A. Hartgers, J. van Dijk, J. Jonkers, and J.A.M. van der Mullen, submitted to Comp. Phys. Comm. (2000).

[125] L. Vriens and A.H.M. Smeets, Phys. Rev. A **22**, 940 (1980).

[126] J.A.M. van der Mullen, Spectrochim. Acta **45B**, 1 (1990).

[127] P. Michel, S. Pfau, A. Rutscher, and R. Winkler, Beitr. Plasmaphys. **20**, 25 (1980).

[128] M. Capitelli, R. Celimberto, and M. Cacciatore, Adv. At. Mol. Opt. Phys. ed: M. Imokuti (London: Academic) (1994).

[129] M. Cacciatore and G.D. Billing, J. Phys. Chem. **96**, 217 (1992).

[130] K.P. Huber and G. Herzberg, editors, *Molecular spectra and molecular structure 4: Constants of diatomic molecules*, (New York: Van Nostrand Reinhold) (1979).

[131] J.P. England, M.T. Elford, and R.W. Crompton, Aust. J. Phys. **41**, 573 (1988).

[132] G. Herzberg, editor, *Molecular spectra and molecular structure 1: Spectra of diatomic molecules*, (London: Van Nostrand) (1965).

[133] J.B.A. Mitchell, Proc. Workshop Diss. Recomb., Theory, Experiment and Applications III (Ein Gedi, Israel) (D. Zajfman, J.B.A. Mitchell, D. Schwalm and B.R. Rowe (editors)), 21 (1995).

[134] P.H. de Haan, G.C.A.M. Janssen, H.J. Hopman, and E.H.A. Granneman, Phys. of Fluids. **25**(4), 592 (1982).

[135] B.J. Wood and H. Wise, J. Phys. Chem. **65**, 1976 (1961).

[136] O. Fukumasa, R. Itatani, and S. Saeki, J. Phys. D: Appl. Phys. **18**, 2433 (1985).

[137] B. Jackson and M. Persson, J. Chem. Phys. **96**(3), 2378 (1992).

172

[138] L. St-Onge and M. Moisan, Plasma Chem. Plasma Proc. **14**(2), 87 (1994).

[139] C.K. Chen, T.C. Chin Wei, L.R. Collins, and J. Phillips, J. Phys. D: Appl. Phys. **32**, 688 (1999).

[140] D.K. Otorbaev, M.C.M. van de Sanden, and D.C. Schram, Plasma Sources Sci. Technol. **4**, 293 (1995).

[141] B.J. Wood and H. Wise, J. Phys. Chem. **66**, 1049 (1962).

[142] M. Green, K.R. Jennings, J.W. Linnett, and D. Schoffield, Trans. Faraday Soc. **55**, 2152 (1959).

[143] Y.C. Kim and M. Boudart, Langmuir **7**, 2999 (1991).

[144] Th. Kammler, S. Wehner, and J. Kuppers, J. Chem. Phys. **109**(10), 4071 (1998).

[145] D.V. Shalashilin and B. Jackson, J. Chem. Phys. **110**(22), 11038 (1999).

[146] T. Amano, J. Chem. Phys. **92**, 6492 (1990).

[147] D.C. Schram, D.K. Otorbaev, R.F.G. Meulenbroeks, M.C.M. van de Sanden, M.J.J. Eerden, and J.A.M. van der Mullen, Proc. Workshop Diss. Recomb., Theory, Experiment and Applications III (Ein Gedi, Israel) (D. Zajfman, J.B.A. Mitchell, D. Schwalm and B.R. Rowe (editors)), 29 (1995).

[148] H.O. Pierson, editor, *Handbook of chemical vapor deposition (CVD): principles, technology and applications*, (Norwich: Noyes Publications) (1999).

[149] M.C.M. van de Sanden, R.J. Severens, J.W.A.M. Gielen, R.M.J. Paffen, and D.C. Schram, Plasma Sources Sci.Technol. **5**, 268 (1996).

[150] The Phoenics J. of Comp. Fluid Dynamics and its appl. **1** - .. (1988 - ..).

[151] C.R. Kleijn, Ph.D. thesis, Delft University of Technology (1991).

[152] R. Clark Jones, Phys. Rev. **59**, 1019 (1941).

[153] M.N. Kogan, editor, *Rarefied gas dynamics*, (New York: Plenum Press) (1969).

[154] D.G. Coronell, Ph.D. thesis, Massachusetts Institute of Technology (1993).

[155] H. Tennekes and J.L. Lumley, editors, *A first course in turbulence*, (Cambridge USA: MIT Press) (1983).

[156] H. Ashkenas and F.S. Sherman, Proc. Rarified Gas Dynamics 4, ed. J.H. de Leeuw (New York: Academic Press) (1966).

[157] W.S. Young, Phys. Fluids **18**(11), 1421 (1975).

[158] R.C. Reid, J.M. Prausnitz, and B.E. Poling, editors, *The Properties of Gases and Liquids*, (New York: McGraw-Hill) (1987).

[159] R.A. Svehla, NASA report NASA-TR 132 (1962).

[160] M.C.M. van de Sanden, Ph.D. thesis, Eindhoven University of Technology (1991).

[161] D.A. Benoy, J.A.M. van der Mullen, M.C.M. van de Sanden, B. van der Sijde, and D.C. Schram, J. Quant. Spectrosc. Radiat. Transfer **49**, 129 (1993).

[162] M. Capitelli, G. Colonna, A. Gicquel, C. Gorse, K. Hassouni, and S. Longo, Phys. Rev. E **54**(2), 1843 (1996).

[163] G.J.H. Brussaard, Ph.D. thesis, Eindhoven University of Technology (1999).

[164] L.M. Biberman, V.S. Vorob'ev, and I.T. Yakubov, Soviet Phys. Usp. **15**, 297 (1973).

[165] P. Geittner, D. Küppers, and H. Lydtin, Appl. Phys. Lett. **28**, 645 (1976).

[166] H. Lydtin, IEEE J. Lightwave Technol. **LT-4**, 1034 (1986).

[167] Th. Hünlich, H. Bauch, R.Th. Kersten, V. Paquet, and G.F. Weidmann, J. Opt. Commun. **8**(4), 122 (1987).

[168] H. Bauch, D. Krause, R.Th. Kersten, V. Paquet, G. Weidmann, J. Mentges, G. Janzen, and E. Raüchle, J. Opt. Commun. **8**(4), 130 (1987).

[169] H. Rau and B. Trafford, J. Phys. D: Appl. Phys. **22**, 1613 (1989).

[170] A.J. Baden Fuller, editor, *Microwaves, an introduction to microwave theory and techniques*, (Oxford: Pergamon Press) (1990).

[171] N. Marcuvitz, editor, *Waveguide handbook*, (New York: McGraw-Hill) (1951).

[172] K.S Yee, IEEE Trans. Antennas Propagat. **AP-14**(8), 302 (1966).

[173] M. Schoenberg and F. Muir, Geophysics **54**(5), 581 (1989).

[174] K.S. Kundert and A. Sangiovanni-Vincentelli, University of California, Berkeley (1986).

[175] G. Gousset, C.M. Ferreira, M. Pinheiro, P.A. Sá, M. Touzeau, M. Vialle, and J. Loureiro, J. Phys. D: Appl. Phys. **24**, 290 (1991).

[176] G. Gousset, M. Touzeau, M. Vialle, and C.M. Ferreira, Plasma Chem. Plasma Process. **9**, 189 (1989).

[177] J. Matsushita, K. Sasaki, and K. Kadota, Proc. 3rd Int. Conf. Reactive Plasmas (ICRP-3) and 14th Symp. Plasma Processing (SPP-14) (Nara, Japan), 297 (1997).

[178] C. Lee, D.B. Graves, M.A. Lieberman, and D.W. Hess, J. Electrochem. Soc. **141**, 1546 (1994).

[179] B. Eliasson and U. Kogelschatz, Basic data for modelling of electrical discharges in gases: oxygen Report KLR 86-11C (Baden: Brown Boveri Konzernforschung) (1986).

[180] J.B. Hasted, editor, *Physics of atomic collisions*, (London: Butterworth) (1972).

[181] M.A. Lieberman and A.J. Lichtenberg, editors, *Principles of Plasma Discharges and Materials Processing*, (New York: Wiley & Sons) (1994).

[182] Y. Itikawa, At. Data Nucl. Data Tables **21**(1), 72 (1978).

[183] S.A. Lawton and A.V. Phelps, J. Chem. Phys **69**(3), 1061 (1978).

[184] M. Vialle, M. Touzeau, G. Gousset, and C.M. Ferreira, J. Phys. D: Appl. Phys. **24**, 301 (1991).

Summary

This thesis describes the design of a general plasma simulation tool, PLASIMO (which stands for PLAsma SImulation MOdel) and its application to several open plasma configurations. PLASIMO solves the conservation equations for mass, momentum and energy (i.e. it is a fluid model) in a specified computational domain. To be applicable to plasmas for a wide pressure range (approximately 10^1 to 10^6 Pa), under LTE (Local Thermal Equilibrium) and non-LTE conditions and with different energy coupling mechanisms, the design of the PLASIMO-software is made modular.

The PLASIMO-software is split into three main parts, namely a *configuration* part, a *transport* part and a *composition* part. The configuration and composition parts consist of modules in which the characteristics of the individual plasma sources and various gases/gas mixtures are stored, respectively. The transport part forms the heart of PLASIMO and contains the tools to solve the set of equations for the conservation of mass, momentum and energy consistently. The configuration and composition parts provide input for the transport part.

Main limitations of PLASIMO are that the plasmas under investigations have to behave as quasi-neutral fluids and that the flow is axi-symmetric, steady and laminar. Due to the modular structure of the software, it is rather straightforward to add new modules. This is proven by the various applications described in this thesis.

To be able to describe molecular plasmas in which different species are dominant in different plasma regions, a correct formulation of the diffusion for plasmas in thermal and chemical non-equilibrium, is needed. Therefore, a complete description is presented of self-consistent multi-component diffusion in plasmas including the two-temperature character of a plasma and the influence of the various types of diffusion: ordinary, pressure, forced and thermal diffusion. It is based on the solution of the set of so-called Stefan-Maxwell equations. From the four diffusion types, ordinary diffusion usually is the most dominant. The influence of forced diffusion and thermal diffusion is studied in a hydrogen cascaded arc (CA) plasma and a non-reacting argon-silane gas mixture in the subsonic region of a vacuum chamber. They were found to be of little influence. However, it is to be expected that for gas mixtures with (large) differences in ionisation energy and mass of the particles, the influence of forced diffusion and thermal diffusion can be large, especially if these systems are in non-LTE.

In the present research, PLASIMO is applied to strongly flowing CA plasmas (argon and hydrogen), expanding jets in the subsonic region of a vacuum chamber (argon-silane gas mixture and argon plasma) and flowing microwave plasmas (argon and oxygen) used for optical fibre production. PLASIMO is also capable of numerically simulating the QL-, TL- and S-lamp, but these configurations are beyond the scope of this thesis.

The atomic argon CA plasma can be simulated very well with PLASIMO. The one-dimensional model for the electric field in the arc proved to be adequate to obtain good agreement of the results of the numerical simulations with those of experiments.

The hydrogen CA plasma is numerically simulated for LTE and non-LTE conditions. Purpose of this work was to design an efficient hydrogen plasma source, based on the CA. This source will be used for the study of divertor-like plasmas in Tokamaks in the FOM-Institute for Plasma

Physics 'Rijnhuizen' in Nieuwegein. From the LTE simulations a configuration was designed that fulfilled the requirement of an ion power flux of at least 10 MW m^{-2}. In the results of the non-LTE computations, the "sombrero-like" cross-sectional temperature profile in the arc, which is very dominant in the LTE computations, appears to be less pronounced. This can partly be explained by the assumptions of the non-LTE hydrogen model. In this respect, important are the rovibrational processes, the completeness of the reaction kinetics, and the wall reaction probability for association of 2 H at the wall to H$_2$. In the reaction kinetics, an important role is played by H$_2^+$, although its number density is small. It is also shown that the wall association probability of H has a large influence on the dissociation degree in the arc.

An expanding non-reacting argon-silane gas mixture in the subsonic region of a vacuum chamber is used to perform a code-to-code comparison with the commercially available tool PHOENICS CVD. It is shown that the results compare very well, which is also true for the influence of thermal diffusion. The expanding argon plasma is used to perform a code-to-experiment validation of PLASIMO. The results of the numerical simulations agree well with the experiments, if the principle of an expansion angle of 45° is not used.

The first steps in the numerical simulation of the microwave plasma used in the production of optical fibres by Plasma Optical Fibre B.V. in Eindhoven, are presented. A microwave energy coupling module is designed and added to the PLASIMO-software. By using this new module, numerical simulations of argon and oxygen plasmas are performed and compared with qualitative observations (argon) and with each other. The results of the argon computations agree well with the observations. The differences between the argon and oxygen computations are explained. Compared to the non-LTE hydrogen model presented in this thesis, the used oxygen model is relatively simple. Therefore, possible ways to extend it are recognised. Whether these extensions are necessary, must be made clear by a quantitative comparison in the future.

Samenvatting

Deze studie heeft betrekking op het ontwerp van een algemeen plasma simulatie model, PLASI-MO (PLAsma SImulation MOdel) en de toepassing daarvan op verschillende stromende plasma configuraties. In PLASIMO worden in een gespecificeerd domein de behoudswetten voor massa, momentum en energie opgelost (het is dus een vloeistofmodel). Om plasma's in een groot drukbereik (van ongeveer 10^1 tot 10^6 Pa), van LTE (Lokaal Thermisch Evenwicht) tot niet-LTE en met verschillende energie-inkoppelings mechanismen te kunnen simuleren, is het ontwerp van de PLASIMO-software modulair gemaakt.

De PLASIMO-code is onderverdeeld in drie hoofddelen, namelijk een *configuratie*deel, een *transport*deel en een *compositie*deel. De configuratie en compositie delen bestaan uit modules waarin de eigenschappen van de individuele plasmabronnen en verscheidene gassen en gasmengsels zijn opgeslagen. Het transportgedeelte vormt het hart van PLASIMO en bevat de gereedschappen om de vergelijkingen voor massa-, momentum- en energiebehoud consistent op te lossen. De configuratie en compositie delen leveren invoer voor het transport gedeelte.

De belangrijkste beperkingen van PLASIMO zijn dat de bestudeerde plasma's beschouwd worden als quasi-neutrale vloeistoffen en dat de stroming axi-symmetrisch, tijdsonafhankelijk en laminair is. De toevoeging van nieuwe modules aan PLASIMO is relatief eenvoudig, hetgeen onder andere wordt aangetoond door de toepassingen die beschreven worden in dit proefontwerp.

Om in staat te zijn moleculaire plasma's te beschrijven waarin verschillende deeltjessoorten in verschillende gebieden dominant aanwezig zijn, moet gebruik gemaakt worden van een correcte beschrijving van diffusie onder omstandigheden waarbij afwijkingen van thermisch en chemisch evenwicht optreden. Dit is de reden waarom een volledige beschrijving van zelf-consistente multi-component diffusie in plasma's wordt gepresenteerd. Hierin is het twee-temperatuur karakter van een plasma en de invloed van de verschillende soorten diffusie, namelijk gewone (concentratiegedreven), druk, geforceerde en thermische diffusie, meegenomen. Deze beschrijving is gebaseerd op de zogenaamde Stefan-Maxwell vergelijkingen. Gewoonlijk is concentratiegedreven diffusie dominant. De invloed van geforceerde en thermische diffusie is bestudeerd in respectievelijk een waterstof cascadeboogplasma en een niet-reagerend argon-silaan gasmengsel in het subsone gebied van een vacuumkamer. Het blijkt dat beide diffusiesoorten weinig invloed hebben op de simulaties. Echter, de verwachting is dat in gasmengsels waarin (grote) verschillen optreden in ionisatieenergie en deeltjesmassa, geforceerde en thermische diffusie wel een belangrijke rol kunnen spelen, in het bijzonder als deze systemen afwijkingen van LTE vertonen.

In dit proefontwerp worden als toepassingen van PLASIMO, een aantal stromende plasma configuraties gesimuleerd: cascadeboogplasma's (argon en waterstof), expanderende jets in het subsone gebied van een vacuumkamer (argon-silaan gasmengsel en argon plasma) en het microgolfplasma (argon en zuurstof) dat gebruikt wordt voor de productie van optische fibers. Daarnaast is PLASIMO ook in staat om de gesloten configuraties QL-, TL- en S-lamp numeriek te simuleren. Deze toepassingen vallen echter buiten het bestek van dit proefontwerp.

Het atomaire argon cascadeboogplasma kan zeer goed numeriek gesimuleerd worden met PLASIMO. Door gebruik te maken van een één-dimensionaal model voor het elektrische veld

in de boog, wordt goede overeenstemming bereikt tussen de resultaten van de simulaties en experimenten.

Het waterstof cascadeboogplasma wordt numeriek gesimuleerd voor LTE en niet-LTE condities. Een van de hoofddoelen van dit onderzoek is het ontwerp van een efficiënte waterstof plasmabron, gebaseerd op de cascadeboog. Deze bron zal door het FOM-Instituut voor Plasma Fysica 'Rijnhuizen' in Nieuwegein gebruikt gaan worden voor de bestudering van divertor-achtige plasma's in Tokamaks. Met behulp van de LTE simulaties is een plasmaconfiguratie ontworpen die voldoet aan de eis van een ionenvermogensflux van 10 MW m^{-2}. Het "sombrero-achtige" profiel van de radiale temperatuursverdeling, dat sterk aanwezig is in de LTE berekeningen, is minder aanwezig in de niet-LTE berekeningen. Dit resultaat kan gedeeltelijk verklaard worden door de aannames in het niet-LTE model. In verband hiermee zijn de rovibrationele processen, de volledigheid van de reaktiekinetiek en kennis van de wandreactiekans voor waterstofassociatie aan de wand belangrijk. In de reactiekinetiek speelt H$_2^+$, ondanks zijn lage deeltjesdichtheid, een belangrijke rol. De wandassociatiekans van atomair waterstof heeft een grote invloed op de dissociatiegraad in de boog.

Om een code-code validatie van PLASIMO uit te voeren met het commerciële beschikbare pakket PHOENICS CVD is een niet-reagerend argon-silaan gasmengsel in het subsone gebied van een vacuumkamer numeriek gesimuleerd met beide pakketten. Aangetoond wordt dat de resultaten van de simulaties zeer goed met elkaar overeenkomen. Dit geldt ook voor de invloed van thermische diffusie. Tevens is een code-experiment validatie uitgevoerd door een expanderend argon plasma numeriek te simuleren in nagenoeg dezelfde vacuumkamer. De resultaten van de berekeningen komen goed overeen met de experimenten, mits het principe van een expansiehoek van 45° wordt losgelaten.

De eerste stappen zijn gezet in de numerieke simulatie van het microgolf plasma dat door Plasma Optical Fibre B.V. in Eindhoven wordt gebruikt in het productieproces van optische fibers. Een microgolfenergie-inkoppelingsmodule is ontworpen en toegevoegd aan PLASIMO. Met behulp van deze nieuwe module zijn numerieke simulaties uitgevoerd van argon en zuurstof plasma's, die vervolgens zijn vergeleken met elkaar en met (kwalitatieve) experimentele waarnemingen (voor argon). Het blijkt dat de overeenstemming met de waarnemingen goed is. Tevens zijn de verschillen tussen de berekeningen voor argon en zuurstof verklaard. Vergeleken met het waterstofmodel voor niet-LTE condities dat ook in dit proefontwerp wordt gepresenteerd, is het gebruikte zuurstofmodel relatief eenvoudig. Vandaar dat mogelijke uitbreidingen worden aangedragen. De noodzaak van die uitbreidingen zal pas blijken na kwantitatieve validatie met behulp van experimenten.

Dankwoord

Onder het inspirerende leiderschap van Joost van der Mullen heb ik ruim drie jaar mogen "proef-ontwerpen". Zijn praktische manier om met fysische problemen om te gaan spreekt me zeer aan, zijn apart gevoel voor humor zorgde menigmaal voor schaterlachen door de gang en in tijden dat het allemaal wat minder ging waren zijn vaderlijke adviezen zeer welkom. Daan Schram wil ik vooral bedanken voor zijn interesse in het waterstof gebeuren: is de dissociatiegraad nu wel of niet 100 % ? Opmerkelijk is, dat Daan vrijwel elk PLASIMO-resultaat dat door mij op het computerscherm werd getoverd fysisch kon verklaren, ook al was de correctheid van die resultaten vaak ver te zoeken. Wim Goedheer, "the best of North-Western Europe", heeft me vanuit FOM-Nieuwegein op zeer prettige wijze begeleid. Hij is niet alleen een absolute kei in zijn vakgebied waarvan ik veel heb opgestoken, maar ook zijn zeer aangename persoonlijkheid en de rust die hij uitstraalt hebben grote indruk op me gemaakt. Mathé van Stralen was namens Plasma Optical Fibre (POF) mijn opdrachtgever in de afgelopen anderhalf jaar. Hij is het brein achter de nieuwe microgolf energie-inkoppelingsmodule, waarvoor ik hem zeer dankbaar ben. Onze samenwerking heb ik als zeer prettig ervaren en de "POFfertjes" die we samen hebben genuttigd waren erg lekker!

Dit proefontwerp was nooit tot stand gekomen zonder de hulp van het PLASIMO-team, die samen de diverse fysische en numerieke problemen te lijf gaan. Jongens: bedankt en succes met PLASIMO in de toekomst! Daarnaast ook een woord van dank aan Jeroen Jonkers, waarmee ik samen heb gekeken naar de modellering van het ICP (waarvan overigens niets is terug te vinden in dit proefontwerp). Mijn kamergenoten - ik heb er nogal wat versleten vanaf het begin van mijn AIO-2 tijd tot het eind van mijn proefontwerp - en die vrijwel allemaal deel uitmaakten van het PLASIMO-team, hebben de sfeer altijd heel gezellig gemaakt. In de begintijd waren dat Dany "roepi roepi" Benoy, Marnix "zullen we even vechten" Tas, Jeroen "ik heb geen scheet gelaten" Jonkers en later de jongere generatie: Colin Johnston, Jan van Dijk, Bart Hartgers, Kurt Garloff en Karel Burm: jongens, zonder jullie was het stukken vervelender geweest! De sfeer binnen ETP is jarenlang erg goed geweest, anders had ik het er zeker niet zolang uitgehouden: bij deze allemaal bedankt! Ik heb er dan ook heel wat vrienden aan over gehouden.

Naast het natuurkundige wereldje, bestaat er gelukkig ook nog zoiets als je directe (sociale) omgeving. Vandaar een bijzonder woord van dank aan mijn (snel)schaakkameraden op de universiteit, Alain Leroux en Arjeh Tal: ik heb altijd erg genoten van onze krachtmetingen. De talloze schaaktoernooien die ik heb afgelopen, samen met enkele clubgenoten van schaakclub 't Pionneke uit Roermond, maakten het heel moeilijk voor me om steeds weer terug te keren naar het computerscherm van mijn workstation. De "donderdagavond-club", die voornamelijk bestaat uit Eindhovense natuurkundigen, wil ik bedanken voor de vele gezellige en ontspannende uren; om op vrijdagochtend hoogstaande fysica te bedrijven was telkens weer een gigantische uitdaging. De bijeenkomsten met mijn makkers uit militaire dienst waren steeds erg amusant en vormden een welkome afwisseling.

Tot slot een woord van dank aan mijn familie, voor hun belangstelling en steun, en in het bijzonder mijn vriendin, Astrid, die me niet alleen gepushed heeft in de laatste maanden van mijn promotie, maar die ook het zonnetje in mijn leven is geworden.

Curriculum Vitae

Ger Janssen was born in Roermond on the 11th of March 1967. From 1979 to 1985 he followed the secondary school in Roermond at the Bisschoppelijk College Broekhin. From 1985 on, he studied Applied Physics at the Eindhoven University of Technology (EUT). After completing his graduation project "Measurements of shock waves using Thomson- and Rayleigh-scattering on an expanding cascaded arc plasma", in the group "Equilibrium and Transport in Plasmas" (ETP) of the Department of Applied Physics at EUT, he received his Masters degree in 1991.

In the beginning of the nineties, the military service still existed and the Dutch Army wanted Ger to join them. So, in 1992 and 1993 he performed his military service in the Artillery. He became an observer of the "43e Afdeling Veldartillerie" in Havelte and reached the rank of lieutenant.

After a year of putting his attention mainly to his big hobby, chess, he started at the end of 1994 the education for Physical Instrumentation of the Stan Ackermans Institute (SAI) at EUT. He performed a joint project of the FOM-Institute for Plasma Physics 'Rijnhuizen' in Nieuwegein and the group ETP at EUT on "The Design of an Efficient Hydrogen Plasma Source Based on the Cascaded Arc". In 1997 he received his "Master of Technological Design" degree. He continued his study as a Ph.D. student of the SAI on the subject "Design of a General Plasma Simulation Model, Fundamental Aspects and Applications". From 1999 on, the main part of his work was performed for Plasma Optical Fibre B.V. in Eindhoven. His thesis was completed in August 2000.